Universitat Autònoma de Barcelona

Engineering Stöber Silica Nanoparticles: Insights into the Growth Mechanism and Development of Silica-Based Nanostructures for Multimodal Imaging

Oscar Hernando Moriones Botero

Engineering Stöber Silica Nanoparticles: Insights into the Growth Mechanism and Development of Silica-Based Nanostructures for Multimodal Imaging

Oscar Hernando Moriones Botero

Bellaterra, 2022

UAB
Universitat Autònoma de Barcelona

ICN2
Institut Català de Nanociència i Nanotecnologia
EXCELENCIA SEVERO OCHOA

Engineering Stöber Silica Nanoparticles: Insights into the Growth Mechanism and Development of Silica-Based Nanostructures for Multimodal Imaging

Engineering Stöber Silica Nanoparticles: Insights into the Growth Mechanism and Development of Silica-Based Nanostructures for Multimodal Imaging

A thesis presented

by

Oscar Hernando Moriones Botero

A thesis submitted to attain the degree of

DOCTOR IN CHEMISTRY of Universitat Autònoma de Barcelona

Directors: Dr. Víctor F. Puntes and Dr. Neus Bastús

Tutor: Dr. Inhar Imaz

2022

“Everything is theoretically impossible, until it is done.”

Robert A. Heinlein.

Table of Contents

V. Experimental Section

VI. Conclusions

VII. Appendix

Acknowledgements

What a fascinating journey has been these past four years, since I embarked on this nano-scale pathway as my new lifestyle. I recognize that the everyday-walking on this scientific trail has not been easy, but it was challenging and enjoyable. It has been my privilege to work and encounter with a lot of pleasant and talented people over the course of my PhD at Catalan Institute of Nanoscience and Nanotechnology (ICN2) and University Autonomous of Barcelona (UAB) of Barcelona, Spain. So I would like to give a special thanks to each and every of the important persons.

Firstly, I would like to express my deep gratitude to my supervisor Prof. Dr. Victor F. Puntes, for gave me the opportunity to work in his amazing group, the *Inorganic Nanoparticles Group (ING).* For inspire me in the field of the metal and metal oxide nanoparticles, for his great support in developing this amazing work and for all the laboratory commodities that he gave me that allowed the mature of my PhD thesis. I will be always in indebted professor.

Similarly, I am extremely grateful to my second supervisor Dr. Neus Gomez Bastús, for her valuable suggestions in the designing of my experimental work throughout all this years, the deep and long discussions of my results in her office, for giving me her valuable knowledge, for the continued encouragement and inspiration during my doctoral studies and finally for hand me down her way of being as a researcher that helped to gain confidence and courage to develop myself as a research scientist.

I wish to express my sincere thanks to all former members and active ones of the *Inorganic Nanoparticles Group (ING),* that walked by my side during my doctoral studies. I would like to further address a sincere thanks to: the Italian “master” Francesco Barbero for his constants advices and friendship, Jordi Piella the Catalan noble-metal “Sage”, for his counsels in synthesis of gold and silver NPs, Javier Patarroyo the “Polyol synthetic Vader”, for helping me in becoming a member of the ING group, for giving me his special friendship and for supporting me in all the scientific troubles I had, the “hard-working” Muriel Freixanet and Dr. Laura Mondragón from VHIR, for all their help during my studies, for

explaining patiently and their incredible biological contributions in the development of my thesis. Moreover, I would like to thank my fellow colleagues: Carmen, Markus, Karen, Elizabeta, Martí and Jana, for the magnificent time, unforgettable experiences shared inside and outside the ICN2. I wish you all the best, you company contributed to my personal and professional growth.

I wish to extend my appreciation to all the members and collaborators of the ICN2 building, for all the support: the crew from Maintenance and Services, IT, Finance, Competitive Funding, Health and Safety and Human resources departments. A special thanks to the members of the Research support facilities: Javier Sainz from Molecular Spectroscopy and Jessica Padilla from the X-ray Diffraction facility. Additionally, from the Research support units: The Electron Microscopy unit, Belen Ballesteros and Marcos Rosado, for teaching me and allowing me the use of the electron microscopies for discover face-to-face my nano-scale creations. Also special thanks to Ignasi Villaroya from the SAQ (Servei de Anàlisi Quìmica, UAB) for the HPLC and ICP-MS services.

I would like to acknowledge and also show my deep gratitude to the government of Spain, for the financial support from the Spanish Ministry of Science and Innovation (MICINN) by the FPI-SO fellowship, resolved by the Agencia Estatal de Investigación (AEI).

Last but not least, I would like to give special thanks my friends: Roberto “Rob” García (my forever “Chemical” friend), Abraham (my “Mexican” brother), Jesús, Daniel “El Chato”, Aliro, Ferrán my catalán friend from “Tesoros Metálicos”, Omar (amazing FIFA gaming together), Paulina, Juanito, Andrés, Suzie and Toni, for the whole enjoyable moments, travels, findings and discussions we had. I am extremely grateful to my family: to my parents, Oscar and Carmen and my sibling Carolina for their love and continuous support. Also, a special thanks with the bottom of my heart, to my future wife, Pilar Martínez, for her unconditional love, mutual respect, her patience, support and encouragement provided me during these years. Also, for bringing to my life, the most adorable, lovely beings “Maja” and “Mojito”, our chihuahua babies. I Love you Pingüi!

Oscar H Moriones.

Motivation and Dissertation Outline

My pathway towards the exiting universe of Nanotechnology begins, when I became an enthusiastic member of the Inorganic Nanoparticles Group (ING) at ICN2. The word “nanoparticle” for me, was only the definition of a material which is at the nanometre scale. The pure conception was exclusively related to their size, not their intrinsic properties. However, what my lack of knowledge was missing, was the part that these interesting small particles own an innate feature of having a large surface area to volume ratio. This remarkable characteristic caused significant effects on the properties of the nanomaterials, such as (increased mechanical strength, different optical properties, altered electrical conductivity and magnetic properties), in comparison with their bulk.

In this regard, our group was focused on the design and development of synthetic strategies for the production of complex nanoparticles. Their main objectives were based on the fine-control of their physicochemical properties, including size, shape, chemical composition, physiochemical stability, crystal structure and surface area. Their main corner-stone nanomaterials, were the noble metals NPs, such as Gold (Au) and silver (Ag), semiconductors, such as, cadmium selenide (CdSe) known as “Quantum dots” and metal oxides, as iron oxide (Fe3O4) nanoparticles. Interesting nanomaterials that present confinement effects that endows exceptional tuneable optical properties (localized surface Plasmon resonance), characteristic X-ray attenuation, enhanced scattering, the ability to convert a spectrum of light into different emitting colours and superior magnetic and contrast agent properties. All highlighted optical-electronics and magnetic features, that are being widely explored for high technology applications, such as biological sensing, bioimaging and drug delivery.

However, to applied these nanomaterials in medical imaging and cell labelling using techniques, such as computed tomography (CT), magnetic resonance imaging (MRI), optical imaging (OI), the need of specific organic ligands or inorganic coatings for avoiding physicochemical transformations, such as (aggregation, melting under irradiation and losing their optical properties) are unavoidable needed for ensuring their stability once expose them in close contact with biological systems.

Nowadays, an inorganic metal-oxide nanomaterial that has been used to assist lessening these challenges, is the silicon dioxide, known as silica (SiO2 NPs). Silica is made of silicon, one of the most widely available material of the Earth's crust. The growth of a thin silica layer on these noble metals and semiconductors surfaces, allowed them to enhance their thermodynamically and chemically stability, increase the biocompatibility, preserve their optical properties, passivate the surface (reducing their high surface energy), enhancing the colloidal stability in water-based medias and the silica shell can be further surface functionalized with different chemical functional groups for bioconjugation with various organic and biologic molecules.

Since the utility of this siliceous oxide nanomaterial has been proved to aid others materials at the nano-scale for numerous biomedical and sensing applications. Therefore, **for my thesis project, we decided to explore in mode detailed, the material capabilities for the development of functional silica-based hybrids nanostructures at the nano-level. Therefore, the functionality of the material was extended creating a dual-label hybrid silica nanocomposite, as a potential multi-contrast agent, suitable for the simultaneously identification by the well-known medical bioimaging techniques**.

In this regard, taking advantage of the expertise in the group on the production of highly monodisperse colloidal nanoparticles**, this thesis aims to fabricate an inorganic-organic complex hybrid nanostructure using silica as supporting material, by applying wet chemistry synthetic methods, for the development of a multifunctional contrast agent with adequate properties for their application in medical imaging**. For that purpose, three main objectives have been addressed: first, the study of the mechanism of nucleation and growth of the SiO2 NPs in order to precisely control the size of the particles. Second, a systematically surface and core modification of the silica nanoparticles, in order to prepare silica-based nanoparticles with functional optical properties and third, exploiting the functionality of the prepared silica hybrids for the development of a hybrid multilayer complex nanostructure with multimodal imaging capabilities.

This manuscript is organized into seven chapters, as follows:

Chapter 1 introduces the field of the production of colloidal silica nanoparticles. It includes a brief scientific review on silica and the wet methodologies for its production, the reported mechanism of nucleation and growth, followed by a description of synthetic strategies for surface and core functionalize the nanomaterial for the production silica-based hybrids systems with synergistic optical properties combining noble metal nanoparticles with silica in a core-shell architecture.

Chapter 2 describes the synthesis and characterization of the silica nanoparticles by the sol-gel method. It includes the evaluation of the different experimental parameters to fine-size tuning the diameter of the nanoparticles. In addition, the detailed time evolution characterization of the mechanism of nucleation and growth is presented.

Chapter 3 presents an experimental methodology for the core and surface functionalization of the silica nanoparticles. The surface charge of the NPs were systematically controlled as a function of pH of the media. The number of amino groups were characterized. Furthermore, the core of the particle was loaded with organic fluorescent molecules for development silica-based fluorescent probes.

Chapter 4 shows a synthetic multilayer strategy for the production of a silica-based hybrid nanostructures as a multimodal contrast agent for the in vivo and in vitro visualization of microplastics. It includes, the evaluation of the experimental synthetic parameters for growing a polymer shell into hybrid core-shell fluorescent SiO_2 and Noble-Metal Au NPs. This chapter includes the preparation of multimodal contrast agent of polystyrene NPs, for the in vivo and in vitro correlation.

Chapter 5 presents the detailed description of the experimental section for the synthesis of the silica nanoparticles and its hybrids.

Chapter 6 contains the general conclusion of this doctoral thesis, future work and perspectives. It includes a list of publications and contributions done during the development of my doctoral studies.

Chapter 7 display the appendix for every chapter. It extended characterization for every chapter.

Resumen

Aprovechando la experiencia del grupo Inorganic Nanoparticles (ING) del ICN2, que tiene como gran experticia en la producción de nanopartículas coloidales altamente monodispersas, **esta tesis tiene como objetivo fabricar una nanoestructura híbrida compleja inorgánica-orgánica utilizando sílice como material de soporte, aplicando métodos sintéticos de química en líquido, para el desarrollo de un agente de contraste multifuncional con propiedades adecuadas para su aplicación en imagen médica**. Para ello se han abordado tres objetivos principales: en primer lugar, el estudio del mecanismo de nucleación y crecimiento de las NPs de SiO_2 para controlar con precisión el tamaño de las partículas. En segundo lugar, una modificación sistemática de la superficie y el núcleo de las nanopartículas de sílice, con el fin de preparar nanopartículas a base de sílice con propiedades ópticas funcionales y, en tercer lugar, explotar la funcionalidad de los híbridos de sílice preparados para el desarrollo de una nanoestructura compleja multicapa híbrida con capacidades de imagen multimodal.

El presente manuscrito está organizado en 7 capítulos, a continuación, se presenta una descripción de los mismos:

El Capítulo 1 introduce el campo de la producción de nanopartículas de sílice de forma coloidal. Incluye una breve revisión científica sobre la sílice y las metodologías sintéticas para su producción, el mecanismo de nucleación y crecimiento, seguido de una descripción de las estrategias sintéticas para la funcionalización de la superficie y el núcleo del nanomaterial para la producción de sistemas híbridos a base de sílice

El Capítulo 2 describe la síntesis y caracterización de las nanopartículas de sílice. Incluye la evaluación de los diferentes parámetros experimentales para el ajuste fino del diámetro de las nanopartículas. Además, se presenta la caracterización detallada de la evolución temporal del mecanismo de nucleación y crecimiento para revelar el mecanismo de formación de la sílice amorfa de Stöber, entendiendo su proceso de mineralización.

El Capítulo 3 presenta una metodología experimental para la funcionalización del núcleo y la superficie de las nanopartículas de sílice. Las carga de superficie de las NPs se controló de manera sistemática en función del pH del medio. Se caracterizó el número de

grupos amino en la superficie. Además, el núcleo de las partículas se cargó con diferentes moléculas orgánicas fluorescentes para desarrollar sondas ópticas basadas en sílice.

El Capítulo 4 muestra una estrategia de multicapa sintética para la producción de nanoestructuras híbridas a base de sílice como un agente de contraste multimodal para la visualización de manera in vivo e in vitro de microplásticos. Incluye, la comprensión de la polimerización con radicales en emulsión para la producción de nanopartículas poliméricas. Además, se realizó una evaluación de los parámetros sintéticos experimentales para hacer crecer una capa de polímero en la estructura núcleo-capa de sílice fluorescente y de metales nobles de Au. Este capítulo incluye la preparación de un agente de contraste multimodal de poliestireno, para la correlación in vivo e in vitro de las partículas poliméricas.

El capítulo 5 presenta la descripción detallada de la sección experimental para la síntesis de las nanopartículas de sílice y sus híbridos. Incluye los reactivos químicos utilizados, la metodología seguida para la síntesis de nanopartículas y las técnicas de caracterización utilizadas para la caracterización fisicoquímica detallada de cada capítulo de esta tesis.

El Capítulo 6, Contiene la conclusión general de esta tesis doctoral, los trabajos a futuro y perspectivas. Incluye una lista de publicaciones y contribuciones realizadas durante el desarrollo de mis estudios de doctorado.

El Capítulo 7 muestra el apéndice de cada capítulo. Incluye la caracterización ampliada para cada capítulo.

List of Abbreviations

AA: Ascorbic acid

Ab: Antibody

ACVA: 4,4 ’-azobis(4-cyanovaleric acid) (ACVA)

AEAPTS: 3-(2-Aminoethylamino)propyltrimethoxysilane

AETAC: Trimethylammonium chloride

AF350: Alexa dye Fluor® 350 NHS Ester

AIBN: 2,2-azobis(isobutyronitrile)

APMA: Methacrylamide hydrochloride (

APMDS: 3-(aminopropylmethy)diethoxy silane

APMS: 3-(aminopropyl)2-(dimethyl)methoxysilane

APTES: 3-(aminopropyl)triethoxysilane

APTMS: 3-(aminopropyl)trimethoxysilane

ATR-FTIR: Attenuated total reflection-Fourier transform infrared

BSA: Bovine serum albumin

CMC: Critical micellar concentration

CTAB: Cetyltrimethylammonium bromide

CTAC: Cetyltrimethylammonium chloride

CTApTS: Cetyltrimethylammonium p-toluene sulfonate

Cy: Cyanine dye

DAMO: N-(2-aminoethyl)-3-aminopropyltrimethoxysilane

DMEM: Dulbecco's Modified Eagle Medium

DMF: Dimethylformamide

DNA: Deoxyribonucleic acid

DOX: Doxorubicin

DVB: 1,4-Divinylbenzene

EDC: 1-etil-3-(3-dimetilaminopropil)carbodiimida hidrocloruro

EDX= Energy dispersive X-ray analysis

Em: Emission

Ex: Excitation

FAM: Carboxyfluorescein

FBS: Fetal bovine serum

FET: Field effect transistors

FITC: Fluorescein isothiocyanate

FRET: Förster resonance energy transfer

GPTMS: 3-glycidoxypropyltrimethoxysilane

GPTS: 3-(glycidyloxypropyl)triethoxysilane

HAADF-STEM: High angle annular dark field scanning transmission electron microscopy

HEK: Human embryonic kidney cells

HEMA: Hydroxyethyl methacrylates

HHDMA: Hexadecyl(2-hydroxyethyl)dimethylammonium dihydrogenphosphate

HPLC: High performance liquid chromatography

ICG: Indocyanine Green

ICPTES: 3-isocyanatopropyltriethoxysilane

IEP= Isoelectric point

INH: Isoniazid

KPS: Potassium persulfate

LSPR: Localized surface plasmon resonance

MOF: Metal organic frameworks

MPs: Microplastics

MPTES: 3-(methacryloxypropyl)triethoxysilane

MPTMS: 3-(mercaptopropyl)trimethoxysilane

MSNP: Mesoporous silica nanoparticle

MUMA: Mercaptoundecyl methacrylate

NB: Nile blue

NBB: Nanobuilding blocks

NCs: Nanocrystals

NHS: N,N-Hydroxysuccinimide

NIPAm: N-isopropylacrylamide

NIR: Near-infrared

NP(s): Nanoparticle(s)

PBS: Phosphate saline buffer

PdI= Polydispersity index

PDMAAm: Poly(N,N-dimethylacrylamide),

PDMS: Poly(dimethylsiloxane

PEF: Plasmon-enhanced fluorescence

PEG: Polyethyleneglycol

PEG-silane: Polyethyleneglycol silane

PEI: Polyethyleneimine

PET: Polyethylene

PHB: Polyhydroxybutyrate

PhTES: (Phenyl)triethoxysilane

PLC: Poly-ε-caprolactone

PLLA: Poly(l-lactide) acid

PMMA: Poly(methyl) methacrylate

PnBMA: Poly(n-butyl) methacrylate

PNIPAAm: Poly(N-isopropyl)acrylamide)

PP: Polypropylene

PS: Polystyrene

PUR: Polyurethane

PVC: Polyvinylchloride

PVP: Poly(vinylpyrrolidone)

PZA: Pyrazinamide

QY: Quantum yield

RAFT: Reversible addition–fragmentation chain transfer

RBITC: Thodamine B isothiocyanate

RDE: Radiative decay engineering

RIF: Rifampin

SAQ: Chemical Analysis Service

SAXS= Small-angle X-ray scattering

SC: Sodium citrate

SDS: Sodium dodecyl sulphate

SEM= Scanning electron microscopy

SERS: Surface enhanced Raman scattering

SMA= Silicomolybdic acid

SN2: Nucleophilic substitution reaction

STEM: Scanning transmission electron microscopy

TEM: Transmission electron microscopy

TEOS: Tetraethyl orthosilicate

TESPC: 3-(triethoxysilyl)propyl isocyanate

THF: Tetrahydrofuran

TMSPMA: 3-(trimethoxysilyl)propyl methacrylate

TNT: Trinitrotoluene

TPE: Tetraphenylethene

TRITC: Tetramethylrhodamine isothiocyanate

UV-Vis: ultraviolet visible

VOCs: Volatile organic compounds

VTES: Vinyltriethoxysilane

VTMS: Vinyltrimethoxysilane

XRD: X-ray diffraction

I. Introduction

"Teaching is not the mere imparting of knowledge

but the cultivation of an inquiring mind"

Jiddu Krishnamurti

Chapter 1

Introduction: Scientific Background

This chapter provides a background review on the development of silica-based hybrid nanostructures with advanced properties for biological applications. In detail, particular emphasis is placed on the synthesis of colloidal silica nanoparticles (SiO_2 NPs) using the sol-gel method, the nucleation and growth mechanism discussed in the literature, the chemistry behind the silica surface functionalisation using organfunctional silanes as crosslinkers and finally the synthesis of core-shell silica nanoparticles using noble-metals nanocrystals (NCs) as cores, towards development complex nanocomposites having innovative optical features for bioimaging applications.

1.1 Silica Nanoparticles (SiO_2 NPs)

Silica, from the Latin *Silex,* also known as silicon dioxide (SiO_2), is a white or colourless compound that contains two of the most abundant elements in the Earth's crust, silicon (Si) and oxygen (O), with a 59% of mass abundance in the continental crust [1]. The Si atom has 14 electrons with four remaining electrons in its outermost "valence" band. These highest energies electrons can be paired with four oxygen atoms by strong covalent bonds, for developing a tetrahedron chemical structure that consists of a central silicon atom surrounded by four oxygen [2]. Silicates are built of long frameworks chains of tetrahedrals, in which every corner is shared. In nature, silica can be found either in crystalline state (quartz, cristobalite and tridymite) or in amorphous state (opal and diatomite) depending on their structural arrangements. Both amorphous and crystalline silica, share a chemical framework composed of siloxane bonds (Si-O-Si) with silanol groups (Si-OH) at the surface, with the difference of being arranged in a fixed geometric pattern in the latter phase. This capability of mineralization into crystalline or amorphous networks, are ascribable to the high flexibility of the siloxane bond (Si-O-Si), which highlight the silica from other metal oxides [3]. In Mother Nature, the formation of amorphous SiO_2 in form of particles, came from the dehydration of the soluble silicic acid species of formula $Si(OH)_4$,

(as shown in **scheme 1.1**), produced by the continuous reversible hydrolysis and condensation reactions of a pH-dependent weathering process [4].

$$(SiO_2)_x + 2H_2O \leftrightarrow (SiO_2)_{x-1} + Si(OH)_4$$

Scheme 1.1 Formation of the silicic-acid species by the weathering process of reversible hydrolysis and condensation reactions.

However, despite the environmental abundance of non-crystalline SiO_2 from natural sources, the presence of metal impurities, as well as the toxic nature of submicrometre particles that cause chronic inflammation and lung disease [5], suggest that the native-material may not be favourable for advanced scientific and industrial applications. Hence, synthetic amorphous silica nanoparticles in colloidal phase, have been conveniently mass-produced in tonnage quantities and the most interesting features of this man-made material is that they present a non-toxic colloidal state with good electronic, thermal and chemical properties and due to their versatile surface chemistry and high surface area, are very suitable for drug delivery, biosensors and bioimaging applications [6].

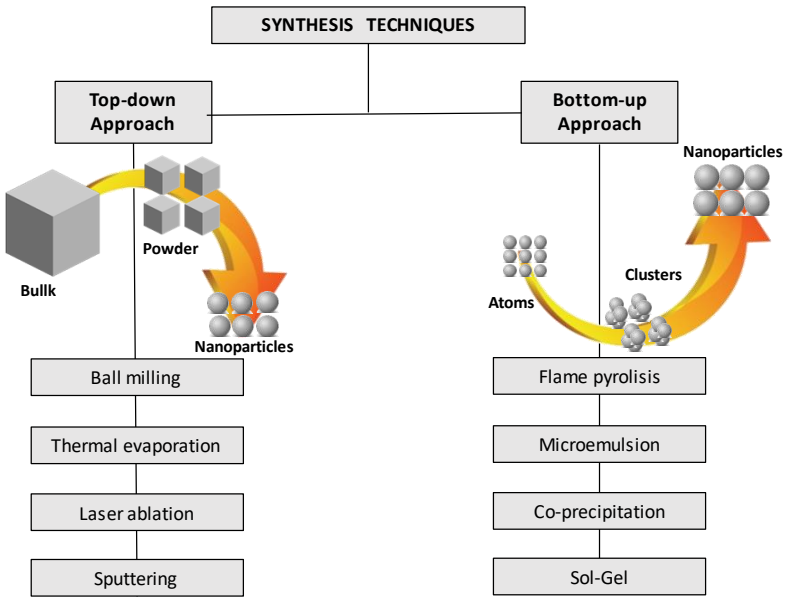

Figure 1.1 Top-down and bottom-up synthesis techniques for the production of silica nanostructures. Adapted from reference [7].

Nowadays, two main approaches, (shown in **figure 1.1**), the top-down and bottom-up methods, have been used to yield amorphous SiO_2 NPs [8], [9]. On one hand, top-down is characterized for the transformation of a bulk material into small-sized particles, using

mechanical and physical approaches, such evaporation, condensation or laser treatment, including: ball-milling [10], thermal evaporation [11], Sputtering [12] or laser ablation [13]. These methodologies allow the production of particles with relatively high capacity and universality with increased efficiency. However, drawbacks, such as introducing structural defects by destroying or disordering the structure, the challenging to achieve a monodisperse particle size and shape, the tendency to aggregate and the contamination of the surface with by-products (e.g., HF derivatives) [14], hamper the use of these techniques. On the other hand, bottom-up, produce particles through the growth and self-assembly of atoms and molecules as their building blocks. The most common methodologies used by this approach are the well-known wet chemistry methods, which comprise the use of flame spray pyrolysis [11]-[12], reverse microemulsion [17], co-precipitation [18] and the sol-gel process [19].

The development of these techniques represented a major breakthrough in the production of colloidal amorphous SiO_2 NPs, with the advantage of low cost, higher productivity and the increased in spatial control over size, functionalization and composition. Nevertheless, the flame-pyrolysis process can lodge toxic volatile metal halides such as $AlCl_3$ or $TiCl_4$, that are vaporized simultaneously with $SiCl_4$ [20], co-precipitation need the carefully readjustment of pH during synthesis in order to obtain the final product [21] and microemulsion use excessive surfactants to produce micelles, limiting the further use in medical application [17]. For this implications, the sol-gel still the most widely used method to produce colloidal amorphous SiO_2 NPs, due to its straightforward simplicity and scalable behaviour that through systematic monitoring of reaction parameters, it is possible to kinetically control the particles size, shape, distribution and morphology [22]. Moreover, this sol-gel technique endows low-temperature routes for synthesizing materials that are either purely inorganic or hybrids structures composed of both inorganic as well as organic [23].

1.2 The Sol-Gel Process: A Wet Methodology for Production SiO_2 NPs

Historically we could say that the sol-gel process emerges in the year 1921, but it was not developed until the 1960s due to the need of the nuclear industry to seek nuclear fuel materials (sol-gel conversion of plutonium and transuranium elements) [24].

Nevertheless, the method become popular in the 90s, with the important guidelines in the sol-gel science by its pioneer Dr. C. Jeffrey Brinker [3]. The sol-gel process is a synthetic route consisting in the development of an oxide network through polycondensations reactions of a molecular precursor, leading to a colloidal suspension (sol) or gelation (gel) system in continuous liquid phase. A sol is a dispersion of stable colloidal particles (1–100 nm) in a liquid that interact by van der Waals forces or hydrogen bonds along with repulsive forces. A gel is an interconnected rigid network of polymeric chains with pores of sub-micron dimensions [25]. Normally, the precursor used consists of a metal or metalloid element surrounded by various ligands and can be divided in two classes depending on the nature of the precursor: inorganic (chlorides, nitrates, sulfides, etc.) or alkoxides. Both can undergo nucleophilic substitution reactions to pass from a one phase solution into a two-phase system comprised of solid metal oxides particles and a solvent.

Generally, sol-gel process is widely used due to its ability to produce high quality and homogenous materials at mild conditions and include four stages namely: hydrolysis, condensation, nucleation and growth [6]. The key to control the sol–gel chemistry of alkoxides is understanding the hydrolysis and condensation reactions, both strongly affected by factors such as the nature of the precursor (e.g. inductive effects by the R-chain), water content, solvent used, temperature, pH and the catalysts [26]. For silica, silicon metalorganic alkoxides of formula $Si(OR)_4$ are the most used. They can undergo hydrolysis reaction, resulting in the replacement of an alkoxy group (RO-) with a hydroxyl (-OH) to form a silanol (Si-OH) by a penta-complexation transition state. This process can be either acid or base catalysed, (as shown in **scheme 1.2**).

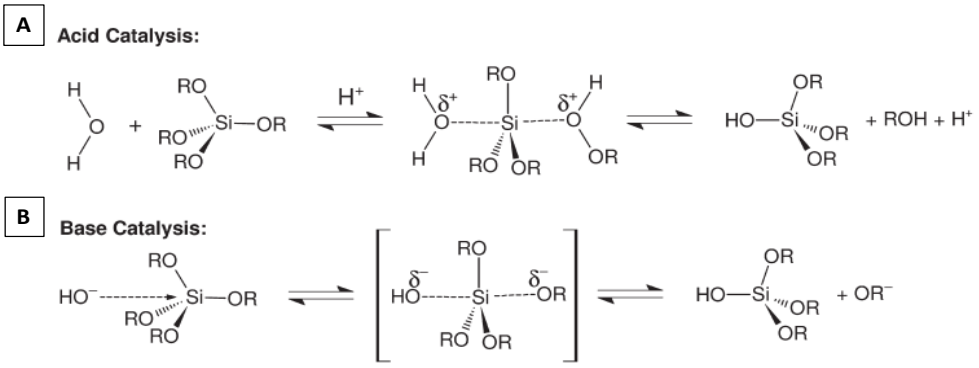

Scheme 1.2 hydrolysis mechanism depending on the type of catalyst used in the silicon-based sol–gel process, (A) acid and (B) based-catalyzed. Adapted from reference [27].

On one hand, in acid catalysed hydrolysis, water acts as nucleophile which attacks the protonated alkoxysilane. The oxygen atom of the Si-OR group is protonated, shifting the electron densiy towards the Si atom. As a results, this process lead to the formation of a (-OR) good leaving group, making the structure more accessible for water hydrolysis. This reaction allows the formation of weakly cross-linked linear polymers, that further intertwine between them by their silanols groups to achieve dense branches microporous networks. On the other hand, in base-catalyzed, the (OH^-) ions formed by water dissociation attacks the alkoxysilane, performing a nucleophilic attack on the central Si atom by a SN_2 type reaction, displacing the good leaving group (–OR) by the(-OH) group [28]. This process lead to highly branched Si clusters due to the rapid hydrolysis of the alkoxide silane. The kinetics of the reaction is facilitated in alkaline medium favouring the further inter-linking of silica clusters.

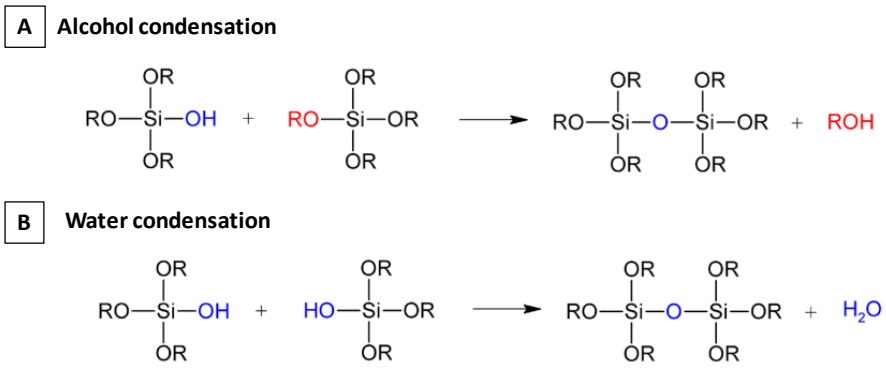

Scheme 1.3 Condensation (A) alcohol and (B) water reactions mechanism in the silicon-based sol–gel process. Adapted from reference [29].

The ccondensation start after hydrolysis (shown in **scheme 1.3**), where the silanol group (Si-OH) of the hydrolysed alkoxide precursor form a siloxane bond (Si-O-Si) by a nucleophilic substitution reaction. In this process the silanol groups of the silicic acid intermediate $[Si(RO)_{4-x}(OH)_X]$ acts as a nucleophile, producing a dimer structure composed of an oxo bridge (Si-O-Si) between two silicon metal centers by an oxalation reaction. Nevertheless, two kind of condensation reactions can occur. When the reaction is between the silicic acid intermediate and the alkoxysilane (silica precursor), is called “alcohol condensation”, characterized by the generation of alcohol as a side product.

In contrast, if the reaction is between two silicic acid intermediates, is called “water condensation”, with the liberation of water molecule [30]. The condensation rate between

silanol monomers will depend on the degree of hydrolysis of the precursor. Generally, a complete hydrolysis of the silicon alkoxide precursor to form the soluble orthosilicic acid of formula $Si(OH)_4$ is very difficult to accomplish. The kinetics is clearly influenced by steric and inductive effects. The kinetics of displacing and (OH-) in form of water is faster than displacing an alkoxy (RO-) group, due to the steric hindrance [31]. In addition, silanol group are deprotonated more easily to increase positive charge density on silicon atom, making it favorable for nucleophilic attacks. This is also the reason why silanol monomers prefer to attach to larger siloxane network clusters rather than to other monomers or small oligomers [32].

Finally, both process, hydrolysis and condensation reactions are further initiated at numerous sites and the kinetics of the reactions are therefore complex. The reactivity of the evolving alkoxysilane species leads to several silica colloidal morphologies, proposed by C. Brinker (shown in **figure 1.2**), which displayed a general overview of the attainable structures when modifying the reaction conditions, such as pH and ionic strength, allowing the control on the particle size and modify the degree of aggregation [33].

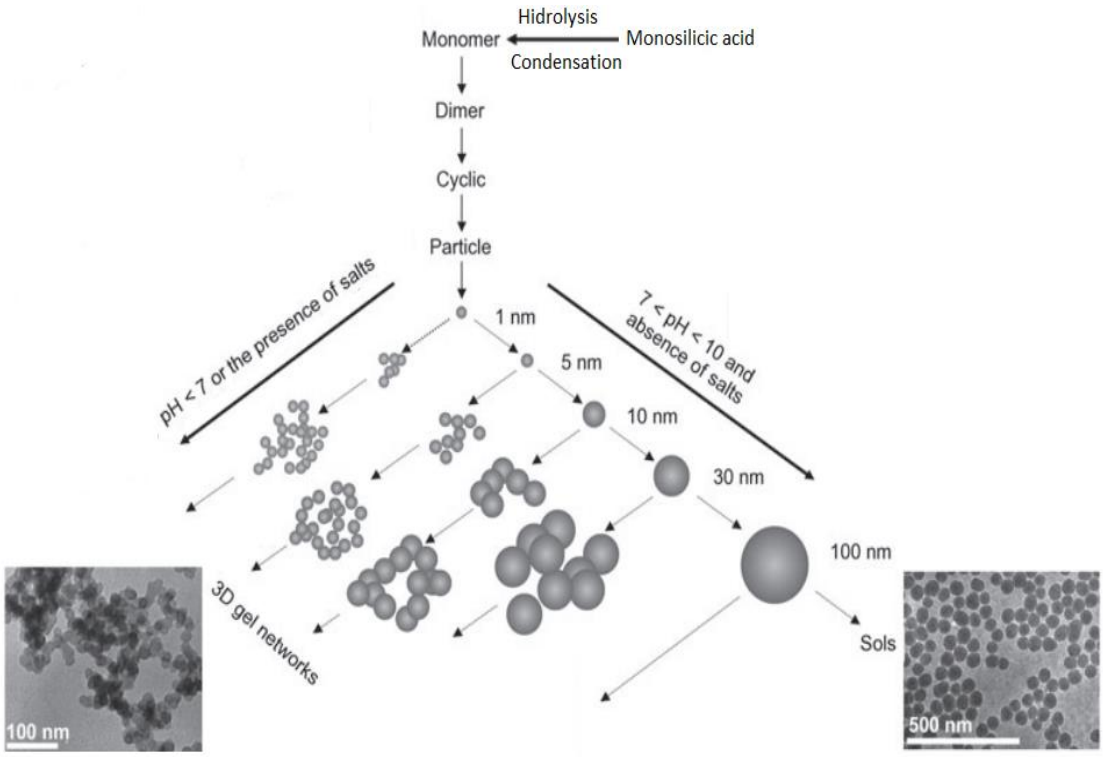

Figure 1.2 Graphic showing the generally accepted pathways to silica formation from precursor orthosilicic acid through oligomers to particles and aggregated structures. Adapted from reference [33].

1.3 The Original Stöber Method

A pioneering approach for the synthesis of colloidal amorphous silica particles was developed in 1968 by Stöber and co-workers [34]. The process followed an ammonia-catalyzed sol–gel reaction in which the hydrolysis of ethoxysilanes takes place in presence of water and ammonia, producing silicic acid monomers that further polycondensate under low molecular-weight alcohols used as interphase. According to this method, the final diameter is considered to be from 50 to 500nm by simple altering the ammonia concentration. Normally, large monodisperse silica particles (≥250nm) are produced using high ammonia.

Two chemical reactions are involved in the Stöber synthesis: hydrolysis and condensation. The interacting species during both reactions are: tetraethyl orthosilicate of formula $Si(OC_2H_5)_4$, namely with the acronym (TEOS) as the most commons Si source, ammonia (NH_3) as basic catalyst and aqueous ethanol as solvent. During the hydrolysis, TEOS experience a nucleophilic substitution of an ethoxy group ($-OC_2H_5$) by a hydroxyl (-OH), forming a silanol group (Si-OH) via a penta-complexation transition state in the presence of water in a base-catalysed process using ammonium hydroxide (NH_4OH), as follows:

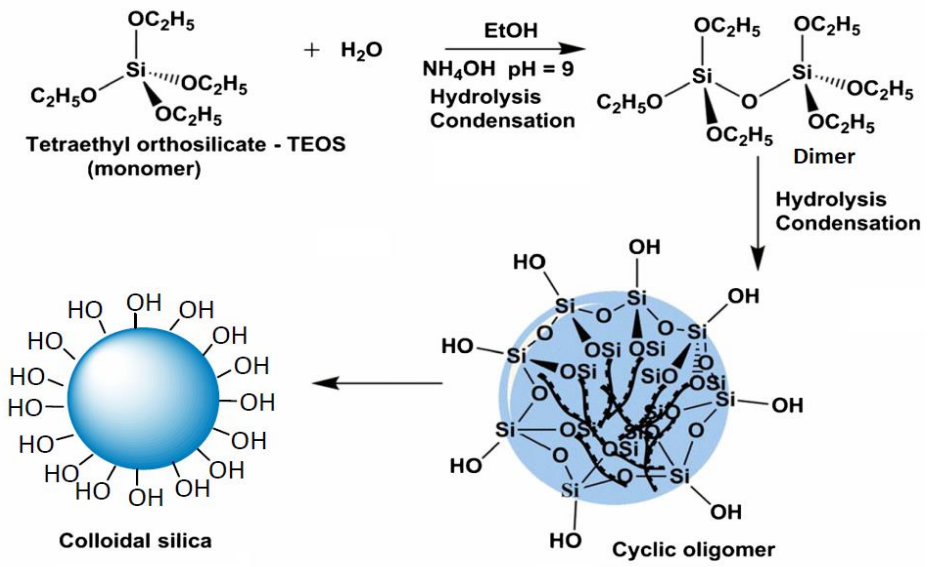

Figure 1.3 Drawing showing the synthesis route of amorphous colloidal silica particles by the Stöber process. Adapted from reference [35].

The ammonia is used as a catalyst to accelerate the hydrolysis rate, because the hydroxyl (OH^-) ions presented in the ammonia solution are more effective nucleophiles compared to water (H_2O) molecules. During the condensation, the silanol groups of the ethoxysilanols monomers, polymerize either with TEOS or another silanol monomer to form siloxane (Si-O-Si) bonds by nucleophilic substitution. The continued further condensations reactions allow the production of cyclic oligomers by polymerization of crosslinking monomers allowing the formation of large branched siloxane network that ultimately lead to the nucleation and growth of amorphous silica particles, (as shown in **figure 1.3**). Finally, depending on the relative rates of the condensation and hydrolysis reactions, kinetically controlled by the experimental conditions used, such as precursor concentration, temperature, catalyst and solvent, the final particle size, distribution and properties can be adjusted.

1.4 Mechanism of Silica NPs Nucleation and Growth: Monomer-Addition and Controlled-Aggregation Models

In the literature, two main models have been accepted so far for explain the chemical and/or physical growth mechanisms of SiO_2 NPs: the *monomer-addition* and *controlled-aggregation* models, (shown in **figure 1.4**). These models divide the formation of silica into two events: nucleation and growth, following different approaches.

The first in develop the *monomer-addition* model were Matsoukas and Gulari in 1988 [36]. This mechanism is based on the Lamer-based growth mechanism of burst nucleation [39]. They proposed that, during the initial phase, the hydrolysed silicic acid species generated during hydrolysis, increase in concentration until the critical supersaturation level. Thereafter, as the concentration further increases, nucleation begins producing small unstable silica nuclei's by the condensation between the silicic acid monomers. The produced nuclei's keep growing by the addition of monomers on their surface, till the generation of stable primary particles. Finally, these primary particles further grow by preferential deposition of soluble monomers on their surface, preserving the uniformity and monodispersity throughout the whole process. This claims that the final number of particles is the same as the number of primary particles produced during the short nucleation period and the further growth proceeds uniformly at the same rate.

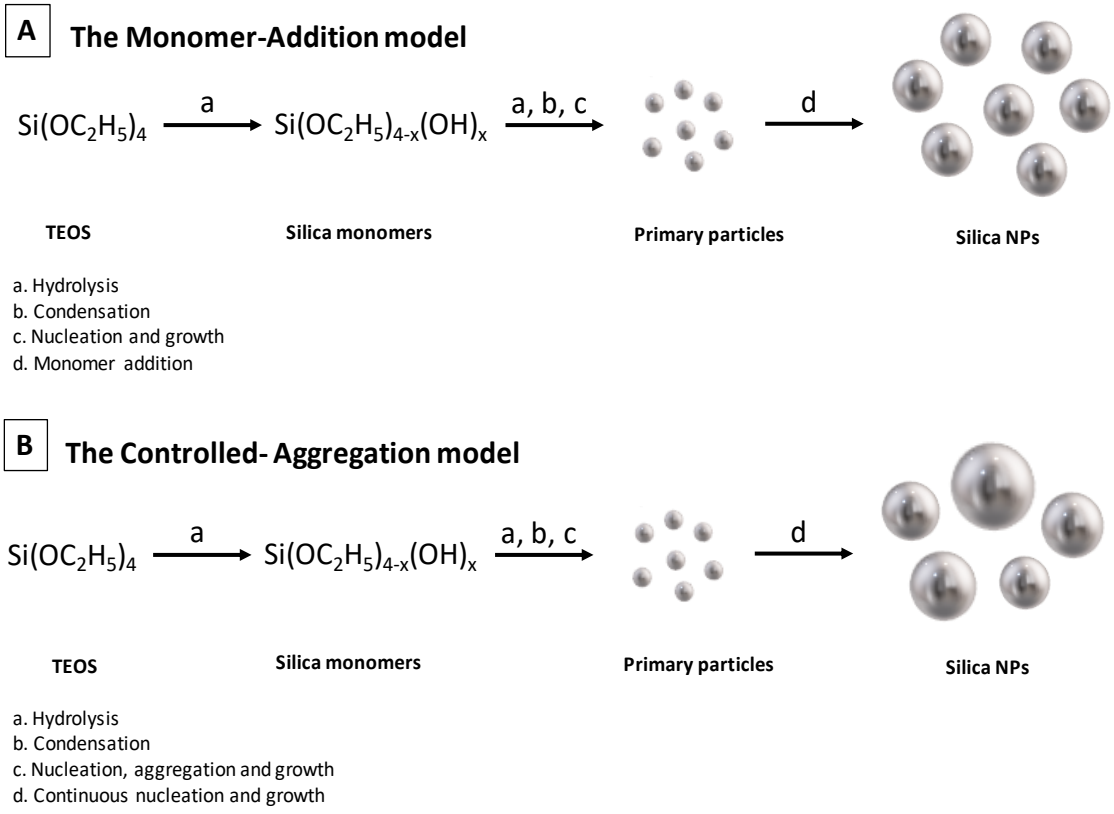

Figure 1.4 Graphical representation of (A) the monomer addition [36] and (B) the controlled-aggregation [37] based models for synthesis of colloidal silica particles. Adapted from references [38].

On the other hand, the *controlled-aggregation* model was proposed in 1992 by Bogush and Zukoski [37] and Harris [40]. In this mechanism, the hydrolysed monomers generated during hydrolysis, condensate into an unstable polymeric structure. Then, the nucleation takes place when the unsteady assembly phase separate generating colloidally unstable small nuclei's that are prone to aggregation. Therefore, a continued aggregation of these nuclei's follows till the generation of stable primary particles with a broad size distribution. These particles keep aggregating, until a colloidally stable size is achieved. Finally, the growth takes place by aggregation with other smaller particles by a self-sharpening mechanism, until the monomer concentration is below the nucleation threshold. Beyond that, growth of silica particles occurs by surface attachment of silanol monomers or oligomers, thereby allowing a narrower size distribution at later stages of the process. These process were described as:

1.5 Surface Functionalization of Silica Nanoparticles

At the nanoscale, materials have a greater ratio of atoms facing the surface which results in a higher surface area to volume ratio. This relationship can result in "surface effects" which are often responsible for the drastic differences in physicochemical properties between bulk materials and their nanoscale equivalents [41]. The surface functionalization of SiO_2 NPs with selectively chosen organofunctional groups, have been extensively used in biological applications because have shown improved adsorption capacities for loading bioactive molecules or pharmaceuticals, increased binding affinity to deliver molecules to specific cell and tissue targets, enhanced cellular uptake with endosomal escape, increase cellular trafficking, along with enhanced overall biocompatibility. Depending on the nature of the selected functional groups, can perform diverse roles, such as tailoring the surface charge of NPs, grafting inside and outside of the structure active functionalities and surface capping for avoid premature release of entrapped drugs or non-specific binding of the particles, once dispersed in different chemical or biological environments. In addition, have proven to be a suitable strategy towards the production of silica-polymer nanocomposites using cross-linkers, due to the enhanced affinity between the organic and inorganic phases improving the dispersion of silica nanoparticles within the polymer matrix [42].

In this regard, silica surfaces are commonly modified by taking advantage of the rich silane chemistry, commercially available with amines, carboxyl, thiols, isocyanates and vinyl groups. The most convenient strategy is performed by silanization reaction. This technique covers the surface creating a covalent (-Si-O-Si-) bonds, taking advantage of the silica surface hydroxyl groups using organofunctional trialkoxysilanes [43]. The surface of sol–gel derived amorphous silica, results in a non-periodic arrangement by a random packing of $[SiO_4]^{4-}$ units. Their bulk structure terminates at the surface in two different fashions; through siloxane groups (≡Si-O-Si≡) exposing an oxygen or silanol groups (≡Si-OH), with different conformations (free, germinal or associated) [44], (as shown in **figure 1.5**). In the literature, the total surface concentration of hydroxyl groups on the amorphous SiO_2 has been reported by different techniques and the most accepted value is around 4-5 hydroxyl groups/nm^2 [45]. There are two prominent synthetic strategies for silica surface

modification: i) stepwise synthesis (namely post-synthetic grafting) or ii) one-pot synthesis (called co-condensation method) [46].

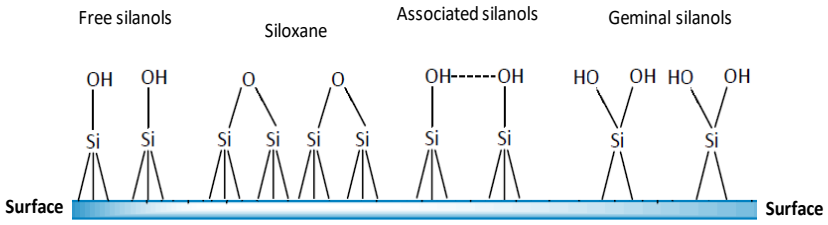

Figure 1.5 Graphic representation of the surface of sol–gel derived amorphous silica, showing the different population of silanol groups. Adapted from references [45].

On one hand, post-modification is a two-step method for covalently linking the alkoxy-silanes with surface silanol groups. The SiO_2 NPs are prepared by sol-gel method prior functionalization and can be performed via aqueous or non-aqueous systems [47]–[50]. In the aqueous system, the mechanism of monolayer formation is quite straightforward as (shown in **figure 1.6**).

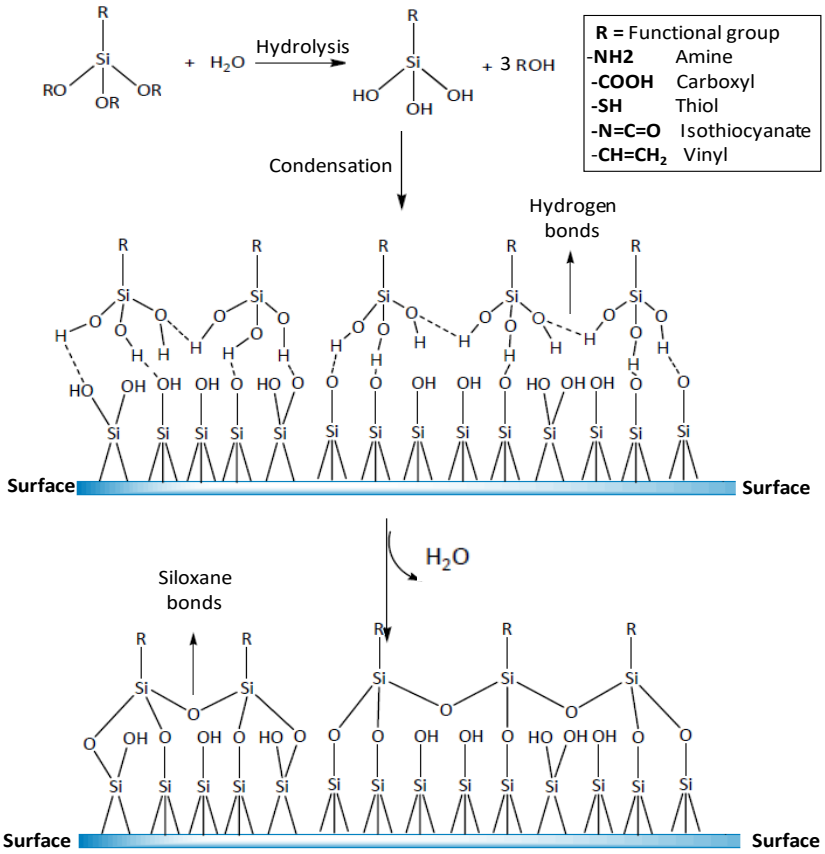

Figure 1.6 Graphic representation of the mechanism of silane monolayer formation, using organofunctional trialkoxysilanes. Adapted from references [51].

Frist, the trialkoxysilanes experience hydrolysis and condensation reaction forming and hydroxyl group before deposition. Later, this group form hydrogen bond with the silanol groups on the silica surface followed by the formation of covalent siloxane bonds with the release of water molecules [51]. In contrast, in non-aqueous system, the trialkoxysilane molecules are directly attached to the silica surface via direct condensation reaction. This strategy normally used high energy reflux conditions using organic solvent for better control the reaction parameters. The main reason of this method is to prevent hydrolysis. For instance, silanes, such as 3-aminopropyltrimethoxysilane (APTES), may undergo uncontrollable hydrolysis and polycondensation reactions in the with the presence of water. On the other hand, the direct-modification method is performed by co-polymerizing the functional alkoxy-silanes together with polymerizable metallo-organic silica precursor. The advantage of this method is that enables a more homogenous surface coverage of functional groups [52]–[54].

In the literature, surface modification of SiO_2 NPs has been carried out by using various types of silanes coupling agents, as shown in **table 1.1**:

Table 1.1 The most used functional silane coupling reagents, their chemical functional groups and their surface applications.

Silane Coupling Agents	Acronym	Functional Group	Application and Effects
3-(Aminopropyl)trimethoxysilane 3-(Aminopropyl)triethoxysilane 3-(aminopropylmethy)diethoxy silane 3- (2-Aminoethylamino)propyltrimethoxysilane 3-(aminopropyldimethyl)methoxysilane	(APTMS) (APTES) (APDMS) (AEAPTS) (APMS)	$-NH_2$	Reduced aggregation, fluorescent labeling, surface charge modification, DNA binding and protection from enzymatic cleavage. [55]–[59].
3-(Mercaptopropyl)-trimethoxysilane	(MPTMS)	–SH	Conjugate with maleimides, thiol/disulfide exchange reactions to attach oligonucleotides, surface charge modification.[60].
Polyethylene glycol-silane	PEG-silane	–PEG	Increased circulation time, reduced aggregation and increases particle dispersity in aqueous solution. [54].
4-(methoxyphenyl)Trimethoxysilane (Phenyl)triethoxysilane	N/A PhTES	$-CH_3$ -Phenyl	Hydrophobic coating, increase ultrasound contrast. [61]

Carboxyethylsilanetriol	N/A	–COOH	Functionalize silica NPs and provide reactive sites for amine [62].
3-(Trihydroxysilylpropyl methyl)phosphonate	N/A	$–PO_3^-$	Functionalize silica NPs and provide reactive sites for amine [62].
3-(Isocyanatopropyl)-triethoxysilane	N/A	–NCO	Functionalize silica NPs and provide reactive sites for amine [62].
3-(Trimethoxysilyl)propyl methacrylate 3-(methacryloxypropyl)triethoxysilane	TMSPMA MPTES	CH2=CH- (vinyl)	Adhesion promotion between dissimilar materials (inorganic-polymer). Covalently link polyacrylamide gels. Preparation of organic/inorganic hybrid nanomaterials. [63], [64].

1.6 Hybrids Nanostructures: Definition and General Classification

We could say that a hybrid nanomaterial is a chemical conjugate which can combine an organic and inorganic components into one individual structure, by developing new electron orbitals or creating chemical bonds between them [65]. The resulting nanomaterial is not a simple assortment of different components but a synergistic material with an increased functionality, associated with the improvement of their physicochemical properties. In the literature, hybrids nanomaterials are classified into two categories: *class I* or *class II,* according to the binding force responsible for the interaction between their organic and inorganic components. It will depend on: i) the nature of the interface and ii) the bonds strength between the organic and inorganic phases and level of interactions, (as shown in **figure 1.7**) [66]–[68].

On one hand, class I hybrids ¨non-covalent¨, is a hybrid system in which the organic and inorganic components interact via weak interactions, such as, Van der Waal's and hydrogen bonding, π-π interactions or weak electrostatic interactions bonding (Coulomb forces, London dispersion and dipole–dipole forces). For instance, entrapping discrete inorganic clusters or particles in an organic polymer without any strong covalent interaction is called Blends (e.g. Zeolite / Low-density polyethylene hybrid). Alternatively, interpenetrating networks are formed entrapping inorganic networks in a cross-linked polymer matrix through weak physical interactions (e.g. Ring-opening metathesis of a polymer with a silica network) [69]. These class of hybrids materials are focused in to

increase the compatibility between phases, improve the mechanical properties and flexibility. On the other hand, class II hybrids ¨covalent¨ corresponds to hybrid materials in which the organic and inorganic components are linked by strong chemical interactions, by covalent bonds or ionic-covalent bonds, allowing to: i) increasing phase coupling and ii) for grafting chemical organic functionalities for advanced applications [65]. This later class are constructed, covalently linking discrete inorganic particles or clusters with organic polymers using organo-functional crosslinkers e.g. Hybrid scaffolds of chitosan/silica). As a general rule, the inorganic material (metal/semiconductor/dielectric particle) will provide: mechanical strength of the overall structure, optical, catalytic, thermal and magnetic properties, while the organic components (organic functional groups or molecules, biomolecules, polymers, etc) delivers bonding between the inorganic building blocks for increasing phase interaction [70].

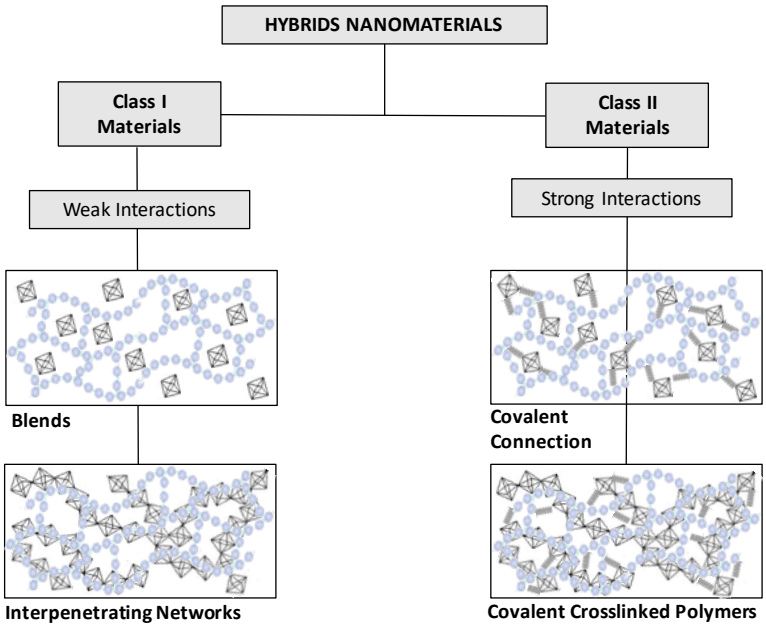

Figure 1.7 Classification of hybrids materials. Adapted from reference [68].

Additionally, hybrids nanomaterials can also be classified and categorized into organic-in-inorganic or inorganic-in-organic hybrids [71], as showed in in **figure 1.8**. Hybrid materials based on the first classification (organic molecule used to modify inorganic materials) can be subdivided into two types, specifically, (i) inorganic materials modified by organic moieties and (ii) colloidal particles stabilized by organic molecules. This class is typically presented by various types of core-shell structures (organic-inorganic or vice

versa) or other inorganic nanoparticles embedded into an organic (e.g., polymer) matrix. On the other hand, the Inorganic-modified organic materials are modified via surface charge or functionalization with ligands [72]. In this class, chemical bonding occurs between two different phases. The building blocks possess at least two distinct functional groups: metal-to carbon links (R-OM bonds).

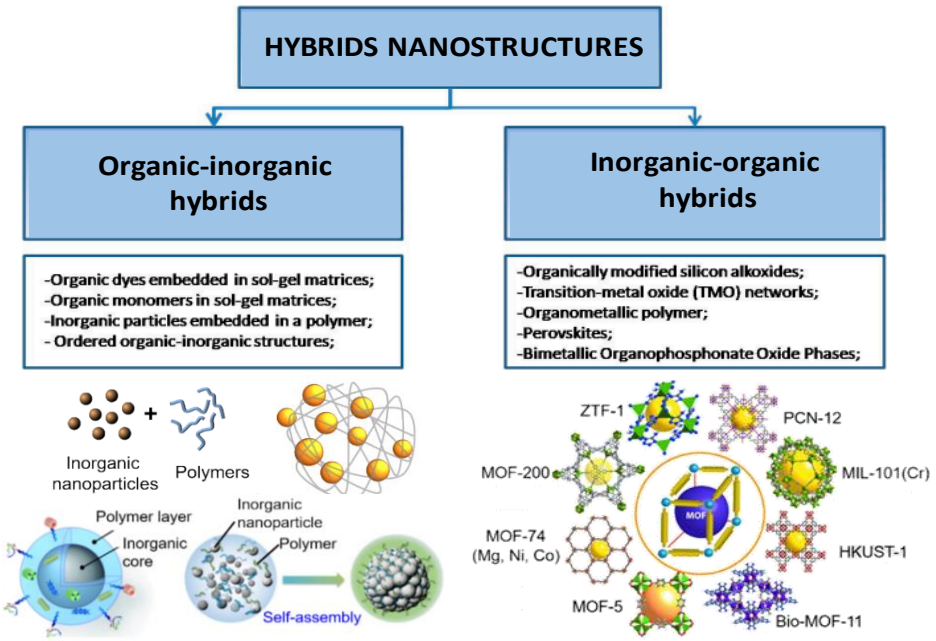

Figure 1.8 Classification of inorganic-organic or organic-inorganic hybrids materials. Adapted from reference [73].

1.6.1 Silica-Based Hybrids Nanostructures: Synthesis and Biological Applications

Nowadays, silica nanoparticles (SiO_2 NPs) and silica hybrids (Si-hybrids) have been attracted tremendous attention in the last decades due to their superior biocompatibility and controllable structures, suitable for industrial and biological applications with potential use in optics, sensing, adsorption, ceramics, catalysis, drug delivery, tissue engineering, photovoltaic applications, among others [74]–[77]. Moreover, research onto silica nanostructures using silica nanoparticles (SiO_2 NPs), has grown significantly as evidenced by the exponential increase in the number of articles published (showed in **figure 1.9**).

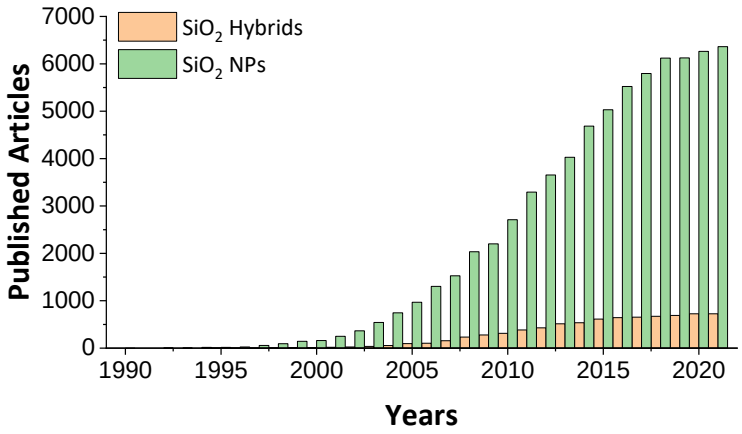

Figure 1.9 Representation of the number of research articles published in the last 30 years in the area of silica according to Web of Science (Science Citation Index) when searching as keywords ¨*silica nanoparticles*¨ *and* ¨*silica hybrid nanostructures*"

Regardless of the biological or industrial applications, as well as the nature of the interface, the Si-hybrids can be prepared by conjugating bare SiO_2 NPs with coupling with polymers or silane linkers for conferring the NPs with surface functionalities or doping them with different inorganic components, such as, metal ions, noble metal particles (Au or Ag NPs), salts, oxides, sulphides, non-metallic elements and their derivatives or with organic components, ligands, fluorophore, organic molecules with functional groups, biomolecules, pharmaceutical substances and polymers for obtaining new materials with multifunctional features, displaying greater chemical, mechanical and thermal properties than other semiconductors, metals, non-metals or metal-oxides [78]–[80]. The most commonly chemical pathways for the production of Si-hybrid materials are: the conventional sol–gel chemistry, hydrothermal synthesis, self-assembling procedures, such as well-defined nanobuilding blocks (NBB) or hybrids MOF (Metal Organic Frameworks) approaches [81]. From here on this dissertation will be focused only using the sol-gel strategy.

1.6.2 Synthesis of Silica-Based Hybrids Nanoparticles

The sol-gel method has been explored for development multifunctional silica-based hybrids particles at the nanoscale with controlled defined shapes (e.g. core-shell, multinuclear, raspberry), structure and composition, due to their mild synthetic conditions offered (low processing temperatures, versatility of the colloidal state and a broad solvent

compatibility) [66]. The chemical strategy is based on the copolymerisation of functional organosilanes and metal alkoxides or the encapsulation of inorganic/organic components via sol–gel science. Interestingly, both routes, allows the formation of macromolecular covalent linkages networks through hydrolysis and condensation reactions close to ambient temperature. This key characteristic allows the possibility to build inorganic networks in presence of organic polymers, during or after the sol–gel process and also, allows overcome the limitation of thermal decomposition of the trapped organic materials during the hybrid formation process, because some molecules present limited thermal stability. Another parameter to take into consideration during the hybrid formation is the phase separation. Polymers, such as polystyrene or polymethacrylates, are immiscible with alcohols. This drawback can be avoided by: i) the properly election of the solvent for increase the phase coupling, for instance, switching from the conventional alcohols to others polar solvents, such as dimethylformamide (DMF) or tetrahydrofuran (THF) or ii) by ionic modifications of the organic polymer making them compatible with the reaction conditions, for instance, using hydroxyethyl methacrylates (HEMA) in the polymerization mixture, for introducing hydroxyl groups (OH-) that can assist linkage between the polymer and the monomer [27] .

For the synthesis of dispersed Si-hybrids, the sol-gel method use polymerizable metallo-organic precursors, such as silicon alkoxides of formula $R'O_nSi(OR)_{4-n}$ (with n = 1, 2, 3) as a silica precursor along with functional trialkoxysilanes of formula $R''Si(OR)_3$, bearing a organic chemical functionality in their structure, for tailoring both phases and controlling the interfaces as crosslinker [82]. The incorporated functional group changes the properties of the final material. Class I Si-hybrids, can be developed by linking the hydroxyl groups of the precipitated silica oxide, with the functional groups that are present in the polymer chains, such as, amide, carboxyl or carbonyl by weak hydrogen or by Van der Waal's bonds. Polymers such as, poly(N,N-dimethylacrylamide) (PDMAAm) [83], poly(vinylpyrrolidone) (PVP) [84], poly(n-butyl methacrylate (PnBMA) [85], poly(dimethylsiloxane) (PDMS) [86], poly(methyl methacrylate) (PMMA) [87], poly-ε-caprolactone (PCL) [88] and polyethyleneglycol (PEG) [89]. Secondly, class II Si-hybrids, have been developed when both the silicon alkoxides used as a silica precursor is polymerized together with a functional trialkoxysilanes, creating covalent siloxane bonds. The alkoxy group of the Si

precursor (RO-Si bond) will produce an oxo-polymer framework by experiencing hydrolysis-condensation reactions in the presence of water. The Si-O-C bonds are stable upon hydrolysis and could link both the organic and inorganic moieties together. Moreover, the organofunctional trialkoxysilanes, provide the structure with chemical functionality. Generally, the R'' group bear reactive organic groups, such as, amines, thiols, carboxyl, isothiocyanates or vinyl. It is noteworthy to highlight that, depending on the nature of the crosslinker radical chain (RO-), they will behave as: network modifier or functionalizer, altering the final network properties [67] . If the RO- is non-hydrolysable (e.g. phenyl aromatic group), will act as a network modifier, modifying only the inorganic network of the final structure by the organic functional group. In contrast, if they present a hydrolysable group (e.g. alkyl groups), will act as network functionalizer, incorporating the functionality into the polymerization matrix system. In the literature, 3-(trimethoxysilyl)propyl methacrylate (TMSPMA) can produce silica/methacrylate hybrids as chain transfer agents [90], (Phenyl)triethoxysilane (PhTES) as ceramic enforcer [91], 3-(aminopropyl)triethoxysilane (APTES) to introduce chromophores with luminescence behaviour, such as, Europium and Gadolinium [92] or flurophores such isothiocyanate rhodamine B (RBITC) with Uranine [93], fluorescein isothiocyanate (FITC) [94], vinyltrimethoxysilane (VTMS) as material for column chromatography [95] and (3-mercaptopropyl)trimethoxysilane (MPTMS) for preparing coatings with special mechanical properties or permeability [96], [97].

1.6.3 Biological Applications of Silica-Based Hybrids Nanoparticles

In this regard, for biological and biomedical applications, either class I or class II Si-hybrids can be applied in the fields of bioimaging, drug delivery, biological sensing, tissue engineering, (as shown in **figure 1.10**).

For molecular imaging applications: fluorescence imaging technologies have been extensively used to address some biological concerns at the cellular and molecular level. Normally, organic dyes and fluorescent probes are the most commonly used molecules for this purpose. They present high quantum yields (%QY) in the visible range and exhibit

absorption and emission wavelengths within the near-infrared (NIR) window [98]. However, some may present hydrophobic nature with low dispersability, limiting their extensive use in physiological environments for biomedicine applications. Moreover, most organic fluorophores undergo irreversible photobleaching after prolonged illumination, hampering the continuous tracking [99].

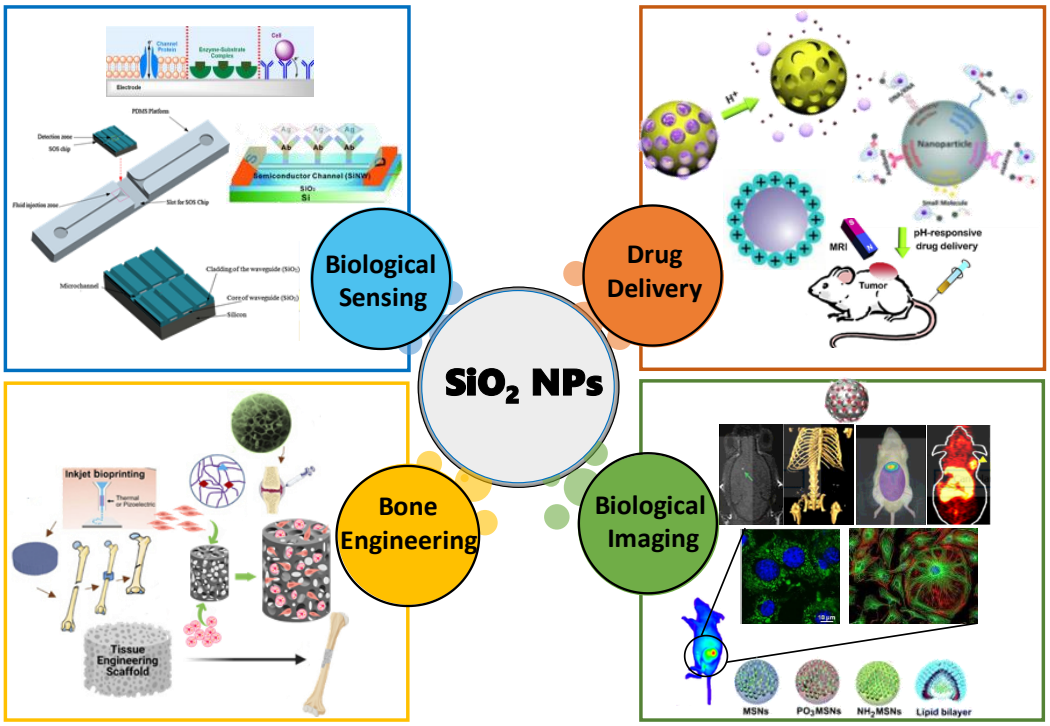

Figure 1.10 Classification of the different biological applications of the silica-based hybrids nanostructures.

Because of this, a nanohybrid systems by encapsulating or bonding organic dyes into inorganic silica matrix, has have been widely explored to overcome this issues. Silica is a suitable candidate, because of its low cost, photophysical and chemical stability in aqueous media, negligible cytotoxicity and facile surface functionalization. In addition, silica-based materials allow the incorporation of fluorescent components with superior loading capability. The inorganic part will provide the photo and chemical stability and will shield from quenching or aggregation in the specific environment [100]. One good approach for achieve fluorescent probes made of silica is by the sol–gel methodology. The strategy is based in the homogeneous polymerization between the silica alkoxide precursor and the modified trialkoxysilanes covalently with the dye during the silica spheres

mineralization. This allows the homogeneous incorporation of organic fluorophores within the silica matrix. Some reported applications are showed in **table 1.2**.

Table 1.2 Molecular imaging applications of the Silica-based hybrids NPs

NPs	Structure type	Size (nm)	Material	Label/ Functionalization	Application
Fluorescent nanostructure (465-485 nm)	Core-shell	45–295	SiO_2	Tetraphenylethene (TPE)	Selectively cell imaging of the cytoplasm in HeLa cells [101].
Fluorescent dots particles (460–625 nm)	Core-shell	2–6	SiO_2	vinyltriethoxysilane (VTES)	Nano-bioimaging visualization of HeLa cells [102].
Multiplexed Fluorescent NPs (490-667nm)	Core-shell	40-60	SiO_2	Rhodamine (RBITC) Fluorescein (FITC) Nile Blue (NB)	Applications in flow cytometry, in which multiplexing increase the speed of detection [103].
pH-responsive contrast agent (690–800 nm)	Core-shell	35	SiO_2	Cyanine dye (CyN-12)	In-vivo NIR bioimaging contrast agent, for real-time endocytosis monitoring into cancer cells y [104].

For drug delivery applications: systems based on silica (SiO_2 NPs) are one of the most commonly used platforms for the active delivery of medical and biological active molecules. The chemical composition of the SiO_2 as a vehicle, display clear advantages, such as, greater biocompatibility, large surface area, controlled porosity and ease-of-functionalization for better drug-loading capabilities and controlled release of the bioactive agents, either covalently or non-covalently, such as antibiotics, peptides, drugs and other functional materials [105]. This silica-based strategy offers a beneficial solution as a protective functional carrier to some of the main drawbacks associated with the drug loading, such as, resistance, crossing over physiological barriers such as enzymes or antibodies, drug solubility and toxicity. Some reported applications can be seen in **table 1.3**.

Table 1.3 Drug delivery applications of the Silica-based hybrids NPs

NPs	Structure type	Size (nm)	Material	Loading/ Functionalization	Application
Hybrid doped NPs	Core-shell	130 ± 30	SiO_2	Triclosan (Irgasan)/ TESPC	Superior bactericidal activity using the FDA-approved antimicrobial agent. [106].
Fluorescent-doped mesoporous NPs	Core-shell	65 ± 10	SiO_2	Vancomycin /FITC / APTES	selective targeting and killing gram-positive bacteria [107]-

Doped mesoporous NPs	Core-shell	100-200	SiO_2	Heparin /APTES	controlled release of heparin as a powerful anticoagulant [108].
Positively charge doped mesoporous NPs	Core-shell	120 ± 5	SiO_2	Levofloxacin/DAMO	Nanoantibiotic for long-term release of levofloxacin for killing bacteria [109].
Thermally and magnetically dual-responsive mesoporous NPs	Core-shell	300-400	Fe_3O_4 / SiO_2	Sophoridine/ PNIPAAm	Nanocarrier for the controlled release of sophoridine, for strong antitumor activities [110].
Thermally and magnetically dual-responsive mesoporous NPs	Core-shell	70 ± 8 - 94 ± 12	SiO_2	Doxorubicin (DOX)/ APMA-NIPAm	Nanocarrier for the controlled release of DOX, as antitumor treatments [111].
Doped mesoporous NPs	Core-shell	100	SiO_2	Isoniazid (INH), rifampin (RIF), pyrazinamide (PZA)/ PEI	Intracellular release of specific drugs for the treatment of tuberculosis [112].
Hollow mesoporous NPs	Core-shell	100	SiO_2	DOX, Nile red/ AETAC	A pH-sensitive amphiphilic nanocarrier for controlled-release of an anticancer agent [113].
Metallic silica-based NPs	Core-shell	12-24 4-12	Ag /SiO_2 Cu/SiO_2	Silver / Copper	Inhibition of growth gram-positive and gram-negative bacteria as well as microscopic fungi. (antimicrobial agent) [114].
Yolk-Shell mesoporous NPs	Core-shell	100-150	Ag/SiO_2	Silver/ PEI	Antimicrobial effect in both B. anthracis and E. coli as antimicrobial coatings [115].
Nanowire Nanohybrid NPs	Core-shell	L: 1200 W:200 A.R: 6.0	Au/SiO_2	Au /tris(bipyridine)-ruthenium(II)chloride	Hyperthermia agents for phototherapeutic cancer therapy. [116].

For biological sensing applications: hybrids have been used for the preparation of silica-based biosensors with complex architectures, such as, fluorescent molecular probes, field-effect transistor (FET) and surface-enhanced Raman scattering (SERS) sensors [116]**.** Si-hybrids exhibit interesting features, such as, rational fabrication of high-quality probes with ultrasensitive biomolecular and dual-mode detection, long-term visualization, essential for real-time biological imaging, for untangle biological events and associated mechanism [117]. The first category, fluorescent silica-based sensors have been designed and fabricated for the detection of biological and chemical species. Evan Phillips and co-workers, developed an ultrasmall Si-inorganic hybrid nanoparticles, known as “C dots”, with dual-optical imaging modality for the first-in-human clinical trial in patients with metastatic melanoma. The SiO_2 NPs were labelled with both, ^{124}I for positron emission

tomography (PET) and Cy5 dye for prepare a hybrid PET-optical imaging tumor-targeted agent [118]. Secondly, the FET sensors induce a negative or positive gate voltage for detecting biological or chemical species by amplify the electronic conductance signals using semicondcutor-metal as support layers [119]. For the last category, silicon-based nanohybrids are ideally for SERS substrates for the analysis of wide biological and chemical samples. Reported applications are presented in **table 1.4**.

Table 1.4 Biological sensing applications of the Silica-based hybrids NPs

Biosensor	Structure type	Size (nm)	Material	Loading/ Functionalization	Application
Fluorescent SiO_2 NPs conjugated (470-560 nm)	Core-shell	2.3 ± 0.5	SiO_2	APTES- 1, 8-naphthalimide or FITC/goat-antimouse IgG	Photostable nanoprobes for tracking live Hela cells in real-time and long-term [120].
Label-free Si quantum dots (435 nm)	Silicon-wafer	2-5	Silicon/ carbon dots	N/A	Photoluminescence probe for glucose detection [121]. Ultrasensitive Detection of Pesticides [122], Nitroaromatic explosives [123], Food additives [124], Human breast cancer (MCF-7) cells [125].
Ion-sensitive field-effect transistors	Silicon nanowires sensors	150	Silicon/Al_2O_3 or HfO_2	Au Layer of 20nm	Real-time, label-free, sensitive, and multiplexed determination of sodium ions [126], nucleic acids [127], [128], gastric cancer biomarkers detecting volatile organic compounds (VOCs) [129], and proteins [130].
Silicon-based SERS sensors	silicon nanowires (SiNWs)	140	Silicon wafer	Silver metal AgNP decorated wafer	enhanced surface-enhanced Raman scattering (SERS) studies [131], single-cell detection of apoptotic cells [132],
Silicon-based SERS sensors	silicon nanowires (SiNWs	100-150	Silicon wafer	Gold (AuNPs)-decorated silicon nanowire array (SiNWAr)	Detection biological and chemical samples, such as, mercury (Hg) (II) [133] and lead ions [134] , DNA [135], Bacteria [136] and trinitrotoluene (TNT) [137].

For bone enginnering applications: silica inorganic/organic hybrids exhibit a great potential, because they can be used: i) as nanocarriers for the fast and safe delivery of necessary growth factors and medicinal agents to the bone cells or ii) they can be used for the development of biodegradable scaffolds for advanced tissue regeneration platforms. [81]. The controllable porosity of these Si-hybrids make them very suitable for the growth and proliferation of bone cells, affecting the degree of mineralization, the

entrance of nutrients and growth factors and the spreading or infiltration. In addition, improved cell growth and enhanced cell adhesion has been observed using nanostructures as extracellular matrix components as particle size was decreased from ∼100 nm to ∼10 nm [138]. Moreover, bioactive and degradable properties (eg. slow or fast dissolution rates) can be added by covalently coupling organosilanes into the hybrids networks, such as, 3-glycidoxypropyltrimethoxysilane (GPTMS), 3-aminopropyltriethoxysilane (APTES) or 3-isocyanatopropyltriethoxysilane (ICPTES) for good control over the nanoscale phase interaction [139]. Reports for applications can be observed in **table 1.5**.

Table 1.5 Bone engineering applications of the Silica-based hybrids NPs

NPs	Structure type	Size	Material	Functionalization	Application
Silica–gelatin hybrid structure	highly porous scaffold	Pores in the range of 2-50 nm	SiO_2 Gelatin	3-glycidoxyproyltrimethoxysilane (GPTMS)	Platform technology for human tissue regeneration using gelatin as C-factor[140].
PHB/PCL/ silica composite scaffold	Fibrous polymer scaffold	0.8-1.0 µm	Fumed SiO_2	Polyhydroxybutyrate (PHB) poly(-caprolactone) (PCL)	Suitabel template for bone tissue engineering [141].
Multifunctional hybrid nanofibrous scaffold	nanofibrous membrane scaffolds	256 ± 73 nm	SiO_2/ Chitosan	poly(ethylene oxide)	Enhancing the mechanical properties of the composite scaffold [142].
Silica-composite hydrogel	Composite scaffold	~122 µm pores (~6 µm)	SiO_2/ Hydroxyapatite (HAp)	poly(l-lactide acid) (PLLA)	Improve bone cell cultivation and reinforced scaffold without any loss of bioactivity [143].

1.7 Core-Shell Silica Nanostructures Using Noble-Metals Nanocrystals

Special attention deserves the core-shell silica nanostructures of hybrid nature, i.e. silica/metal or metal/silica NPs, consisting of a silica core and a metal shell or vice versa, have been attracted a lot of attention because of their unique potential applications ranging from catalysis and biosensing to optical devices and nanomedicine [144]. The resulting nanocomposites are considered highly interesting because one of the main advantages is the ability to develop one unique hybrid material with the combination of different properties (optical from noble metals and support-functionalization from silica) by controlling their geometry, shell morphology and shell composition [145].

In this sense, silica is an interesting semiconducting material used for preparation of core-shell nanomaterials. The SiO_2 shells can be used as a spacer providing effective steric-hindrance and electrostatic protection, enhancing the colloidal stability (e.g. high-Ionic strength aqueous solutions), as well as the natural thermal stability (e.g. insulator properties) for enduring elevated temperatures. In addition, the surface reactivity and biocompatibility can be increased by the widely known silane chemistry for covalent incorporation of active pharmaceutical, fluorophores and biomolecules necessary for biomedical, diagnostic and therapeutic applications. Lastly, due to its transparency to electromagnetic radiation in wavelength range from 300 to 800 nm, make the silica very suitable for the production of multilayer structures with noble-metal particles of high refractive index with plasmonic properties suitable for optical and sensing [141]. These advantages render silica an ideal, low-cost material to tailor surface properties.

Various spherical core–shell nanostructures, in which silica is used as a core, shell or medium, have been studied. Xueqin Liu and co-workers [147] divided the core-shell hybrid nanostructures according to the geometrical configuration into: i) noble metal decorated metal oxide NPs; ii) noble metal/metal oxide shell nanostructures; iii) noble metal/metal oxide yolk/shell nanostructures; and iv) janus noble metal–metal oxide nanostructures (as shown in **figure 1.11**).

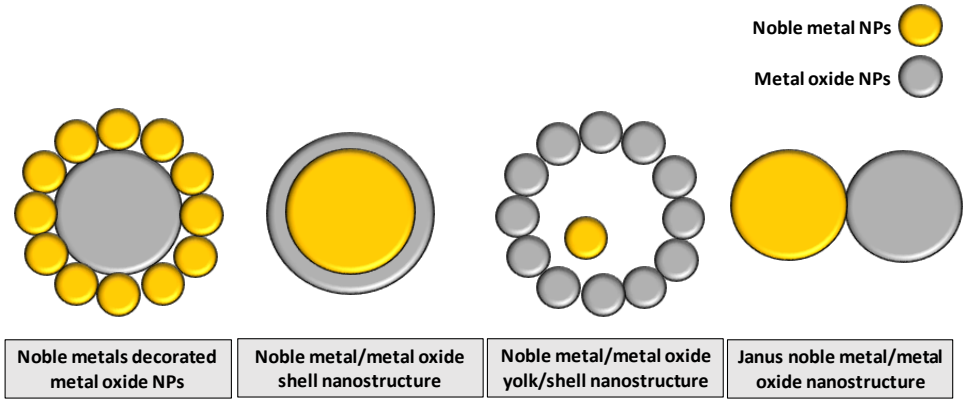

Figure 1.11 Schematic representation of the different core-shell conformations of noble meta-metal oxide nanostructures. Adapted from references [147].

These core–shell nanostructures can be produced by using various synthetic methodologies including: chemical deposition [148], seed induced deposition [149], layer-

by-layer synthesis [150], inverse micelle [31–34], sol–gel condensation [151], sonochemical approach [152], electroless plating [153], [154] and others [146], [155], [156]. However, the scope of this thesis will be related to production of metal@silica shell NPs, using noble-metals NCs as by the sol-gel approach. Therefore, the most common strategy for the production of silica coated nano-sized metals is by using pre-synthesized metal nanoparticles as seeds for further overcoated with silica shells. This strategy can be done using a sol-gel silica-coating approach, divided in “aqueous based” or “organic solvent based” techniques [157], [158].

On one hand, the aqueous –based synthesis route rely on water-soluble silane precursors and silicates, such as sodium silicate, 3-(mercaptopropyl)-trimethoxysilane (MPTMS), 3-(mercaptopropyl)-triethoxysilane (MPTES) and 3-(methyltrimethoxy)-silane (MTMS), that can be hydrolyzed in water prior to condensation to form oxide shell structures at the nanoscale. However, this strategy is generally applicable only to hydrophilic core-materials and is considered an emergent field relatively new with limited literature. On the other hand, the solvent-based (eg; ethanol, DMF, etc.) approach for silica coating are prepared via classic sol-gel Stöber synthesis. This method comprise a multi-step approach, involving the synthesis of the metal core material and the further deposition of the silica shell layers [159].

Gold is currently the most often used metal, due to its chemical stability and more importantly, due to many potential applications. The methodology follows, first the production of the Au metallic NPs synthesized via reduction of Au ions using their corresponding metal-salts ($AuCl_3$), either using external reducing agents (such as NaBH4, hydrazine, sodium citrate) or via trans-metallation utilizing the intrinsic redox properties of the metal precursors. Thereafter, the metal particles act as nucleation centres for the condensation of silicic acids species, produced via hydrolysis and condensation of the trialkoxysilane (TEOS) in an alkaline alcohol/water mixture. The scheme of the process is shown in **figure 1.12**.

This method requires the strict control of each step-in order to obtain structures with desired properties and the production of nanostructures with a narrow distribution with the preferred degree of coverage. In addition, because the metal colloids are

dispersed into alcohol-based medium for the oxide layer growth, the use of surface primers, such as silane coupling agents, surfactants or polymers, is essential to effective growth a homogenous silica shells on the metal nanoparticles, avoiding problems of low chemical compatibility between components.

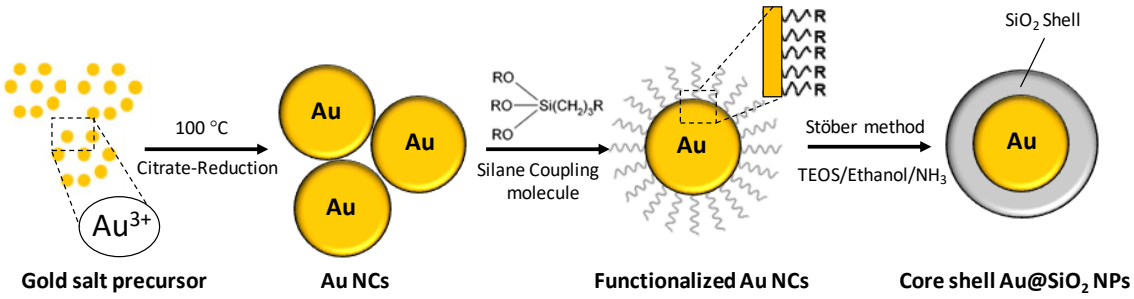

Figure 1.12 Schematic representation of the synthesis of core-shell gold-silica nanoparticles using a modified sol-gel Stöber process. Adapted from references [160].

One of the first remarkably reports preparing silica-coated gold nanoparticles was published by Liz-Marzán and co-workers in 1996 [161]. They use the silane coupling agent (3-aminopropyl) trimethoxysilane as a primer to render the gold vitreophilic surface for growth a silica shell on top of gold colloids in ethanol-based medium using a modified Stöber process. After some years, additional efforts to directly coat gold nanoparticles with silica was published by Xia and co-workers through the hydration and condensation of tetraethyl orthosilicate [162]. However, this work used commercial gold colloids with poor description of the chemistry involved on the surface. Hence, the interaction involved in the silica-coating process was not discussed. Interestingly, a year later, in 2003 Liz-Marzán and co-workers [163] continued working on improving the coating of metal colloids with silica and they successfully developed a method for direct coating the gold nanoparticles by a seeded polymerization technique based on the Stöber method, with the advantage of any silane coupling agents for activate the surface. Only was necessary to add ammonia to the sodium citrate stabilized gold colloids after the addition of TEOS/ethanol and water. Since these reports, several surface-attachment strategies have been developed with other metals particles using bi-functional molecules by means of strong surface-coordination or electrostatic interaction onto others metal nanoparticles for creating colloidally stable surface-protected surfaces under alcoholic solutions for successful achieving a silica surface-coating. For instance, Han and co-workers synthesized highly monodisperse silica-

coated Au NPs without using any primer [159], silver-silica coated NPs [160], such as silica-coated cobalt NPs [161], SiO_2-coated CeO_2 NPs [162], core-shell $Cu@SiO_2$ NPs [163], platinum $Pt@SiO_2$ NPs [164], iron oxide SiO_2-coated Fe_2O_3 NPs [165], [166] and silica encapsulated CdSe quantum dots [167].

1.8 The Surface Plasmon Resonance (SPR) towards Plasmon-Enhance Fluorescence (PEF)

1.8.1 Localized Surface Plasmon Resonance (LSPR) on Metal NCs

One of the most interesting features of the noble-metals NPs, such as gold (Au NPs) and silver (Ag NPs), is that they can interact with electromagnetic radiation by the coherent oscillation of the conduction band electrons, inducing a large surface electric field which enhance their radiative properties. This collective oscillatory motion of the electrons, as (shown in **figure 1.13)**, is characterized by a dominant resonance band in the Vis-NIR, called surface plasmon resonance (SPR) [164], [165].

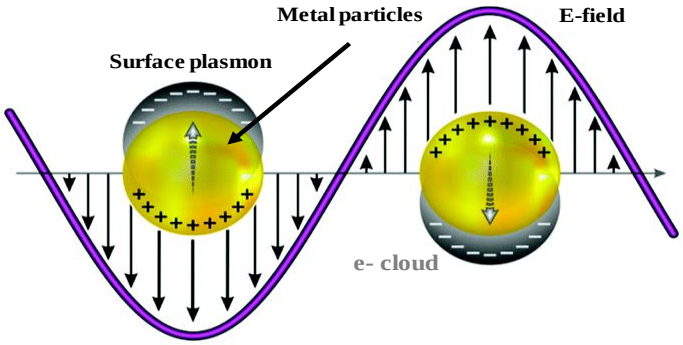

Figure 1.13 Schematic representation of the coherent dipolar oscillation of the conduction band electrons for the metal core, induced by the interacting electromagnetic field of the light. Adapted from references [167].

These unique properties of the plasmonic materials, make them very attractive for sensing applications and hyperthermia cancer treatments [171]–[174]. This displayed optical features is directly related to the NPs size and shape making the absorption cross-section, as well as the scatter light, orders of magnitude more intense than fluorescence of organic dyes [166]. In addition, because this optical property is very sensitive to the surface environment (e.g. molecule adsorption or attachment, aggregation, precipitation), have been subject of many biochemical sensing applications taking advantage of these electron oscillations at the boundary of the metal surface. For instance, the gold surface can be

modified with thiol-based chemistry to immobilize a series of molecular receptors (such as antibodies, DNA, enzymes and proteins among others). This bioconjugation cause a refractive index change near the metal surface, triggering a shift in its resonant wavelength that can be accurately measured by analytical devices (optical biosensors) based on surface plasmon resonance (LSPR) [167]–[169].

On the other hand, gold nanoparticles have been readily used in bio-optical imaging techniques, for enhancing sensitivity and improving resolution, based on their absorption and scattering properties [170]. The exceptional tuneable optical properties near-infrared region, the characteristic X-ray attenuation, the surface enhanced scattering, their chemical inertness and the easy surface modification for enabling their targeting of specific subcellular locations, allows overcome most of the imaging limitations, such as resolution, sensitivity, speed, and penetration depth. However, for their successfully Integration into imaging applications, the controlled modification of the position of the resonance peak and the associated scattering and absorption are required for optimal use [171].

Interestingly, Au NPs present the ability of tuning these optical properties by controlling the particle size, shape or by increasing the refractive index near the particle surface. Therefore, one approach that allow the modification of the SPR band for the specific use is by embedding the Au NPs surface with high index materials, such as silica. Silica is an interesting material because, can displays optically transparency to the Vis-NIR radiation (important because biology is opaque to visible region) and several report have shown that the extinction spectra of the gold nanoparticles, can be tuned by growing a SiO_2 shell on the metal surface [172]. The strength is determined by the shell thickness, as the silica shell increases, the refractive index (change dielectric constant) near the nanoparticle surface (environment) also increases, as a consequence, the nanoparticle extinction spectrum shifts to longer wavelengths (known as red-shifting). This core-shell strategy allows: i) tuning the SPR from the visible into the near-infrared (NIR) region, where main biological absorption is minimal, ii) passivate the surface, enhancing the colloidal stability suitable for avoiding any physical transformation (e.g. non-specific interactions with protein on nanoparticles surface), thereby preserving their optical properties and iii) provides additional cargo capacity for therapeutic molecules [173]. These advantages,

make the gold-core silica shell NPs an attractive candidate for theragnostic applications [174].

1.8.2 Plasmon-Enhance Fluorescence (PEF) on Hybrids Metal@SiO_2 NPs

One interesting application that have been exploited using plasmonic metal/SiO_2 hybrid nanoparticles, is by developing multimodal contrast agents for fluorescence-based detection technologies [175]. The inclusion of the silica shell into noble metal NCs, such as Au NPs, provides an additional reservoir for the encapsulation of fluorescent molecules as spectroscopic tags via covalent attachment within the silica matrix. These dye-embedded silica-coated gold nanoparticles consist of a Au metallic core for optical signal enhancement, a reporter dye molecule for spectroscopic signature and silica shell for protection and further conjugation, that together can be used for multiplexed detection and spectroscopy. In the literature, the history of fluorescence on plasmonic metal surfaces begin with an interesting report of Drexhage and co-workers in 1960s [176], studying the distance-dependent decay rate (lifetime) of a fluorophore when energy transfer in front of a mirror. This metal–molecule distance dependence is the signature of electromagnetic origin and is one of the corner stones in developing this class of metal−dye nanocomposites for fluorescence-based biosensor platforms. The effective distance between the fluorescent molecule and the plasmonic metal is reported that has beneficial effects on optical properties, such as an increased quantum yield, improved photostability and a reduced lifetime of fluorophores [177]. This phenomenon is known as plasmon-enhanced fluorescence (PEF) [178]. On the contrary, a direct contact between the plasmonic metal surface and the dye may result in luminescence quenching by non-radiative energy transfer processes. This explain why a thin metal oxide silica layer as a stable insulating spacer is an interesting approach to control and tune their optimal distance [179].

This strong enhancement of the fluorescence absorption and emission of the dye near a metal surface arises from interactions with the surface plasmon resonances of the metal particles and usually expressed in terms of the apparent quantum yield, measuring the difference of the number of emitted photons in the presence of enhancement and the number of absorbed photons in the absence of enhancement [187]. In the literature, the

enhancement of PEF has been explained by three main factors (shown in **figure 1.14**), due to the electromagnetic dynamic interactions [178], [180].

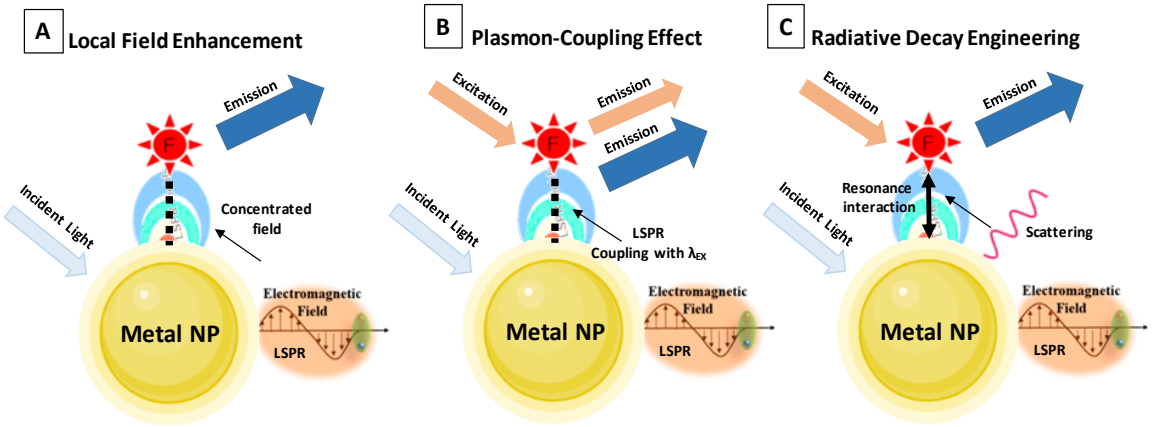

Figure 1.14 Schematic representation of the plasmon- enhanced fluorescence (PEF) mechanism: (A) local field enhancement by the LSPR effect, (B) plasmon coupling effect due to non-radiative interactions and (C) radiative decay engineering effect. Adapted from references [180].

The first factor, is called local field enhancement and results from the efficient coupling of the fluorophores between the electromagnetic field and the spatially confined free-electrons of the nanoparticle. Here, the incident light interacts with the metal NPs, producing a localized surface plasmon oscillations of the electrons (LSPR), that allow the generation of concentrated electromagnetic field around the structure that ultimately affect the optical properties of the confined fluorophores, resulting an enhanced fluorescence intensity [181], [182] . The second factor, is called plasmon-coupling effect mediated by a non-radiative interaction and results from the spectral overlapping between the SPR and the fluorophores absorption band near or over the surface of the metallic nanostructure [183]. This enhancement by non-radiative energy transfer depends on two things: i) the strength of the electric field and ii) the degree of spectral overlapping between the metal surface and the fluorophore (absorption, scattering, emission). If the SPR and the fluorophore are at close distance, the energy transfer between them is dominated by Förster resonance energy transfer (FRET) [184]. If the separation is larger, is dominated by the Purcell effect [185] . Finally, the third factor, is called radiative decay engineering or intrinsic lifetime (RDE) [186], and is the results of the non-radiative energy transfer from the metallic nanostructures to the fluorophores, allowing the fluorophores to excite and

transmit energy to the far-field as radiative transfer, thus enhancing the fluorescence intensity [187]. These interactions correspond to the absorption and scattering properties of metallic nanostructures that can increase the emission the fluorophore, quantum yield and the fluorophore's brightness while decreasing the lifetime [182] .

For PEF-based nanostructures applications, silica has been used as: (i) rigid spacer to control the gap distance between the plasmonic metal surface and the fluorescent dye. This is done because the LSPR band associated with the size of metal NPs, need to be in an optimal proximity with the emission wavelength of the dye molecule, in order to experience the fluorescence intensity enhancement. Moreover, (ii) as a functional surface, for the growing of a second SiO_2 layer on the PEF hybrid nanostructure, that is beneficial for protecting the NP from harsh environments (increasing the colloidal stability) and the possibility to target specific sites of interest by the proper surface functionalization with functional groups (eg; -NH_2, -COOH, -SH, -PEG) using silane linkers.

In the literature, the functionalization of the silica surface is often exploited to achieve selective recognition for certain analytes. For instance, Shan Zhang and co-workers [188], prepared Au@SiO_2 core–shell NPs doped with fluorescein isothiocyanate (FITC), for applications in ultrasensitive detection. They found that the optimum fluorescence enhancement factor of 5.0. occurred using a silica shell thickness of 34 nm. Similarly, Jiao Chen and company [189], developed an Au@SiO_2 nanocomposite FITC doped as effective model for studying metal-enhanced fluorescence mechanism at the nanoscale. They reported an enhancement factor of 9.2 using 36.6 ± 4.4 nm of silica shell as spacer. Other authors have been reported PEF nanostructures as sensing platforms using other dyes, such as Ag@SiO_2 using rhodamine dye yielded up to 20-fold PEF increased [190], Au@SiO_2 with a core of 100 nm producing an enhancement factor of 110 fold using crystal violet dye [191], cascade yellow (CYe) and carboxyfluorescein (FAM) dyes were used to build, CYe-labeled Ag@SiO_2 and FAM-labeled Au@SiO_2 NPs, displaying a 12.5 fold and 6.8 fold fluorescence enhancement, respectively [192], Au@SiO_2 doped with near-infrared (NIR)-emitting fluorescent molecules Indocyanine Green (ICG), presented a fluorescence enhancement of 50-fold increase [193], gold nanobipyramids and nanorods Au@SiO_2@Cy7, were doped with a NIR cyanine dye (Cy7 NHS ester), showing a maximum

enhancement of 10.5 and 4.5-fold respectively, at a distance of approximately 17 nm [194], finally, silver@silica (Ag@SiO_2) nanocubes coated with an ultrathin silica shell of thickness ≈1.5 nm, displayed a significantly metal-enhanced photoluminescence increase by 2.28 fold on alumina-coated foil substrate [195].

1.9 References

[1] S. R. Taylor, "Abundance of chemical elements in the continental crust: a new table," *Geochim. Cosmochim. Acta*, vol. 28, no. 8, pp. 1273–1285, 1964, doi: https://doi.org/10.1016/0016-7037(64)90129-2.

[2] X. J. Wang, X. Y. Wang, H. F. Zhu, and X. Y. Cong, "The Change of Silica Tetrahedron in Cement-Silica Fume Blends Hydration," *Mater. Sci. Forum*, vol. 743–744, pp. 280–284, 2013, doi: 10.4028/www.scientific.net/MSF.743-744.280.

[3] C. J. Brinker and G. W. Scherer, "CHAPTER 1 - Introduction," C. J. Brinker and G. W. B. T.-S.-G. S. Scherer, Eds. San Diego: Academic Press, 1990, p. xvi-18.

[4] R. K. Iler, "The chemistry of silica : solubility, polymerization, colloid and surface properties, and biochemistry." Wiley, New York, 1979.

[5] W. J. Sandberg *et al.*, "Comparison of non-crystalline silica nanoparticles in IL-1β release from macrophages," *Part. Fibre Toxicol.*, vol. 9, no. 1, p. 32, 2012, doi: 10.1186/1743-8977-9-32.

[6] I. A. Rahman and V. Padavettan, "Synthesis of silica nanoparticles by sol-gel: size-dependent properties, surface modification, and applications in silica-polymer nanocomposites — a review," *J. Nanomater.*, vol. 2012, p. 8, 2012, doi: 10.1155/2012/132424.

[7] T. J. Merkel, K. P. Herlihy, J. Nunes, R. M. Orgel, J. P. Rolland, and J. M. DeSimone, "Scalable, Shape-Specific, Top-Down Fabrication Methods for the Synthesis of Engineered Colloidal Particles," *Langmuir*, vol. 26, no. 16, pp. 13086–13096, Aug. 2010, doi: 10.1021/la903890h.

[8] M. P. Pileni, "Semiconductor Nanocrystals," *Nanoscale Materials in Chemistry*. pp. 61–84, 23-Aug-2001, doi: https://doi.org/10.1002/0471220620.ch3.

[9] E. Reverchon and R. Adami, "Nanomaterials and supercritical fluids," *J. Supercrit. Fluids*, vol. 37, no. 1, pp. 1–22, 2006, doi: https://doi.org/10.1016/j.supflu.2005.08.003.

[10] M. Salavati-Niasari, J. Javidi, and M. Dadkhah, "Ball Milling Synthesis of Silica Nanoparticle from Rice Husk Ash for Drug Delivery Application," *Comb. Chem. High Throughput Screen.*, vol. 16, Aug. 2012, doi: 10.2174/1386207311316060006.

[11] A. R. Dogra, V. Sharma, R. Gahrotra, and P. Kumar, "Evaporation induced self-assembly of silica nanoparticles on ITO substrates in a confined cell for vertical alignment of liquid crystals and performance analysis," *Colloids Surfaces A Physicochem. Eng. Asp.*, vol. 642, p. 128712, 2022, doi: https://doi.org/10.1016/j.colsurfa.2022.128712.

[12] X. Zeng *et al.*, "Sputtering of silicon nanopowders by an argon cluster ion beam," *Beilstein J. Nanotechnol.*, vol. 10, pp. 135–143, 2019.

[13] J. Zhang, J. Claverie, M. Chaker, and D. Ma, “Colloidal Metal Nanoparticles Prepared by Laser Ablation and their Applications,” *ChemPhysChem*, vol. 18, no. 9, pp. 986–1006, May 2017, doi: https://doi.org/10.1002/cphc.201601220.

[14] N. Abid *et al.*, “Synthesis of nanomaterials using various top-down and bottom-up approaches, influencing factors, advantages, and disadvantages: A review,” *Adv. Colloid Interface Sci.*, vol. 300, p. 102597, 2022, doi: https://doi.org/10.1016/j.cis.2021.102597.

[15] B. Sun *et al.*, “Reduction of Acute Inflammatory Effects of Fumed Silica Nanoparticles in the Lung by Adjusting Silanol Display through Calcination and Metal Doping,” *ACS Nano*, vol. 9, no. 9, pp. 9357–9372, Sep. 2015, doi: 10.1021/acsnano.5b03443.

[16] E. D. E. R. Hyde, A. Seyfaee, F. Neville, and R. Moreno-Atanasio, “Colloidal Silica Particle Synthesis and Future Industrial Manufacturing Pathways: A Review,” *Ind. Eng. Chem. Res.*, vol. 55, no. 33, pp. 8891–8913, Aug. 2016, doi: 10.1021/acs.iecr.6b01839.

[17] K. S. Finnie, J. R. Bartlett, C. J. A. Barbé, and L. Kong, “Formation of Silica Nanoparticles in Microemulsions,” *Langmuir*, vol. 23, no. 6, pp. 3017–3024, Mar. 2007, doi: 10.1021/la0624283.

[18] Y. Hu, G. Cheng, H. Li, and Y. He, “Synthesis of SiO2 nanoparticles by chemical precipitation,” vol. 67, pp. 379–383, Aug. 2016, doi: 10.11949/j.issn.0438-1157.20160565.

[19] J. Zha and H. Roggendorf, “Sol–gel science, the physics and chemistry of sol–gel processing, Ed. by C. J. Brinker and G. W. Scherer, Academic Press, Boston 1990, xiv, 908 pp., bound—ISBN 0-12-134970-5,” *Adv. Mater.*, vol. 3, no. 10, p. 522, Oct. 1991, doi: https://doi.org/10.1002/adma.19910031025.

[20] K. Cho, H. Chang, D. S. Kil, J. Park, H. D. Jang, and H. Y. Sohn, “Mechanisms of the Formation of Silica Particles from Precursors with Different Volatilities by Flame Spray Pyrolysis,” *Aerosol Sci. Technol.*, vol. 43, no. 9, pp. 911–920, Aug. 2009, doi: 10.1080/02786820903025986.

[21] L. A. Kolahalam, I. V Kasi Viswanath, B. S. Diwakar, B. Govindh, V. Reddy, and Y. L. N. Murthy, “Review on nanomaterials: Synthesis and applications,” *Mater. Today Proc.*, vol. 18, pp. 2182–2190, 2019, doi: https://doi.org/10.1016/j.matpr.2019.07.371.

[22] C. J. Brinker and G. W. Scherer, “CHAPTER 4 - Particulate Sols and Gels,” C. J. Brinker and G. W. B. T.-S.-G. S. Scherer, Eds. San Diego: Academic Press, 1990, pp. 234–301.

[23] G. M. Patel, G. J. Bhatt, and P. T. Deota, “2 - Synthesis and characterization of silicon-based hybrid nanoparticles,” in *Micro and Nano Technologies*, S. Thomas, T. A. Nguyen, M. Ahmadi, G. Yasin, and N. B. T.-S.-B. H. N. Joshi, Eds. Elsevier, 2022, pp. 11–43.

[24] D. D. Sood, “The role sol–gel process for nuclear fuels-an overview,” *J. Sol-Gel Sci. Technol.*, vol. 59, no. 3, pp. 404–416, 2011, doi: 10.1007/s10971-010-2273-y.

[25] L. P. Singh *et al.*, “Sol-Gel processing of silica nanoparticles and their applications,” *Adv. Colloid Interface Sci.*, vol. 214, pp. 17–37, 2014, doi: https://doi.org/10.1016/j.cis.2014.10.007.

[26] A. E. Danks, S. R. Hall, and Z. Schnepp, “The evolution of ‘sol–gel’ chemistry as a technique for materials synthesis,” *Mater. Horizons*, vol. 3, no. 2, pp. 91–112, 2016, doi: 10.1039/C5MH00260E.

[27] G. Kickelbick, “Introduction to Hybrid Materials,” *Hybrid Materials*. pp. 1–48, 18-Dec-

2006, doi: https://doi.org/10.1002/9783527610495.ch1.
[28] C. R. Silva and C. Airoldi, “Acid and Base Catalysts in the Hybrid Silica Sol–Gel Process,” *J. Colloid Interface Sci.*, vol. 195, no. 2, pp. 381–387, 1997, doi: https://doi.org/10.1006/jcis.1997.5159.
[29] K. Do Kim and H. T. Kim, “New Process for the Preparation of Monodispersed, Spherical Silica Particles,” *J. Am. Ceram. Soc.*, vol. 85, no. 5, pp. 1107–1113, 2002, doi: 10.1111/j.1151-2916.2002.tb00230.x.
[30] G. Kickelbick, “Hybrid Materials – Past, Present and Future.,” *Hybrid Mater.*, vol. 1, Apr. 2014, doi: 10.2478/hyma-2014-0001.
[31] C. J. Brinker, “Hydrolysis and condensation of silicates: Effects on structure,” *J. Non. Cryst. Solids*, vol. 100, no. 1, pp. 31–50, 1988, doi: https://doi.org/10.1016/0022-3093(88)90005-1.
[32] A. van Blaaderen and A. P. M. Kentgens, “Particle morphology and chemical microstructure of colloidal silica spheres made from alkoxysilanes,” *J. Non. Cryst. Solids*, vol. 149, no. 3, pp. 161–178, 1992, doi: https://doi.org/10.1016/0022-3093(92)90064-Q.
[33] C. J. Brinker and G. W. Scherer, “CHAPTER 3 - Hydrolysis and Condensation II: Silicates,” in *Sol-Gel Science*, C. J. Brinker and G. W. Scherer, Eds. San Diego: Academic Press, 1990, pp. 96–233.
[34] W. Stöber, A. Fink, and E. Bohn, “Controlled growth of monodisperse silica spheres in the micron size range,” *J. Colloid Interface Sci.*, vol. 26, no. 1, pp. 62–69, 1968, doi: https://doi.org/10.1016/0021-9797(68)90272-5.
[35] C. Rosu, S. Selcuk, E. Soto-Cantu, and P. Russo, “Progress in silica polypeptide composite colloidal hybrids: From silica cores to fuzzy shells,” *Colloid Polym. Sci.*, vol. 292, Jan. 2014, doi: 10.1007/s00396-014-3170-7.
[36] T. Matsoukas and E. Gulari, “Dynamics of growth of silica particles from ammonia-catalyzed hydrolysis of tetra-ethyl-orthosilicate,” *J. Colloid Interface Sci.*, vol. 124, no. 1, pp. 252–261, 1988, doi: https://doi.org/10.1016/0021-9797(88)90346-3.
[37] G. H. Bogush and C. F. Zukoski, “Uniform silica particle precipitation: An aggregative growth model,” *J. Colloid Interface Sci.*, vol. 142, no. 1, pp. 19–34, 1991, doi: https://doi.org/10.1016/0021-9797(91)90030-C.
[38] P. P. Ghimire and M. Jaroniec, “Renaissance of Stöber method for synthesis of colloidal particles: New developments and opportunities,” *J. Colloid Interface Sci.*, vol. 584, pp. 838–865, 2021, doi: https://doi.org/10.1016/j.jcis.2020.10.014.
[39] V. K. LaMer and R. H. Dinegar, “Theory, Production and Mechanism of Formation of Monodispersed Hydrosols,” *J. Am. Chem. Soc.*, vol. 72, no. 11, pp. 4847–4854, Nov. 1950, doi: 10.1021/ja01167a001.
[40] M. T. Harris, “Ultrafine ceramic precursor powders by homogeneous precipitation and electrodispersion.” The University of Tennessee, 1992.
[41] D. Agrawal, *Introduction to Nanoscience and Nanomaterials*. 2013.
[42] P. Yang, S. Gai, and J. Lin, “ChemInform Abstract: Functionalized Mesoporous Silica Materials for Controlled Drug Delivery,” *Chem. Soc. Rev.*, vol. 41, pp. 3679–3698, Mar. 2012, doi: 10.1039/c2cs15308d.
[43] B. Qiao, T.-J. Wang, H. Gao, and Y. Jin, “High density silanization of nano-silica particles using γ-aminopropyltriethoxysilane (APTES),” *Appl. Surf. Sci.*, vol. 351, pp. 646–654, 2015, doi: https://doi.org/10.1016/j.apsusc.2015.05.174.

[44] L. T. Zhuravlev, “Concentration of hydroxyl groups on the surface of amorphous silicas,” *Langmuir*, vol. 3, no. 3, pp. 316–318, May 1987, doi: 10.1021/la00075a004.

[45] L. T. Zhuravlev, “Surface characterization of amorphous silica—a review of work from the former USSR,” *Colloids Surfaces A Physicochem. Eng. Asp.*, vol. 74, no. 1, pp. 71–90, 1993, doi: https://doi.org/10.1016/0927-7757(93)80399-Y.

[46] F. Hoffmann, M. Cornelius, J. Morell, and M. Fröba, “Silica-Based Mesoporous Organic–Inorganic Hybrid Materials,” *Angew. Chemie Int. Ed.*, vol. 45, no. 20, pp. 3216–3251, May 2006, doi: https://doi.org/10.1002/anie.200503075.

[47] Z. Meng, C. Xue, Q. Zhang, X. Yu, K. Xi, and X. Jia, “Preparation of Highly Monodisperse Hybrid Silica Nanospheres Using a One-Step Emulsion Reaction in Aqueous Solution,” *Langmuir*, vol. 25, no. 14, pp. 7879–7883, Jul. 2009, doi: 10.1021/la900458b.

[48] X. S. Zhao and G. Q. Lu, “Modification of MCM-41 by Surface Silylation with Trimethylchlorosilane and Adsorption Study,” *J. Phys. Chem. B*, vol. 102, no. 9, pp. 1556–1561, Feb. 1998, doi: 10.1021/jp972788m.

[49] S. R. Hall, S. A. Davis, and S. Mann, “Cocondensation of Organosilica Hybrid Shells on Nanoparticle Templates: A Direct Synthetic Route to Functionalized Core−Shell Colloids,” *Langmuir*, vol. 16, no. 3, pp. 1454–1456, Feb. 2000, doi: 10.1021/la9909143.

[50] M. H. Lim and A. Stein, “Comparative Studies of Grafting and Direct Syntheses of Inorganic−Organic Hybrid Mesoporous Materials,” *Chem. Mater.*, vol. 11, no. 11, pp. 3285–3295, Nov. 1999, doi: 10.1021/cm990369r.

[51] E. F. Vansant, P. Van Der Voort, and K. C. B. T.-S. in S. S. and C. Vrancken, Eds., “Chapter 8 Chemical modification of silica: applications and procedures,” in *Characterization and Chemical Modification of the Silica Surface*, vol. 93, Elsevier, 1995, pp. 149–192.

[52] C. Oh *et al.*, “New approach to the immobilization of glucose oxidase on non-porous silica microspheres functionalized by (3-aminopropyl)trimethoxysilane (APTMS),” *Colloids Surfaces B Biointerfaces*, vol. 53, no. 2, pp. 225–232, 2006, doi: https://doi.org/10.1016/j.colsurfb.2006.09.007.

[53] R. Richer, “Direct synthesis of functionalized mesoporous silica by non-ionic alkylpolyethyleneoxide surfactant assembly,” *Chem. Commun.*, no. 16, pp. 1775–1777, 1998, doi: 10.1039/A803285H.

[54] H. Xu, F. Yan, E. E. Monson, and R. Kopelman, “Room-temperature preparation and characterization of poly (ethylene glycol)-coated silica nanoparticles for biomedical applications,” *J. Biomed. Mater. Res. Part A*, vol. 66A, no. 4, pp. 870–879, 2003, doi: doi:10.1002/jbm.a.10057.

[55] S. Kang, S. Il Hong, C. R. Choe, M. Park, S. Rim, and J. Kim, “Preparation and characterization of epoxy composites filled with functionalized nanosilica particles obtained via sol–gel process,” *Polymer (Guildf).*, vol. 42, no. 3, pp. 879–887, 2001, doi: https://doi.org/10.1016/S0032-3861(00)00392-X.

[56] Y. Sun, Z. Zhang, and C. P. Wong, “Study on mono-dispersed nano-size silica by surface modification for underfill applications,” *J. Colloid Interface Sci.*, vol. 292, no. 2, pp. 436–444, 2005, doi: https://doi.org/10.1016/j.jcis.2005.05.067.

[57] P. Vejayakumaran, I. Ab Rahman, C. Sipaut, J. Ismail, and C. Chee, “Structural and thermal characterizations of silica nanoparticles grafted with pendant maleimide

and epoxide groups," *J. Colloid Interface Sci.*, vol. 328, pp. 81–91, Oct. 2008, doi: 10.1016/j.jcis.2008.08.054.

[58] K. Pham, D. Fullston, and K. Sagoe-Crentsil, "RETRACTED: Surface modification for stability of nano-sized silica colloids," *J. Colloid Interface Sci.*, vol. 315, pp. 123–127, Dec. 2007, doi: 10.1016/j.jcis.2007.06.064.

[59] T. M. Suzuki, T. Nakamura, K. Fukumoto, M. Yamamoto, Y. Akimoto, and K. Yano, "Direct synthesis of amino-functionalized monodispersed mesoporous silica spheres and their catalytic activity for nitroaldol condensation," *J. Mol. Catal. A Chem.*, vol. 280, no. 1, pp. 224–232, 2008, doi: https://doi.org/10.1016/j.molcata.2007.11.012.

[60] N. Karaca, "The synthesis and characterization of polyorganosiloxane nanoparticles from 3-mercaptopropyltrimethoxysilane for preparation of nanocomposite films via photoinitiated thiol-ene polymerization," *TURKISH J. Chem.*, vol. 45, pp. 761–774, Jun. 2021, doi: 10.3906/kim-2012-48.

[61] J. Kobler and T. Bein, "Porous Thin Films of Functionalized Mesoporous Silica Nanoparticles," *ACS Nano*, vol. 2, no. 11, pp. 2324–2330, Nov. 2008, doi: 10.1021/nn800505g.

[62] E. J. Cueto-Díaz *et al.*, "APTES-Based Silica Nanoparticles as a Potential Modifier for the Selective Sequestration of CO(2) Gas Molecules," *Nanomater. (Basel, Switzerland)*, vol. 11, no. 11, p. 2893, Oct. 2021, doi: 10.3390/nano11112893.

[63] Y. Q. Yu, C.-Y. Chen, and W.-C. Chen, "Synthesis and characterization of organic-inorganic hybrid thin films from poly(acrylic) and monodispersed colloidal silica," *Polymer (Guildf).*, vol. 44, pp. 593–601, Feb. 2003, doi: 10.1016/S0032-3861(02)00824-8.

[64] I. Freris, D. Cristofori, P. Riello, and A. Benedetti, "Encapsulation of submicrometer-sized silica particles by a thin shell of poly(methyl methacrylate)," *J. Colloid Interface Sci.*, vol. 331, no. 2, pp. 351–355, 2009, doi: https://doi.org/10.1016/j.jcis.2008.11.052.

[65] P. Gómez-Romero and C. Sanchez, "Functional Hybrid Material," 2005, pp. 1–14.

[66] P. Judeinstein and C. Sanchez, "Hybrid organic–inorganic materials: a land of multidisciplinarity," *J. Mater. Chem.*, vol. 6, no. 4, pp. 511–525, 1996, doi: 10.1039/JM9960600511.

[67] P. Gómez-Romero and C. Sanchez, "Hybrid materials. Functional properties. From Maya Blue to 21st century materials," *New J. Chem.*, vol. 29, no. 1, pp. 57–58, 2005, doi: 10.1039/B416075B.

[68] A. Singh, N. Verma, and K. Kumar, "Chapter 2 - Hybrid composites: a revolutionary trend in biomedical engineering," V. Grumezescu and A. M. B. T.-M. for B. E. Grumezescu, Eds. Elsevier, 2019, pp. 33–46.

[69] E. Bourgeat-Lami, "Hybrid Organic/Inorganic Particles," *Hybrid Materials*. pp. 87–149, 18-Dec-2006, doi: doi:10.1002/9783527610495.ch3.

[70] N. Bastús *et al.*, "Exploring New Synthetic Strategies for the Production of Advanced Complex Inorganic Nanocrystals," *Zeitschrift für Phys. Chemie*, vol. 229, Jan. 2015, doi: 10.1515/zpch-2014-0611.

[71] M. Nanko, "Definitions and Categories of Hybrid Materials," *Adv. Technol. Mater. Mater. Process.*, vol. 11, pp. 1–8, Jan. 2009, doi: 10.2240/azojomo0288.

[72] M. S. Saveleva *et al.*, "Hierarchy of Hybrid Materials—The Place of Inorganics-in-Organics in it, Their Composition and Applications ," *Frontiers in Chemistry* , vol. 7.

2019.
[73] W. Park, H. Shin, B. Choi, W.-K. Rhim, K. Na, and D. Keun Han, “Advanced hybrid nanomaterials for biomedical applications,” *Prog. Mater. Sci.*, vol. 114, p. 100686, 2020, doi: https://doi.org/10.1016/j.pmatsci.2020.100686.
[74] Pratibha and J. K. Rajput, “10 - Application of silicon-based hybrid nanoparticles in catalysis,” in *Micro and Nano Technologies*, S. Thomas, T. A. Nguyen, M. Ahmadi, G. Yasin, and N. B. T.-S.-B. H. N. Joshi, Eds. Elsevier, 2022, pp. 199–246.
[75] S.-H. Wu, C.-Y. Mou, and H.-P. Lin, “Synthesis of mesoporous silica nanoparticles,” *Chem. Soc. Rev.*, vol. 42, no. 9, pp. 3862–3875, 2013, doi: 10.1039/C3CS35405A.
[76] I. Pontón, A. Martí del Rio, M. Gómez Gómez, and D. Sánchez-García, “Preparation and Applications of Organo-Silica Hybrid Mesoporous Silica Nanoparticles for the Co-Delivery of Drugs and Nucleic Acids,” *Nanomaterials* , vol. 10, no. 12. 2020, doi: 10.3390/nano10122466.
[77] M. Davidson, Y. Ji, G. J. Leong, N. C. Kovach, B. G. Trewyn, and R. M. Richards, “Hybrid Mesoporous Silica/Noble-Metal Nanoparticle Materials—Synthesis and Catalytic Applications,” *ACS Appl. Nano Mater.*, vol. 1, no. 9, pp. 4386–4400, Sep. 2018, doi: 10.1021/acsanm.8b00967.
[78] A. B. D. Nandiyanto, Y. Akane, T. Ogi, and K. Okuyama, “Mesopore-Free Hollow Silica Particles with Controllable Diameter and Shell Thickness via Additive-Free Synthesis,” *Langmuir*, vol. 28, no. 23, pp. 8616–8624, Jun. 2012, doi: 10.1021/la301457v.
[79] “Fabrication of hollow silica spheres and their application in polyacrylate film forming agent,” *J. Mater. Sci.*, vol. 49, no. 24, pp. 8215–8225, Jan. 2014.
[80] Q. Liu, M. H. Nayfeh, and S.-T. Yau, “A silicon nanoparticle-based polymeric nano-composite material for glucose sensing,” *J. Electroanal. Chem.*, vol. 657, no. 1, pp. 172–175, 2011, doi: https://doi.org/10.1016/j.jelechem.2011.03.022.
[81] O. Mahony *et al.*, “Silica-Gelatin Hybrids with Tailorable Degradation and Mechanical Properties for Tissue Regeneration,” *Adv. Funct. Mater.*, vol. 20, pp. 3835–3845, Nov. 2010, doi: 10.1002/adfm.201000838.
[82] M. Ochi and R. Takahashi, “Phase structure and thermomechanical properties of primary and tertiary amine-cured epoxy/silica hybrids,” *J. Polym. Sci. Part B Polym. Phys.*, vol. 39, no. 11, pp. 1071–1084, Jun. 2001, doi: https://doi.org/10.1002/polb.1084.
[83] R. Tamaki, K. Naka, and Y. Chujo, “Synthesis of Poly(N,N-dimethylacrylamide)/Silica Gel Polymer Hybrids by in situ Polymerization Method,” *Polym. J.*, vol. 30, no. 1, pp. 60–65, 1998, doi: 10.1295/polymj.30.60.
[84] M. Toki, T. Y. Chow, T. Ohnaka, H. Samura, and T. Saegusa, “Structure of poly(vinylpyrrolidone)-silica hybrid,” *Polym. Bull.*, vol. 29, no. 6, pp. 653–660, 1992, doi: 10.1007/BF01041151.
[85] K. A. Mauritz and C. K. Jones, “Novel poly(n-butyl methacrylate)/titanium oxide alloys produced by te sol–gel process for titanium alkoxides,” *J. Appl. Polym. Sci.*, vol. 40, no. 7–8, pp. 1401–1420, Oct. 1990, doi: https://doi.org/10.1002/app.1990.070400726.
[86] K. Landfester, “Miniemulsion Polymerization and the Structure of Polymer and Hybrid Nanoparticles,” *Angew. Chemie Int. Ed.*, vol. 48, no. 25, pp. 4488–4507, Jun. 2009, doi: https://doi.org/10.1002/anie.200900723.

[87] F. Yang and G. L. Nelson, “PMMA/silica nanocomposite studies: Synthesis and properties,” *J. Appl. Polym. Sci.*, vol. 91, no. 6, pp. 3844–3850, Mar. 2004, doi: https://doi.org/10.1002/app.13573.

[88] M. Joubert, C. Delaite, E. Bourgeat Lami, and P. Dumas, “Synthesis of poly(ε-caprolactone)–silica nanocomposites: from hairy colloids to core–shell nanoparticles,” *New J. Chem.*, vol. 29, no. 12, pp. 1601–1609, 2005, doi: 10.1039/B508649C.

[89] I. Gill, “Bio-doped Nanocomposite Polymers: Sol−Gel Bioencapsulates,” *Chem. Mater.*, vol. 13, no. 10, pp. 3404–3421, Oct. 2001, doi: 10.1021/cm0102483.

[90] A. L. B. Maçon, T. Kasuga, C. Remzi Becer, and J. R. Jones, “Silica/methacrylate class II hybrid: telomerisation vs. RAFT polymerisation,” *Polym. Chem.*, vol. 8, no. 23, pp. 3603–3611, 2017, doi: 10.1039/C7PY00516D.

[91] D. Devapal, P. Shanmugam, S. Krishnan, P. Ravindran, and B. George, “Synthesis, Characterization and Ceramic Conversion Studies of Borosiloxane Oligomers from Phenyltrialkoxysilanes,” *J. Inorg. Organomet. Polym. Mater.*, vol. 20, pp. 666–674, Dec. 2010, doi: 10.1007/s10904-010-9380-7.

[92] A.-C. Franville, D. Zambon, R. Mahiou, and Y. Troin, “Luminescence Behavior of Sol−Gel-Derived Hybrid Materials Resulting from Covalent Grafting of a Chromophore Unit to Different Organically Modified Alkoxysilanes,” *Chem. Mater.*, vol. 12, no. 2, pp. 428–435, Feb. 2000, doi: 10.1021/cm9904739.

[93] N. Klippel, G. Jung, and G. Kickelbick, “Hybrid inorganic-organic fluorescent silica nanoparticles—influence of dye binding modes on dye leaching,” *J. Sol-Gel Sci. Technol.*, 2021, doi: 10.1007/s10971-021-05578-y.

[94] A. Van Blaaderen and A. Vrij, “Synthesis and characterization of colloidal dispersions of fluorescent, monodisperse silica spheres,” *Langmuir*, vol. 8, no. 12, pp. 2921–2931, 1992, doi: 10.1021/la00048a013.

[95] S. Liu, J. Peng, Z. Liu, Z. Liu, H. Zhang, and R. Wu, “One-Pot Approach to Prepare Organo-silica Hybrid Capillary Monolithic Column with Intact Mesoporous Silica Nanoparticle as Building Block,” *Sci. Rep.*, vol. 6, no. 1, p. 34718, 2016, doi: 10.1038/srep34718.

[96] S. Amberg-Schwab, M. Hoffmann, H. Bader, and M. Gessler, “Inorganic-Organic Polymers with Barrier Properties for Water Vapor, Oxygen and Flavors,” *J. Sol-Gel Sci. Technol.*, vol. 13, no. 1, pp. 141–146, 1998, doi: 10.1023/A:1008628029870.

[97] K.-H. Haas, S. Amberg-Schwab, and K. Rose, “Functionalized coating materials based on inorganic-organic polymers,” *Thin Solid Films*, vol. 351, no. 1, pp. 198–203, 1999, doi: https://doi.org/10.1016/S0040-6090(99)00203-5.

[98] S. Yang and Y. Li, “Fluorescent hybrid silica nanoparticles and their biomedical applications,” *WIREs Nanomedicine and Nanobiotechnology*, vol. 12, no. 3, p. e1603, May 2020, doi: https://doi.org/10.1002/wnan.1603.

[99] Q. Shao and B. Xing, “Photoactive molecules for applications in molecular imaging and cell biology,” *Chem. Soc. Rev.*, vol. 39, no. 8, pp. 2835–2846, 2010, doi: 10.1039/B915574K.

[100] D. Li and J. Yu, “AIEgens-Functionalized Inorganic-Organic Hybrid Materials: Fabrications and Applications,” *Small*, vol. 12, no. 47, pp. 6478–6494, Dec. 2016, doi: https://doi.org/10.1002/smll.201601484.

[101] M. Faisal *et al.*, “Fabrication of Fluorescent Silica Nanoparticles Hybridized with AIE

Luminogens and Exploration of Their Applications as Nanobiosensors in Intracellular Imaging," *Chem. – A Eur. J.*, vol. 16, no. 14, pp. 4266–4272, Apr. 2010, doi: https://doi.org/10.1002/chem.200901823.

[102] L. Yang, L. Wang, C. Cui, J. Lei, and J. Zhang, "Stöber strategy for synthesizing multifluorescent organosilica nanocrystals," *Chem. Commun.*, vol. 52, no. 36, pp. 6154–6157, 2016, doi: 10.1039/C6CC01917J.

[103] S. A. M. A. Peerzade, N. Makarova, and I. Sokolov, "Ultrabright Fluorescent Silica Nanoparticles for Multiplexed Detection," *Nanomaterials* , vol. 10, no. 5. 2020, doi: 10.3390/nano10050905.

[104] X. Wu *et al.*, "Constructing NIR silica–cyanine hybrid nanocomposite for bioimaging in vivo: a breakthrough in photo-stability and bright fluorescence with large Stokes shift," *Chem. Sci.*, vol. 4, no. 3, pp. 1221–1228, 2013, doi: 10.1039/C2SC22035K.

[105] V. Selvarajan, S. Obuobi, and P. L. R. Ee, "Silica Nanoparticles-A Versatile Tool for the Treatment of Bacterial Infections," *Front. Chem.*, vol. 8, p. 602, Jul. 2020, doi: 10.3389/fchem.2020.00602.

[106] I. Makarovsky, Y. Boguslavsky, M. Alesker, J. Lellouche, E. Banin, and J.-P. Lellouche, "Novel Triclosan-Bound Hybrid-Silica Nanoparticles and their Enhanced Antimicrobial Properties," *Adv. Funct. Mater.*, vol. 21, Nov. 2011, doi: 10.1002/adfm.201101557.

[107] G. Qi, L. Li, F. Yu, and H. Wang, "Vancomycin-Modified Mesoporous Silica Nanoparticles for Selective Recognition and Killing of Pathogenic Gram-Positive Bacteria Over Macrophage-Like Cells," *ACS Appl. Mater. Interfaces*, vol. 5, no. 21, pp. 10874–10881, Nov. 2013, doi: 10.1021/am403940d.

[108] M. M. Wan *et al.*, "Sustained Release of Heparin on Enlarged-Pore and Functionalized MCM-41," *ACS Appl. Mater. Interfaces*, vol. 4, no. 8, pp. 4113–4122, Aug. 2012, doi: 10.1021/am300878z.

[109] D. Pedraza, J. Díez, Isabel-Izquierdo-Barba, M. Colilla, and M. Vallet-Regí, "Amine-Functionalized Mesoporous Silica Nanoparticles: A New Nanoantibiotic for Bone Infection Treatment," *Biomed. Glas.*, vol. 4, no. 1, pp. 1–12, 2018, doi: doi:10.1515/bglass-2018-0001.

[110] L. Dong *et al.*, "Thermally and magnetically dual-responsive mesoporous silica nanospheres: preparation, characterization, and properties for the controlled release of sophoridine," *J. Appl. Polym. Sci.*, vol. 131, no. 13, Jul. 2014, doi: https://doi.org/10.1002/app.40477.

[111] N. Singh *et al.*, "Bioresponsive Mesoporous Silica Nanoparticles for Triggered Drug Release," *J. Am. Chem. Soc.*, vol. 133, no. 49, pp. 19582–19585, Dec. 2011, doi: 10.1021/ja206998x.

[112] D. L. Clemens *et al.*, "Targeted intracellular delivery of antituberculosis drugs to Mycobacterium tuberculosis-infected macrophages via functionalized mesoporous silica nanoparticles," *Antimicrob. Agents Chemother.*, vol. 56, no. 5, pp. 2535–2545, May 2012, doi: 10.1128/AAC.06049-11.

[113] X. Mei *et al.*, "Hollow mesoporous silica nanoparticles conjugated with pH-sensitive amphiphilic diblock polymer for controlled drug release," *Microporous Mesoporous Mater.*, vol. 152, pp. 16–24, 2012, doi: https://doi.org/10.1016/j.micromeso.2011.12.015.

[114] P. Maniprasad and S. Santra, "Novel Copper (Cu) Loaded Core-Shell Silica

Nanoparticles with Improved Cu Bioavailability: Synthesis, Characterization and Study of Antibacterial Properties," *J. Biomed. Nanotechnol.*, vol. 8, pp. 558–566, Aug. 2012, doi: 10.1166/jbn.2012.1423.

[115] M. Liong, B. France, K. A. Bradley, and J. I. Zink, "Antimicrobial Activity of Silver Nanocrystals Encapsulated in Mesoporous Silica Nanoparticles," *Adv. Mater.*, vol. 21, no. 17, pp. 1684–1689, May 2009, doi: https://doi.org/10.1002/adma.200802646.

[116] H. Wang, X. Jiang, and Y. He, "Highly sensitive and reproducible silicon-based surface-enhanced Raman scattering sensors for real applications," *Analyst*, vol. 141, no. 17, pp. 5010–5019, 2016, doi: 10.1039/C6AN01251E.

[117] X. Ji, H. Wang, B. Song, B. Chu, and Y. He, "Silicon Nanomaterials for Biosensing and Bioimaging Analysis," *Front. Chem.*, vol. 6, p. 38, Feb. 2018, doi: 10.3389/fchem.2018.00038.

[118] P. Evan *et al.*, "Clinical translation of an ultrasmall inorganic optical-PET imaging nanoparticle probe," *Sci. Transl. Med.*, vol. 6, no. 260, p. 260ra149-260ra149, Oct. 2014, doi: 10.1126/scitranslmed.3009524.

[119] O. Knopfmacher *et al.*, "Highly stable organic polymer field-effect transistor sensor for selective detection in the marine environment," *Nat. Commun.*, vol. 5, no. 1, p. 2954, 2014, doi: 10.1038/ncomms3954.

[120] Y. Zhong *et al.*, "Facile, Large-Quantity Synthesis of Stable, Tunable-Color Silicon Nanoparticles and Their Application for Long-Term Cellular Imaging," *ACS Nano*, vol. 9, no. 6, pp. 5958–5967, Jun. 2015, doi: 10.1021/acsnano.5b00683.

[121] Y. Yi, J. Deng, Y. Zhang, H. Li, and S. Yao, "Label-free Si quantum dots as photoluminescence probes for glucose detection," *Chem. Commun.*, vol. 49, no. 6, pp. 612–614, 2013, doi: 10.1039/C2CC36282A.

[122] Y. Yi *et al.*, "A Label-Free Silicon Quantum Dots-Based Photoluminescence Sensor for Ultrasensitive Detection of Pesticides," *Anal. Chem.*, vol. 85, no. 23, pp. 11464–11470, Dec. 2013, doi: 10.1021/ac403257p.

[123] C. M. Gonzalez *et al.*, "Detection of high-energy compounds using photoluminescent silicon nanocrystal paper based sensors," *Nanoscale*, vol. 6, no. 5, pp. 2608–2612, 2014, doi: 10.1039/C3NR06271F.

[124] A. R. Jose, U. Sivasankaran, S. Menon, and K. G. Kumar, "A silicon nanoparticle based turn off fluorescent sensor for sudan I," *Anal. Methods*, vol. 8, no. 28, pp. 5701–5706, 2016, doi: 10.1039/C6AY01125J.

[125] B. Chu, H. Wang, B. Song, F. Peng, Y. Su, and Y. He, "Fluorescent and Photostable Silicon Nanoparticles Sensors for Real-Time and Long-Term Intracellular pH Measurement in Live Cells," *Anal. Chem.*, vol. 88, no. 18, pp. 9235–9242, Sep. 2016, doi: 10.1021/acs.analchem.6b02488.

[126] M. Wipf *et al.*, "Selective Sodium Sensing with Gold-Coated Silicon Nanowire Field-Effect Transistors in a Differential Setup," *ACS Nano*, vol. 7, no. 7, pp. 5978–5983, Jul. 2013, doi: 10.1021/nn401678u.

[127] A. Gao *et al.*, "Signal-to-Noise Ratio Enhancement of Silicon Nanowires Biosensor with Rolling Circle Amplification," *Nano Lett.*, vol. 13, no. 9, pp. 4123–4130, Sep. 2013, doi: 10.1021/nl401628y.

[128] N. Lu *et al.*, "CMOS-Compatible Silicon Nanowire Field-Effect Transistors for Ultrasensitive and Label-Free MicroRNAs Sensing," *Small*, vol. 10, no. 10, pp. 2022–2028, May 2014, doi: https://doi.org/10.1002/smll.201302990.

[129] N. Shehada, G. Brönstrup, K. Funka, S. Christiansen, M. Leja, and H. Haick, “Ultrasensitive Silicon Nanowire for Real-World Gas Sensing: Noninvasive Diagnosis of Cancer from Breath Volatolome,” *Nano Lett.*, vol. 15, no. 2, pp. 1288–1295, Feb. 2015, doi: 10.1021/nl504482t.

[130] V. Krivitsky, M. Zverzhinetsky, and F. Patolsky, “Antigen-Dissociation from Antibody-Modified Nanotransistor Sensor Arrays as a Direct Biomarker Detection Method in Unprocessed Biosamples,” *Nano Lett.*, vol. 16, no. 10, pp. 6272–6281, Oct. 2016, doi: 10.1021/acs.nanolett.6b02584.

[131] S.-Y. Wang, X.-X. Jiang, T.-T. Xu, X.-P. Wei, S.-T. Lee, and Y. He, “Reactive ion etching-assisted surface-enhanced Raman scattering measurements on the single nanoparticle level,” *Appl. Phys. Lett.*, vol. 104, no. 24, p. 243104, Jun. 2014, doi: 10.1063/1.4884060.

[132] X. Jiang *et al.*, “Surface-Enhanced Raman Scattering-Based Sensing In Vitro: Facile and Label-Free Detection of Apoptotic Cells at the Single-Cell Level,” *Anal. Chem.*, vol. 85, no. 5, pp. 2809–2816, Mar. 2013, doi: 10.1021/ac303337b.

[133] B. Sun *et al.*, “Surface-Enhancement Raman Scattering Sensing Strategy for Discriminating Trace Mercuric Ion (II) from Real Water Samples in Sensitive, Specific, Recyclable, and Reproducible Manners,” *Anal. Chem.*, vol. 87, no. 2, pp. 1250–1256, Jan. 2015, doi: 10.1021/ac503939d.

[134] Y. Shi *et al.*, “Ultrasensitive, Specific, Recyclable, and Reproducible Detection of Lead Ions in Real Systems through a Polyadenine-Assisted, Surface-Enhanced Raman Scattering Silicon Chip,” *Anal. Chem.*, vol. 88, no. 7, pp. 3723–3729, Apr. 2016, doi: 10.1021/acs.analchem.5b04551.

[135] Y. Zhu *et al.*, “A Poly Adenine-Mediated Assembly Strategy for Designing Surface-Enhanced Resonance Raman Scattering Substrates in Controllable Manners,” *Anal. Chem.*, vol. 87, no. 13, pp. 6631–6638, Jul. 2015, doi: 10.1021/acs.analchem.5b00676.

[136] H. Wang *et al.*, “Simultaneous Capture, Detection, and Inactivation of Bacteria as Enabled by a Surface-Enhanced Raman Scattering Multifunctional Chip,” *Angew. Chemie Int. Ed.*, vol. 54, no. 17, pp. 5132–5136, Apr. 2015, doi: https://doi.org/10.1002/anie.201412294.

[137] N. Chen *et al.*, “Portable and Reliable Surface-Enhanced Raman Scattering Silicon Chip for Signal-On Detection of Trace Trinitrotoluene Explosive in Real Systems,” *Anal. Chem.*, vol. 89, no. 9, pp. 5072–5078, May 2017, doi: 10.1021/acs.analchem.7b00521.

[138] Y. Tang, Y. Zhao, X. Wang, and T. Lin, “Layer-by-layer assembly of silica nanoparticles on 3D fibrous scaffolds: Enhancement of osteoblast cell adhesion, proliferation, and differentiation,” *J. Biomed. Mater. Res. Part A*, vol. 102, no. 11, pp. 3803–3812, Nov. 2014, doi: https://doi.org/10.1002/jbm.a.35050.

[139] S.-H. Rhee, J.-Y. Choi, and H.-M. Kim, “Preparation of a bioactive and degradable poly(ε-caprolactone)/silica hybrid through a sol–gel method,” *Biomaterials*, vol. 23, no. 24, pp. 4915–4921, 2002, doi: https://doi.org/10.1016/S0142-9612(02)00251-X.

[140] O. Mahony *et al.*, “Silica–gelatin hybrids for tissue regeneration: inter-relationships between the process variables,” *J. Sol-Gel Sci. Technol.*, vol. 69, no. 2, pp. 288–298, 2014, doi: 10.1007/s10971-013-3214-3.

[141] Y. Ding, Q. Yao, W. Li, D. W. Schubert, A. R. Boccaccini, and J. A. Roether, “The

evaluation of physical properties and in vitro cell behavior of PHB/PCL/sol–gel derived silica hybrid scaffolds and PHB/PCL/fumed silica composite scaffolds," *Colloids Surfaces B Biointerfaces*, vol. 136, pp. 93–98, 2015, doi: https://doi.org/10.1016/j.colsurfb.2015.08.023.

[142] K. Li *et al.*, "Composite mesoporous silica nanoparticle/chitosan nanofibers for bone tissue engineering," *RSC Adv.*, vol. 5, no. 23, pp. 17541–17549, 2015, doi: 10.1039/C4RA15232H.

[143] S. Guerzoni *et al.*, "Combination of silica nanoparticles with hydroxyapatite reinforces poly (l-lactide acid) scaffolds without loss of bioactivity," *J. Bioact. Compat. Polym.*, vol. 29, no. 1, pp. 15–31, Dec. 2013, doi: 10.1177/0883911513513093.

[144] B. Jankiewicz, D. Jamiola, J. Choma, and M. Jaroniec, "Silica-metal core-shell nanostructures," *Adv. Colloid Interface Sci.*, vol. 170, pp. 28–47, Nov. 2011, doi: 10.1016/j.cis.2011.11.002.

[145] M. B. Gawande *et al.*, "Core–shell nanoparticles: synthesis and applications in catalysis and electrocatalysis," *Chem. Soc. Rev.*, vol. 44, no. 21, pp. 7540–7590, 2015, doi: 10.1039/C5CS00343A.

[146] S. Kalele, S. W. Gosavi, J. Urban, and S. K. Kulkarni, "Nanoshell particles: synthesis, properties and applications," *Curr. Sci.*, vol. 91, no. 8, pp. 1038–1052, May 2006.

[147] X. Liu *et al.*, "Noble metal–metal oxide nanohybrids with tailored nanostructures for efficient solar energy conversion, photocatalysis and environmental remediation," *Energy Environ. Sci.*, vol. 10, no. 2, pp. 402–434, 2017, doi: 10.1039/C6EE02265K.

[148] V. Pol *et al.*, "Sonochemical Deposition of Silver Nanoparticles on Silica Spheres," *Langmuir*, vol. 18, Apr. 2002, doi: 10.1021/la0155552.

[149] S. J. Oldenburg, S. L. Westcott, R. D. Averitt, and N. J. Halas, "Surface enhanced Raman scattering in the near infrared using metal nanoshell substrates," *J. Chem. Phys.*, vol. 111, no. 10, pp. 4729–4735, Aug. 1999, doi: 10.1063/1.479235.

[150] F. Caruso, M. Spasova, V. Salgueiriño-Maceira, and L. M. Liz-Marzán, "Multilayer Assemblies of Silica-Encapsulated Gold Nanoparticles on Decomposable Colloid Templates," *Adv. Mater.*, vol. 13, no. 14, pp. 1090–1094, Jul. 2001, doi: https://doi.org/10.1002/1521-4095(200107)13:14<1090::AID-ADMA1090>3.0.CO;2-H.

[151] J. Chruściel and L. ŚLUSARSKI, "Synthesis of nanosilica by the sol-gel method and its activity toward polymers," *Mater. Sci. Pol.*, vol. 21, pp. 461–469, Jan. 2003.

[152] V. G. Pol, A. Gedanken, and J. Calderon-Moreno, "Deposition of Gold Nanoparticles on Silica Spheres: A Sonochemical Approach," *Chem. Mater.*, vol. 15, no. 5, pp. 1111–1118, Mar. 2003, doi: 10.1021/cm021013+.

[153] Y. Kobayashi, V. Salgueiriño, and L. Liz-Marzán, "Deposition of Silver Nanoparticles on Silica Spheres by Pretreatment Steps in Electroless Plating," *Chem. Mater. - CHEM MATER*, vol. 13, Apr. 2001, doi: 10.1021/cm001240g.

[154] J. E. Chen, Q. Wang, K. R. Shull, and J. J. Richards, "Control over electroless plating of silver on silica nanoparticles with sodium citrate," *J. Colloid Interface Sci.*, vol. 576, pp. 376–384, 2020, doi: https://doi.org/10.1016/j.jcis.2020.05.024.

[155] L. Liz-Marzán *et al.*, "Core-Shell Nanoparticles and Assemblies Thereof," in *Handbook of Surfaces and Interfaces of Materials*, vol. 3, 2001, pp. 189–237.

[156] Y. Xia, B. Gates, Y. Yin, and Y. Lu, "Monodispersed Colloidal Spheres: Old Materials

with New Applications," *Adv. Mater.*, vol. 12, pp. 693–713, May 2000, doi: 10.1002/(SICI)1521-4095(200005)12:10<693::AID-ADMA693>3.0.CO;2-J.
[157] C. Hanske, M. N. Sanz-Ortiz, and L. M. Liz-Marzán, "Silica-Coated Plasmonic Metal Nanoparticles in Action," *Adv. Mater.*, vol. 30, no. 27, p. 1707003, Jul. 2018, doi: https://doi.org/10.1002/adma.201707003.
[158] S. Kwok Wei, "Nanosynthesis Techniques of Silica-Coated Nanostructures," 2018.
[159] H. Chen, L. Zhang, M. Li, and G. Xie, "Synthesis of Core–Shell Micro/Nanoparticles and Their Tribological Application: A Review," *Materials* , vol. 13, no. 20. 2020, doi: 10.3390/ma13204590.
[160] S. Liu and M.-Y. Han, "Silica-Coated Metal Nanoparticles," *Chem. – An Asian J.*, vol. 5, no. 1, pp. 36–45, Jan. 2010, doi: https://doi.org/10.1002/asia.200900228.
[161] L. M. Liz-Marzán, M. Giersig, and P. Mulvaney, "Synthesis of Nanosized Gold−Silica Core−Shell Particles," *Langmuir*, vol. 12, no. 18, pp. 4329–4335, Jan. 1996, doi: 10.1021/la9601871.
[162] Y. Lu, Y. Yin, Z.-Y. Li, and Y. Xia, "Synthesis and Self-Assembly of Au@SiO2 Core−Shell Colloids," *Nano Lett.*, vol. 2, no. 7, pp. 785–788, Jul. 2002, doi: 10.1021/nl025598i.
[163] E. Mine, A. Yamada, Y. Kobayashi, M. Konno, and L. M. Liz-Marzán, "Direct coating of gold nanoparticles with silica by a seeded polymerization technique," *J. Colloid Interface Sci.*, vol. 264, no. 2, pp. 385–390, 2003, doi: https://doi.org/10.1016/S0021-9797(03)00422-3.
[164] A. A. P., "Semiconductor Clusters, Nanocrystals, and Quantum Dots," *Science (80-.).*, vol. 271, no. 5251, pp. 933–937, Feb. 1996, doi: 10.1126/science.271.5251.933.
[165] Z. Xu, "Optical Properties of Metal Clusters By Uwe Kreibig (I. Physikalisches Inst. der RWTH Aachen, Gmermany) and Michael Vollmer (Technische Physik Brandenburg, Germany). Springer: New York. 1994. xvii + 532 pp. $69.00. ISBN 0-387-57836-6.," *J. Am. Chem. Soc.*, vol. 118, no. 25, p. 6098, Jan. 1996, doi: 10.1021/ja955378p.
[166] S. Link and M. A. El-Sayed, "Spectral Properties and Relaxation Dynamics of Surface Plasmon Electronic Oscillations in Gold and Silver Nanodots and Nanorods," *J. Phys. Chem. B*, vol. 103, no. 40, pp. 8410–8426, Oct. 1999, doi: 10.1021/jp9917648.
[167] J.-F. Masson, "Portable and field-deployed surface plasmon resonance and plasmonic sensors," *Analyst*, vol. 145, no. 11, pp. 3776–3800, 2020, doi: 10.1039/D0AN00316F.
[168] A. Bonyár, T. Lednický, and J. Hubálek, "LSPR Nanosensors with Highly Ordered Gold Nanoparticles Fabricated on Nanodimpled Aluminium Templates," *Procedia Eng.*, vol. 168, pp. 1160–1163, 2016, doi: https://doi.org/10.1016/j.proeng.2016.11.390.
[169] C. M. Miyazaki, F. M. Shimizu, and M. Ferreira, "6 - Surface Plasmon Resonance (SPR) for Sensors and Biosensors," in *Micro and Nano Technologies*, A. L. Da Róz, M. Ferreira, F. de Lima Leite, and O. N. B. T.-N. T. Oliveira, Eds. William Andrew Publishing, 2017, pp. 183–200.
[170] Y. Wu, M. R. K. Ali, K. Chen, N. Fang, and M. A. El-Sayed, "Gold nanoparticles in biological optical imaging," *Nano Today*, vol. 24, pp. 120–140, 2019, doi: https://doi.org/10.1016/j.nantod.2018.12.006.
[171] O. Bibikova *et al.*, "Optical properties of plasmon-resonant bare and silica-coated nanostars used for cell imaging," *J. Biomed. Opt.*, vol. 20, no. 7, pp. 1–11, Jul. 2015, doi: 10.1117/1.JBO.20.7.076017.
[172] A. Guerrero-Martínez, J. Pérez-Juste, and L. M. Liz-Marzán, "Recent Progress on Silica

Coating of Nanoparticles and Related Nanomaterials," *Adv. Mater.*, vol. 22, no. 11, pp. 1182–1195, Mar. 2010, doi: 10.1002/adma.200901263.

[173] Y. Kobayashi, K. Shibuya, M. Tokunaga, Y. Kubota, T. Oikawa, and K. Gonda, "Preparation of high-concentration colloidal solution of silica-coated gold nanoparticles and their application to X-ray imaging," *J. Sol-Gel Sci. Technol.*, vol. 78, Apr. 2016, doi: 10.1007/s10971-015-3921-z.

[174] A. F. Moreira, C. F. Rodrigues, C. A. Reis, E. C. Costa, and I. J. Correia, "Gold-core silica shell nanoparticles application in imaging and therapy: A review," *Microporous Mesoporous Mater.*, vol. 270, pp. 168–179, 2018, doi: https://doi.org/10.1016/j.micromeso.2018.05.022.

[175] J.-F. Li, C.-Y. Li, and R. F. Aroca, "Plasmon-enhanced fluorescence spectroscopy," *Chem. Soc. Rev.*, vol. 46, no. 13, pp. 3962–3979, 2017, doi: 10.1039/C7CS00169J.

[176] K. H. Drexhage, H. Kuhn, and F. P. Schäfer, "Variation of the Fluorescence Decay Time of a Molecule in Front of a Mirror," *Berichte der Bunsengesellschaft für Phys. Chemie*, vol. 72, no. 2, p. 329, Mar. 1968, doi: https://doi.org/10.1002/bbpc.19680720261.

[177] C. D. Geddes and J. R. Lakowicz, "Editorial: Metal-Enhanced Fluorescence," *J. Fluoresc.*, vol. 12, no. 2, pp. 121–129, 2002, doi: 10.1023/A:1016875709579.

[178] Y. Jeong, Y.-M. Kook, K. Lee, and W.-G. Koh, "Metal enhanced fluorescence (MEF) for biosensors: General approaches and a review of recent developments," *Biosens. Bioelectron.*, vol. 111, pp. 102–116, 2018, doi: https://doi.org/10.1016/j.bios.2018.04.007.

[179] M. Thomas, J.-J. Greffet, R. Carminati, and J. R. Arias-Gonzalez, "Single-molecule spontaneous emission close to absorbing nanostructures," *Appl. Phys. Lett.*, vol. 85, no. 17, pp. 3863–3865, Oct. 2004, doi: 10.1063/1.1812592.

[180] M. A. Badshah, N. Y. Koh, A. W. Zia, N. Abbas, Z. Zahra, and M. W. Saleem, "Recent Developments in Plasmonic Nanostructures for Metal Enhanced Fluorescence-Based Biosensing," *Nanomaterials* , vol. 10, no. 9. 2020, doi: 10.3390/nano10091749.

[181] M. Li, S. K. Cushing, and N. Wu, "Plasmon-enhanced optical sensors: a review," *Analyst*, vol. 140, no. 2, pp. 386–406, 2015, doi: 10.1039/C4AN01079E.

[182] J. R. Lakowicz *et al.*, "Plasmon-controlled fluorescence: a new paradigm in fluorescence spectroscopy," *Analyst*, vol. 133, no. 10, pp. 1308–1346, 2008, doi: 10.1039/B802918K.

[183] K. Aslan, Z. Leonenko, J. R. Lakowicz, and C. D. Geddes, "Annealed Silver-Island Films for Applications in Metal-Enhanced Fluorescence: Interpretation in Terms of Radiating Plasmons," *J. Fluoresc.*, vol. 15, no. 5, p. 643, 2005, doi: 10.1007/s10895-005-2970-z.

[184] A. Govorov, P. L. Hernández Martínez, and H. V. Demir, "Förster-Type Nonradiative Energy Transfer Models BT - Understanding and Modeling Förster-type Resonance Energy Transfer (FRET): Introduction to FRET, Vol. 1," A. Govorov, P. L. Hernández Martínez, and H. V. Demir, Eds. Singapore: Springer Singapore, 2016, pp. 19–27.

[185] J.-W. Liaw, J.-H. Chen, C.-S. Chen, and M.-K. Kuo, "Purcell effect of nanoshell dimer on single molecule's fluorescence," *Opt. Express*, vol. 17, no. 16, pp. 13532–13540, 2009, doi: 10.1364/OE.17.013532.

[186] J. R. Lakowicz, J. Malicka, I. Gryczynski, Z. Gryczynski, and C. D. Geddes, "Radiative decay engineering: the role of photonic mode density in biotechnology," *J. Phys. D. Appl. Phys.*, vol. 36, no. 14, pp. R240–R249, 2003, doi: 10.1088/0022-

3727/36/14/203.
[187] K. Ray *et al.*, “Plasmon-Controlled Fluorescence Towards High-Sensitivity Optical Sensing BT - Optical Sensor Systems in Biotechnology,” G. Rao, Ed. Berlin, Heidelberg: Springer Berlin Heidelberg, 2009, pp. 1–28.
[188] S. Zhang, X. Xu, G. Zhang, B. Liu, and J. Yang, “One-pot one-step synthesis of Au@SiO2 core–shell nanoparticles and their shell-thickness-dependent fluorescent properties,” *RSC Adv.*, vol. 9, no. 31, pp. 17674–17678, 2019, doi: 10.1039/C9RA02543J.
[189] J. Chen, Y. Jin, N. Fahruddin, and J. X. Zhao, “Development of Gold Nanoparticle-Enhanced Fluorescent Nanocomposites,” *Langmuir*, vol. 29, no. 5, pp. 1584–1591, Feb. 2013, doi: 10.1021/la3036049.
[190] K. Aslan, M. Wu, J. R. Lakowicz, and C. D. Geddes, “Fluorescent Core−Shell Ag@SiO2 Nanocomposites for Metal-Enhanced Fluorescence and Single Nanoparticle Sensing Platforms,” *J. Am. Chem. Soc.*, vol. 129, no. 6, pp. 1524–1525, Feb. 2007, doi: 10.1021/ja0680820.
[191] S. A. Camacho, P. H. B. Aoki, P. Albella, O. N. Oliveira, C. J. L. Constantino, and R. F. Aroca, “Increasing the Enhancement Factor in Plasmon-Enhanced Fluorescence with Shell-Isolated Nanoparticles,” *J. Phys. Chem. C*, vol. 120, no. 37, pp. 20530–20535, Sep. 2016, doi: 10.1021/acs.jpcc.5b09215.
[192] O. G. Tovmachenko, C. Graf, D. J. van den Heuvel, A. van Blaaderen, and H. C. Gerritsen, “Fluorescence Enhancement by Metal-Core/Silica-Shell Nanoparticles,” *Adv. Mater.*, vol. 18, no. 1, pp. 91–95, Jan. 2006, doi: https://doi.org/10.1002/adma.200500451.
[193] R. Bardhan, N. K. Grady, and N. J. Halas, “Nanoscale Control of Near-Infrared Fluorescence Enhancement Using Au Nanoshells,” *Small*, vol. 4, no. 10, pp. 1716–1722, Oct. 2008, doi: https://doi.org/10.1002/smll.200800405.
[194] C. Niu, Q. Song, G. He, N. Na, and J. Ouyang, “Near-Infrared-Fluorescent Probes for Bioapplications Based on Silica-Coated Gold Nanobipyramids with Distance-Dependent Plasmon-Enhanced Fluorescence,” *Anal. Chem.*, vol. 88, no. 22, pp. 11062–11069, Nov. 2016, doi: 10.1021/acs.analchem.6b03034.
[195] M.-K. Nguyen, W.-N. Su, and B.-J. Hwang, “A Plasmonic Coupling Substrate Based on Sandwich Structure of Ultrathin Silica-Coated Silver Nanocubes and Flower-Like Alumina-Coated Etched Aluminum for Sensitive Detection of Biomarkers in Urine,” *Adv. Healthc. Mater.*, vol. 6, no. 10, p. 1601290, May 2017, doi: https://doi.org/10.1002/adhm.201601290.

II. Size Controlled Synthesis of Silica Nanoparticles

“The greatest discovery of my generation is that a human being can alter his life by altering his attitudes”

William James

Chapter 2

Kinetically Controlled Seeded Growth One-Pot Synthesis of Monodisperse Silica: The Convivence of Two Growth Mechanism

Nowadays, silica nanoparticles (SiO_2 NPs) have been drawing widespread attention owed to their tailorable morphology, large specific surface area, adjustable pore size, scalable production, facile surface modification, high molecular loading capacity and excellent biocompatibility [1]. This remarkably features make silica as prominent candidate for countless industrial and biological applications in several evolving areas, such as catalysis, chromatography, drug delivery, biological imaging, diagnostics and sensors [2]. During the last decade, remarkable efforts have been made on novel processing methodologies for the production of monodisperse and uniform-size colloidal silica particles (SiO_2 NPs) with diameters ranging from a few to several hundreds of nanometres. On the field of material science, the sol-gel process, emerges as a fashion bottom-up wet synthetic technique for producing colloidal silica, due to ability to achieve pure homogenous products at mild conditions under a broad spectrum of solvents [3]. The method is based on the sequential hydrolysis and condensation reactions of molecular precursors (alkoxysilanes) to form an interconnected oxide networks that through a continued polymerization leads to a sol system (solid particles suspended in the liquid phase constantly showing Brownian movement). The idea behind sol-gel synthesis is to "dissolve" the precursor in a soluble liquid, in order to return it as a precipitated solid in a controlled manner. This remarkably feature, is an appealing advantage, because allows a better control over the structure composition, dimension, morphology and geometry [4]. Nevertheless, it is important to highlight that several factors, such as temperature, pH, the nature and concentration of precursor, solvent, catalyst, water, surfactants, electrolytes , rate of mixing and time, strongly influence the final particle size and monodispersity of the particles [5], [6].

In 1968, Stöber and co-workers [7], developed a pioneering method for the production of colloidal SiO_2 NPs, performing an ammonia catalysed hydrolysis and condensation of ethoxysilanes using low molecular-weight alcohols as solvent. Drawing showing the synthesis route of amorphous colloidal silica particles by the Stöber process (showed in **figure 1.3** of Chapter 1). They were the first in introduce ammonia as a base-catalyst in the reaction. One of the main advantages of their method, is that allows the possibility to control the particle size, distribution and morphology by systematic variation of the reaction parameters. The size can be readily tuned in a wide range, simply by altering the nature and concentration of the alkyl silicates, the solvent (molecular weight of the alcohol) and catalyst (ammonia) concentrations. For instance, particles prepared in ethanol were the smallest, meanwhile increasing the chain length of the alcohol (n-butanol), increased the size (around 200nm) with a broadening of the size distribution. Similarly, bigger particles up to micron-sizes were produced by this method, when the ammonia and water concentration were increased.

However, their methodology displayed three notable drawbacks. First, larger particles (between 0.2-1 µm) usually were produced with an occasionally nonspherical morphology. This observation indicates that the size control in the sub-100nm region, were rather difficult by their method. In the literature, smaller SiO_2 particles (e.g., about 10-40 nm in diameter) were reported by using amino acids as catalyst, such as L-lysine [8], [9], or using organic solvents (e.g. cyclohexane, dimethylformamide) [10], [11] or by water in oil micro-emulsion method [12], [13], producing micelles using surfactants. Second, particle sizes were not precisely reproduced and unusually high standard deviations of the size distribution (SD) were obtained. Stöber prepared their tetraesters of silicic acid by reacting silicon tetrachloride with alcohols. Authors have claimed that using a low-quality silica precursor, highly affects the polidispersity of the SiO_2 particles. Therefore, the use of high purity reagents are required for narrow the SD [14], [15]. Finally, Stöber used different alkyl silicates than the tetraethyl orthosilicate (TEOS) for tuning the size which nowadays is one of the tetraester of silicic acid commercially available in a pure form and ammonium hydroxide (26°Bé.U.S.P) as catalyst, which contains a amount of water [16].

Ever since the inception of the revolutionary Stöber method, large numbers of studies tried to improve their synthesis, focusing on the control and prediction of the silica particle size and distribution for a range of the initial reactant concentrations. For instance, In 1988 Bogush and co-workers [14], extended the Stöber work by investigating the correlation between silica particle size and concentrations of the reagents, working in the given conditions (0.1–0.5 M [TEOS]; 0.5–17.0 M [H_2O]; and 0.1–3.0 M [NH_3]). The range of particle size achievable using these conditions at 25°C for 24h were 50-800 nm. Moreover, authors also concluded that stirring rate not affected the particle size, while size decreased as the temperature increased. A year later, Matsoukas and Gulari [17], achieved to produce SiO_2 NPs having a size between 50-300 nm, measured by light scattering. They were the first in introduce the ‘‘monomer addition model”, a LaMer-like mechanism of burst-nucleation and further grow atom by atom, which explain the mechanism of formation of the silica. They reported bigger particles increasing ammonia concentration, meanwhile the opposite effect was observed increasing the water content. Curiously, their last observations went in contradiction with the findings of Stöber [7] and Bogush [14].

Later in 1991, Bogush et al [18], proposed their “controlled aggregation model”, to explain the mechanism of formation. Here, primary stable particles were formed by the aggregation of colloidally unstable small nuclei´s, that once the aggregates reached to certain stable size, growth continued by aggregating smaller particles until the monomer is below nucleation threshold. In 1992, A Van Blaaderen and co-workers [19], followed the Hydrolysis of TEOS by ^{13}C NMR and compared with the particle growth measurements using time-resolved static light scattering. They discovered that the final particle size was strongly influenced by the ionic strength of the reaction medium and revealed that the final particle size dependent on the stability of the intermediates particles. They claimed that the addition of NH_3 and/or water may result an increase in the ionic strength through the production of ions (NH_4^+ and OH^-) and destabilizing effects, decreasing the double layer thickness, thus increasing particle size by aggregating NPs. They concluded that both mechanisms (monomer-addition and controlled-aggregation) were responsible for growth of the particles. In the same year, J.K.Bailey and co-workers [20] employed cryo TEM to access the structural evolution of silica. They found the formation of 4 nm silica particles which subsequently aggregate into a gel network. They proposed a collapse mechanism for

particle densification to explain their observations. The explained that particle formation (nucleation) takes place through aggregation of siloxane substructures, while growth proceeded through surface reaction-limited condensation of hydrolyzed monomers.

Similarly, in 1994, Giesche et al [21], study the SiO_2 NPs formation, following the silicate monomers by gas chromatography and gas adsorption experiments. He found that after hydrolysis and condensation, the percentage of monomers found were 80-90% as monomeric, 10-20% dimers, <2% trimer silicic acid and <1% higher oligomers. According to their study, low density particles (average size ~26 nm) were seen initially, which collapsed to form stable high-density particles (~20 nm) known as seeds or primary particles, that further grew by addition of monomer and polymeric network on their surface, revealing a growth by ‘‘polymer addition”. Their experimental conditions allowed the production of particles with sizes between 90-700nm and claimed that the induction period (transition period from molecular precursor to soluble monomers) decreased with increasing water and ammonia content or temperature.

Years later, in 2002, Park and co-workers [22] concluded that both water and ammonia increase the particle size if their concentrations are increased. Similar results were reported by Kim et al [23], but they notice that the particle size start to decreased between 5 to 20 M of water. In addition, they found that particle size increased as TEOS concentration increases, but they observe that were less reproducible with broader size distributions. This results went along with the reported by Bogush [14]. Others authors reported that silica size increase along with TEOS, water or ammonia, Ibrahim [24] Wang [15]. However, opposite results were found by Rao and co-workers [4]. They conclude that the effect on the particle size by the temperature, depends on the reaction conditions, contrary to the literature that states that the average size of the produced particles varied inversely with temperature [16], [25].

Several authors also continuing exploring the Stöber method for explaining the mechanism of formation of silica. In one hand, some authors favoured the aggregation model for predict the particle growth profile of the Stöber systems for a range of conditions. Kangtaek Lee and co-workers [26], [27], suggested a competition between

nucleation and aggregation is important for achieving the optimal particle size. While others, rely that both mechanisms (monomer-addition and aggregation) were responsible for the silica growth, such as T.Harris and co-workers [23], Yagh et al [29], Xijia Zhao et al [30].

Considering these aspects, in the following chapter, the evaluation of the different experimental variables (TEOS, water and ammonia concentration) and their effect in the final particle size, morphology and SD by revisiting and adapting the Stöber synthesis, was studied in detail. In addition, the explanation of the possible mechanism of nucleation and growth of monodisperse SiO_2 NPs was presented, by an extended monitorization of the mineralization process under certain fixed conditions by different characterization techniques. Finally, the role of water as key reagent for tailoring the particle size and distribution beyond Stöber was revealed, allowing us to developed an enabling methodology for systematically reliably control the final particle size using a one-pot strategy maintaining monodispersity of the NPs.

2.1 Evaluation of the Different Experimental Parameters Adapting the Stöber Method

As can be seen, despite the Stöber process is experimentally uncomplicated and quite known, it presents features that make intricate the control of the particle size. As previously discussed, the synthetic variables interact with each other causing different effects on the final particle size and morphology that explain the contradictory results described above. These extended modifications in the initial reactants concentrations has made the precise size control increasingly complex with unclear benefits affecting the reproducibility, making the comparison difficult with inconsistent trends. Therefore, in this section, we study the effect of the silica precursor, namely tetraethylorthosilicate (TEOS), the catalyst ammonia (NH_3) and water (H_2O) on the final particle size. In order to understand the role of each reactant specie during the synthesis, our strategy followed the modification of only one parameter at time, while others remained constant. The experiments were conducted following a one-pot strategy using anhydride ethanol as solvent, ammonia in ethanol as catalyst, at room temperature (25°C) with the same stirring

rate (800 r.p.m.) for 24h of reaction, because one of the main scopes of our study is to keep the synthesis, facile, simple and reproducible.

2.1.1 Tailoring the particle size of monodisperse colloidal silica

Before start the systematic evaluation of reagents, it is noteworthy to highlight that for the complete transformation of the TEOS into silica, it progresses through a series of chemical hydrolysis and condensations reactions (chapter 1, **scheme 1.2 and scheme 1.3**) that have subtle interdependencies. Therefore, if we suppose that liberated water plays a minor, or even negligible role in secondary hydrolysis of TEOS (it is reported that hydrolysis is faster than condensation reactions, due to steric effects) [17], the stoichiometric amount of water required for the complete hydrolysis of TEOS of formula $Si(OC_2H_5)_4$ to silicic acid monomers of formula $Si(OH)_4$, would be a molar ratio of 4:1. Thus, an excess of water will be assumed for all the systematic experiments. **Table 2.1** summarizes the different reaction iterations of the evaluation.

Table 2.1 Summary of detailed experimental conditions for the evaluation of the different experimental parameters for the synthesis of SiO_2 NPs by adapting the Stöber method.

Condition	TEOS [M]	NH_3 [M]	H_2O [M]	Size ± SD (nm)[a]	Yield (mg SiO_2/mL)	Yield (%)
1	0.05	0.55	4.00	145.4 ± 8.5	2.78	92.5
2	0.10			143.2 ± 8.3	5.42	90.2
3	0.15			144.5 ± 8.3	8.38	92.8
4	0.30			124.3 ± 17.9	16.6	92.1
5	0.45			105.5 ± 16.3	24.8	91.7
6	0.70			100.4 ± 19.1	38.5	91.4
7	0.15	0.20	4.00	49.2 ± 5.5	7.30	80.9
8		0.40		121.8 ± 8.6	7.91	87.6
9		0.55		184.6 ± 11.8	8.47	93.8
10		1.00		317.9 ± 18.8	8.39	92.9
11		1.20		322.0 ± 20.2	8.58	95.0
12		1.50		363.0 ± 18.7	8.49	94.0
13	0.15	0.55	2.50	51.7 ± 5.6	8.34	92.4
14			3.00	84.7 ± 7.2	8.36	92.6
15			4.00	153.2 ± 12.9	8.46	93.7
16			5.00	225.2 ± 14.2	8.41	93.1
17			7.00	249.0 ± 14.5	8.43	93.4
18			13.0	326.7 ± 16.5	8.38	92.8

Effect of the TEOS concentration

In order to evaluate the effects of TEOS on the final SiO_2 NPs size, we prepared SiO_2 NPs under identical conditions (0.55M NH_3, 4.0M H_2O and 32mL of anhydride ethanol) a part from TEOS concentration, that was varied from 0.05M to 0.70M, for 24h of reaction.

Figure 2.1-A, shows the effect of TEOS concentration on particle size, yield and size distribution (SD) of SiO_2 NPs. It can be seen, that the final morphology of the SiO_2 NPs is slightly determined by the TEOS concentration. Increasing TEOS concentration beyond 0.15M, resulted in a particle size decrease with a broadening of the size distribution. The size decreased from 144.5 ± 8.3 nm using 0.15M to 100.5 ± 19.1 nm using 0.70M of TEOS, with a conversion yield by weight around 92.0%, comparable in all cases (condition 1 to 6, showed in **table 2.1**). The optimal size control was achieved using 0.15M of TEOS, leading to the production of spherical SiO_2 NPs with the narrow SD. Our results revealed that, above 0.15M of TEOS, particle size started to be more polidisperse. The appearance of a secondary population beyond 0.30M also can be observed by SEM.

In the literature, similar results of heterodisperse particles at high TEOS concentration have been reported. Rahman and co-workers [23], found a multimodal size distribution increasing TEOS, attributed to an excessive generation of primary particles at super saturation state. They claimed that the consumption of TEOS to grow the primary stable particles, occurred at much slower rate, therefore a higher saturation sate leaded the system to generate more primary particles. Stöber and co-workers [7], explained that the condensation rate between monomers were slowed down increasing the concentration of TEOS, leading to an increase in the SD. He found a system having two size distributions using concentrations of TEOS above (≥0.2M). Bogush et al [14], also found that at elevated TEOS concentrations, the particle size was less reproducible with the broadening of the SD. Similarly, Van Helden and co-workers [10] and Rao K.S. and co-workers [4], reported a decreased in silica particles size when TEOS was increased in the reaction. They explained these results by looking the rate of hydrolysis of TEOS. They reported a first-order hydrolysis rate of TEOS and claim that the rate was increased raising TEOS, leading to faster kinetics, thereby favouring the continued production of larger quantity of smaller particles.

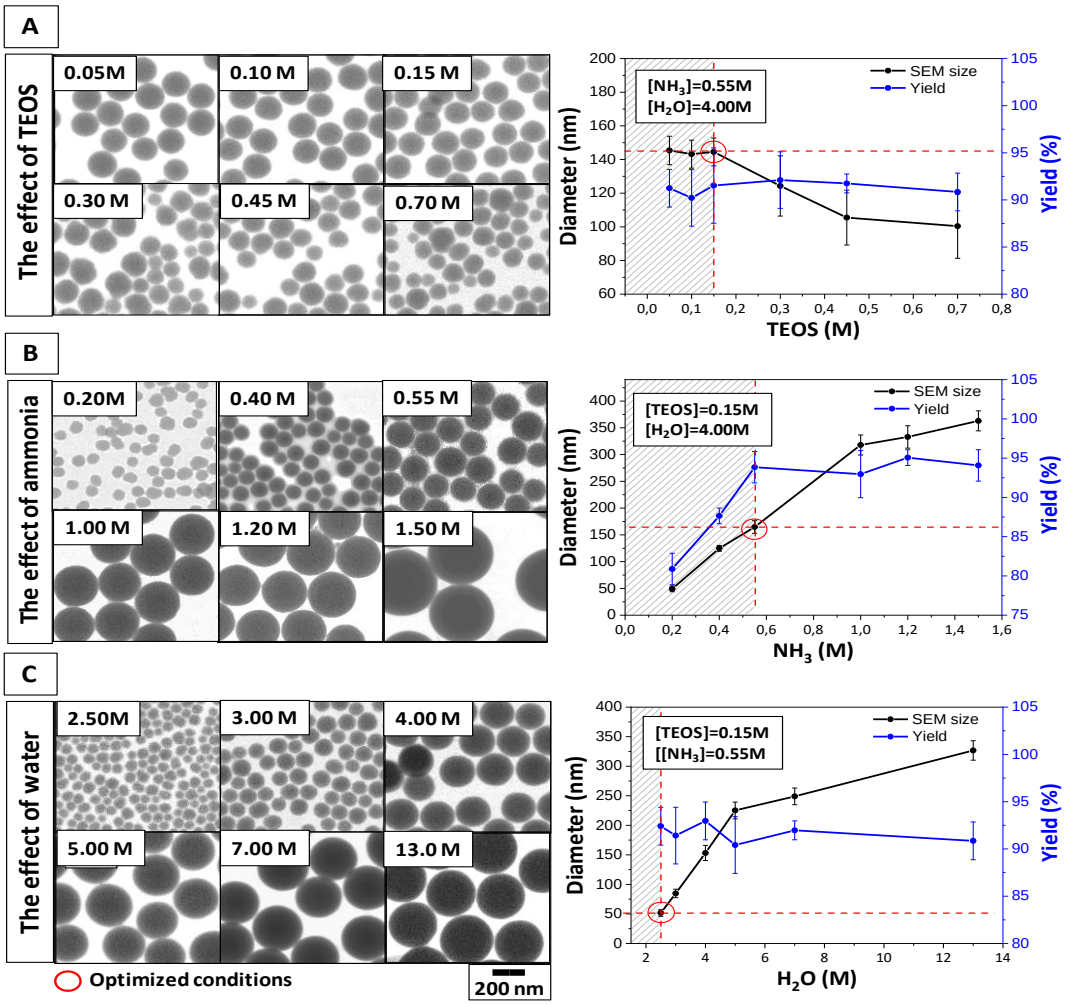

Figure 2.1 Graphic representation of the characterization by electron microscopy (STEM) and yield, for the different tested conditions for the synthesis of SiO_2 NPs by adapting the Stöber method, after 24h. (A) Evaluation of the effect of TEOS, (B) evaluation of the effect of ammonia and (C) evaluation of the effect of water. The yield was calculated by the difference of TEOS conversion and the obtained solid dry powder SiO_2 NPs. The mean size and SD was calculated measuring at least 300 particles by image J software and error bars are indicative of the standard distribution (SD showed in **Appendix A1**). The red dotted lines and shaded area highlight the optimal concentrations for every case.

In this regard, the effect of the TEOS on the final particle size can be explained based on LaMer Model. Since increasing the monomer concentration beyond saturation, resulted in a size decreased. It seems that in a high monomer condition, the hydrolysis and condensation rate of TEOS were prolonged, causing longer induction periods that lead to an extended nucleation process. This continuous nucleation causes the total number of particles in solution be higher, thereby reducing the particle size, because the monomer diffused to a higher number of growing particles in solution. In addition, we can expect that the prolonged supply of hydrolysed monomer in the reaction, caused an increased

supersaturation state, that may offset the growth rate in the system over nucleation. It is known that an extended nucleation period contributes to broader the SD by the introduction of anew smaller NPs at later stages when some population has grown to larger size. This consideration can be done, because the obtained yields were comparable in all cases. Hence this evidence suggest that the number of nucleated particles were different for every condition.

Effect of the NH_3 concentration

In this section, the effect of catalyst on the final SiO_2 NPs size after 24h was evaluated by preparing silica NPs under identical conditions (0.15M TEOS, 4.0M H_2O and 32mL of anhydride ethanol), except the NH_3 concentration, that was varied from 0.20M to 1.50M.

As shown by **figure 2.1-B**, it can be seen that the kinetics of the reactions were highly dependent on the NH_3 concentration. Increasing NH_3, resulted in a strongly increased in the particle size with narrow SD. The size varied from 49.2 ± 5.5 nm using 0.20M to 363.0 ± 18.7 nm using 1.50M of ammonia. The optimal yield of the reaction was achieved beyond 0.55M of NH_3 (conditions 9-12, **table 2.1**). However, using the optimal NH_3 concentration and beyond, leaded to the production of bigger spherical SiO_2 NPs, as shown by the SEM images. In contrast, at lower NH_3 (0.20M), smaller silica NPs were observed, but presented lower yields (around 80%). Interestingly, our results did not reveal the formation of any secondary population of particles, within the range of the evaluated ammonia concentrations.

In the literature, previous studies also reported similar trends increasing the NH_3 catalyst, [4], [7], [14], [17], [22]–[24], [31]. Rahman and co-workers, [32], observed a faster hydrolysis and condensation rate of TEOS by increasing NH_3, leading to yields of ∼95% using 3.0M NH_3. Dongming Qi et al [25], mention that ammonia promote the hydrolysis rate, however, it also promote the condensation rate to an even higher degree, thereby, resulting in larger particle size by the decreased in the nucleation rate. Yang and co-workers [29], found that increasing NH_3 produced fully hydrolyzed silanol monomers from TEOS. The presence of the complete hydrolysed monomers enhances the degree of

polymerization/condensation leading to larger SiO_2 sizes. Also state that lower NH_3 concentration, produced branched aggregated siloxane clusters with fewer negative charges on the surface, resulting in small-sized silica particles. Wang and company [15], state that apart from its role as basic catalyst, ammonia not only accelerate the hydrolysis and condensation of TEOS producing more branched oligomers to form larger particles, but also supply the system with hydroxyl ions (OH^-) that prevent the coagulation of the particles controlling the aggregation of SiO_2 in solution. Greasly et al [33] explain that the role of ammonium hydroxide in the process is to raise the pH, which accelerates the condensation reaction but also creates an environment with a pH much higher than the isoelectric point of the silicic acid monomers (IEP: 2.2), creating repulsive charges between the particles, which is critical for monodispersity.

In this regard, the effect of the ammonia in the particle size can be explained in terms of the increased rate of hydrolysis and condensation reactions of TEOS by the NH_3. Within the optimal amount (0.55M), ammonia led to a faster mineralization by accelerating both reactions. The equilibrium of these reactions directly affects the mechanism of nucleation and growth of the silica. This behaviour was evident because the precipitation time of SiO_2 NPs was reduced from hours to minutes (not show) when ammonia was raised. The induction period was reduced by not only increasing the hydrolysis, but increasing the condensation between monomers, generating particles bigger in size. Therefore, the role of the NH_3 in the system, can be summarized as follows: **i) as a source of hydroxyl ions (OH^-).** Upon in contact with water, it undergoes ionization triggering the water dissociation, generating hydroxyl ions (OH^-) in solution. These negative charge ions are more effective nucleophiles than water; therefore, the hydrolysis rate was increased producing silanol (Si-OH) monomers and the condensation rate by accelerating the polymerization, leading to highly branched condensed Si clusters, that ultimately produced larger particles. This hypothesis was evaluated because any SiO_2 NPs were precipitated even at high ammonia concentrations 1.50M, when the reactions were done without using water. Therefore, this evidence reveals the need of water in the system for the generation of nucleophilic hydroxyl ions. **ii) As a stabilizing agent for the nucleated particles**. Ammonia raises the pH of the solution by the increased ions (OH^-) in the media. The supply of hydroxyl ions in the system increases the colloidal stabilization of the suspension by electrostatic repulsion

against van der Waals attractive forces, leading to stable and monodisperse particles. These (OH^-) ions transfer the negative charge to the silica surface (with negative silanol groups $Si\text{-}O^-$) avoiding particle aggregation. Finally, **iii) as catalyst in order to overcome the energy barriers.** The NH_3 decrease the ionization energy of the system required to start the nucleation. The presence of hydroxyl ions displaces the equilibrium favouring both, the nucleation and growth process, enhancing the condensation and hydrolysis by the increased siloxane bonds in the system. Thus, an appropriate NH_3 concentration should be chosen.

Effect of the Water concentration

In this section, the effects of water on the final SiO_2 NPs size after 24h was evaluated by preparing SiO_2 NPs under identical conditions (0.15M TEOS, 0.55M NH_3 and 32mL of anhydride ethanol), a part from the H_2O concentration that was varied from 2.50M to 13.0 M.

Similarly, to ammonia, the formation of the SiO_2 NPs was also highly dependent on the water concentration. As seen in **figure 2.1-C**, the size of the SiO_2 NPs increased with narrow SD by adjusting the initial water concentration. The diameter increased from 51.7 ± 5.6 nm using 2.50M to 326.7 ± 16.5 nm using 13.0M after 24h, as shown by the SEM images. Interestingly, the obtained yield by weight were around 93.0%, comparable to all conditions (condition 13- 18, **table 2.1**). These results indicate that nearly all Si was used for mineralize the SiO_2 particles. The optimal H_2O content that allow us to produce the smallest SiO_2 NPs having narrower SD with a yield around 92% was 2.50M, together with 0.55M of NH_3. Interestingly, this condition allowed the mineralization of smallest SiO_2 NPs, comparable in size with the obtained using lower NH_3 (condition 7, **table 2.1**). These results indicate that H_2O plays and important role for production smaller SiO_2 NPs with high yields. Finally, any multimodal distributions of particles were observed within the range of all water concentrations.

In the literature, previous studies reported similar behaviour when H_2O concentration was increased [14], [18], [21], [26]. Stöber and co-workers [7] explained that the condensation rate depends strongly upon the water content of the system, achieving a

maximum particle size at water concentrations around 6.0M. This observation was in agreement with Bogush et al [14], who also reported that size increased with water, but their maximum particle size were achieved at 7.0M. According to Sung Kyoo Park et al [22], a higher water concentration leads to higher nucleation rates, as a consequence, lot of small sub-particles were prepared at a short period. Thereafter, these sub-particles agglomerated with each other to grow into larger particles. He explained that the hydrogen bond of SiO_2 sub-particles under higher water condition is stronger than in lower water concentration. Bourebrab M. and co-workers [34] reported that the water content has a strong influence on the size of synthesised particles. He found that the size increased until a concentration of 9.0 M. Beyond this point, the silica size decreased. They explained this behaviour by the change of stability of the siloxane intermediates. TEOS is immiscible with water, therefore phase separate. This is why alcohols are used as co-solvents. A high-water concentration, would impact the solubility of the evolving silane/siloxanes, reducing the availability of monomers to participate in condensation reactions. Similarly, Raham et al [32] reported that the concentration of silicate in the system is reduced significantly increasing the water content. They explained this due to the reduced hydrolysis and condensation reactions which resulted in slower particle growth. In addition, they state that higher water promotes siloxane bond hydrolysis, which also reduce particle size.

In this sense, the effect of the water on the final particle size followed a similar trend to the NH_3 catalyst, but in a better controlled manner. It seems that H_2O also increase the rate of the hydrolysis for producing monomers, but also the condensation rate between them for producing bigger-sized particles. The main difference between both parameters (NH_3 and H_2O), can be explained in terms of electrostatic stability and differences in kinetics of the reactions. During the mineralization of silica, both processes are occurring simultaneously and are in equilibrium. As previously discussed, ammonia strongly accelerates in a higher degree the condensation rate by increasing the degree of monomers to branched siloxane structures that favours the growth process to bigger sizes. In addition, the increased addition of ammonia supplied the system with an increased NH_4^+ ions that compromise the electro stability of the growing particles. Therefore, if the ammonia is fixed during the reaction, it is possible decoupled two major effect that are affecting the size at the same time. A lower H_2O (below 3.00M), can be translated into a reduced (OH^-) ions in

solution, producing a slower hydrolysis and condensation rate, as a consequence, the induction period is increased, favouring the nucleation process, which eventually lead to a lot of smaller particles. This behaviour was observed in the lower water samples (conditions 13 and 14, **table 2.1**). The mineralization of SiO_2 NPs took longer times than ammonia conditions (data not showed). Oppositely, increasing the water (above 4.00 M), the particles started to become bigger in size, suggesting that the hydrolysis and condensations is increased together with a more controlled destabilization of the siloxane structures, due to the increased hydroxyl ions OH^- and NH_4^+ in media, as a consequence, the induction period is decreased, thereby reducing the nucleation rate, favouring the equilibrium towards bigger particles.

2.2 Understanding the Mineralization Process of the Colloidal Silica formation: Monitoring The Mass Balance of the System

As discussed in the previous section, water and ammonia seems to regulate the induction period by controlling the generated species during the hydrolysis and condensation reactions, allowing us to tailoring the final particle size. Together both reactions, allowed the conversion of TEOS to silanol monomers and its further condensation towards the production of SiO_2 NPs particles. The generation of these nucleophilic hydroxyl ions (OH-) in solution, during the induction time and before nucleation, seems to be size-dependent process.

As we are interested in the synthesis of smaller monodisperse SiO_2 particles (20-100nm), in this section we studied the kinetics of colloidal silica particles formation as a function of time, in three water conditions, lower (2.00M), middle (3.50M) and high (5.00M).

2.2.1 Monitoring Colloidal Particle Formation

Here, we study the colloidal amorphous SiO_2 NPs formation in three different regimes of H_2O concentrations (2.00M, 3.50M and 5.00M) while the others parameters (TEOS, NH_3, temperature, stirring rate, solvent volume of ethanol) remain fixed during the

reaction after 24h, monitorizing the silica nucleation and growth by SEM/TEM, UV-Vis spectroscopy and DLS, measuring the temporal evolution profile of NPs size and morphology, surface charge (mV), conductivity (mS/cm), hydrodynamic diameter, monomer concentration and number of particles (NPs/mL) in solution.

Temporal Evolution Profile of Size and Monomer Concentration by SEM and UV-Vis Spectroscopy as a Function of Time

In order to study the mass balance of the system, we monitor the temporal evolution of the size of the SiO_2 NPs at three water conditions, fixing all the other reaction parameters (TEOS 0.15, NH_3 0.55M and 32mL anhydride ethanol) during the reaction. In addition, the concentration of the monomer in solution was measured as a function of time by means of the silicomolybdic acid (SMA) spectrophotometric method [35]. The calibration curve and the recorded temporal evolution UV-Vis spectrums are showed in (**Appendix A3**). Summary of the characterization of the SiO_2 NPs obtained in the three different water concentrations after 24h, is showed in **table 2.2**.

As shown in **figure 2.2,** the formation of SiO_2 with three different H_2O concentrations presented a strong difference in the final silica diameter. The evolution of the size of the particles, increases as the water concentration were increases as expected. On one hand, in the low water regime (2.00M), **figure 2.2-A**, the SEM images displayed the appearance of large inhomogeneous objects in the initial stages of the reaction, about 10-15 minutes. Result that can be ascribed to polymeric structures organized into siloxane networks, derived from the condensation of silanol monomers resulted from TEOS hydrolysis. Interestingly, after 30 minutes, we observed the appearance of highly small denser protoparticles that seems to gather around a siloxane structure. After 60min, the SEM images revealed the appearance of small-sized colloidal stable silica particles with a mean size of 23.8 ± 9.7 nm, indicating nucleation has started. Remarkably, the monomer concentration revealed a decay to 72.8 % during the first 60min, indicating that around 27.2 % of the monomer was consumed to star the nucleation. Finally, at longer times (from 1 hour on), these nuclei gradually increase in size to achieve a final diameter of 40.0 ± 4.2

nm, at the end of the reaction. In this interval, the monomer concentration decayed progressively to 9.0 %, with a yield of 91% after 24 hours.

On the other hand, when the initial water concentration was increased from 3.50M to 5.00M H_2O, as shown in **figure 2.2-B** and **C**, the large siloxane networks were not observed in the initial stages of the reaction (5 minutes). In contrast, the formation of a large solid object (around 100-200nm in size) surrounded with abundant small protoparticles, were seen within the first minutes of both reactions. Surprisingly, using 3.50M H_2O, the SEM images revealed the appearance of heterodisperse silica particles with a broad SD having mean size of 48.9 ± 16.6nm, after 30min. In contrast for the regime 5.00M H_2O, the polydisperse NPs appeared even faster (at 15 min) having a size of 108.0 ± 29.2 nm.

Table 2.2 Physicochemical characterization of the temporal evolution profile of the SiO_2 NPs in all water concentrations by STEM Size and monomer concentration after 24h.

H_2O [M]	TEOS [M]	NH_3 [M]	TEM diameter (nm)	SD (%)	I.T (min)	TEOS consumed after I.T (%)	Yield Uv-Vis SMA (mg Si/mL)	Yield (%)
2.50	0.15	0.55	40.0 ± 4.2	10.4	60	27.2	3.91	91.0
3.50	0.15	0.55	142.3 ±11.5	8.0	30	25.3	4.17	98.0
5.00	0.15	0.55	332.1 ± 31.5	9.5	15	24.2	4.17	98.0

IT: induction time (time when particles were first observed by STEM)

These outcomes suggested a faster nucleation of the hydrolyzed condensed monomers as water increases, revealing that the kinetics of the reactions were clearly accelerated. In addition, we observed that the induction time was considerably reduced from 30 to 15 minutes. Surprisingly, the concentration of the silicic acid species decayed in a similar trend for both conditions, but faster raising the water. For instance, using 3.50M, the monomer decayed to 74.8% during the induction time (30min), revealing that 25.3 % of the monomer was consumed for nucleation. On the other hand, using 5.00M, the monomer decreased to 75.5% in 10 minutes, showing that 24.2 % of monomer were consumed for nucleation. Finally, at longer times (beyond 1 hour), the particle size progressively increased for both conditions, to a final diameter of 142.3 ± 11.5 nm and 332.0 ± 31.5 nm, respectively after 24 hours. In the high water, the final diameter seems to be more heterodisperse, suggesting that particles remained growing during the reaction,

possibly by monomer addition rather than by Oswald ripening. The remaining monomer concentration found was around 2.00% for both syntheses, (suggesting a 98% yield of conversion). The evolution of the silanols showed that the concentration of monomers needed for start nucleation were comparable for all water concentrations (around 24-27%), with the difference in induction time. This observation was mentioned in the previous section, when we state that the induction period to start nucleation is decreased by raising the water content.

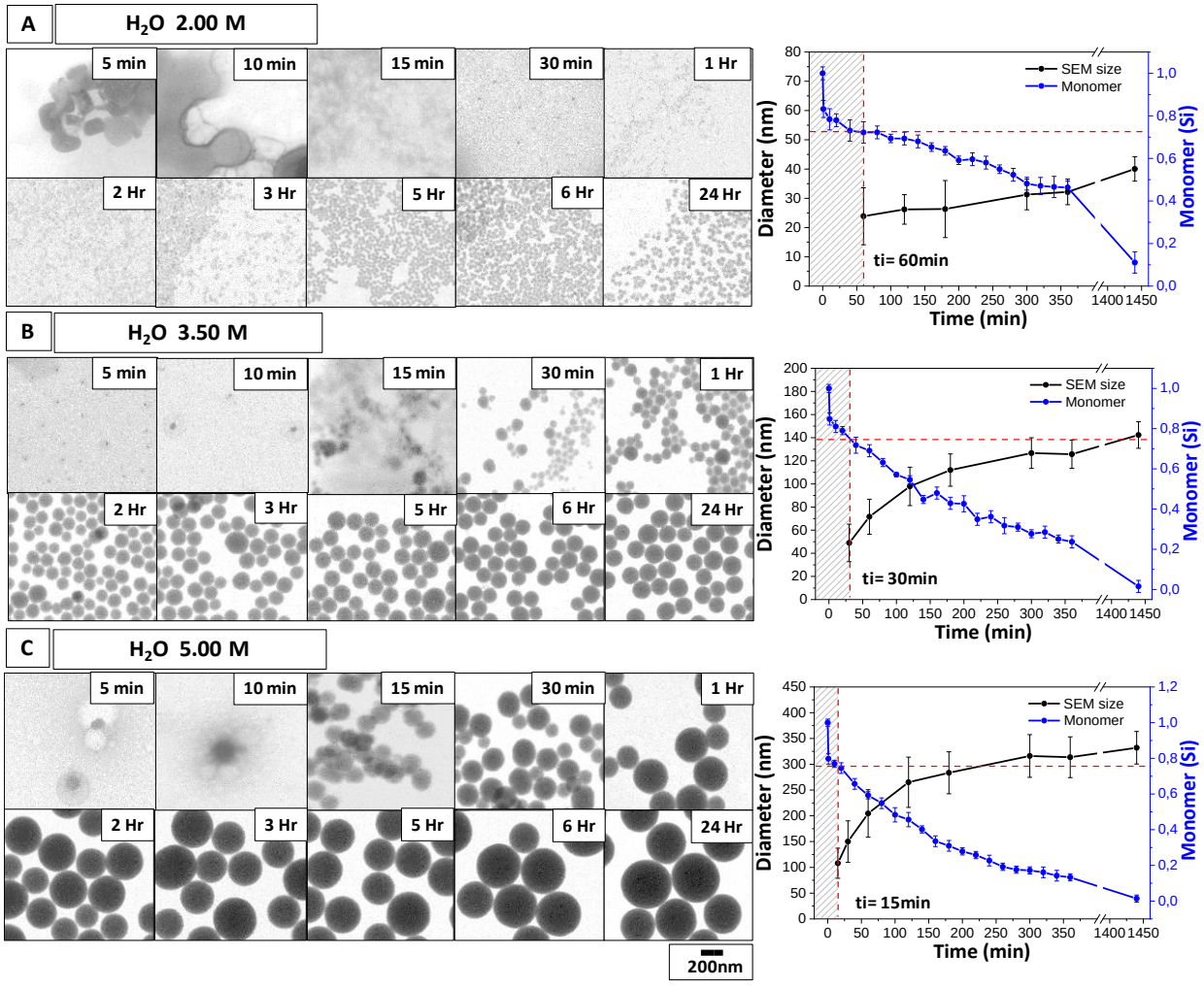

Figure 2.2 Graphic representation of the temporal evolution profile of the colloidal SiO_2 particle formation in the three different water conditions, by electron microscopy in STEM mode and monomer concentration as a function of time. (A) Concentration of H_2O 2.00M, (B) H_2O 3.50M, (**C**) H_2O 5.00M. The experiments were done taking aliquots at certain times for characterization until 24h. *The size distribution was calculated measuring at least 300 particles by image J software and error bars are indicative of the standard distribution (showed in **Appendix A2**). The red dotted line and shaded area highlight the time in which stable particles were seen.

Temporal Evolution Profile by Dynamic Light Scattering (DLS) as a Function of Time Zeta Potential and Conductivity

Since the nucleation and growth of SiO_2 NPs, results from the condensation of hydrolyzed silanol monomers, an increase in the reaction conductivity, may be ascribed to an increase in concentration of these monomers in solution, attributed to the oxygen negative charge of its hydrolyzed state [29]. On the contrary, a decrease in the zeta potential to a value of around (±30mV) can be attributed to the precipitation of stable colloidal particles in the reaction media. In this regard, the evolution of the produced monomers by the hydrolysis and the further mineralization of silica particles were recorder as a function of time, measuring simultaneously the ZP (mV) and conductivity (mS/cm) of the three different water regimes, as showed in **figure 2.3**. Summary of the characterization in the three different water concentrations after 24h, is showed in **table 2.3.**

Table 2.3 Physicochemical characterization of the temporal evolution profile of the SiO_2 NPs in all water concentrations by DLS after 24h.

H_2O [M]	TEOS [M]	NH_3 [M]	I.T (min)	DLS_{number} (nm)	PdI	Particle concentration (NPs/mL)	ζ-potential (mV)	Cond. (mS/cm)
2.50	0.15	0.55	40	57.5 ± 1.2	0.085	$2{,}58x10^{13}$	-36.5 ± 2.2	0.0428
3.50	0.15	0.55	30	127.2 ± 2.3	0.096	$2{,}18x10^{12}$	-36.8 ± 1.6	0.0039
5.00	0.15	0.55	15	418.5 ± 8.7	0.077	$2{,}28x10^{11}$	-42.2 ± 2.2	0.0038

IT: induction time (time when ZP achieve a value of -30mV)

As shown **in figure 2.3-A-C**, the evolution of the conductivity derived from the monomers in solution produced by the hydrolysis reaction, revealed a similar trend for all water regimes, with the difference of being fasten as water increases. On one hand, at lower water (2.00M), **figure 2.3-A,** the conductivity exhibited a noticeable increase from 0.020 ± 0.001 to 0.038 ± 0.002 mS/cm between the first 40min. These results can be associated to the induction time, due to the formation of the charged silanol monomers by hydrolysis of TEOS. In addition, the measured electrophoretic mobility decreased rapidly to a ZP value of -34.0 ± 2.2 mV at the end of this period, suggesting the precipitation of colloidal stable silica particles, that can be associated nucleation process. Both parameters reached a plateau during the first 40 min. Surprisingly, as the reaction proceeds (from 40 minutes on), the conductivity slightly increasing in a steady state, suggesting an equilibrium between the continuous hydrolysis of TEOS into silanol monomers (increase conductivity),

and the consumption of monomers (decrease cond.) to precipitate SiO_2 NPs. The ZP decreased to lower values o until achieve a stable value of -40.3 ± 3.1 mV after 24h. Result in agreement with the good degree of electrostatic repulsion for stabilization of the SiO_2 particles.

On the other hand, when the water concentration was increased to 3.50M and 5.00M, the increase in conductivity, as well as the drop of the zeta potential, followed same tendency, but were achieved in shorter times, as shown in **figure 2.3-B,C**.

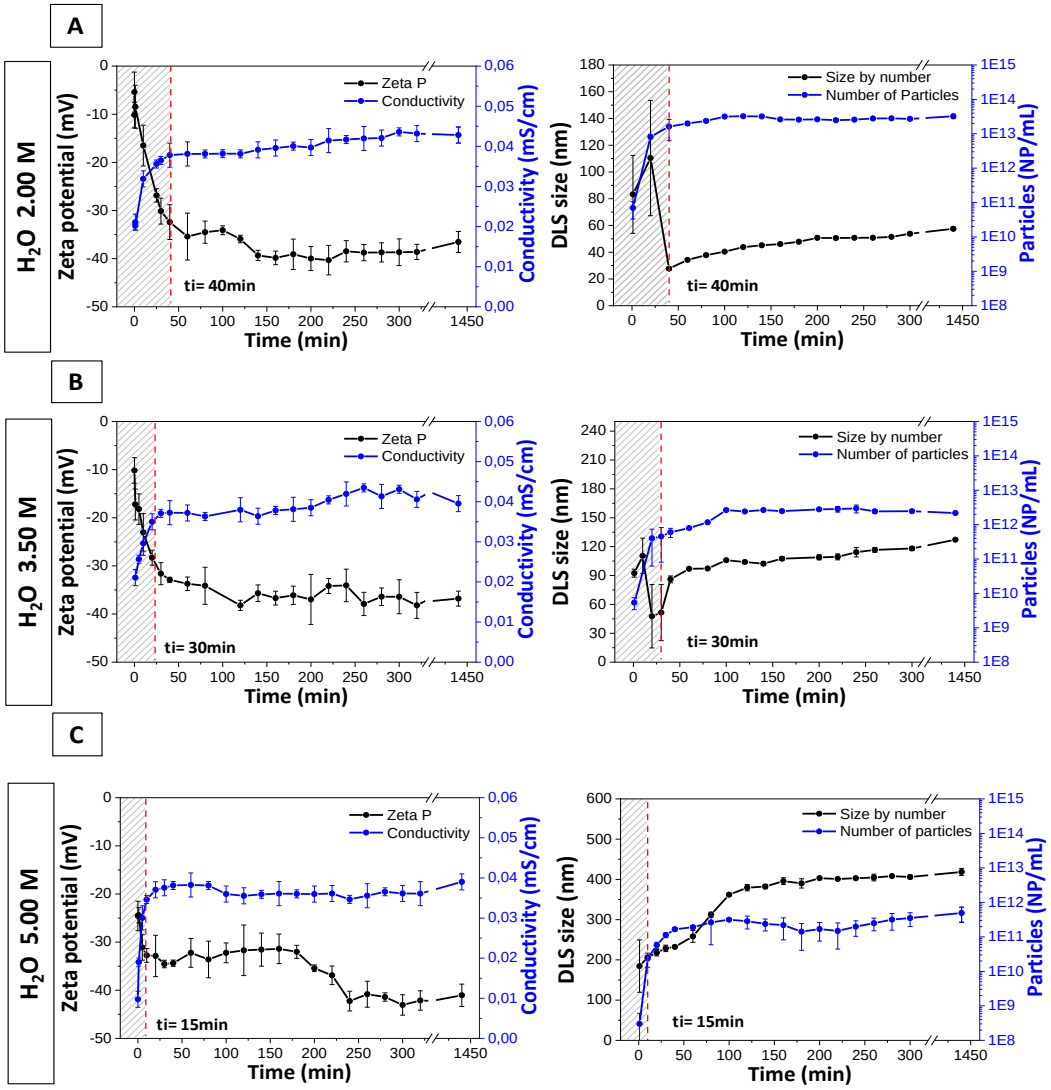

Figure 2.3 Graphic representation of the temporal evolution profile of the zeta potential (mV), conductivity (mS/cm), hydrodynamic size (nm) and number of particles (NPs/mL), as a function of time by dynamic light scattering (DLS). (A) Concentration of H_2O 2.00M, (B) H_2O 3.50M, (C) H_2O 5.00M. *The mean size distribution was calculated measuring at least three independent measurements and error bars are indicative of the standard distribution (raw data can be seen in **Appendix A4**). The red dotted line highlights the time in which particles were seen by STEM.

These results were in agreement from the previous analysis, that revealed a reduced the induction time as water increases. For instance, using 3.50M, the conductivity evolved from 0.021 to 0.0371 mS/cm at 30min. For 5.00M H_2O, increases from 0.019 to 0.0370, but only in 15min. Concomitantly, the electrophoretic mobility dropped to a ZP of -36.8 ± 1.6 mV and to -41.9 ± 2.3 mV respectively. Therefore, the transition from precursor to soluble silanol monomers in solution (induction time), and from silanol monomers to colloidal silica NPs (nucleation period), were elucidated as a function on time, following the same trend in all conditions, but as previously discussed, fastened by water.

Hydrodynamic Size and Number of Nanoparticles in Solution

For a better comprehension of the mechanism of formation followed by the SiO_2 NPs, the hydrodynamic size and number of particles in solution were recorder as a function of time, at three different water conditions, while all the other reaction parameters were kept constant. This study allows us to measures the temporal fluctuations of the light scattered of the particles due to the Brownian motion, that refers to how particles diffuse within a fluid, correlating a function with their hydrodynamic diameter, as well as the measurement of the number of particles in solution by an ultra DLS, during the reaction.

As seen in **figure 2.3-A-C**, the evolution of the hydrodynamic size of the silica particles increases along with the water concentration, in a similar trend as previously shown by the SEM images**.** However, the evolution of the number of particles (NPs/mL) followed and opposite tendency, decreasing as water increases. On one hand, at low water (2.00M) **figure 2.3-A**, the hydrodynamic size increases from 83.2 ± 29.1 nm to 100.4 ± 43.1 nm during the first 40min. Results that are in agreement with the formation of large inhomogeneous siloxane structures from TEOS hydrolysis and condensation, during the initial stages of the reaction (induction time). Similarly, the particle concentration to $8.16x10^{12}$ ± $1.11x10^{12}$ NPs/mL with high standard deviation, derived from the large siloxane networks. Interestingly, after 40 min, the hydrodynamic size was 27.6 ± 1.2 nm having a low SD, suggesting the appearance of stable SiO_2 NPs. This interval correlates with the ZP and conductivity measurements at the same condition, and displayed a number of particles of $1.63x10^{13}$ ± $9.82x10^{12}$ NPs/mL. Beyond that time (from 40 minutes on), the

hydrodynamic size exhibited a progressively increase over time, until achieve a value of 57.5± 1.2 nm after 24 hours. Surprisingly, the number of NPs followed a slightly increased, explained by the nucleation, but later, further evolved exhibiting a steady state over time, to a final concentration of $3.21x10^{13}$ ± $4.54x10^{12}$ NPs/mL, in the end of reaction. This observation revealed that the number of particles increases during the initial stages of the reaction, suggesting and aggregative growth (nucleation), but at the later stages, the NPs seems to preferentially growth by consumption of the monomers at surface.

On the other hand, when the water concentration was increased to 3.50M and 5.00M **figure 2.3-B, C**, the evolution of the hydrodynamic size showed higher values with broad SD again due to the siloxane networks (around 100-200 nm in size), below 10 minutes, explained because the system is under the induction time. Later, at 30 minutes, the 3.50M regime achieved a monodisperse size by number of 51.5 ± 2.9 nm, in comparison with the 5.00M, which were achieved earlier (15 minutes) with a size of 217.8 ± 7.9 nm, respectively. These results were in agreement with the previous results when the nucleation started. Similarly, the number of particles presented higher standard deviation in the beginning of the reaction for both conditions (below 10 minutes), with values of $5.41x10^{9}$ ± $2.05x10^{9}$ NPs/mL for 3.50M and $3.00x10^{8}$ ± $3.1x10^{8}$ NPs/mL for 5.00M, ascribed to the large siloxane networks. However, after the induction time, the number evolved to greater values around $4.52x10^{11}$ ± $3.71x10^{10}$ NPs/mL at 30 min and $2.34x10^{10}$ ± $1.03x10^{10}$ NPs/mL at 15 min. Interestingly, the number of mineralized particles were one and two orders of magnitude less than in the previous water conditions (2.00M), suggesting that after the induction period, the number of nucleated particles were less as water increase and the number is highly dependent by the initial amount of water.

Beyond the induction time (30min), **figure 2.3-B**, the hydrodynamic size evolved increasing in size until a value of 127.2± 0.7 nm after 24 hours. Interestingly, the number of NPs exhibited first a slightly increase during the first 100 minutes, explained for the generation of particles by the nucleation, but after that time, further evolved following a steady state to a final number of $2.17x10^{12}$ ± $4.04x10^{10}$ NPs/mL after 24 hours. These evolution of number of particles suggested that at later stages the NPs preferentially growth by addition of monomers. Similarly, at higher water (5.00M) **figure 2.3-C**, beyond the induction time (15min), the hydrodynamic size further increases dramatically during

the first 100 minutes, suggesting an aggregative growth in this interval. In contrast, at longer stages, the NPs slightly increased until a size of 418.5± 8.7 nm at the end of reaction. Interestingly, the particles concentration also exhibited an increase to $3.61x10^{11}$ ± $2.34x10^{10}$ NPs/mL during the first 100 minutes, also explained by the nucleation, but beyond that time, they followed a quasi-static state until a number of $4.65x10^{11}$ ± $2.28x10^{11}$ NPs/mL after 24 hours. These similarly in tendency of size and particle number, suggested that during the first 100 minutes, the NPs were growing by aggregation of protoparticles that were continuously nucleated, and beyond that time, the nucleation stopped, and the mechanism were favoured by atom by atom for NPs growth. Interestingly, the evolution of number of particles presented a higher standard deviation over time, explained by the produced heterodisperse particles by an aggregative growth after the nucleation. The DLS technique is greatly affected for the aggregation state of the NPs for calculations. Finally, these results were consistent for all the three water concentrations (2.0, 3.50, 5.00M), suggesting a particle-particle aggregative growth during nucleation, but displayed a monomer addition at the later stages of the reaction.

2.2.2 Silica Mineralization During The initial stages of the Reaction

The previous results revealed that the Stöber silica particles are very sensitive to the initial amount of water in the system. It Is clearly evident that this water dependence during the initial phases of the reaction, regulate both: the initial amount of precipitated particles, and the primary size of the first SiO_2 particles after the induction period, larger in size as water increases. In addition, the SEM and DLS analysis showed the formation of heterogeneous large objects during the initial stages of the reaction, that shrank over the course of the induction time to yield heterodisperse SiO_2 NPs in the nucleation period, suggesting and aggregative behaviour. Therefore, these evidences may suggest that the mechanism of silica nucleation in the initial stages can be either by coalescence of small building units or by aggregation of small unstable nuclei`s (protoparticles) towards a stable primary size and thereafter, they followed a controlled diffusion of monomers on particles surface.

In this regard, here we decided to study in detail the SiO_2 formation, using a high-resolution technique, SEM in STEM mode and TEM coupled with an Energy Dispersive X-Ray Analysis (EDX), to resolve the pathways followed before and after the nucleation process, performing three experiments as follows:

(i) Temporal evolution of the silica formation during the initial phase, recording the size by high resolution TEM coupled with EDX for elemental analysis

In order to observe the presence of the silica protoparticles or small nuclei`s/clusters that can suggest that the growth during nucleation is through controlled nuclei`s/clusters aggregation mechanism, the first experiment was done, taking aliquots of the reaction at certain times and recording the evolution of the reaction by a TEM using 3.50M H_2O and performing a chemical analysis by Energy Dispersive X-Ray Analysis (EDX) as a function of time, focusing on the morphology and composition of the generated species (showed in **figure 2.4**).

As seen in **figure 2.4**, the size of the SiO_2 NPs increases as the reaction proceeds, as expected. During the first minute, high TEM resolution images revealed the presence of dense white cloud, composed of small particles with few nanometres in size. The calculated mean size of the resulted sub-particles was 2.04 ± 0.5 nm. The EDX spectrum revealed that the main species were silicon and oxygen as the predominant elements, besides the other constituents of the grid (e.g. copper and carbon). The high carbon signal can be attributed to the presence organic matter from the TEOS and ethanol, and the low Si signal due to the low density of the small sub-particles. Interestingly, others author has reported similar observations of these primary nucleus having different sizes. For instance, Bogush et al [18] reported a radius between 1–2 nm, Harris et al [26] reported a size between (~4 nm) and later he observe a size (10–20 nm) by cryo-TEM and SAXS in other report [27], Lee et al [26] suggests that the radii of the initial nuclei in ethanol should range between 5 and 10 nm.

Later at 5 minutes, as shown by the TEM images, these small-sized particles, started to gather together around an assembly, to achieve a more colloidal stable structure. The elemental mapping revealed the increased Si signal with a decrease in the carbon content. Interestingly, the further evolution of the reaction yields a high density heterodisperse

coagulated particles at 15 minutes, similarly to the observed by SEM in **figure 2.2-B** at the same time. The main chemical composition of these particle was again silicon and oxygen.

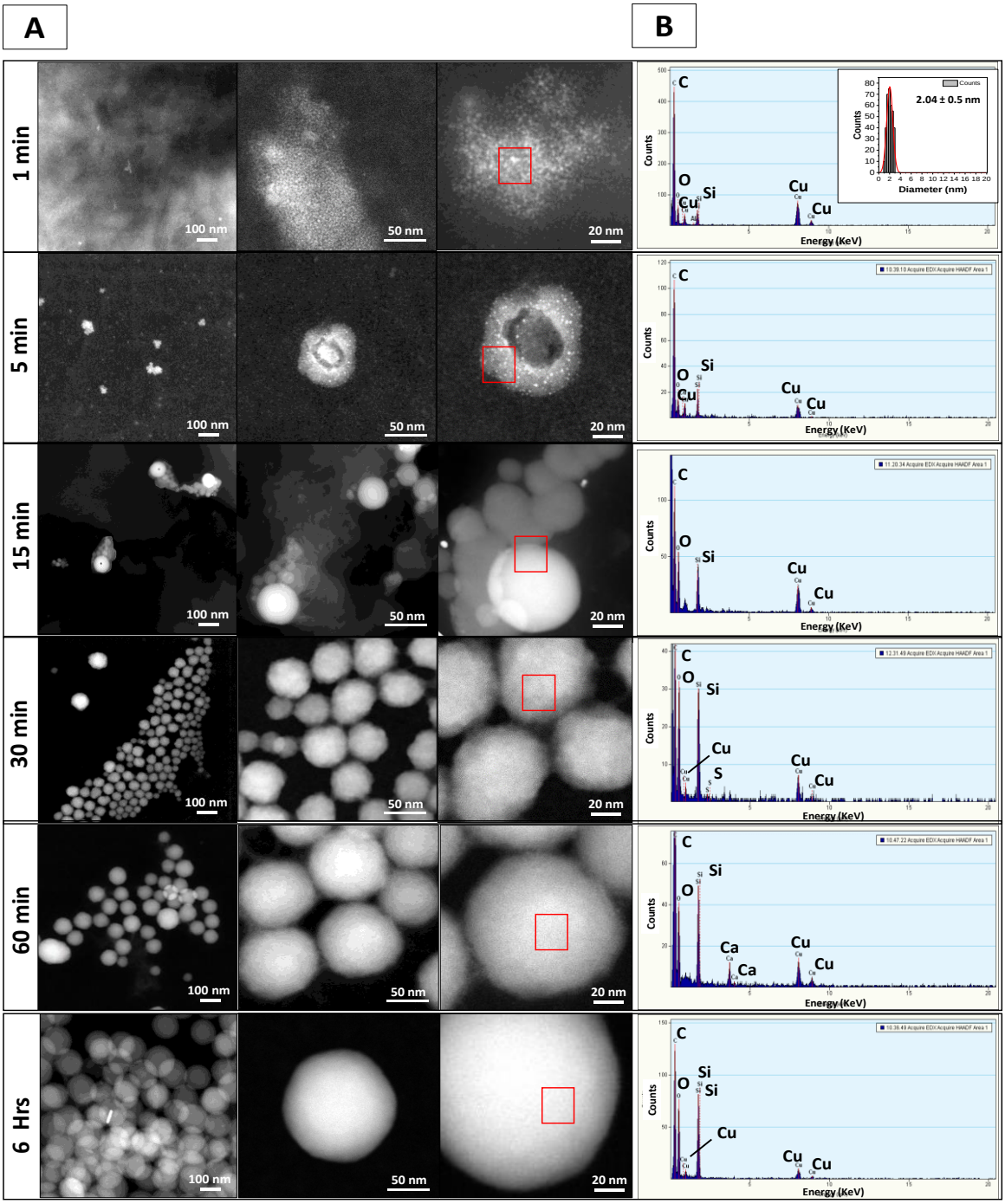

Figure 2.4 Graphic representation of the temporal evolution profile of the colloidal SiO_2 particle formation, recording the particle morphology by (A) TEM as a function of time using 3.50M H_2O and (B) elemental analysis by Energy-dispersive X-ray spectroscopy (EDX). The EDX inset shown the calculated mean size and size distribution of the protoparticles. The experiment was done dropping an aliquot into the carbon grid at certain times for characterization until 6h. The red square highlights the area in which the EDX were measured. *The size distribution of the small particles was calculated measuring at least 300 particles by image J software.

Finally, after 30 minutes, the mineralized colloidal SiO_2 NPs displayed a broader distribution. These results were in agreement with our previous observations of heterodisperse particles once the nucleation after the induction time. Beyond this interval and until 6 hours, the precipitated SiO_2 NPs evolved increasing their diameter. The absence of sub-particles with a few nanometres in the later phase of the growth (from 1 hour on), suggests that, the remaining silanol monomers in solution were seized by the growing particle's surface, possibly following a ''monomer-addition ''.

(ii) Temporal evolution adding a fixed amount of water in different intervals of an ongoing reaction, in order to observe if the addition of an extra water can induce aggregation or coalescence of particles towards larger sizes.

The second experiment were done recording the evolution of the diameter by STEM mode and measuring the final yield by weight as dried solid, when a fixed amount of water (3.00M) was added at different times (during the induction period and after nucleation) into an ongoing synthesis using 2.00M of H_2O, for achieved a total 5.00M of water, for test our hypothesis. The main idea is to observe if we can tune the size of the reaction by simply adding water at certain intervals to induce the formation of bigger particles. Results as follows in **table 2.4** and **figure 2.5** and **2.6**:

Table 2.4 Physicochemical characterization of the temporal evolution profile of the SiO_2 NPs by adding extra water (3.00M) in different intervals of the reaction.

H_2O [M]	TEOS [M]	NH_3 [M]	Added 3.00 M H_2O (min)	Total H_2O (M)	TEM diameter (nm)	SD (%)	Yield by weight (mg SiO_2/mL)	Yield (%)
2.00	0.15	0.55	0	2.00	31.8 ± 2.9	9.1	8.28	91.8
			5	5.0	269.3 ± 29.1	10.8	8.19	90.7
			10		283.2 ± 29.6	10.5	8.21	91.0
			20		184.3 ± 17.9	9.7	8.26	91.5
			30		63.4 ± 8.8	13.8	8.16	90.4
			60		44.3 ± 6.9	15.6	8.12	90.0
			120		42.0 ± 3.6	8.6	8.15	90.3
			240		38.8 ± 3.6	9.3	8.11	89.9
5.00	0.15	0.55	0	5.00	332.1 ± 31.5	9.5	8.29	91.9

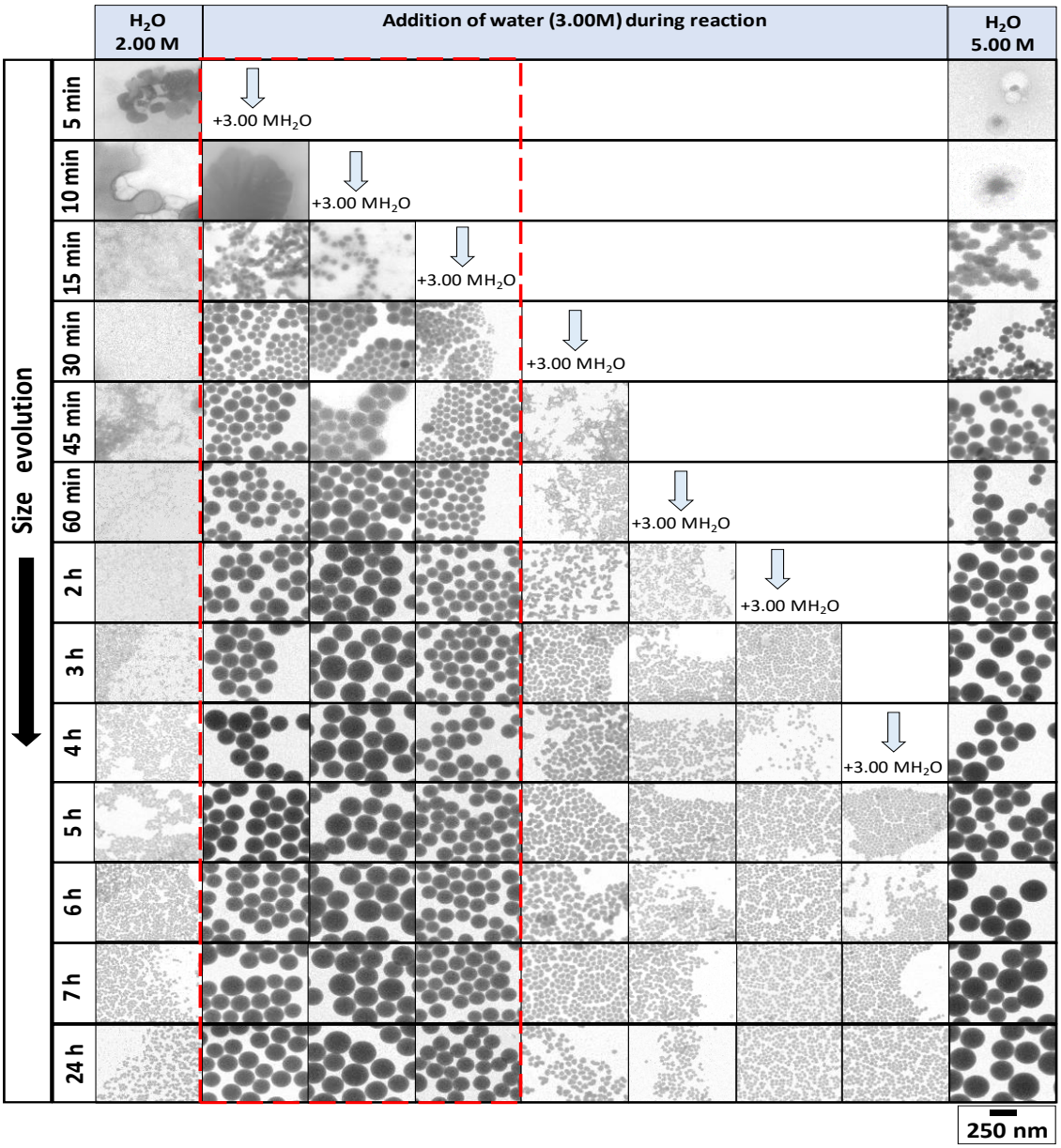

Figure 2.6 Representation of the colloidal SiO_2 particle formation when 3.00M of H_2O were added at different intervals into an on-going synthesis using initial water of 2.00M H_2O, recording the particle size and morphology by STEM mode. The 5.00M of water were putted for comparison. The red dotted line highlights the time in which adding 3.00M of H_2O highly affect the size of the SiO_2 NPs. The calculated SD are showed in (**Appendix A5**).

As seen in **figure 2.6**, the final size of silica can be strongly altered towards bigger sizes, depending in the interval in which the extra water was added. Adding the water at short times (below 20 minutes), the NPs size evolved to bigger diameters, similarly to the synthesis using 5.00M of water, presented as control for comparison. These results revealed that the system is extremely sensitive during the inducting time, period which the monomers are being produced by hydrolysis and condensation reactions of TEOS. In

contrast, adding the extra water at longer times (after 30 minutes) the silica was comparable in size to the 2.00M of water condition. These results suggest that small unstable sub-particles of SiO_2 were produced in the beginning of reaction and are prone to aggregation during the induction time. After this interval, the already formed particles became electrostatically stable in solution, further growing favoured by the addition of monomers on surface. The biggest size was achieved, when the water was introduced at 10 minutes. Interestingly, as shown in **figure 2.5**, the final yield of the reaction was equivalent for all conditions, revealing that the same amount of monomer was consumed for the silica mineralization, despite the differences in sizes.

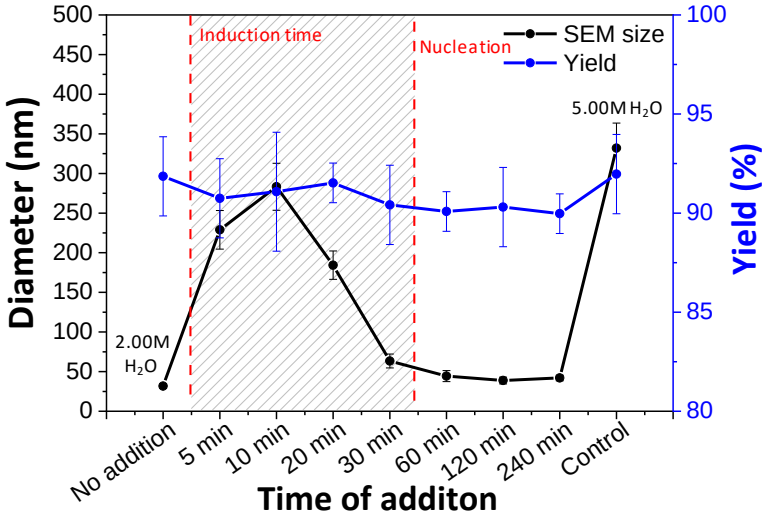

Figure 2.5 Graphic representation of the measured particle size distribution by STEM mode as a function of the yield of the SiO_2 particles after 24 hours, when fixed amount of water (3.00M) were added to a 2.00M synthesis, during the induction time and after the nucleation. The total amount of water in the system after the addition is 5.00M. * The size distribution was calculated measuring at least 300 particles by image J software and error bars are indicative of the standard distribution (**Appendix A5**). The red dotted line shows interval in which size was highly affected.

These observations clearly suggest that the number of NPs is different in every condition and gave a strong indication that water can induce an aggregative growth during the induction time, inducing a destabilization of the forming protoparticles towards bigger stable sizes in the initial phases. The increased generation of hydroxyl and ammonia ions (OH^-) during water dissociation with ammonia can decrease the double layer thickness, hence stability of species.

(iii) Temporal evolution of the SiO_2 NPs diameter, as a function of the ionic strength by adding different NaCl concentration, while other parameters remained fixed (TEOS, NH_3, H_2O), in order to observe if aggregation of protoparticles or small nuclei's is occurring in the reaction with the presence of counter ions.

The third experiment were done recording the final size of the SiO_2 NPs by STEM mode and measuring the final yield, when the ionic strength of the reaction was systematically increased by adding small quantities of sodium chloride (NaCl), meanwhile all the other synthetic parameters were constant. The main objective with this experiment is to evidence if presence of counter ions, such as Na^+ and Cl^-, affect the mechanism of formation of silica NPs, by inducing an aggregative growth or the NPs remained stable. Results showed in **figure 2.7** and summary of characterization shoed in **table 2.5**.

Table 2.5 Physicochemical characterization of the temporal evolution profile of the SiO_2 NPs by adding different NaCl (mM) concentrations.

H_2O (M)	TEOS [M]	NH_3 [M]	NaCl (mM)	TEM diameter (nm)	SD (%)	Yield by weight (mg SiO_2/mL)	Yield (%)
2.00	0.15	0.55	0	31.4 ± 3.5	11.1	8.31	92.0
			0.10	42.7 ± 4.9	11.4	8.40	93.1
			0.30	50.9 ± 6.3	12.4	8.29	91.8
			0.50	74.7 ± 10.5	14.1	8.35	92.5
			0.80	96.9 ± 9.9	10.2	8.26	91.4
			1.00	134.7 ± 15.6	11.6	8.24	91.3
			1.50	92.3 ± 18.1	19.6	8.15	90.3
			3.00	153.2 ± 44.1	28.9	8.10	89.8

As shown in **figure 2.7**, the mean size and SD of the SiO_2 NPs is strongly determined by the ionic strength of the media. Our results showed that the final size of the NPs increase along with the ionic strength, until a concentration (beyond 1.50M) in which particles with a broader size distribution were obtained. Interestingly, the yields of the reaction were comparable in all cases, suggesting that the conversion of the TEOS to monomer and the further consumption to precipitate particles, is not conditioned by the presence of ions in solution. However, the mechanism of silica formation is highly affected. These results revealed once more that a mechanism of formation by aggregative growth is happening. The decrease in the double layer thickness of the sub-particles, induce a lower the stability

of the forming nanoparticles, thus causing an increase in the mean size of the precipitated particles. These results revealed that growth is favoured by aggregation of protoparticles until a stable size, which is highly dependent by the stability of the dispersion. The monodipsersity of the particles can be maintained until certain concentration (0.80M NaCl), beyond this point, the polydispersity of the NPs was maintained until the end of reaction, suggesting a chaotic aggregation.

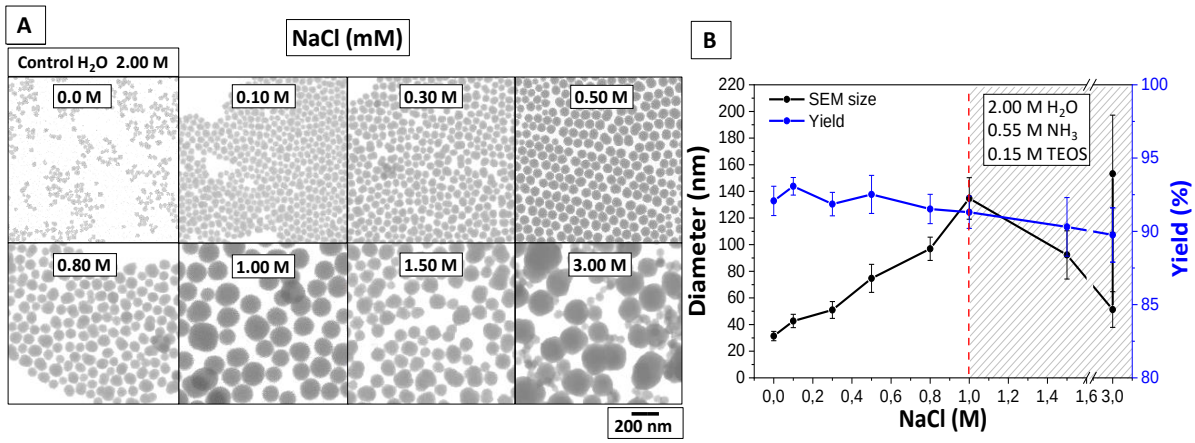

Figure 2.7 Detailed representation of the electron microscopy images as a function of the yield of the reaction, using 2.00M H_2O and increasing NaCl (mM) concentration. (A) Representative STEM images after 24 hours, (B) Graphic illustration for mean size and SD against yield of the reaction as a function of NaCl concentration. * The size distribution was calculated measuring at least 300 particles by image J software and error bars are indicative of the standard distribution (showed in **Appendix A6**). The red dotted line and shaded area highlight the NaCl concentration in which were no longer monodisperse.

2.3 The Convivence of the Two Growth Mechanism in the Stöber silica NPs: The Controlled-Aggregation and The Monomer-Addition Models

In the previous section we observed that the mechanism of formation of the SiO_2 NPs, in the different tested conditions (water addition at different intervals or by adding NaCl), presented different colloidal behaviours that allowed the NPs growth to larger sizes. This set of experiments revealed that the size of the silica NPs can be kinetically controlled towards larger sizes, either by addition of water or electrolytes during the induction time, inducing an aggregative growth of the silica. However, from the other set of results, the time evolution experiments, revealed that at certain intervals of the reaction (later stages of reaction), the number of particles in solution were kept constant and the remaining

silanol monomers in solution from TEOS were consumed for particle growth. These results suggest that a monomer-addition mechanism is also happening in the reaction.

In this regard, in order to study this kinetic behaviour in detail and evidence the mechanism of formation of the silica nanoparticles, a theoretical size evolution model of the SiO_2 NPs was done by plotting an atom-by-atom growth model in which the concentration of [NPs] was maintained constant and the growth was based on the monomer that was consumed. For performing the calculations (explained in **Appendix B7**), the experimental values of the measured mineralized monomer by UV-Vis (SMA method) and the size obtained by DLS at different intervals, were used. The concentration of NPs for every interval of time were calculated. Later the further growth was plotted by considering they are monodisperse and all had of the same size. Finally, we compare the obtained valued with the one experimentally measured by DLS. Results showed in **figure 2.8**.

As shown by the **figure 2.8-A**, the mechanism of formation of the silica nanoparticles in all water concentrations, revealed that the silica NPs followed a growth mechanism of atom by atom, at later stages of the reaction, preferentially by the consumption of the remaining silanol monomers. In the low water concentration (2.00M), we can observe that the calculated model of homogenous growth was comparable with the DLS size around 120 minutes of reaction. From thus point, the evolution of the size followed the same trend. Below that time (100 minutes and below), the calculated diameter was lower to the obtained by DLS number, suggesting that below this interval, the mechanism of formation was different than monomer addition. Thus, our evidences suggested that after 120 minutes' interval, the SiO_2 NPs growth by a monomer addition model.

On the other hand, as shown by the **figure 2.8-B-C**, the theoretical growth model for the 3.50M and 5.00M of water, revealed the same trend at short times. The calculated size did not fit the measured by DLS, revealing a different mechanism of growth in the beginning of the reaction. In contrast, after 100 minutes, the calculated atom by atom model, followed the same trend with the measured DLS for both conditions. These

observations revealed that after 100 minutes, the silica NPs preferentially growth by a homogenous process, explained by Lamer model of controlled diffusion of the monomer.

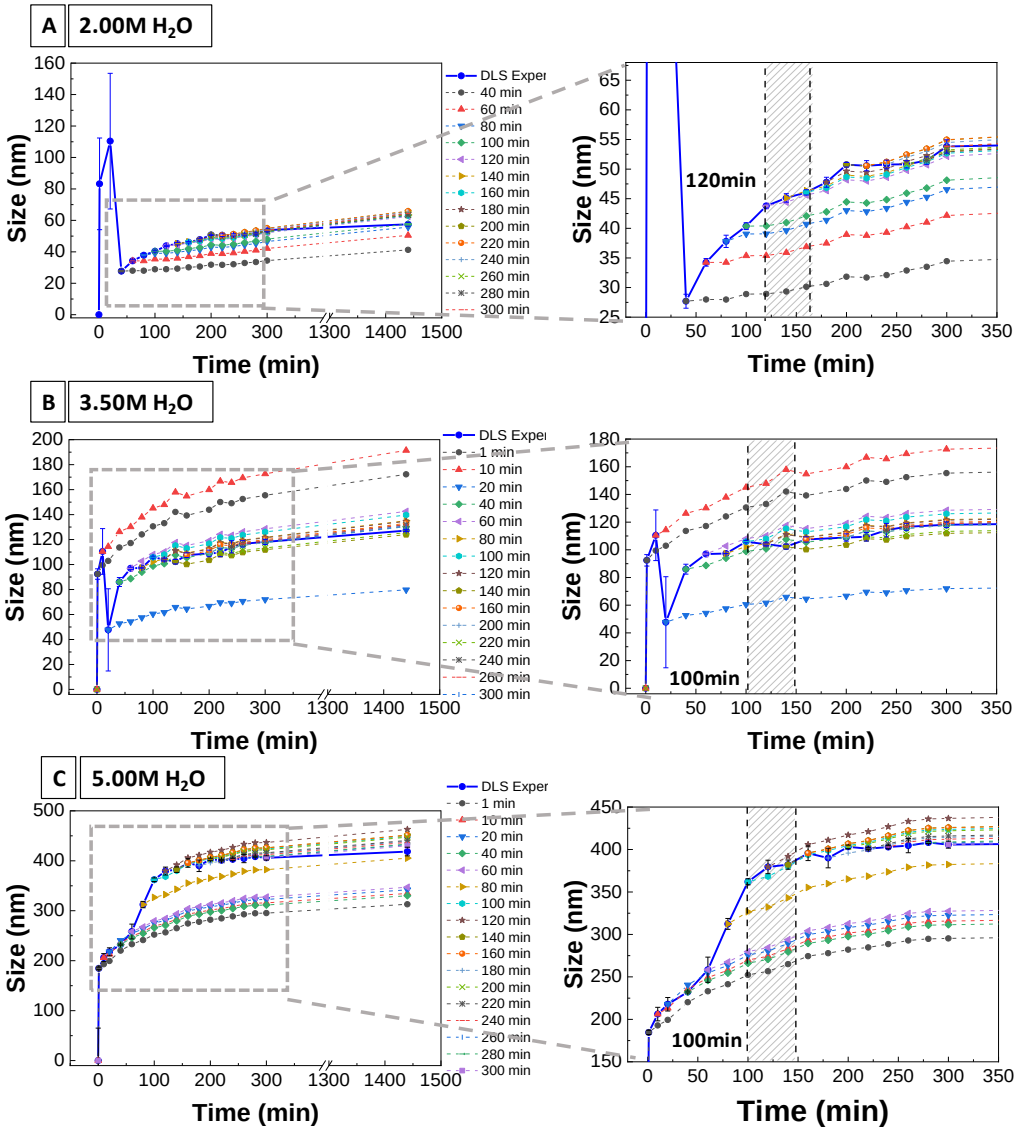

Figure 2.8 Graphical representation as a function of time of the theoretical size evolution of the SiO_2 NPs at different intervals, assuming a homogenous growth with constant number of particles. For calculated the size of the particles, the measured monomer concentration (mg Si/ml) and the DLS by number size (nm), were used. (A) for the 2.00M, (B) for the 3.5M and (C) for 5.00M of water. Calculations are (showed in **Appendix B7**). The gray dotted line showed the extended area for visualization and the shaded area highlight the time in which particles grow by monomer addition.

2.4 Unrevealing the Nucleation and Growth Mechanism of the SiO_2 NPs: The role of water

From the above results, several conclusions can be made regarding the formation mechanism of SiO_2 NPs.

First, **the induction time for the monomers to overcome the activation barrier of self-nucleation decreases as the initial amount of water were increased**. This statement was done, because our results showed that the induction period followed an opposite trend to the water content.

Our experiments revealed that the hydrolysis rate for producing silanol monomers (induction time), as well as the condensation rate between monomers that lead to particles (nucleation), were clearly accelerated by the presence of water. These observation were in agreement with the reported by others authors that claimed similar behaviour [21] [27], [28]. They explain that this longer period is caused by a slower hydrolysis of TEOS which extends the time of monomer production below its solubility limit; thus, extending the induction phase. Additionally, In a recent report, other author reported that the hydrolysis rate is the crucial factor determining the formation of silica nanoparticles [29]. However, water alone cannot increase the hydrolysis rate of TEOS. In fact, both species are incompatible and water is considered a poor nucleophile for hydrolyse TEOS. Therefore, the kinetics of the reactions were increased because, the water acted as a source of hydroxyl ions (OH^-), derived from the water dissociation catalysed by the ammonia ionization. These nucleophilic negative ions are superior nucleophiles than water and can modify both reactions (hydrolysis and condensation) towards short or longer induction times that lead to a slow or faster initiation of the nucleation. In the literature, it is reported that ammonia solutions, are a source of water and hydroxyl ions that caused an increased degree of polymerization that lead to larger sizes, resulting in faster kinetics [17]**.** Harris MT and Green DL showed that [H_2O] concentration controls the induction period [27], [28]**.** They claimed that the generation of these hydrolysed monomers were the rate-determining step for the particles growth by tracking the concentrations of hydrolysed mono mers by NMR and the formation of particles by Small-angle X-ray scattering (SAXS). In addition, Matsoukas and E. Gulari [17], stated that hydrolysis plays a dominant role since it controls the availability of the hydrolyzed monomers that has a direct effect upon nucleation and the resulting particle size.

Second, **the initial number of mineralized silica particles (nucleation) and their initial morphology (size distribution), were regulated by the initial amount of water after the induction period.** This conclusion can be made, because our experiments revealed that the number of mineralized particles in solution, increased as water decreased. But, the mean size of these particles followed an opposite trend, increasing in diameter, while the number decreased.

On one hand, our evidences showed a higher number of nucleated particles, when the content of water was decreased from (5.00M to 2.00M) in the beginning of the reaction. Similar results were observed by R. Lindberg et al [36]. They found that their systems produced more individual SiO_2 particles when water content was kept low. They claimed that the initial supersaturation level of hydrolysed monomer (during induction period) was critical in determining the particle formation in the sol-precipitation. They observed higher number particles formation, when the initial supersaturation conditions were prolonged (e.g extended induction time). Behaviour that can also be correlated by the fact that, longer nucleation times lead to higher number of particles, principle explained by LaMer model of burst nucleation [36]. On the other hand, our experimental evidences showed the production of a lot SiO_2 NPs smaller size, in the low water regime (2.00M), in comparison with the high-water system (5.00M), in which were larger in size but fewer in numbers. This observation indicates that depending on the amount of water in the initial phases, the mechanism of silica formation can be kinetically controlled favouring the aggregative growth towards bigger particles. Y. Xia and co-workers [6] state that the type and number of nuclei or seeds formed in the early stage of a synthesis can be drastically changed when a kinetic parameters is altered (e.g., reductant and precursor, concentrations of reagents, pH value, as well as the introduction of additives). In the lower water system, the aggregative growth was outpaced by nucleation, thereby producing smaller particles higher in number. The systematically addition of water allows us to control the aggregative rate between protoparticles by gradually decreasing the double layer thickness of the small sub-particles by the generation of OH^- and also counter ions, such as NH_4^+. In addition, with the increased hydrogens bonds that authors have reported that assist the coalescence between SiO_2 particles [22]. This conclusion can be made because

our synthetic analysis of size by using NaCl instead of water, showed that in the initial phase of the reaction, the aggregative growth of siloxane structures plays and important role. Some authors have explained this behaviour looking the colloidal stability of the siloxanes intermediates. For instance, Bogush and co-workers claimed that the colloidal stability is an important factor in the mechanisms describing how many particles are formed early in the reaction and at what size these particles obtain the colloidal stability that prevents further aggregation [18]. A. Van Blaaderen and A. Vrij [19], stated that the addition of ammonium hydroxide in the reaction, produced destabilizing effects because of the increased ionic strength through the production of ions (ammonium ions NH_4^+ and hydroxyl ions OH^-). Thus, these ionic species decrease the double layer thickness and lead to a dispersion that is more easily flocculated. Similarly, H. Giesche et al [21], claimed that the colloidal stability and aggregation rate of the primary nuclei determined the number and size of the particles. They observed smaller number of aggregate units at the beginning but further grew larger in size, because of the lowered colloidal stability in a higher ionic strength system, upon addition of NaCl. Others author have also proven the aggregative growth of silica by the addition of other monovalent electrolytes, such as (KCl, $LiNO_3$, KI, ammonium salts NH_4NO_3) [35]–[37].

Third, **the growth mechanism followed by the SiO_2 NPs at the beginning of the reaction is by an aggregative-growth of protoparticles and during the later stages occurs by monomer addition**, allowing the incorporation of atoms at the silica surface for a homogenous growth of at the end of the reaction.

This conclusion can be made, because our experimental results showed that after certain time and below nucleation threshold, the evolution of the amount of particles in solution remained in a steady-state, while the diameter of the silica NPs increases by a size focusing mechanism, consuming the remaining silanol monomers from hydrolysis TEOS, explained by the homogenous growth of the controlled-diffusion of monomer, principle also described by LaMer. In addition, our experiments of the theoretical growth atom by atom model confirmed these evidences. In the literature, some authors have reported that both mechanisms are responsible for growth for the SiO_2, suggesting an aggregation

mechanism of nanometer-sized primary nuclei during the first stage of the reaction, followed by a monomer addition growth mechanism thereafter, leading to smoothing of the colloid surface at the end [21], [27], [28]. In addition, our experimental evidences revealed that the addition of water or salt after the induction period, when the particles were already electrostatically stable enough, did not affect the particles size, because the aggregation is probably not important anymore in that stage. An Oswald ripening effect mechanism were out ruled during the growth after the nucleation because the dissolution of SiO_2 NPs was not observed. On the contrary, the evolution of the size distributions (**Appendix A5**), revealed that after nucleation, all the mineralized particles (even in a heterodisperse system), depleted the remaining monomer in solution for growth. This explain why Stöber particles usually present a tendency towards broader size distributions. Van Blaaderen and A. Vrij [19], explained this polydispersity because particles of different size compete for the monomers with efficiencies that depend on the growth mechanism, which the smaller spheres are growing faster than larger spheres.

Finally, with the help of all the above observations and conclusions found by monitoring colloidal particle formation described in the section 2.2.1 and section 2.3.1 of this dissertation, the proposed mechanism of SiO_2 formation, as a function of the role of water, is presented in **figure 2.9**. The mechanism begins with the generation of the monomers, here *silanol monomers*, which constantly increase in concentration over time. These species are generated by TEOS hydrolysis using water molecules, but ammonia catalysed. Thereafter the condensation between silanol monomers takes place forming an inhomogeneous highly branched siloxane structures together with the continuously generation of more silanol monomers necessary for achieved the supersaturation state. Once the concentration level achieved a higher critical value that allows the system to surpass the barrier for nuclei generation, the nucleation process starts and the branched-polymeric structure becomes unstable and collapses generating a lot of smaller low-density nuclei's prone to aggregation. These colloidally unstable sub-nanometre structures aggregate forming clusters. The size of the structures will depend on the initial water concentration.

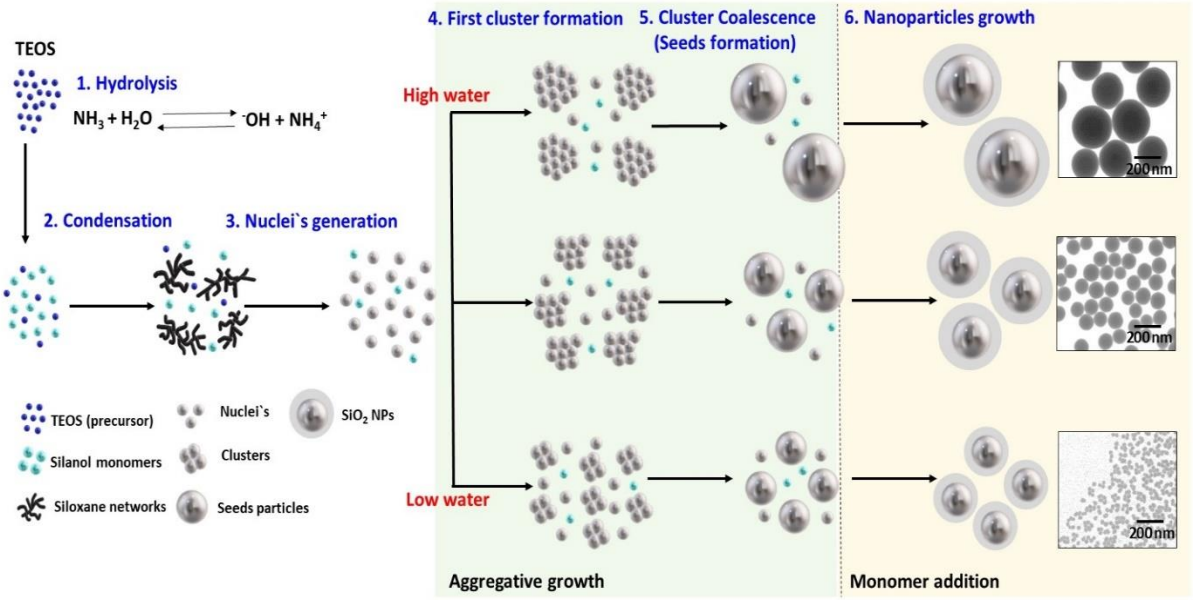

Figure 2.9 Graphical illustration of the SiO_2 NPs mechanisms of nucleation and growth. Five main steps can be observed. (1) The hydrolysis, to convert TEOS to soluble silanol monomers by the hydroxyl ions formed in the ammonia-catalysed reaction, (2) subsequent condensation of the silanol monomers for formation of siloxane branched structures, (3) nuclei`s generation (protoparticles prone to aggregation) by the collapsing of the unstable siloxane branched assembly, (4) first cluster formation by the aggregative-growth of protoparticles into subcritical clusters. The aggregative growth will depend on the initial amount of water concentration, (5) cluster coalescence beyond a critical size which the high-energy barrier is circumvented, forming the stable seed primary particles and (6) Seed nanoparticles growth by diffusion of Si atoms from the remaining silanol monomers, by a process known monomer-addition, forming the final SiO_2 NPs.

The further aggregation of nearby subcritical clusters structures takes place overcoming the energy barrier, until colloidally stable seeds particles are attained achieving the critical size by developing a strongly repulsive electrical double layer that maintains their stability in solution. This nuclear aggregation is occurring during the nucleation phase. Bogush and co-workers [18], state that this self-sharpening mechanism is related to the size-dependent aggregation rate that depends on many parameters in the reaction, including concentration and nature of reactants, temperature and the properties of particles and surface potentials [18]. Also, A. Van Blaaderen and A. Vrij [19], claimed that this aggregative mechanism is strongly dependent on the stability of the (intermediates) particles during nucleation. Our evidences showed that formation of these smaller low-density sub-structures (protoparticles of 2 nm) in the initial stages, were always thermodynamically produced (because in all conditions were generated), but the initial size of the primary seeds particles formed by the aggregative growth of the unstable nuclei`s were kinetically controlled by the addition of H_2O.

This can be explained by looking the model described by Jörg Polte [39], of growth by coalescence or thermodynamically but colloidal unstable nuclei's. Afterwards, the reaction continues, but because of the nucleus generation and the aggregative growth consume [monomer], this decreasing in monomer concentration below nucleation threshold, stop the generation of new nuclei at the end of the nucleation period. Finally, these formed colloidal seeds particles further growth by the homogenous incorporation of monomers by the addition of the remaining silanol species on the NPs surface, following a monomer addition by a size focusing mechanism. This is state because the Stöber process which are considered a one-pot homogenous nucleation system in which no nuclei or particles are initially present, our experimental data showed that smaller particles growth faster than larger particles, decreasing the size distribution at the latter stages of the reaction. As explained by Howard Reiss [40], if the diffusional growth is only dependent on the flux of monomer, smaller NPs will then growth faster in the presence of larger NPs, narrowing the size distribution.

2.5 The Water as Key Reagent for Controlling the Mineralization Process Beyond Stöber: Size tuning from 20 to 320nm the SiO_2 NPs

Based on the previous analysis of the mechanism of formation of SiO_2 NPs, which supports that water sensitively affects significantly the final size of the colloidal silica, in order to systematically reliably control the final particle size using a one-pot strategy while maintaining the monodispersity in the sub-100nm region, our approach was based on the modification of only one parameter. In this regard, stoichiometry additions of pure water were chosen as a convenient independent variable, while volume and concentration of reaction (32mL ethanol anhydride), (0.15M TEOS) and ammonia (0.55M NH_3) were fixed during the reaction. To the best of our knowledge, this synthetic optimized procedure is the simplest and reproducible fashion to produce homogenous highly stable and monodispersed silica particles, without the application of complex and time-consuming seeded-growth methods [41], [42], semi-batch [43]–[45] or multi-step strategies [22], [46], [47]. A shown in **figure 2.10**, particles in the range of 20–320 nm with relative low standard deviations of <10.0% was demonstrated by application of this one-pot strategy and are their characterization is summarized in **table 2.7** as follows:

Table 2.7 Summary of the size control characterization of the SiO_2 NPs obtained after the our one-pot adapted Stöber method.

H_2O [M]	SEM Size (nm)	SD (%)[a]	DLS size (nm)[b]	PdI	Zeta P (mV)[c]	Optical density at λ 300nm (cm^{-1})	Yield ($mgSiO_2/mL$)	Yield (%)
1.80	22.6 ± 2.3	10.2	50.9 ± 1.0	0.092	-36.4 ± 4.4	0.071 ± 0.002	8.29	91.9
2.30	31.9 ± 3.0	9.4	59.8 ± 1.8	0.030	-41.2 ± 2.3	0.565 ± 0.003	8.33	92.3
2.40	40.5 ± 3.8	9.4	63.6 ± 0.4	0.091	-43.5 ± 7.8	1.000 ± 0.004	8.41	93.2
2.50	52.4 ± 5.0	9.5	78.8 ± 1.9	0.029	-40.0 ± 0.9	1.885 ± 0.005	8.22	91.1
2.70	63.5 ± 6.2	9.7	95.5 ± 2.0	0.038	-42.3 ± 1.9	3.058 ±0 .006	8.40	93.1
2.80	71.3 ± 7.0	9.8	101.4 ± 2.4	0.071	-43.1 ± 0.7	3.394 ± 0.007	8.38	92.9
3.10	92.2 ± 6.5	7.0	123.8 ± 1.1	0.021	-41.4 ± 0.6	4.865 ± 0.008	8.31	92.1
3.30	104.9 ± 6.4	6.1	142.6 ± 2.3	0.032	-42.2 ± 2.2	6.169 ± 0.009	8.36	92.6
3.50	117.5 ± 8.0	6.8	167.5 ± 2.0	0.031	-31.6 ± 0.2	6.949 ± 0.010	8.31	92.1
3.70	135.5 ± 5.4	4.0	174.0 ± 3.5	0.036	-39.1 ± 1.5	7.704 ± 0.012	8.44	93.5
3.90	150.3 ± 8.7	5.8	193.3 ± 3.0	0.038	-47.0 ± 0.5	9.207 ± 0.025	8.29	91.9
4.20	177.7 ± 8.6	4.8	238.8 ± 6.2	0.059	-41.2 ± 0.4	13.144 ± 0.095	8.31	92.1
4.70	208.1 ± 8.5	4.1	269.8 ± 5.1	0.040	-38.2 ± 1.4	15.549 ± 0.099	8.32	92.2
6.20	236.1 ± 13.5	5.7	320.7 ± 8.2	0.035	-42.6 ± 0.6	17.929 ±0 .104	8.36	92.6
8.20	263.1 ± 12.7	4.8	366.3 ± 7.6	0.074	-42.8 ± 0.2	21.172 ± 0.125	8.37	92.7
13.0	322.9 ± 16.6	5.5	408.3 ± 8.7	0.067	-35.6 ± 1.2	22.351 ± 0.153	8.41	93.2

[a] Standard deviation mean from size distribution high resolution STEM images (see **appendix A7**). [b] DLS size by number mean and SD from three independent runs, measured in pure water. [c] ZP mean and standard deviation from three independent runs, measured in pure water at pH 8.50 with a conductivity below 1µs/cm.

As seen in **Figure 2.10** and **figure 2.11-B**, showed the morphological and hydrodynamic size characterization by STEM mode and DLS of the resultant SiO_2 NPs, summarized in **table 2.7**. The particle size distribution studies were performed by systematically analysis of at least 350 particles for each silica sample. As shown in **figure 2.10**, the size of the NPs can be kinetically controlled towards larges sizes by increasing the water concentration, leading to an aggregative growth in the initial stage and a monomer-addition at the end of the reaction, for smoothing the surface and increase the monodispersity of the silica NPS, correlated with the standard deviation, which becomes narrower from 10.2% to 4.08% as particle size increased from 22.6 ± 2.3 nm using 1.60M to 322.9 ± 16.6 nm using 13.0M of water. Same trend of both SEM and DLS characterization methods have been showed in the literature [3, 28, 29], but with the difference of being able to controlled systematically by our strategy. Interestingly, the yield of the reactions was comparable in all conditions, suggesting that almost all TEOS were consumed for the mineralization. The DLS gave monomodal distributions with a polydispersity index (PdI) of

below (<0.1) for the majority of samples indicating that NPs were monodisperse (without the presence of aggregates). The size distribution profiles measured by DLS were always slightly higher than the calculated by TEM due to the fact that DLS measures the hydrodynamic radius of the particles which depends in the random Brownian motion and the physicochemistry of the medium in which the particles are dispersed, affecting their mobility in solution [30].

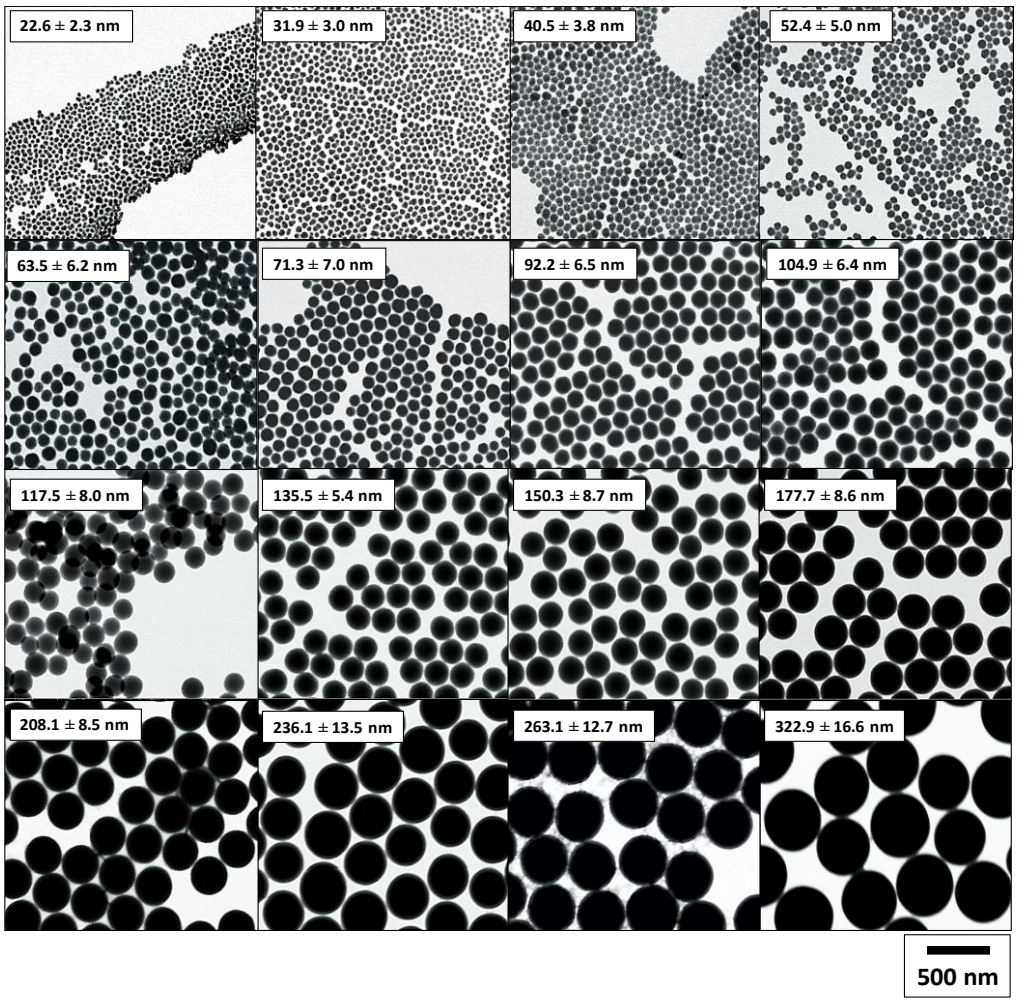

Figure 2.10 Representation of the transmission electron microscopy images of size by STEM mode, obtained with different water conditions after 24h, as showed in **table 2.2**. The particle mean size and SD increase from (22.6 ± 2.3 nm) using 1.80M to (322.9 ± 16.6 nm) using 13.0M of water respectively. In all cases, the main reagents were kept constant (0.15M TEOS, 0.55M NH_3 and 32 mL of anhydride ethanol) at room temperature 25°C with the same stirring rate 800 r.p.m.* The size distribution was calculated measuring at least 300 particles by image J software and error bars are indicative of the standard distribution (showed in **Appendix A8**).

Later, as shown in **Figure 2.11-A**, the optical characterization by means of UV–Vis spectroscopy of all synthetized SiO_2 nanoparticles were done in all water conditions. The

results showed that intensity in the UV region (200-400 nm) was increased, when the size of the particles were increased from sample 1.60M (22.6 ± 2.3) to 13.0M (322.9 ± 16.6 nm) of water respectively. It is well known, the UV-Vis light absorption of silica NPs is related to the presence of different defects due to incomplete formation of Si–O–Si tetrahedral network at the silica surface, such as oxygen and silicon vacancies [31]. In addition, the absence of any absorption peak in the visible region of pure SiO2 nanoparticles spectrum was in good agreement with the wide band gap nature of the material and its inability to absorb in the visible range [32].

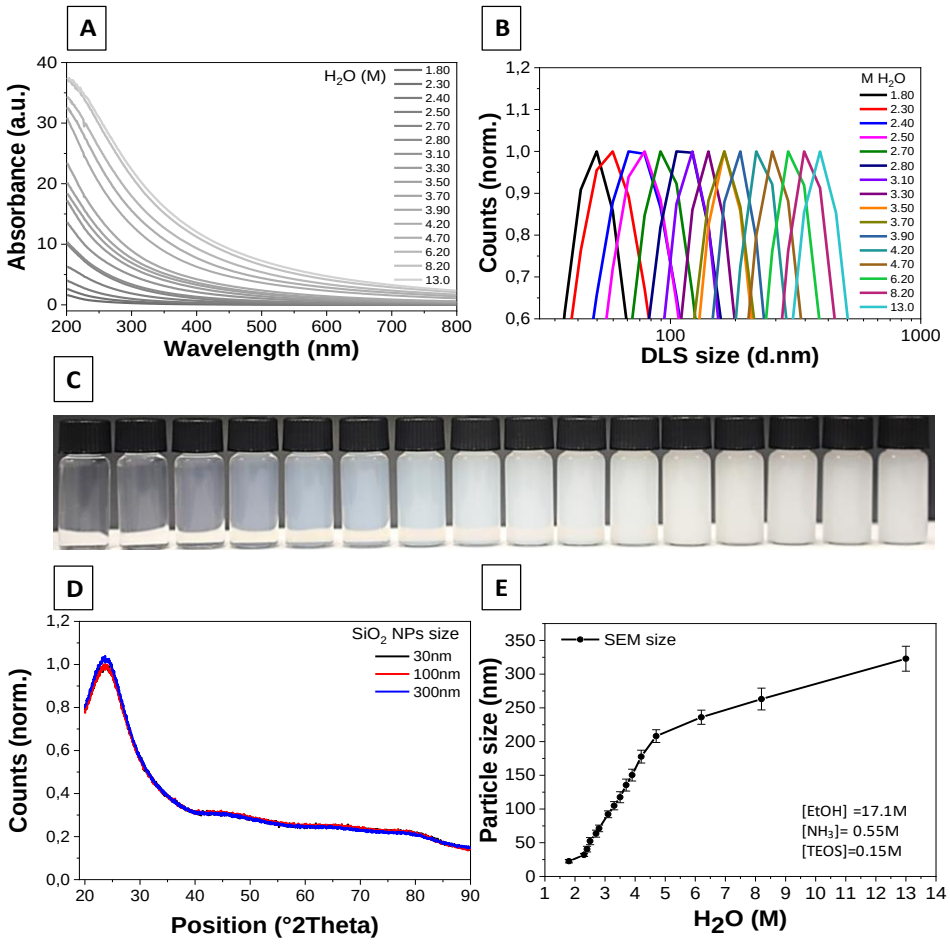

Figure 2.11 Graphic representation of the characterization of the different SiO_2 NPs obtained using different water concentrations, after 24h (A) Uv-Vis absorption spectra of the different SiO_2 nanoparticles obtained. From down to up spectra, scattering at 300nm of the SiO_2 increases along with mean size. (B) Hydrodynamic size by number, by dynamic light scattering (DLS). Monomodal curves were obtained, (C) Colloidal solutions image of SiO_2 NPs, size increasing from left (1.80M) to right (13.0M). Small SiO_2 NPs particles appear almost transparent and larger particles were opalescence as the scattering contributions are dominating. (D) X-ray diffraction (XRD) pattern of three SiO_2 NPs samples: 2.30M (31.9 ± 3.0 nm), 3.30M (104.9 ± 6.4 nm) and 13.0M (322.9 ± 16.6 nm), indicating a broad peak with the equivalent Bragg angle at 2θ = 23º, which reveals the amorphous nature of the silica nanoparticles samples. (E) Graphical representation of the

STEM diameter as a function of water concentration. The mean size and SD were calculated measuring at least 300 particles by image J software and error bars are indicative of the standard distribution.

According to Beer-Lambert's law, the "extinction" is proportional to the absorbance and scattering of a sample in a particular wavelength of light. However, amorphous silica does not absorb photons in the visible portion of the spectrum; thus, the attenuation of transmitted light of silica comes from the Rayleigh scattering, because It is reported that silica colloids elastically scatter light [33]. This may be seen, by the colloid colour which appears white since all wavelengths of light are scattered. Further investigation into the atomic structure of the particles was carried out using X-ray diffraction (XRD), in order to determine whether any crystalline phase was present in the silica NPs. For this purpose, three representative sizes of silica were chosen: samples 2.30M (31.9 nm), 3.30M (104.9nm) and 13.0M (322 nm) of H_2O, respectively. Results showed, a broad peak in the powder diffraction pattern with the equivalent Bragg angle of approximately at 2θ = ~23º, for the three samples, which reveals the amorphous nature of the silica nanoparticles as seen and characterized in previously reports [34]. Therefore, the absence of sharp peaks in the XRD pattern confirms the absence of any ordered crystalline structure. Finally, as seen in **figure 2.11-E**, the size of silica NPs can be fine-tuned with the amount of water. Below 5.00M of water, smaller size-particles were obtained, revealing a linear behaviour. However, beyond that water concentration and until 13.0M, bigger SiO_2 NPs were obtained, but with different trend. One explanation in the change of the linear behaviour in high water system is related to TEOS solubility [34], it is well known that silicon alkoxides such as TEOS are incompatible with water and phase separate when mixed with water, which is why alcohols are used as co-solvents. Therefore, this is indicating that from 5M to 13M of water, there might be a change of stability of the siloxane intermediates or the nascent particles at this water content.

2.6 References

[1] Z. Li, Y. Mu, C. Peng, M. F. Lavin, H. Shao, and Z. Du, "Understanding the mechanisms of silica nanoparticles for nanomedicine," *Wiley Interdiscip. Rev. Nanomed. Nanobiotechnol.*, vol. 13, no. 1, pp. e1658–e1658, Jan. 2021, doi:

10.1002/wnan.1658.
[2] H. E. Bergna, “Colloid chemistry of silica: An overview,” in *Colloidal Silica: Fundamentals and Applications*, 2005, pp. 9–35.
[3] N. A. Hassan, J. N. Hasnidawani, N. Hassan, and S. Surip, “Synthesis of SiO 2 Nanostructures Using Sol-Gel Method,” *Acta Phys. Pol. A*, vol. 129, pp. 842–844, Apr. 2016, doi: 10.12693/APhysPolA.129.842.
[4] K. S. Rao, K. El-Hami, T. Kodaki, K. Matsushige, and K. Makino, “A novel method for synthesis of silica nanoparticles,” *J. Colloid Interface Sci.*, vol. 289, no. 1, pp. 125–131, 2005, doi: https://doi.org/10.1016/j.jcis.2005.02.019.
[5] L. Manna, E. C. Scher, and A. P. Alivisatos, “Shape Control of Colloidal Semiconductor Nanocrystals,” *J. Clust. Sci.*, vol. 13, no. 4, pp. 521–532, 2002, doi: 10.1023/A:1021175612112.
[6] Y. Xia, X. Xia, and H.-C. Peng, “Shape-Controlled Synthesis of Colloidal Metal Nanocrystals: Thermodynamic versus Kinetic Products,” *J. Am. Chem. Soc.*, vol. 137, no. 25, pp. 7947–7966, Jul. 2015, doi: 10.1021/jacs.5b04641.
[7] W. Stöber, A. Fink, and E. Bohn, “Controlled growth of monodisperse silica spheres in the micron size range,” *J. Colloid Interface Sci.*, vol. 26, no. 1, pp. 62–69, 1968, doi: https://doi.org/10.1016/0021-9797(68)90272-5.
[8] T. Yokoi *et al.*, “Mechanism of Formation of Uniform-Sized Silica Nanospheres Catalyzed by Basic Amino Acids,” *Chem. Mater.*, vol. 21, no. 15, pp. 3719–3729, Aug. 2009, doi: 10.1021/cm900993b.
[9] T. Yokoi, Y. Sakamoto, O. Terasaki, Y. Kubota, T. Okubo, and T. Tatsumi, “Periodic Arrangement of Silica Nanospheres Assisted by Amino Acids,” *J. Am. Chem. Soc.*, vol. 128, no. 42, pp. 13664–13665, 2006, doi: 10.1021/ja065071y.
[10] A. K. Van Helden, J. W. Jansen, and A. Vrij, “Preparation and characterization of spherical monodisperse silica dispersions in nonaqueous solvents,” *J. Colloid Interface Sci.*, vol. 81, no. 2, pp. 354–368, 1981, doi: https://doi.org/10.1016/0021-9797(81)90417-3.
[11] Q. Guo, G. Yang, D. Huang, W. Cao, L. Ge, and L. Li, “Synthesis and characterization of spherical silica nanoparticles by modified Stöber process assisted by slow-hydrolysis catalyst,” *Colloid Polym. Sci.*, vol. 296, no. 2, pp. 379–384, 2018, doi: 10.1007/s00396-017-4260-0.
[12] F. J. Arriagada and K. Osseo-Asare, “Synthesis of Nanosize Silica in a Nonionic Water-in-Oil Microemulsion: Effects of the Water/Surfactant Molar Ratio and Ammonia Concentration,” *J. Colloid Interface Sci.*, vol. 211, no. 2, pp. 210–220, 1999, doi: https://doi.org/10.1006/jcis.1998.5985.
[13] Y. Naka, Y. Komori, and H. Yoshitake, “One-pot synthesis of organo-functionalized monodisperse silica particles in W/O microemulsion and the effect of functional groups on addition into polystyrene,” *Colloids Surfaces A-physicochemical Eng. Asp. - COLLOID Surf. A*, vol. 361, pp. 162–168, May 2010, doi: 10.1016/j.colsurfa.2010.03.034.
[14] G. H. Bogush, M. A. Tracy, and C. F. Zukoski, “Preparation of monodisperse silica particles: Control of size and mass fraction,” *J. Non. Cryst. Solids*, vol. 104, no. 1, pp. 95–106, 1988, doi: https://doi.org/10.1016/0022-3093(88)90187-1.
[15] X.-D. Wang *et al.*, “Preparation of spherical silica particles by Stöber process with high concentration of tetra-ethyl-orthosilicate,” *J. Colloid Interface Sci.*, vol. 341, no.

1, pp. 23–29, 2010, doi: https://doi.org/10.1016/j.jcis.2009.09.018.
[16] C. G. Tan, B. D. Bowen, and N. Epstein, “Production of monodisperse colloidal silica spheres: Effect of temperature,” *J. Colloid Interface Sci.*, vol. 118, no. 1, pp. 290–293, 1987, doi: https://doi.org/10.1016/0021-9797(87)90458-9.
[17] T. Matsoukas and E. Gulari, “Dynamics of growth of silica particles from ammonia-catalyzed hydrolysis of tetra-ethyl-orthosilicate,” *J. Colloid Interface Sci.*, vol. 124, no. 1, pp. 252–261, 1988, doi: https://doi.org/10.1016/0021-9797(88)90346-3.
[18] G. H. Bogush and C. F. Zukoski, “Uniform silica particle precipitation: An aggregative growth model,” *J. Colloid Interface Sci.*, vol. 142, no. 1, pp. 19–34, 1991, doi: https://doi.org/10.1016/0021-9797(91)90030-C.
[19] A. Van Blaaderen, J. Van Geest, and A. Vrij, “Monodisperse colloidal silica spheres from tetraalkoxysilanes: Particle formation and growth mechanism,” *J. Colloid Interface Sci.*, vol. 154, no. 2, pp. 481–501, 1992, doi: https://doi.org/10.1016/0021-9797(92)90163-G.
[20] J. K. Bailey and M. L. Mecartney, “Formation of colloidal silica particles from alkoxides,” *Colloids and Surfaces*, vol. 63, no. 1, pp. 151–161, 1992, doi: https://doi.org/10.1016/0166-6622(92)80081-C.
[21] H. Giesche, “Synthesis of monodispersed silica powders I. Particle properties and reaction kinetics,” *J. Eur. Ceram. Soc.*, vol. 14, no. 3, pp. 189–204, 1994, doi: https://doi.org/10.1016/0955-2219(94)90087-6.
[22] S. K. Park, K. Do Kim, and H. T. Kim, “Preparation of silica nanoparticles: determination of the optimal synthesis conditions for small and uniform particles,” *Colloids Surfaces A Physicochem. Eng. Asp.*, vol. 197, no. 1, pp. 7–17, 2002, doi: https://doi.org/10.1016/S0927-7757(01)00683-5.
[23] J. W. Kim, L. U. Kim, and C. K. Kim, “Size Control of Silica Nanoparticles and Their Surface Treatment for Fabrication of Dental Nanocomposites,” *Biomacromolecules*, vol. 8, no. 1, pp. 215–222, Jan. 2007, doi: 10.1021/bm060560b.
[24] M. A. Sharaf, “Preparation of spherical nanoparticles: Stober silica,” *J. Am. Sci.*, vol. 6, pp. 985–989, Jan. 2010.
[25] D. Qi, C. Lin, H. Zhao, H. Liu, and T. Lü, “Size regulation and prediction of the SiO2 nanoparticles prepared via Stöber process,” *J. Dispers. Sci. Technol.*, vol. 38, no. 1, pp. 70–74, Jan. 2017, doi: 10.1080/01932691.2016.1143373.
[26] K. Lee, A. N. Sathyagal, and A. V McCormick, “A closer look at an aggregation model of the Stöber process,” *Colloids Surfaces A Physicochem. Eng. Asp.*, vol. 144, no. 1, pp. 115–125, 1998, doi: https://doi.org/10.1016/S0927-7757(98)00566-4.
[27] K. Lee, J.-L. Look, M. T. Harris, and A. V McCormick, “Assessing Extreme Models of the Stöber Synthesis Using Transients under a Range of Initial Composition,” *J. Colloid Interface Sci.*, vol. 194, no. 1, pp. 78–88, 1997, doi: https://doi.org/10.1006/jcis.1997.5089.
[28] D. L. Green, J. S. Lin, Y.-F. Lam, M. Z. C. Hu, D. W. Schaefer, and M. T. Harris, “Size, volume fraction, and nucleation of Stober silica nanoparticles,” *J. Colloid Interface Sci.*, vol. 266, no. 2, pp. 346–358, 2003, doi: https://doi.org/10.1016/S0021-9797(03)00610-6.
[29] Y. Han *et al.*, “Unraveling the Growth Mechanism of Silica Particles in the Stöber Method: In Situ Seeded Growth Model,” *Langmuir*, vol. 33, no. 23, pp. 5879–5890, 2017, doi: 10.1021/acs.langmuir.7b01140.

[30] X. Zhao, Y. Wang, J. Luo, P. Wang, P. Xiao, and B. Jiang, “The Influence of Water Content on the Growth of the Hybrid-Silica Particles by Sol-Gel Method,” *Silicon*, vol. 13, no. 10, pp. 3413–3421, 2021, doi: 10.1007/s12633-020-00756-z.

[31] R. Lindberg, G. Sundholm, B. Pettersen, J. Sjöblom, and S. E. Friberg, “Multivariate analysis of the size dependence of monodisperse silica particles prepared according to the sol-gel technique,” *Colloids Surfaces A Physicochem. Eng. Asp.*, vol. 123–124, pp. 549–560, 1997, doi: 10.1016/S0927-7757(96)03832-0.

[32] I. A. Rahman *et al.*, “An optimized sol–gel synthesis of stable primary equivalent silica particles,” *Colloids Surfaces A Physicochem. Eng. Asp.*, vol. 294, no. 1, pp. 102–110, 2007, doi: https://doi.org/10.1016/j.colsurfa.2006.08.001.

[33] S. L. Greasley *et al.*, “Controlling particle size in the Stöber process and incorporation of calcium,” *J. Colloid Interface Sci.*, vol. 469, pp. 213–223, 2016, doi: https://doi.org/10.1016/j.jcis.2016.01.065.

[34] M. A. Bourebrab *et al.*, “Influence of the initial chemical conditions on the rational design of silica particles,” *J. Sol-Gel Sci. Technol.*, vol. 88, no. 2, pp. 430–441, 2018, doi: 10.1007/s10971-018-4821-9.

[35] T. Coradin, D. Eglin, and J. Livage, “The silicomolybdic acid spectrophotometric method and its application to silicate/biopolymer interaction studies,” *J. Spectrosc.*, vol. 18, Jan. 2004, doi: 10.1155/2004/356207.

[36] R. Lindberg, J. Sjöblom, and G. Sundholm, “Preparation of silica particles utilizing the sol-gel and the emulsion-gel processes,” *Colloids Surfaces A Physicochem. Eng. Asp.*, vol. 99, no. 1, pp. 79–88, 1995, doi: https://doi.org/10.1016/0927-7757(95)03117-V.

[37] S.-S. Kim, H.-S. Kim, S. G. Kim, and W.-S. Kim, “Effect of electrolyte additives on sol-precipitated nano silica particles,” *Ceram. Int.*, vol. 30, no. 2, pp. 171–175, 2004, doi: https://doi.org/10.1016/S0272-8842(03)00085-3.

[38] I. A. Rahman *et al.*, “Effect of anion electrolytes on the formation of silica nanoparticles via the sol–gel process,” *Ceram. Int.*, vol. 32, no. 6, pp. 691–699, 2006, doi: https://doi.org/10.1016/j.ceramint.2005.05.004.

[39] J. Polte, “Fundamental growth principles of colloidal metal nanoparticles – a new perspective,” *CrystEngComm*, vol. 17, no. 36, pp. 6809–6830, 2015, doi: 10.1039/C5CE01014D.

[40] H. Reiss, “The Growth of Uniform Colloidal Dispersions,” *J. Chem. Phys.*, vol. 19, no. 4, pp. 482–487, Apr. 1951, doi: 10.1063/1.1748251.

[41] C. Ajina, M. A. Fathima Shabana, P. S. Krishnendu, and S. Thomas, “Silica nano-spheres prepared by modified Stober process for colloidal crystal growth,” *AIP Conf. Proc.*, vol. 1849, no. 1, p. 20041, Jun. 2017, doi: 10.1063/1.4984188.

[42] S.-L. Chen, P. Dong, G.-H. Yang, and J.-J. Yang, “Characteristic Aspects of Formation of New Particles during the Growth of Monosize Silica Seeds,” *J. Colloid Interface Sci.*, vol. 180, no. 1, pp. 237–241, 1996, doi: https://doi.org/10.1006/jcis.1996.0295.

[43] K. Nozawa *et al.*, “Smart Control of Monodisperse Stöber Silica Particles: Effect of Reactant Addition Rate on Growth Process,” *Langmuir*, vol. 21, no. 4, pp. 1516–1523, 2005, doi: 10.1021/la048569r.

[44] K. Nozawa, M.-H. Delville, H. Ushiki, P. Panizza, and J.-P. Delville, “Growth of monodisperse mesoscopic metal-oxide colloids under constant monomer supply,” *Phys. Rev. E*, vol. 72, no. 1, p. 11404, 2005, doi: 10.1103/PhysRevE.72.011404.

[45] K.-S. Kim, J.-K. Kim, and W.-S. Kim, “Influence of reaction conditions on sol-precipitation process producing silicon oxide particles,” *Ceram. Int.*, vol. 28, no. 2, pp. 187–194, 2002, doi: https://doi.org/10.1016/S0272-8842(01)00076-1.

[46] K. Do Kim and H. T. Kim, “New Process for the Preparation of Monodispersed, Spherical Silica Particles,” *J. Am. Ceram. Soc.*, vol. 85, no. 5, pp. 1107–1113, 2002, doi: 10.1111/j.1151-2916.2002.tb00230.x.

[47] Z. Lei, Y. Xiao, L. Dang, M. Lu, and W. You, “Fabrication of ultra-large mesoporous carbon with tunable pore size by monodisperse silica particles derived from seed growth process,” *Microporous Mesoporous Mater.*, vol. 96, no. 1, pp. 127–134, 2006, doi: https://doi.org/10.1016/j.micromeso.2006.06.031.

III. Surface and Core Functionalization of Silica Nanoparticles

"We shall not cease from exploration, and the end
of all our exploring will be to arrive where we started
and know the place for the first time"
T. S. Eliot

Chapter 3

Synthetic Strategy for Preparing Silica-Based Nanoparticles with Functional Properties for Biological Imaging

In the past decades, the increasing need to understand the biological processes and the influence of therapeutic and diagnostics compounds inside biologic organisms, led to an increasing search for bioimaging systems at the nanoscale. These structures need to be developed with the intention of overcoming the current limitations of the directly used of parhmaceutical or imaging-targeting molecules, such as biocompatibility, toxicity or internalization problems that might limit their application in living systems or tissues [1]. In recent years, functional and structured hybrid nano-scale materials arises as a solution, because they can confer the ability to overcome biological barriers, the ability to deliver hydrophobic poorly water-soluble drugs and biologics, encapsulating or bonding organic tag molecules, such as ``fluorescent dyes´´ and the potential ability to selectively target a preferred site in the body by the appropriate functionalization [2]. In this context, silica particles (SiO_2 NPs) has been gained higly interest in the fields of nanomedicine for gene or drug delivery systems, in cancer therapy, for protein immobilisation and for imaging purposes, developing fluorescent imaging probes by bonding organic dyes into inorganic silica matrix [3]. Their stable chemical structure, low cost of the material, large surface to volume ratios, ease of surface modification and biodegradability, make silica an attractive candidate for the aforementioned applications [4]. However, a key prerequisite for every possible biological application is the proper surface or core functionalization of such nanoparticles, which determines their function and their colloidal stability with the environment [5]. In order to synthetize well-designed multifunctional silica nanostructures, the development of silica-based hybrids particles at the nanoscale by the sol-gel method has been explored [6]. The sol-gel method, is a wet chemical process for making silicon oxide-based hybrid materials starting from molecular hydrolysable precursors, via hydrolysis and condensation reactions to form colloids, as commented in previous chapters [7]. The very mild reaction conditions, particularly the low temperature and pressure of the

reaction, the broad solvent compatibility and the size control achieving uniform nanostructures, make it an attractive strategy to core-loading or surface functionalize the SiO_2 NPs [8]. As explained in the Chapter 1, for the preparation of functional Si-hybrids, the sol-gel method normally use a polymerizable metallo-organic precursors, such as TEOS of formula $Si(OC_2H_5)_4$, together with the functional trialkoxysilanes of formula R``Si(OR`)$_3$, also called silane-coupling agents, bearing an organic chemical functionality in their structure as a linker, for tailoring both phases and controlling the interfaces [9]. The most common functional trialkoxysilanes molecules and their use, were presented in detail in the **table 1.1**, from the Chapter 1 of this dissertation. However, the synthetic sol-gel strategy for developing the functional hybrid structure will depend on the final application and the nature of the selected functional groups, because it will possible to tailor the surface charge of NPs, (e.g. NH_2 groups), grafting inside or outside of the structure active functionalities and molecules, such as ¨fluorophores¨ and surface capping with PEG or PVP for avoid premature release of entrapped pharmaceuticals or avoid non-specific binding of the particles, once dispersed in different chemical or biological environments [10].

3.1 Synthetic Methods for Functionalization Silica Nanoparticles (SiO_2 NPs)

3.1.1 Surface Grafting the Colloidal Amorphous Silica

On one hand, the surface engineering of SiO_2 NPs is one of the most widely used strategies to diversify their functionality and improve their biocompatibility [11] . Most studies have focused on modifying the surface chemistry by various functional groups, (e.g amino groups (NH_2), carboxyl functionality (COOH) or polyethylene glycol (PEG) to endow the silica with a stealth properties, increasing cellular trafficking, controllable cargo release, traceability and increased binding affinity to deliver molecules to specific cell and tissue targets [12]. Furthermore, by engineering the surface charge and hydrophobicity, their biological behaviours, such as enhanced cellular uptake with endosomal escape, biodistribution and immunostimulatory activities, can also be controlled [13], [14]. Therefore, to graft the SiO_2 NPs surface, the most convenient strategy performed is by silanization reaction using the sol-gel method, which allows the surface coverage by creating a covalent siloxane (-Si-O-Si-) bonds using silane-coupling agents [15]. However,

this strategy can be performed by using two different approaches: the direct method (also known as co-condensation) or the post-grafting method (known as post-functionalization) [16]. The direct method allows the functionalization in a short time and involves the one step synthesis ¨one-pot¨ between the metallo-organic silica precursor with one or more organofunctional alkoxysilanes through the sol-gel process. The advantages of this method is that produce a homogeneous distribution of the functional groups, while the disadvantage is that it produces materials with a less ordered structures with the strain to properly control the final diameter [17], [18]. On the contrary, the two-steps synthesis procedure, the functional groups are attached to the surface of the nanoparticles, but the synthesis and functionalization are done at separate stages. This method allows a better control of particle size, morphology and pore diameter [13]. However the distribution of the functional groups on the pore surfaces is generally believed to be non-uniform, with most of the groups attached around the particle outer surface [19]. Therefore, a strict control of the synthetic conditions allows achieving more homogeneous surface coverage [20] .

In this regard, surface modifications by post-functionalization of colloidal silica has been explored [21]–[23], the general scheme process of the surface functionalization is shown in **figure 3.1**.

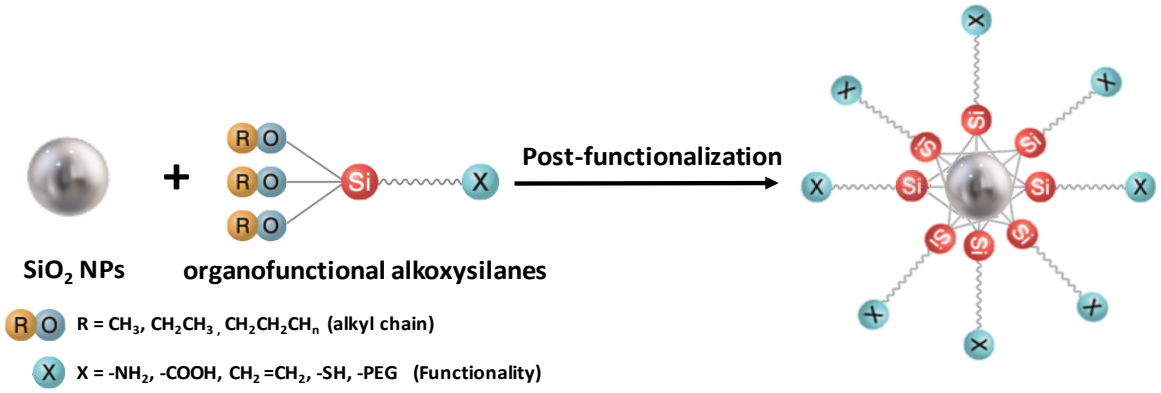

Figure 3.1 Graphic representation of the post-functionalization procedure of the SiO_2 NPs with organofunctional alkoysilanes (silane coupling agents) by a modification of the Stöber method.

In the reported literature, to modify the highly negative surface charge of silica, three different categories of coating agents having cationic centers are commonly explored: cationic polymers, basic amino acids and amine containing molecules (silanes) [24] . Cationic polymers present the drawback of using high temperatures and radical polymerizations in order to coat the silica. If the polymer is physical adsorbed, are thermally and solvolytically unstable due to the relatively weak van der Waals forces or hydrogen bonding that anchors them to the surface. In addition, the grafting densities are low because of steric crowding of reactive sites by previously attached polymers [25]. Amino acids, in the aspect of cationic charge density, are not considered effective coating materials as they retain the zwitterionic property in a wide range of pH values (pH 4–8), and only a few amino acids have basic functional groups [26]. Therefore, the chemical modification with organofunctional alkoxisilanes molecules containing amino groups, have been reported [27].

Among the silane-coupling agents, the 3-aminopropiltriethoxysilane (APTES) is one of the most widely explored by many researchers. This molecule is considered to induce a positive surface charge by forming siloxane bonds with the silica surface and leaving the amine ends available [28]. This system undergoes hydrolysis and self-condensation before deposition on the surface due to the alkoxy molecules are hydrolyzed in contact with water. Then, the silane molecules are deposited on the silica surface through formation of siloxane bonds between the silanol groups and hydrolyzed silanes with the release of water molecules [29]. Moreover, the APTES molecule can react with the succinic anhydride by ring-opening reaction to form a carboxylate acid-modified silane, the (4-(aminopropyltriethoxysilane)-4-oxo-butanoic acid) [30], which can be used to graft the surface of the silica with COOH groups. However, the ability to systematic tune the surface charge and reliable control the quantity of grafted functional groups in the functionalized silica nanoparticles with different isoelectric points, while maintaining particle size, avoiding agglomeration or flocculation during the purification or phase transfer (e.g., ethanol to water), are preferred, using one-pot simple-straight methodologies, in order to applied silica particles with positive or highly negative surface charge, during biological testing.

3.1.2 Core Loading the Colloidal Amorphous Silica

On the other hand, the loading of SiO_2 NPs with relevant molecules, such as ¨fluorescent organic dyes¨ have been studied, developing a core-shell architectures, in order to create more robust emitters for biological testing [31]. Silica is an interesting material, because provides a chemically and mechanically stable vehicle for fluorescent probes, which can protect the encapsulated dye from external perturbations, while exposing a biocompatible and easily functionalized surface to the environment and in some cases enhancing the photophysical properties of the encapsulated dyes [32] . in addition, silica is a hydrophilic material that is inert (biocompatible), transparent to visible light and is not involved in energy- and electron-transfer processes [33]. This kind of hybrids structures with increased functionality are usually prepared by two chemical approaches: reverse microemulsion method [34] or sol–gel synthesis (by a modification of the Stöber method) [35], as shown in **Figure 3.2**.

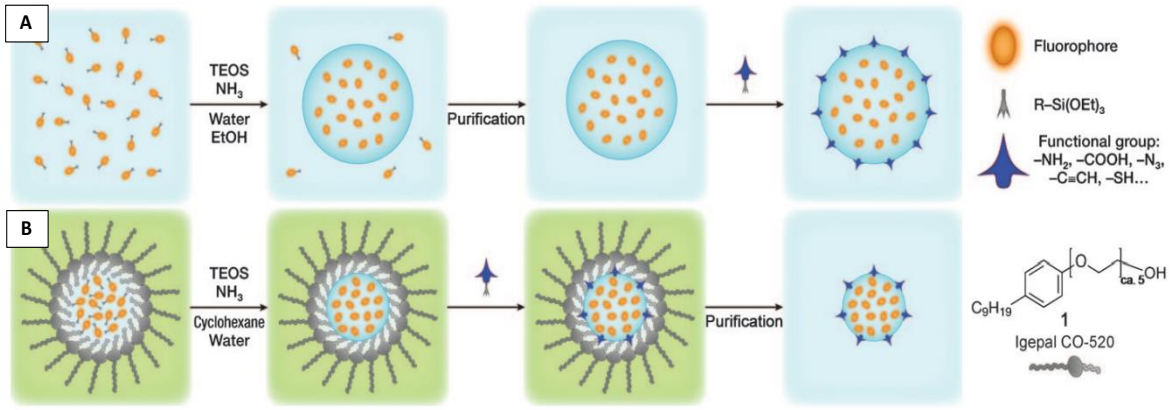

Figure 3.2 Graphic representation of the two synthetic strategies for incorporation organic dyes molecules to SiO_2 NPs., (A) Sol–gel synthesis by a modification of the Stöber method and (B) the reverse microemulsion method. Taken from reference [33].

The Reverse microemulsion techniques rely on the controlled aqueous environment within surfactant-confined micelles in a non-polar solvent to create monodisperse spherical colloids. Such nanoparticle syntheses were extensively explored by Arriagada and Osseo-Asare in the 1990s [36]. However, using this strategy present several drack backs, such as lack of covalent attachment of the fluorophore to the silica matrix, dye leaching over time, increasing background signal and exposing the dyes to their environment. In addition, the use of surfactants needs an extensive cleaning to remove the

excess of surfactant molecules before any biological application. On the contrary, the Stöber method, based on the sol–gel chemistry of silicon alkoxides, involves the basic hydrolysis and condensation of tetraethoxysilane in ethanol solution to create monodisperse particles. The first author in modify the Stöber method to covalently incorporate organic dyes in to the SiO_2 matrix, were A. Van Blaaderen and A. Vrij in 1992 [37]. They were able to covalently core-loaded with fluorophores molecules (in this case, fluorescein isothiocyanate (FTIC) into the silica NPs by coupling them with to reactive organosilicates during the polymerization. The covalent coupling involves the incorporation of amino-reactive dyes into silica particles, using a silane agent, such as 3-aminopropyltriethoxysilane (APTES) to form a dye-APTES complex as precursor, and then together with tetraethoxysilane (TEOS) are simultaneously hydrolyzed and condensed to form silica particles. However, the particle sizes reported remained in the hundreds of nanometres to micron regime, which are useful for many applications such as the study of colloid dynamics and photonic crystals, but they may be too large to be truly effective probes for biology.

Considering these aspects, in the following chapter, a systematic surface charge modification of the silica nanoparticles is presented by a modified sol-gel method. To modify the surface, particles were first synthetized following the well-known Stöber method and subsequently were covalently grafted by silanization using the silane-coupling agents 3-aminopropiltriethoxysilane (APTES) by a post-functionalization synthesis, in order to achieve a highly positive surface charge into the silica particles. Furthermore, the degree of amine grafting on the surface of the functionalized-silica cores, were determined by the ninhydrin assay and the particles were well characterized by dynamic light scattering (DLS), measuring the zeta potential as function of pH in water and by Fourier-transform infrared spectroscopy (FT-IR) to see the characteristic stretching, bending and twisting bands of the amino functional groups. On the other hand, fluorescent SiO_2 NPs having a core-shell architecture were prepared by the modified Stöber method, using different organic dyes molecules (FITC, rhodamines RBITC, TRITC and Alexa Fluor® 350 NHS Ester) together with an amine-containing silane (APTES) as a crosslinker by a thiourea and carboxamide-linkage, to prepare an organic dyes-silane coupling agent (complex), for the subsequent a co-polymerization with the silica precursor in the sol-gel synthesis. The optical properties of

the particles were characterized by UV-Vis, electron microscopy (STEM), DLS and photoluminescence spectroscopy. Finally, as proof-of-principle, we developed a multilayer optical sensor with dual-emission properties, made of SiO_2 nanoparticles having a core-shell architecture, incorporating two different fluorophores, one in the core (RBITC) and other in the outer external layer (FITC) as a fluorescent probe sensor on the nanoscale for in-vitro analysis in physiological conditions using a cell line.

3.2 Precise Surface Charge Control of the SiO_2 NPs: A Post-Synthetic Modification

The amine-functionalization is very popular for modification the SiO_2 NPs surfaces. This conjugation is very useful because allows perform binding studies. For instance, the amino group can be easily coupled further with carboxyl-containing molecules through carbodiimides EDAC coupling, or with amine-reactive esters, such as N-hydroxysuccinimide (NHS) and maleimide-functionalized, water-soluble linkers strategies for crosslinking peptides and thiol-containing proteins and immobilizing macromolecules for use in numerous protein and cell biology detection and analysis methods [38]. In addition, the NH_2 groups also allows the covalent binding with dyes molecules bearing isothiocyanate (ITC) groups by the thiourea linkage for the preparation of biomolecular probes [39]. Due to their positive surface charge, amine-SiO_2 NPs can be coupled strongly with DNA to build stable gene transfer vectors with potential applications in gene therapy [40]. The amines at the colloid surface can be protonated at acidic pH to yield particles with a large positive zeta potential. Ninhydrin reagent is often used to detect residual free amines in the field of biochemical synthesis [41]. The ninhydrin react with the primary or secondary amines of the nanoparticles in a weakly acidic solution yielding a bright purple complex known as Ruhemann´s purple that is determined at 570nm (reaction showed in **Appendix B1**) [42]. As can be observed, given the variety of potential applications of aminated silica-based nanomaterials, it is important to assess their hazards for humans [43]–[45]. Although SiO_2 NPs are generally considered to be nontoxic, some adverse effects have been described in cell culture as well as in animal models, such as cytotoxicity, hemolysis and inflammation [46]–[48]. Toxicity most likely results from strong interactions between silanol groups on the unmodified silica surface and biological membranes composed of lipids and proteins

[49]. Amine-modified amorphous SiO_2 NPs were shown to be less toxic than pristine SiO_2 NPs in vitro and in vivo. [50], [51] However, contradictory reports also exist [52], [53], that revealed that cationic NPs are considered to present potential adverse effects arising from cellular and tissue interactions and immune stimulation, by a mechanism underlying their toxicity, such as the induction of inflammatory response [54].

In order to modify the surface charge of colloidal silica while maintaining the particle size and size distribution, first, pristine SiO_2 NPs particles of approximately 30nm and 50nm in size, were synthetized following the modified sol-gel Stöber method (experimental section, **chapter 5. Section 5.2.2.1**), and their physicochemical characterization were done by STEM and DLS, as shown by the **figure 3.3.**

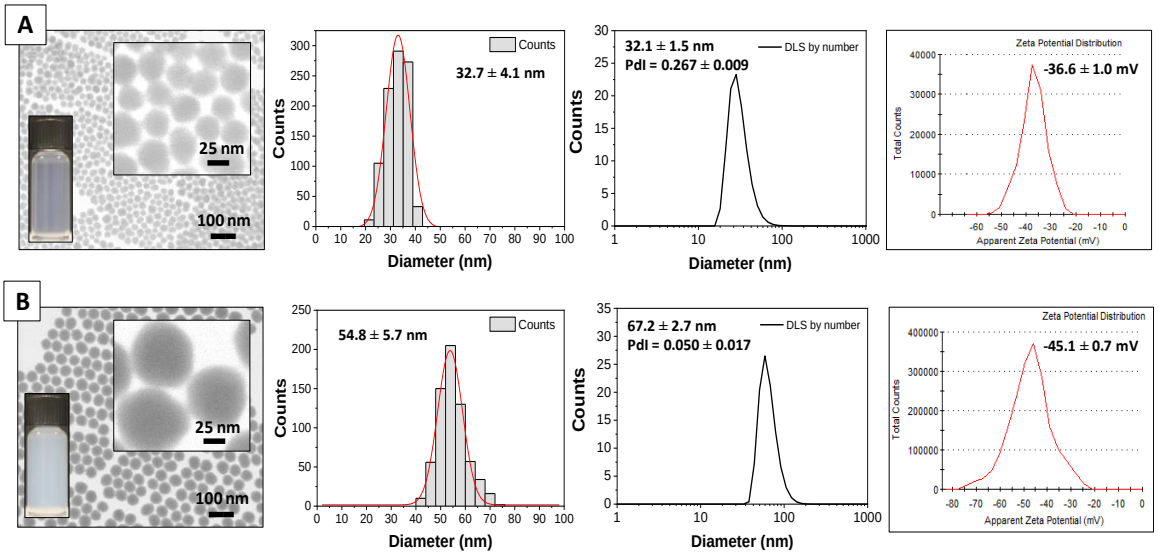

Figure 3.3 Characterization of the pristine SiO_2 NPs synthetized by the modified Stöber method. From left to right, electron microscopy image by STEM mode, calculated mean size and SD, hydrodynamic size distribution by number and zeta potential distribution. For the pristine SiO_2 NPs of (A) 30nm and (B) 50nm. The SD was calculated measuring at least 300 particles by image J software and for DLS size the standard deviation was calculated with at least three independent measurements. ZP was measured in pure water at pH 8.50 with a conductivity below 1µs/cm.

As shown by the **figure 3.3**, the morphology of the synthetized SiO_2 NPs was almost spherical. The calculated mean size and size distribution were 32.7 ± 4.1 nm and 54.8 ± 5.4 nm, respectively. These results were in agreement with the hydrodynamic size by number of 32.1 ± 1.5 nm and 67.2 ± 2.7 nm, respectively. The DLS values were slightly higher, but is expected because rely on the Brownian motion of the NPs for calculation. The zeta potential indicates that both particles presented a good colloidal stability (-36.6 ± 1.0 mV and -45.1 ± 0.7 mV) after purification by dialysis in water. Both pristine silica NPs presented

highly negative values, due to the deprotonation of the silanol groups (Si-O-) on surface. The pH of the solution was around 8.00 after purification.

Once the silica particles were prepared, subsequently were performed a post-functionalization with the molecule 3-aminopropiltriethoxysilane (APTES), by carefully adding directly to both SiO_2 NPs colloidal solution of 30 nm and 50 nm in size, a fixed scalar concentration of APTES ranging from 0.35mM to 14.5mM, for grafting with amino functional groups the surface of the particles. This approach was done in order to systematically control the positive surface charge by tuning the NH_2 groups density. The reactions were left under stirring at 500 r.p.m. for 24h at room temperature, for conjugation. Once the functionalized particles were purified by one cycle of centrifugation (10.000g for 10 minutes) and by dialysis against water overnight, the surface charge for all APTES conditions were characterized measuring the zeta potential ZP by DLS as a function of medium pH in water. The pH of every solution was adjusted by titration using diluted HCl 10mM or NaOH 10mM maintaining the conductivity below 1 µs/cm3, in order to avoid masking the surface with counter ions in solution, results showed in **figure 3.4**.

The surface charge characterization of both silica particles is showed in **figure 3.4**. Our results showed that the surface modification did not affect the particle size and morphology of the silica but altered effectively the surface charge. With our strategy, it was possible to systematically modify the zeta potential of both silica particles, increasing the silane coupling agent APTES concentration during the conjugation. The silica surface modification leads to a different titration curve of the pH-dependent zeta potential values.

As can be observe in **figure 3.4-C**, the zeta potential of the aminated 50nm silica can be tuned from 47.7 ± 2.4 mV to -45.1±0.7 mV, changing the pH of the media from 3.0 to 10, respectively. Similarly **figure 3.4-D**, revealed the same trend for the ZP of the aminated 30nm silica, modified from 46.3± 2.6 mV to -40.3±0.3 mV, in the same interval of pH. These results indicate the successfully surface charge modification of both particles, from the highly negative values towards highly positive ones, in which, both of the SiO_2-NH_2 NPs displayed ZP curves depending the concentration of functionalization and pH of the dispersed medium. At low pH values, most of the negative groups (silanol Si-OH) were hydrated by the abundant H+ ions in solution, so that the surface was mainly positive. In

addition, the surface of the silica particles became highly positively charged, because the NH_2 groups were fully protonated (NH_3^+).

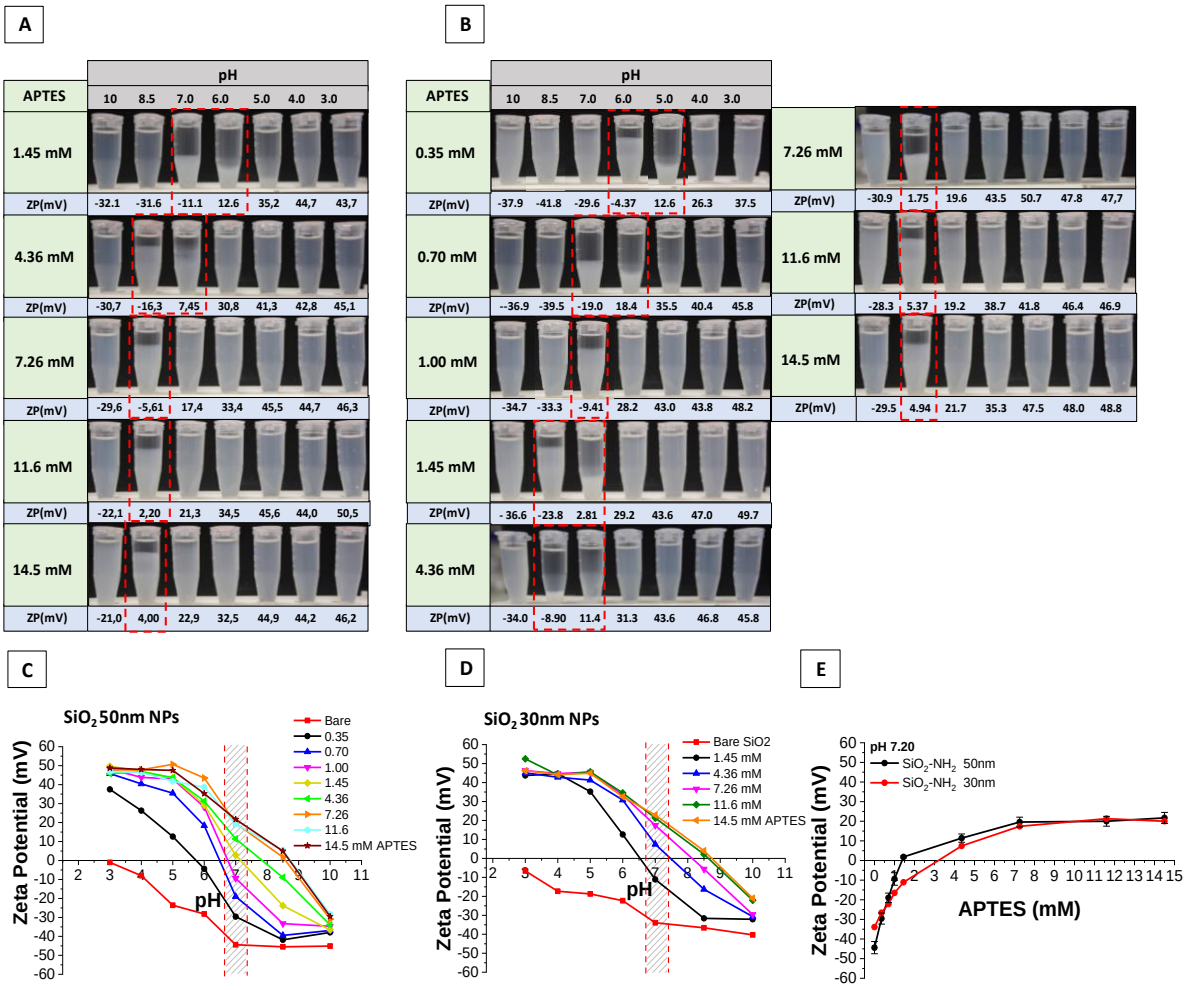

Figure 3.4 Graphical representation of the surface charge characterization for both 30nm and 50nm SiO_2 NPs after post-functionalization with different APTES concentrations (0.35mM to 14.5mM), recording the Zeta Potential (ZP) as a function of pH of the reaction. Colloidal images after functionalization for (A) 30 nm and (B) 50nm SiO_2–NH_2 NPs. The red dotted lines highlight the ZP in which particles flocculate because of the poor colloidal electrostatic stabilization. ZP as a function of pH for the aminated (C) 50nm and (D) 30nm SiO_2–NH_2 NPs. The red dotted line highlights the ZP at neutral pH. (E) Comparison of ZP as a function of APTES concentration at neutral pH 7.00 in water for both SiO_2 NPs. DLS experiments was calculated with at least three independent measurements in water. Conductivity was kept below 1 µs/cm3.

In contrast, under alkaline conditions, the amino groups were at neutral charge and the negative values were attributed to the deprotonated surface silano groups ($Si\text{-}O^-$). This systematic strategy for grafting different densities of amino groups is highly important because may exhibit important roles in protein-particle interactions. Authors have

reported that proteins can be adsorbed by electrostatic interactions between charged amino acid residues and -OH groups of the silica surface. This attractive interaction competes with the Coulombic repulsion. Therefore, at the isoelectric point where the overall charge vanishes, the protein−silica interaction will be dominated by van der Waals forced, as well as polar interactions forming a dense packing of molecules, called protein corona [55]. These findings may suggest that adsorption behavior of the functionalized particles with proteins can be altered as a function of pH.

Because one of our main interests was to keep a ZP positive value at neutral pH, our results showed that at fixed pH of 7.00, the optimal APTES concentration needed to maintain the positive ZP at the silica surface, were beyond 7mM of concentrations, achieving a value around ±22mV in water, as can be observe in **figure 3.4-E**. We conclude that it was possible to systematically modify the ZP at neutral pH for SiO_2-NH_2 50nm NPs. However, using an APTES concentration beyond 7mM, the ZP values remained comparable, suggesting a saturation of the silica surface. The same experiment was also conducted for the 30nm aminated silica for comparison, revealing a similar trend in the ZP curve, until saturation at APTES concentration of approximately 10 mM. This small difference in ZP value obtained between the 30nm and 50nm, can be explained due to the curvature effects, in which some reports describe that particle's surface charge also depends on its size [56]. This dual behavior of the surface ZP of the NPs depending on pH is in agreement with the described in the literature which denote that when a particle is immersed in an aqueous medium, it becomes charged due to protonation/deprotonation on their groups on the particle surface [57]. Thus, tuning the surface charge from negative to positive opens a wide window for biological applications. In addition, the transport behavior of nanoparticles highly depends on the particle's surface charge properties. For instance, the process of nanoparticle translocation through a nanopore depends on the surface charge densities of the particle, because they are mainly governed by the competing effects of electrophoresis, hydrodynamic drag acting and electro-osmosis [58]–[60]. M. Niknam Hamidabad et al [58] showed that there is strong electrostatic adsorption when negatively charged microspheres particles go through positively charged nanochanel [61]. The isoelectric point (IEP) of a colloidal nanoparticle is the pH at which the sample has a neutral

zeta potential or surface charge of zero. At a neutral charge, the silica particles have very low colloidal stability and are very prone for flocculation (the images of flocculated NPs close to IEP were shown in **figure 3.4-A-B**). Moreover, as shown in the **figure 3.4-C-D**, revealed that it is possible to fine-tune the isoelectric point (IEP) of the aminated silica, adjusting the concentration of silane coupling agent during the post-functionalization. The results are shown in **table 3.1**:

Table 3.1 Isoelectric point (IEP) of the aminated SiO_2 NPs as a function of the APTES concentrations

APTES (mM)	**SiO_2–NH_2 NPs 50nm (IEP)**	**SiO_2–NH_2 NPs 30nm (IEP)**
Pristine	3.0	<3.0
0.35	5.7	Not measured
0.70	6.4	Not measured
1.00	6.8	Not measured
1.45	7.2	6.5
4.35	7.9	7.4
7.25	8.6	8.2
11.5	8.7	8.6
14.5	8.8	8.7

On one hand, for the non-functionalized silica, the IEP was around 3.0, very close to the reported in the literature of pH 2.5 [62]. Therefore, if the pristine SiO_2 NPs get close to that pH, they displayed a poorly colloidal stability. This behavior is typical for silica nanoparticles due to the weakly acidic silanol groups on the silica surface at this pH [63]. Therefore, the pristine silica particles have a good stability (ZP around -30mV) at pH values above 5.0. On the other hand, the synthetized animated silica particles, revealed different isoelectric points in the range of IEP= 5.7-8.8 as a function of pH, depending on the surface concentration. These values were in agreement with the reported in the literature for APTES molecules, using a concentration of maximum 10mM [64]. Using higher APTES concentration (beyond 11.6mM), resulted in any modification of the IEP, suggesting surface coverage saturation with APTES molecules, as previously showed.

It is important to highlight that the surface modification with amino groups also influences the charge stabilization of the silica as a colloid. Increasing numbers of amino

groups might contribute to amine-silanol hydrogen bonding, thereby enhancing the inter-particle attractive forces and the agglomeration/floculation [26]. The maximum ZP value obtained in the pH range close to physiological conditions (pH of 7.2), was found to be the around ±22 mV. Particles with lower ZP values, resulted in having lower colloidal stability, thereby showing flocculation in the bottom of the vials, as shown in dotted red lines in the **figure 3.4-A-B**. These results may be explained due the fact that at certain pH, happens to be very close to the isoelectric point of the amine functionalized silica, as a results, SiO_2-NH_2 NPs flocculated and were felled out of the solution due to there is no driving force on the surface of the nanoparticles to keep them apart. Thus, in order to maintain the aminated SiO_2 nanoparticles colloidal stable in solution, it is necessary to suspend them in a solution with a pH that is far away from their isoelectric point. One way to overcome the flocculation of NPs, were done by dispersing the aminated particles, in milli-q water at pH 5, for protonating the NH_2 groups, allowing the electrostatic repulsion achieve a high electrostatic stability. Nevertheless, for longer storage times, anhydride ethanol suspension is reported to preserve the integrity of the amine functional groups on the surface, due to the silica has high solubility in water (siloxane bonds Si-O-Si cleavage), therefore the silica surface network will partially dissolve, leading to the detachment of some of the amino functional groups [65].

3.3 Quantification the Degree of Amino Groups onto the SiO_2 NPs surface

The degree of amine grafting of the SiO_2-NH_2 50nm NPs, was determined by the ninhydrin assay [66]. The ninhydrin reaction is basically a redox reaction, in which the ninhydrin acts as an oxidizing agent, getting reduced. It reacts with the primary or secondary amines grafted on the nanoparticles in a weakly acidic solution, yielding a di-ketohydrin product which forms a bright coloured complex, known as Ruhemann´s purple, that gives to the solution a deep purple coloration, that is determined at 570nm, (Mechanism showed in **Appendix B2**). An important feature of the ninhydrin strategy is that is possible to separate the blue colored supernatant from the NPs in solution by centrifugation, because of the scattering interference of the indecent light. Thus, the purple complex absorption can be measured without interference from scattering by Uv-

Vis. The preparation of the calibration curve and the paticles measurements were described in experimental section, (**Chapter 5, section 5.2.3**).

In this regard, for the quantification of the grafted surface amino groups on the passivated silica particles of 50nm, was done by UV−Vis spectrometry. First, a calibration curve was built using aminopropiltriethoxysilane (APTES) as the source of amino groups, using a concentration ranging from 0.1mM to 1.00 mM (as shown in **figure 3.5**). The maximum intensity of the peaks obtained was measured at 577nm due to the formation of Ruhemann´s complex. The curve presented a linear behavior in accordance with Beer-Lambert's law and the obtained fitting equation was Y= 1.90708X-0.1595 with a coefficient of determination of r_2 =0.99907. With the obtained data from the calibration curve, it is possible to convert from mmol/L (mM) of APTES to number of amino groups per nm^2 on the silica surface (NH_2/nm^2), suing Avogadro's number ($6.02x10^{23}$).

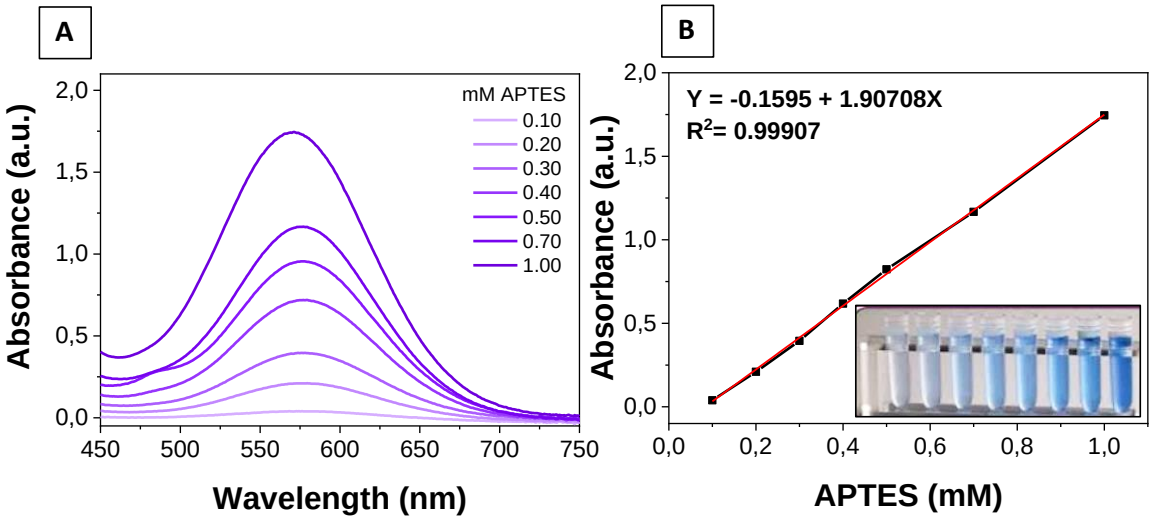

Figure 3.5 Graphical representation of calibration curve using different aminopropiltriethoxysilane (APTES) as the standard source of primary amino groups. (A). UV-Vis spectra of scalar standard APTES concentration with ninhydrine, from 0.10mM to 1.00mM). Maximum absorbance recorded at wavelength 577nm. (B) Calibration curve as a function of APTES (mM), the given equation displaying a good correlation of the data.

Once the calibration curve was built, the aminated 50nm SiO_2 NPs functionalized using different APTES concentrations (from 0.35mM to 14.5mM), prepared in the previous section, were purified and further reacted with the ninhydrine reagent for determination the amino surface groups. The colored purple complex product was separated by centrifugation and the absorbance was recorded at 577 nm using a UV-Vis

spectrophotometer (Extended amino calculations are explained in **Appendix B3**). Our results are shown in **figure 3.6.**

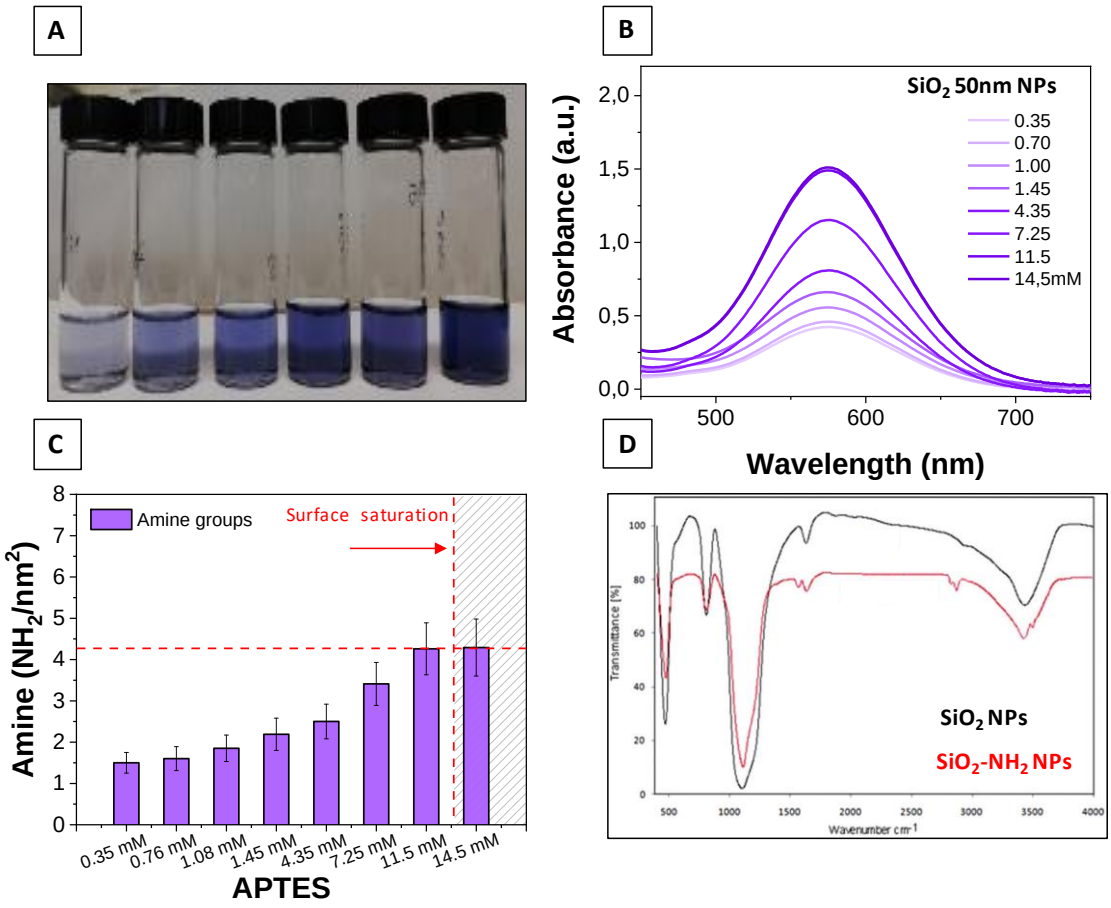

Figure 3.6 Graphical representation of the amino content analysis of the 50nm SiO_2-NH_2 NPs with different APTES concentrations from 0.35mM to 14.5mM. (A) Colloidal image of the NPs after exposure to ninhydrin essay. Characteristic purple color was revealed. (B) UV-Vis absorption spectra of the different SiO_2-NH_2 NPs after ninhydrine essay. Maximum absorbance peak at 577nm. (C) Amine groups content per surface area (NH_2 molecules/nm^2) as a function of APTES concentration. The red dashed line and shaded area represents the maximum grafted density with a value 4.0 NH_2 molecules/nm^2. (D) FT-IR analysis of the SiO_2-NH_2 NPs functionalizes with 11.5mM APTES. The red line represents the spectra after amino functionalization. If we consider that one APTES molecule occupies maximum 3 hydroxyl groups of the silica surface, theoretically, the maximum surface coverage would yield a value of 2.0 APTES molecules/nm2 (taking into account the OH-group surface density of 4–6 OH/nm2) [67].

As shown in **figure 3.6-A-B**, the ninhydrin analysis work well in determining the number of amino groups on the SiO_2 surface, according to the obtained results. The number of amine molecules per surface area (NH_2 molecule/nm^2) grafted on the aminated-silica NPs were calculated by dividing the quantity of amino molecules in solution (QAM), calculated by the calibration curve by total surface area (SA) of the 50nm NPs (detailed

calculations are showed in **Appendix B3**). Our results in **figure 3.6-C**, showed that when the APTES concentration used were carefully increased, the surface density per surface area on the surface of the aminated-silica also increased from 1.5 to 4.29 NH_2 molecule/nm^2. These results suggest that amine groups have been grafted on the NPs surface in a systematically manner, controlling the concentration of amino-silane coupling reagent and the experimental conditions. Although the increment did not follow a linear behaviour, these results are in agreement with several reports, in which by using different essays to determine the amount of grafted amine groups on the surface, as shown in **table 3.2**:

Table 3.2 number of amine molecules per surface area (NH_2 molecule/nm^2), into the SiO_2 NPs reported in the literature.

Author	Grafting strategy	Material SiO_2 size	NH_2 (molecule/nm^2)	Method/Reference
Hsu-Tung et al	Post-functionalization	Sphere, 40nm Sphere, 80nm	4.4 6.1	Ninhydrin, [68]
Erick soto et al	Post-functionalization	Sphere, 100nm	4.0	Ninhydrin, [69]
Filip Kunc et al	Post-functionalization	Sphere, 20nm Sphere, 100nm	1.4 9.8	Ninhydrin, [66]
Fadeev et al	Post-functionalization	Silicon oxide wafer, 100mm	5.0	XPS, [70]
Krishna et al	Post-functionalization	Amorphous fumed, 14nm	6.0	^{29}Si NMR, XPS, [39]
Hsiao et al	Post-functionalization	Sphere, 50nm	2.8	Fluorescaminen, [26]
Schiestel et al	Post-functionalization	Sphere, 100nm	1.80	Fluorescence biotin-4-fluorescein ,[71]
Hak-Sung Jung et	Post-functionalization	Sphere, 100nm	1.3	Fluorescence rhodamine (RBITC), [72]

All these reported values were in agreement with our previous results of 4 amino NH_2 per NP. However, as shown in **Figure 3.4-C**, despite using increasing APTES concentrations for the post-functionalization of the 50nm silica particles, the grafted number of amino groups reach saturation level using 11.5mM of APTES. These results indicate that the surface of the SiO_2 NPs is completely covered. In addition, the number of

amino groups 4.0 NH_2/nm^2 found were higher than the theoretical value of maximum yield of 2.0 NH_2/nm^2

This result can be explained by kind of several factors, such as orientation packing density, chemical reactivity, the portion of the amines that may be accessible for conjugation and the analytical technique for amino analysis. Some authors reported that the production of aminated silica present challenges such as: i) polymerization of the initial silane in solution, ii) the possibility of forming heterogeneous multilayers on the surface in the presence of excess silane, and iii) the lack of stability of the aminated surfaces [72]–[74]. Hydrolysis is particularly problematic with short aminoalkyl silanes such as aminopropyl triethoxysilane (APTES), which have been shown to undergo self-catalyzed amine-mediated cleavage [59]. In addition, different types of bonding/interaction between aminopropylethoxysilane molecules and silicon oxide substrates have been reported [73]. The amine groups can catalyze, inter- or intramolecular, the reaction between silane molecules and surface silanol groups to form siloxane bonds [74]. For the same reason, aminoalkoxysilanes are more reactive than alkylalkoxysilanes toward water, which can cause uncontrolled polymerization/oligomerization of aminosilanes in solution.

Additionally, amine groups can hydrogen bond with surface silanol groups. Thus, covalently attached aminosilane layers typically have low grafting densities due to the presence of vertically as well as horizontally positioned silane molecules. In addition, Filip Kunc et al. [75] found that the amine contents measured by a ninhydrin colorimetric assay were typically ∼20% lower than those measured by analytical ^{29}SiNMR. These results are consistent with only ninhydrin react accessible amines. Li et al. [76] reported similar findings. They found that despite the majority of the amines are located on the surface of the NPs, the obtained lower ninhydrin values suggest that some amines are not accessible to the reagent, possibly due to crowding on the surface at close to monolayer coverages, surface multilayers, or locations in interior pores of the microporous silica. Soto-Cantu et al. [69] measured the surface density at low and at high amino group concentrations using APTES and MTMS for surface modification of silica. They reported that at low fraction of APTES, values are in agreement with the expected for a monolayer of about 4 functional groups per nm2, while at high concentrations bilayers or multilayers of APTES and MTMS are formed resulting in higher-than-expected measured amino group concentrations.

Further characterizing the amino silica particles were done by infrared spectroscopy, as shown in **figure 3.6-D**, the FT-IR characterization displayed the spectrum of the SiO_2 NPs before and after APTES functionalization. We can observe the characteristics (fingerprint) bands of the pristine silica NPs at 473-810 and 1050 cm^{-1} assigned to Si–O–Si stretching and Si–O–Si bending, respectively. The absorption bands at 1112 cm^{-1} are due to the siloxane vibrations of (SiO)n groups and the peaks at 3443 and at 1634 cm^{-1} are attributed to O–H stretching band of the surface of silanol groups and free water adsorbed on silica surface through hydrogen bonding [77]. After amino modification of silica nanoparticles with APTES the new peaks can be assigned as follows: the bands at 2870 and 2824 cm^{-1} are due to asymmetrical and symmetrical stretching vibrations of CH2 groups, the new band at approximately 1564 cm^{-1} is due to N–H bending vibration of amine groups indicated the presence of NH_2 groups. Moreover, the peak at 3501 cm^{1} can be assigned to N–H stretching vibration [78], but is expected to overlap with the stretching vibrations of O-H groups at ~3500 cm^{-1}.

3.4 Core-Loading the SiO_2 NPs for Preparation Silica-Based Fluorescent Probes

Nowadays, it is well known that the directly use of traditional fluorescent dyes, such as fluorescein, rhodamine, Cy3 and Cy5 for bioimaging applications, present clear disadvantages, due to their high photobleaching, low stability and limited fluorescence intensity make them unsuitable for high-sensitivity detection and real-time monitoring [80]. With the advancement of nanoparticle technology, engineered fluorescent nanomaterials such as dye-doped silica nanoparticles or quantum dots, have attracted a lot of attention in recent years [79]. However, despite quantum dots have shown interesting optical properties that can be exploited in a range of photonic applications, due to their broad excitation spectrum, size-tunable fluorescence properties, long fluorescence time and increased photostability [80], they present clear disadvantages, such as poor solubility, agglutination, blinking, low quantum yield, and toxicity in biological systems [81]. In addition, the emission wavelength of quantum dots depends on the particle size; when the size of quantum dots is shifted to a bigger size, the peak of emission is shifted to a longer wavelength [82]. In contrasts, silica nanoparticles present clear benefits, because they are

highly hydrophilic due to their silanol groups on surface (Si-OH), easy to prepare and control the size by a modified sol-gel method, possible to separate using centrifugation, can be surface modified with commercial silane coupling agents and core-label with relevant molecules. In addition, fluorescent silica nanoparticles possess several advantages, such as high fluorescence intensity, good photostability due to the exclusion of oxygen by silica encapsulation protecting the dyes form environment and good potential for surface modification with various biomolecules [83]. For this purpose, nano-scale materials, such as dye-doped silica nanoparticles, have demonstrated a high potential to overcome the limitations presented by conventional organic dyes. In this regard, we development several core-doped SiO_2 NPs using different organic dyes, as fluorescent probes in order to apply our SiO_2 NPs into biological research, such as bioimaging, bioassay, and nanomedicine [84]–[86].

A fluorescent dye can be incorporated into silica particles by a simple strategy during particle formation, either by directly adding the dyes [87], [88] or by attaching the dye on the silica network via the formation of covalent bonds (siloxane bond) between the dye, silane coupling reagent and silica particles, called the imposition method [3], [37], [89], [90]. However, fluorescent dyes tare difficult to incorporate into silica nanoparticles by the directly attachment, because the lack of strong covalent attachment [85], therefore, the imposition methodology is a preferred method, because used silane coupling agents for creating a an complex molecule (covalent bond between the dye and the amino group of the silane linker) that will be incorporated dunging the silica synthesis by a siloxane covalent bond (Si-O-Si), during the formation of the SiO_2 NPs by the hydrolysis and condensation reaction, as shown in **figure 3.7**.

The strategy incorporates covalently the fluorescent dye FITC by using an amine-containing silane as a crosslinker (usually, APTES) by a thiourea-linkage reaction (-NH-C=S-NH-), through the amino-terminated alkyltrialkoxysilane compounds and the dye molecules having an isothiocyanate functional group (–N=C=S). In addition, others fluorophores that were incorporated by this strategy were the Rhodamine B isothiocyanate (RBITC) and Tetramethylrhodamine isothiocyanate (TRITC). The other route was done performing a reaction between the amino group in the silane reagents with the succinimidyl ester group of the dyes to form a carboxamide complex (-C=O-NH-). The

fluorophores that undergo this kind of incorporation, are the commercial Alexa dyes. Therefore, in this study, we used the Alexa Fluor® 350 NHS Ester, called AF350, a blue-fluorescent dye with moderate photostability and excitation that matches the UV region at 350 nm of wavelength.

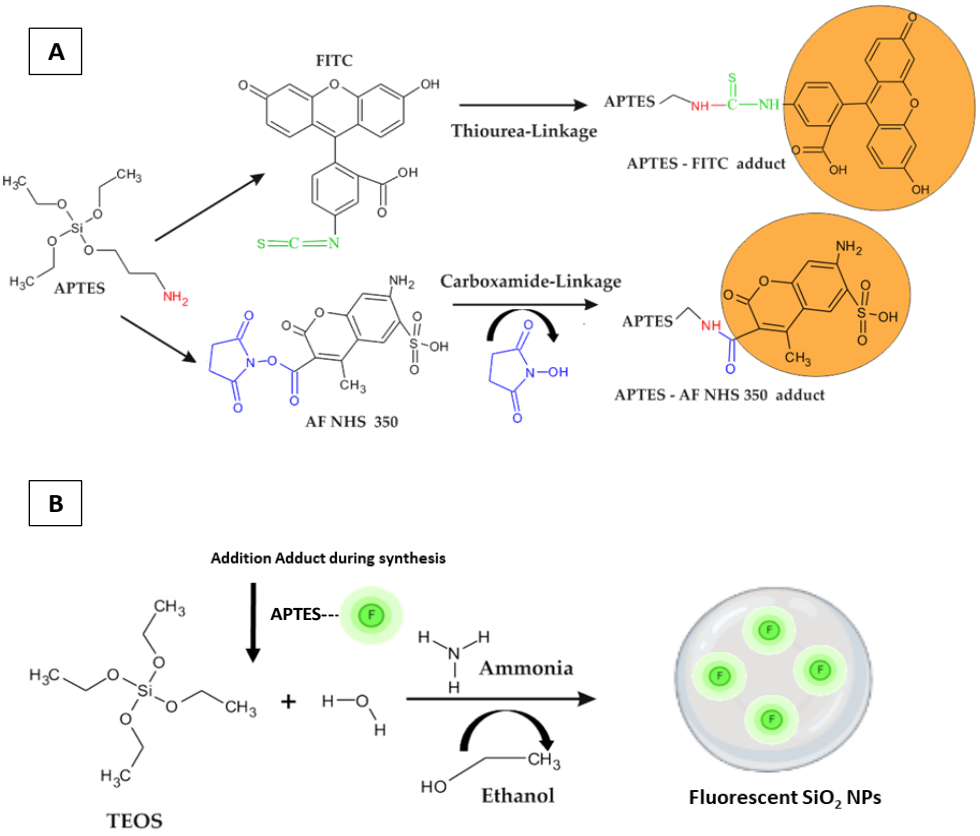

Figure 3.7 Graphical representation of the synthesis of the dye-doped SiO_2 NPs. (A) Formation of the silane-dye complex for the preparation of the loaded silica particles via thiourea-linkage (APTES-FITC) and carboxamide-lingake (APTES-Alexa dye AF NHS 350) by reaction with APTES. (B) Synthetic strategy followed for the preparation of the fluorescent SiO_2 NPs by the modified Stöber method (imposition method). The dye was incorporated within the silica matrix by a covalent siloxane bond (Si-O-Si) of the APTES-dye complex molecule, during the nucleation and growth of the silica particles.

3.4.1 Systematically Core-Doping the SiO_2 NPs with A Single Fluorescent Dye

In order to optimize the loading of FITC molecules in the core of the SiO_2 NPs by using the thiourea-linkage. The effective coupling of the FITC-APTES complex formation, by reacting the amino group of the silane linker molecule and the isothiocyanate group of the fluorophore were evaluated. For this purpose, the yield of this reaction was addressed by using high performance liquid chromatography (HPLC), in order determine the yield of the formed complex, after 24h of conjugation. Because of the APTES silane linker only have one

amino group in its structure, the reaction is considered to be 1:1 in relation with the dye FITC that also have only one isothiocyanate group per molecule. Therefore, for this purpose, 1mM of FITC and 1mM of APTES were conjugated together in ethanol in a closed vial under slow stirring and after 24 hours and were analysed by HPLC. The calibration curve of scalar FITC concentrations were also analysed from 0-0.25mM.

The HPLC analysis were done in collaboration with the Chemical Analysis Service (SAQ) of the Scientific and technical services of the University Autonomous of Barcelona (UAB). The HPLC results are as shown in **figure 3.8**. The standard calibration curve of the different scalar FITC concentrations, showed a good linear response. The standard FITC molecules presented a characteristic retention time of 12.693 seconds. The area under the peaks were used for the calculation of the yield of the reaction. **Figure 3.8-A**, showed that the solvent, which is anhydrous ethanol and the APTES molecules, which is the silane linker, didn't revealed a retention time signal in the HPLC analysis as expected. In contrast, the standard fluorescein isothiocyanate (FITC) presented a retention time of 12.693 seconds using the second reverse-phase chromatography C18 column.

The retention time is known to be the amount of time spends on the column after a molecule has been injected. Each compound will spend a different amount of time on the column depending to its chemical composition. Thus, validating all conditions, this can be used to identify a certain compound. According to the results, the FITC molecule in different concentrations took 12 ± 1 seconds from injection. On the other hand, the FITC-APTES complex, presented a retention time of 14.424 seconds, almost two second more than the standard FITC alone. These results clearly indicate that the molecule presented different chemical composition. One explanation may be, looking their chemical composition of the APTES-FITC molecule. Due to the thiourea-linkage, the molecular weight increased as well as the polarity of the, due to the presence of the three siloxane groups.

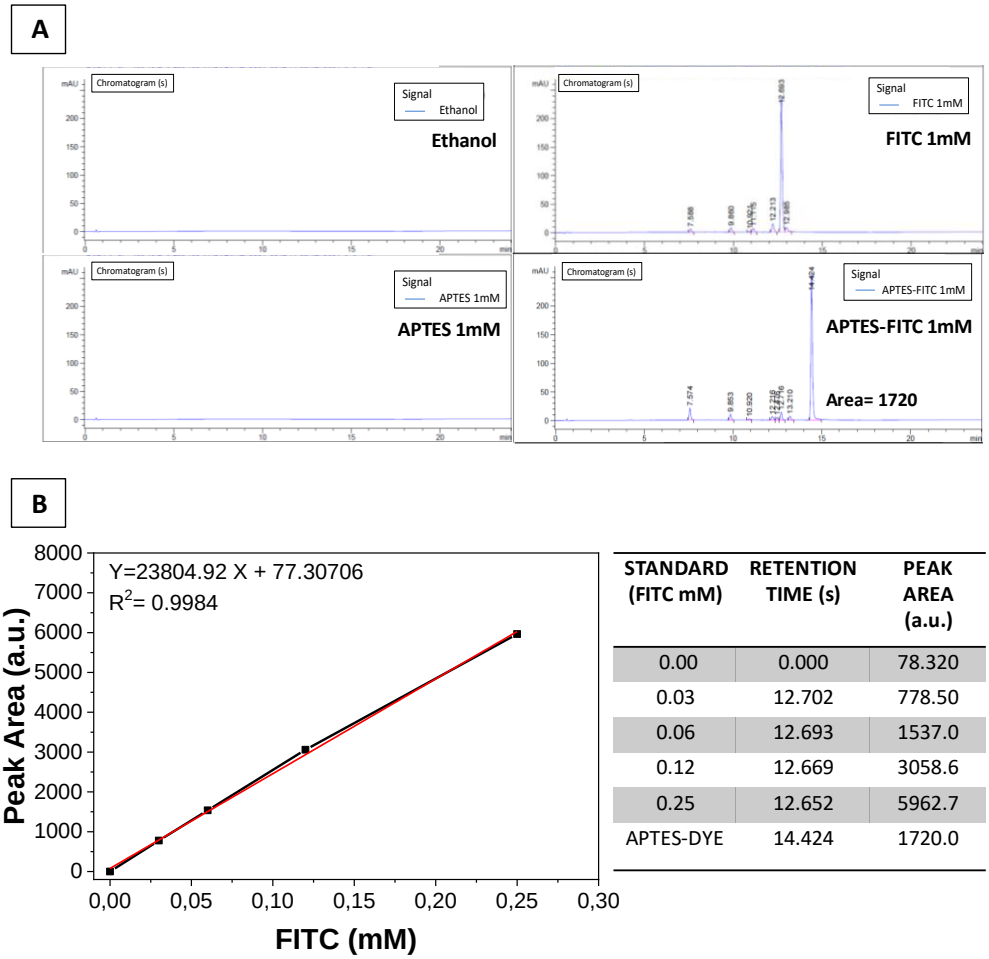

STANDARD (FITC mM)	RETENTION TIME (s)	PEAK AREA (a.u.)
0.00	0.000	78.320
0.03	12.702	778.50
0.06	12.693	1537.0
0.12	12.669	3058.6
0.25	12.652	5962.7
APTES-DYE	14.424	1720.0

Figure 3.8 High performance liquid chromatography (HPLC) results. (A) calibration curve as a function of increasing FITC concentration. The peak area is used for calculations for the yield of the APTES-FITC complex. The given equation displayed a good correlation of the data. (B) high performance liquid chromatography (HPLC) chromatograms: Ethanol and APTES showing no signal, fluorescein isothiocyanate (FITC) showed a retention time of 12.693s, and the FITC-APTES complex showed a retention time of 14.424 seconds.

This explained the increased retention time, because the C18 column is and column made of octadecyl group bonded to a silica gel surface, therefore the silane-dye precursor may display more affinity to the siloxane bonds, thus it spends more time on the column from injection. From the calibration curve, it was calculated the amount of silane-dye (APTES-FITC) precursor formed during the thiourea-linkage formation. The concentration approximately of FITC on the silane-dye precursor is 0.70mM from the calibration curve. The FITC-APTES complex used for the reaction were 1mM. Therefore, it can be concluded, that the yield of free complex in solution were around 70%.

Once the yield of the APTES-FITC complex was evaluated the synthesis of the fluorescent silica particles core-doped with FITC (Ex=490nm and Em=525nm), was done following the modified Stöber method by imposition of the dye on the silica network (Experimental described in **Chapter 5, section 5.2.2.2**). For the loading, different scalar volumes of the complex APTES-FITC (2mM:2mM) in a molar relation 1:1 were added before the synthesis and the reaction was left for 24 hours under stirring in dark conditions. Dialysis was done for the purification of the unreacted subproducts. Although the determination of an accurate number of dye molecules trapped inside the NPs is not possible, because of the potential effect of self-quenching of dye molecules in close proximity and the inherent particle scattering, it is possible to determine the average fluorescence of the NPs compared with pure dyes. Therefore, calibration curves with the pure fluorophore (FITC) were performed in order to elucidate the equivalent number of dye molecules trapped inside the matrix, as shown in **figure 3.9**.

In addition, the pH for the whole measurements was maintained at 9, because the FITC has a pKa of 6.4, its ionization equilibrium leads to pH-dependent absorption and emission over the range of 5 to 9, thus pH 9 will ensure the maximum absorbance. All the above experiments were conducted at room temperature, (Extended characterization of the NPs showed in **Appendix B4)**. The summary of characterization results of the FITC core-doped SiO_2 NPs are shown in **table 3.3** and **figure 3.9**.

Table 3.3 Summary of the characterization of the fluorescent core-doped SiO_2 NPs with FITC after purification.

APTES-FITC (mL)	FITC added (mM)	NPs absorbance (a.u)	FITC Doped (mM)[a]	Doped FITC %	SEM Size (nm)[b]	CONCENTRATION (NPs/mL) [c]	FITC/mL	FITC/NP
1	0.0260	0.339	0.0040	15.4	38.9 ±3.7	$8.71x10^{13}$	$2.41x10^{15}$	27.6
5	0.1300	0.979	0.0130	10.0	36.6 ±4.5	$1.05x10^{14}$	$7.83x10^{15}$	74.5
10	0.2600	2.304	0.0290	11.1	38.2 ±4.2	$9.20x10^{13}$	$1.75x10^{16}$	190.2
15	0.3900	3.093	0.0400	10.2	40.1 ±4.4	$7.95x10^{13}$	$2.41x10^{16}$	303.1
20	0.5200	2.839	0.0360	6.90	40.5 ± 5.7	$7.72x10^{13}$	$2.17x10^{16}$	281.8
30	0.7800	2.395	0.0310	3.94	41.4 ± 5.7	$7.23x10^{13}$	$1.87x10^{16}$	258.6

a=Calculated from calibration curve, b= Size distribution of NPs by image J, c= calculated NPs concentration, showed in Appendix C3.

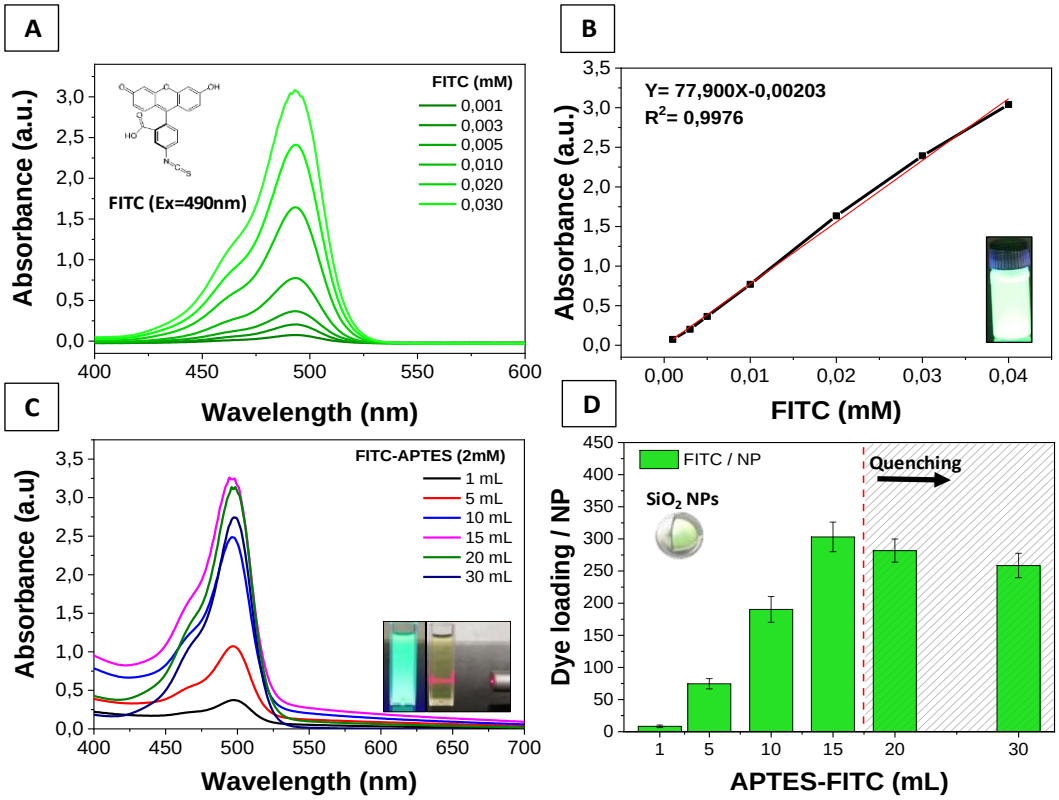

Figure 3.9 Characterization of the fluorescent core-doped SiO_2 NPs with FITC. (A) Uv-Vis absorption spectra of different standard FITC solutions, maximum absorbance recorded at 490nm. (B) Calibration curve as a function of FITC concentration. The given equation displayed a good correlation of the data. (C) Uv-Vis absorption spectra of different fluorescent SiO_2 NPs after purification. On inset the colloidal image of the NPs under UV-light, displaying their characteristic green fluorescent colour. (D) Graphic representation of the calculated FITC molecules per SiO_2 NP. The dashed red line indicates the concentration in which quenching effect were observed. (STEM and SD characterization of the NPs were showed in **Appendix B4**).

As showed in **figure 3.9-C**, the recorded absorbance intensity at 490nm of the core-doped SiO_2 NPs increases, when the volume of silane APTES-FITC complex were increased during the synthesis. This result indicates that FITC molecules were entrapped into the silica matrix by the covalent bonding without any modification in the final morphology of the particles, as showed by the STEM analysis (showed in **Appendix C4**). The calculated mean size and size distribution of the NPs showed that they presented a comparable size, suggesting that the process did not affect the particle size during synthesis. Moreover, the yield of the incorporated FITC were around 15-10% in the first four conditions (1-15mL APTES-FITC). However, when the volume of APTES-FITC (2mM) were beyond 15 mL (FITC 0.390mM), the absorbance intensity decreased, as well as the yield of incorporated FITC to 3.94%. This lower intensity of these NPs can be explained by the self-quenching of the FITC

molecules due to non-radiative energy transfer between the dyes [91]. This phenomenon is explained due to dye-dye interactions and possible stacking between them. Interestingly, at low APTES-FITC concentration (below 0.390mM FITC), the **figure 3.9-D**, showed a linear incorporation of FITC molecules per NP, as expected. This result suggest that is possible to systematically control the number of loaded FITC molecules in every condition, from 28 to 303 FITC dyes per NP.

Alternatively, other fluorophores molecules having the isothiocyanate functional group, such as rhodamines RBITC and TRITC, or with the succinimidyl ester group, such as the Alexa Flour NHS350 (AF350), can also be incorporate using the same strategy, because the APTES molecule can form the Silane-Dye complex by strong thiourea-linkage or carboxamide-linkage, using their amino functional group. Our one-pot synthetic methodology is particularly interesting, because allowed us to increase the spectrum of emission of the fluorescent SiO_2 particles, as well as the possibility to develop different fluorescent and visible colors after exposing the NPs to electromagnetic radiation, suitable for a broad range of applications. Therefore, the synthesis of the different fluorescent silica particles core-doped with RBITC (Ex=551nm and Em=585nm), TRITC (Ex=549nm and Em=580nm) and AF350 (Ex=346nm and Em=445nm), were done by one-pot imposition method previously discussed (Experimental described in **Chapter 5, section 5.2.2.3**).

For the core-loading, different scalar volumes of the complexes APTES-RBITC and APTES-TRITC (2mM:2mM) and APTES-AF350 (0.24mM:0.24mM), always having a molar relation 1:1, were added before the synthesis, following the aforementioned reaction conditions. The concentration of the loaded dye molecules was calculated using their respective absorbance and plotted the calibration curve of standards in **figure 3.10-B, F, J**. The extended characterization of the NPs is showed in **Appendix B5**). The results of the core-shell SiO_2 NPs with RBITC, TRITC and AF350 are shown in **figure 3.10** and **Table 3.4.**

Table 3.4 Summary of the characterization of the fluorescent core-doped SiO_2 NPs with RBITC, TRITC and AF350 after purification.

APTES-RBITC (mL)	RBITC added (mM)	NPs absorbance (a.u) 1/2	RBITC Doped (mM)[a]	Doped RBITC %	SEM Size (nm)[b]	CONCENTRATION (NPs/mL) [c]	RBITC/ mL	RBITC/ NP
1	0.0260	0.103	0.0022	8.50	48.0 ± 4.7	$4.64x10^{13}$	$1.32x10^{15}$	28.5
3	0.0780	0.268	0.0081	10.4	46.8 ± 6.4	$5.00x10^{13}$	$4.88x10^{15}$	97.6
5	0.1300	0.414	0.0129	9.92	47.6 ± 6.2	$4.76x10^{13}$	$7.76x10^{15}$	163
8	0.2080	0.576	0.0181	8.72	51.5 ± 7.9	$3.75x10^{13}$	$1.09x10^{16}$	290.7
10	0.2600	0.794	0.0252	9.69	52.4 ± 8.7	$3.56x10^{13}$	$1.52x10^{16}$	426.9
15	0.3900	1.204	0.0386	9.97	53.2 ± 9.0	$3.41x10^{13}$	$2.32x10^{16}$	680.3
APTES-TRITC (mL)	**TRITC added (mM)**	**NPs absorbance (a.u) 1/2**	**TRITC Doped (mM)[a]**	**Doped TRITC %**	**SEM Size (nm)[b]**	**CONCENTRATION (NPs/mL) [c]**	**TRITC/ mL**	**TRITC/ NP**
1	0.0260	0.192	0.0034	13.0	40.9 ± 5.3	$7.50x10^{13}$	$2.05x10^{15}$	27.3
3	0.0780	0.459	0.0096	12.3	42.6 ± 5.2	$6.63x10^{13}$	$5.78x10^{15}$	87.2
5	0.1300	0.703	0.0152	11.7	41.7 ± 5.0	$7.07x10^{13}$	$9.15x10^{15}$	129.4
8	0.2080	1.003	0.0222	10.7	43.6 ± 4.6	$6.19x10^{13}$	$1.34x10^{16}$	216.5
10	0.2600	1.177	0.0262	10.1	43.7 ± 4.9	$6.15x10^{13}$	$1.58x10^{16}$	257
APTES-AF350 (mL)	**AF350 added (mM)**	**NPs Fluorescence (a.u)**	**AF350 Doped (mM)[a]**	**Doped AF350 %**	**SEM Size (nm)[b]**	**CONCENTRATION (NPs/mL) [c]**	**AF350/ mL**	**AF350/ NP**
1	0.0045	147.5	0.0005	10.6	36.6 ± 4.1	$1.05x10^{14}$	$2.89x10^{14}$	2.80
3	0.0134	228.9	0.0014	10.5	37.9 ± 4.8	$9.42x10^{13}$	$8.55x10^{14}$	9.1
5	0.0225	329.5	0.0026	11.5	35.8 ± 4.6	$1.12x10^{14}$	$1.55x10^{15}$	13.8
8	0.0350	434.7	0.0038	10.8	36.8 ± 4.5	$1.03x10^{14}$	$2.29x10^{15}$	22.2
10	0.0450	525.2	0.0048	10.7	38.5 ± 4.0	$9.00x10^{13}$	$2.91x10^{15}$	32.4

a=Calculated from calibration curve, b= Size distribution of NPs by image J, c= calculated NPs concentration, showed in Appendix C3.

As showed in **figure 3.10**, the three calibration curves using the standards RBITC, TRITC land AF350, presented a good linear correlation. Moreover, the recorded absorbance and emission for the different core-doped SiO_2 NPs with RBITC (at 551nm), TRITC (at 449nm) and AF350 (at 445nm) were increased, when the volume of their respective APTES-Dye complex were increased during the synthesis. This observation revealed the possibility of load the SiO_2 NPs with different dyes and concentrations, without any evidence of losing their final morphology, as shown by the SEM analysis (showed in **Appendix B5**). The calculated size distribution of the NPs showed that they presented a comparable size within the same conditions, suggesting that the presence of the APTES-dye complex not affected the growth of the NPs

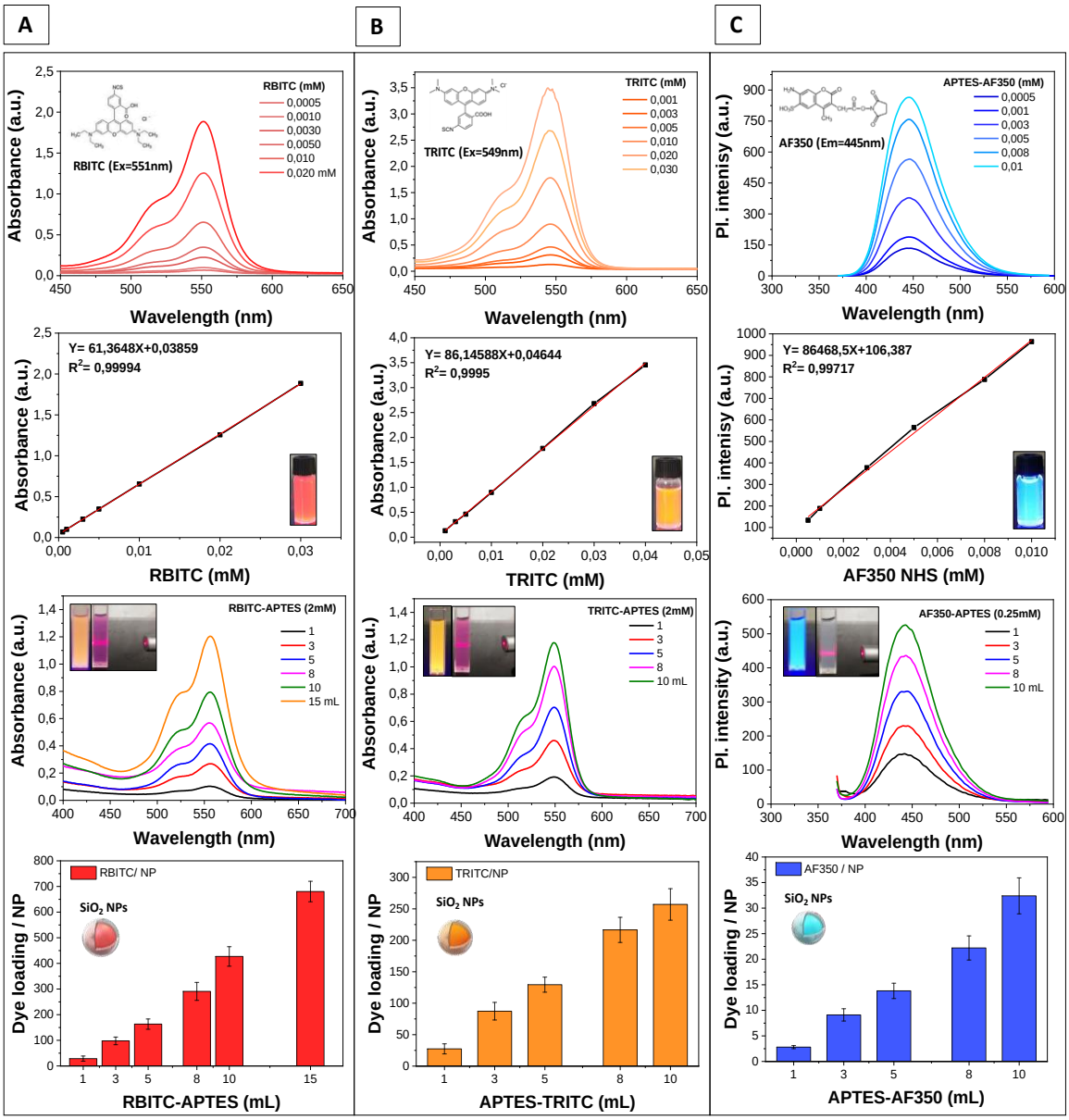

Figure 3.10 Characterization of the fluorescent core-doped SiO_2 NPs with different dyes. From left to right, (A) SiO_2 NPs loaded with RBITC, from up to down, Uv-Vis absorption spectra of different standard RBITC mM, maximum absorbance at 551nm, Calibration curve as a function of RBITC concentration, Uv-Vis absorption spectra of different SiO_2 NPs doped with RBITC. On Inset is the colloidal image of the NPs under UV-light, displaying their characteristic red-orange fluorescent colour. Graphic representation of the calculated RBITC molecules per NP. (B) Identical characterization for SiO_2 NPs loaded with TRITC, maximum absorbance recorded at 549nm. NPs displayed their characteristic orange fluorescent colour under UV-light and (C) For SiO_2 NPs loaded with AF350. maximum emission recorded at 445nm. NPs displayed their characteristic blue fluorescent colour under UV-light. The emission spectra were done using a photoluminescence spectrophotometer.

The fluorescent SiO_2 NPs using RBITC and TRITC (of average diameter of 50nm) were bigger size in comparison with the particles with AF350 (average size 35nm), despite using the same synthetic strategy. In addition, it is possible to observe a trend in increasing the

size, when the APTES-RBITC and APTES-TRITC were increased in the same vessel reaction. This can be explained looking the nature of the rhodamine dyes in comparison with the Alexa AF350. The commercial RBITC and TRITC are supplied in the monochloride form as a salt, having (Cl^-) ions. Additionally, both structures present an overall positive charge. In this sense, as commented before in the previous chapter, the increase in ionic strength affects the formation mechanism of the SiO_2 NPs towards bigger sizes, because the nucleation of silica relies on the aggregative growth, depdeping in the electrostatic stability of the species. Interestingly, in all the synthetic conditions the incorporated yield of RBITC, TRITC and AF350 dyes into the SiO_2 NPs were comparable, with a values around 13-10%.

Finally, as shown in **figure 3.10,** revealed a progressively linear incorporation of the dyes per NP, as expected, revealing that we were able to systematically control the number of loaded fluorescent molecules in every condition. However, the number of RBITC per NP were the highest loading (680 number of RBITC per NP), explained by the fact that the NP presented a bigger size, in comparison with the ones loaded with AF350, that presented the lowest incorporated number. Moreover, two things can be concluded, i) silica particles with AF350 were the smaller in diameter and ii) the concentration of the APTES-AF350 complex were lower in factor of 10, in comparison with the rhodamine complexes. This result explains the lower number of loaded AF350 molecules.

3.4.2 Systematically Core-Doping the SiO_2 NPs With a Mixture of Fluorescent Dyes

Besides, the directly incorporation of a single commercial organic dyes with specific absorption and emission wavelengths, the encapsulation of two different dyes with multiple fluorescence spectra into silica enables the synthesis of dual-emission fluorescent NPs, in comparison to single-dye-doped NPs, because of the development of multi-fluorescent NPs may provide a better information upon detection and sensing. Based on the desired spectroscopic characteristics, dual-emission fluorescent NPs have gained increasing attention for various applications, including multiplexed bioassays [92]. In this sense, our one-pot sol-gel synthetic strategy allows us to synthetize dual-emission SiO_2 NPs with two organic dyes for effective cellular detection and for instance, discrimination from

multiple fluorescently stained cellular components. Then, fluorescent core-shell silica particles with different APTES-Dye complexes mixtures using two diverse dyes were done in a systematically manner. The main objective was to loading two different fluorophores in the same particle for increasing the spectrum of absorption and emission of the fluorescent particles, as well as the opportunity to develop a rainbow-like palette of different colors, using silica as carrier. Nevertheless, any energy transfer mechanisms in which two or more dyes were closely positioned (strong attractive dye–dye interactions that led to excitonic coupling) were not analyzed because were out of the scope of this study. Further studies of this interactions can be made by the molecular exciton model for molecular aggregates, Frenkel exciton [93].

In this regard, for the preparation of the multi-fluorescent silica NPs, two different strategies were done, as follows:

The first batch of the dual-emission SiO_2 NPs, were prepared by using a single APTES-Dye complex solution, by mixing two different dyes (RBITC + FTIC) with the APTES in the same vessel solution. For this purpose, a mixture composed of APTES (2.0mM) and FTIC(1.80mM)/RBITC(0.20mM) for a total dye concentration of 2.0mM, were prepared and (1,3,5 mL) of these APTES-FITC/RBITC complex mixture were used in our modified Stöber method for the dual emission dye-doped NPs (sample S1, S2 and S3). Summary of the characterization showed in **table 3.6**.

The second batch of dual-emission SiO_2 NPs particles, were prepared by using two different APTES-Dye complex solutions. The first complex composed of APTES-RBITC (0.24mM) and the second one made of APTES-AF350 (0.24mm). Later the dual-emission silica NPs were prepared by mixing different proportions of these two complexes (50:50, 80:20, 90:10, samples (S4, S5 and S6). Characterization showed in **table 3.5**. Experimental described in detail, (**Chapter 5, section 5.2.2.4**).

Table 3.5 Summary of the characterization of the dual-emission SiO_2 NPs with the dyes FTIC/RBITC (sample S1-S3) and RBITC/AF350 (sample S4-S6) after purification.

APTES-DYE mix (mL)	FITC added (mM)	NPs absorbance (a.u)	FITC Doped (mM)[a]	Doped Yield %	SEM Size (nm)[b]	CONCENTRATION (NPs/mL)[c]	FITC/ mL	FITC/ NP
S1	0.0235	0.397	0.0052	21.0	39.8 ± 4.4	$8.14x10^{13}$	$3.13x10^{15}$	38.5
S2	0.0704	1.011	0.0130	18.4	40.7 ± 5.3	$7.61x10^{13}$	$7.83x10^{15}$	102.9
S3	0.1173	1.580	0.0203	17.3	40.0 ± 5.1	$8.01x10^{13}$	$1.22x10^{16}$	152.3
APTES-DYE mix (mL)	**RBITC added (mM)**	**NPs absorbance (a.u)**	**RBITC Doped (mM)[a]**	**Doped Yield %**	**SEM Size (nm)[b]**	**CONCENTRATION (NPs/mL)[c]**	**RBITC/ mL**	**RBITC/ NP**
S1	0.0037	0.080	0.0007	18.9	39.8 ± 4.4	$8.14x10^{13}$	$4.21x10^{14}$	5.2
S2	0.0111	0.202	0.0027	24.3	40.7 ± 5.3	$7.61x10^{13}$	$1.62x10^{15}$	21.3
S3	0.0185	0.353	0.0051	28.1	40.0 ± 5.1	$8.01x10^{13}$	$3.07x10^{15}$	38.3
APTES-DYE mix (mL)	**RBITC added (mM)**	**NPs absorbance (a.u)**	**RBITC Doped (mM)[a]**	**Doped Yield %**	**SEM Size (nm)[b]**	**CONCENTRATION (NPs/mL)[c]**	**RBITC/ mL**	**RBITC/ NP**
S4	0.0220	0.413	0.0061	27.1	37.4 ± 4.9	$9.80x10^{13}$	$3.67x10^{15}$	37.5
S5	0.0090	0.193	0.0025	28.0	32.7 ± 4.6	$1.13x10^{14}$	$1.51x10^{15}$	13.4
S6	0.0045	0.094	0.0009	20.5	34.7 ± 4.8	$1.23x10^{14}$	$5.42x10^{14}$	4.4
APTES-DYE mix (mL)	**AF350 added (mM)**	**NPs absorbance (a.u)**	**AF350 Doped (mM)[a]**	**Doped Yield %**	**SEM Size (nm)[b]**	**CONCENTRATION (NPs/mL)[c]**	**AF350/ mL**	**AF350/ NP**
S4	0.0220	351.1	0.0028	12.7	37.4 ± 4.9	$9.80x10^{13}$	$1.50x10^{15}$	15.3
S5	0.0360	430.6	0.0038	10.5	32.7 ± 4.6	$1.13x10^{14}$	$2.29x10^{15}$	20.3
S6	0.0400	531.9	0.0049	12.3	34.7 ± 4.8	$1.23x10^{14}$	$2.95x10^{15}$	26.4

a=Calculated from calibration curve, b= Size distribution of NPs by image J, c= calculated NPs concentration, showed in Appendix B3.

The concentration of the dye doped molecules were calculated using the previously calculated calibration curves of their standard dye solution, matching the absorption of the free dyes and the particle solutions. The extended STEM and SD characterization of the NPs showed in **Appendix B6)**. The optical results of the dual-emission SiO_2 NPs are shown **figure 3.11**. respectively.

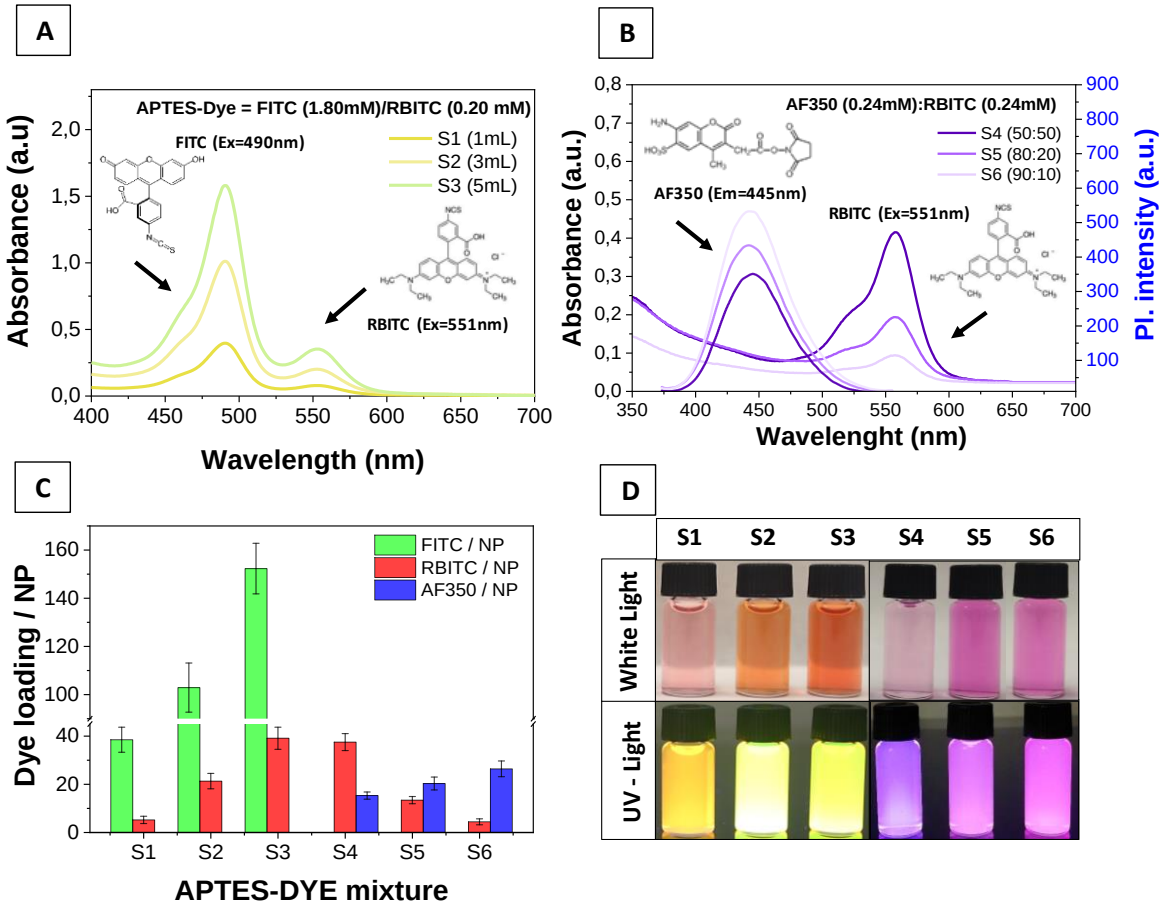

Figure 3.11 Characterization of the dual-emission SiO_2 NPs using mixtures of APTES-dye complex, FTIC/RBITC (sample S1-S3) and RBITC/AF350 (sample S4-S6) after purification. (A) Uv-Vis absorption spectra of different fluorescent SiO_2 NPs using scalar additions (1,3,5 mL) of a APTES-Dye, composed of APTES (2.0mM) and FTIC(1.80mm)/RBITC(0.20mM). The maximum absorbance intensity was at 490nm and 551nm, respectively. (B) Uv-Vis absorption spectra of different fluorescent SiO_2 NPs using different APTES-AF350 (0.24mM) and APTES-RBITC (0.24mM) proportions (50:50, 80:20, 90:10). The maximum absorbance intensity was recorded at 551nm and emission at 445nm, respectively. (C) Graphic representation of the calculated FITC, RBITC and AF350 molecules per SiO_2 NP of the different samples (S1-S6). (D) Colloidal image of the different particles under white light and UV-light.

On one hand, as showed in **figure 3.11-A**, the recorded absorbance at 490nm and 551nm for the dual-label silica particles with the RBITC/FITC increases (S1-3), when the volume of the APTES-Dye complex mixture was increased during the synthesis. The appearance of the dual peaks in in the spectra revealed that both RBITC and FITC were progressively entrapped into the silica matrix. Interestingly the NPs retain their spherical morphology, and a low mean size around 40nm, as shown by the SEM analysis (**Appendix B6**).

The NPs presented a comparable size, even if the number of combined dyes were increased in the core. This was possible because the RBITC concentration were kept very diluted (0.2mM) in comparison of FITC (1.80mM), as previously discussed, the RBITC slightly increase the final diameter, due their nature. Interestingly, as shown in figure **3.11-C**, the samples S1, S2 and S3, revealed a scalar increase of the RBITC and FITC dyes per NP when the volume of APTES-FITC/RBITC mixture were increased. This trend was expected because we used a fixed APTES-Dye complex concentration. The FITC molecules increase from 40 to 150 FTIC/NP, while RBITC with values from 5 to 38 RBITC/NP. Curiously, the dual-emission NPs presented a slightly higher loading of dyes per NP in comparison with the single-doped particles. These results may suggest that possible strong attractive dye–dye interactions that led to excitonic coupling, can be occurring.

On the other hand, as showed in **figure 3.11-B**, the measured absorbance at 551nm decreases and the fluorescence emission intensity at 445nm increases for the dual-label silica (S4-6) with the AF350 and RBITC dyes, when different proportions of the APTES-Dye complex mixture was used during the synthesis, as anticipated. This is because during the process of silica formation, the APTES-dye complex concentration was varied. The APTES-AF350 (0.24mM) concentration were increased, while the APTES-RBITC (0.24mM) were decreased, displaying different fluorescent purple colours. The appearance of the peaks in the absorption and emission spectra revealed that both RBITC and AF350 were integrated into the silica matrix. In addition, this synthetic strategy revealed that it is possible to integrate dyes with different chemistry of covalent bonding, because the RBITC was linked by thiourea bond, while AF350 was coupled by carboxamide bond, in the same reaction, opening to multiple possible combinations using different organic dyes. Also, the dual-emission NPs kept their spherical morphology having smaller diameter around 30nm, shown by the SEM analysis (**Appendix B6**). The NPs were all comparable size, because the RBITC concentration were again diluted (0.2mM), as previously discussed. Figure **3.11-C**, samples S4-S6, revealed an opposite incorporation of the dyes molecules per NP, the RBITC decreases from 38 to 4.0, while AF350 increases from 15 to 26 per NP. As commented before, this class of dual-emission NPs presented a slightly higher loading capacity that the single-doped particles, suggesting the same conclusion tan before of possible dye–dye interactions. Finally, **figure 3.11-D**, showed the colloidal image of the dual-emission NPs

(S1-S6) under white and UV light, revealing the possibility of different multifluorescent colors of the NPs by combination the different dyes by our synthetic strategies, red orange from RBITC and green from FITC, gave the characteristic yellow colour and the combination of AF350 blue and RBITC red orange, gave a characteristic light purple colour.

3.4.3 Evaluation of the Covalent Attachment of the Fluorescent Dyes in The SiO_2 NPs

Finally, in order to evaluate the covalent encapsulation of the different dyes (FITC, RBITC, TRITC and AF350), using the imposition strategy (APTES as cross-linker for copolymerisation during silica sol-gel synthesis), the extent of leaching of the organic dye from the silica as carrier was evaluated. For this purpose, the single-doped fluorescent SiO_2 NPs with the highest dye loading, were subjected an incubation using phosphate saline buffer (PBS) for 2 hours and then sonicated for 1 minute. Thereafter, the NPs were centrifuged at 10.000g for 10 minutes and suspended again in water at the same level, avoiding the dilution of the sample. The absorbance and fluorescence emission intensities were recorded at the same conditions and the process were repeated up to four cycles.

As shown in **figure 3.12**, the recorded absorbance and emission spectra of the different single-doped particles (A to D), revealed the same characteristic peak for every dye, out ruling possible transformation of the NPs, such as aggregation. The increased intensity towards lower wavelength is due to the SiO_2 NPs absorption scattering behaviour. **Figure 3.12-E**, revealed that the intensity of the NPs decreased almost 18.0%, in contrast with the initial signal, revealing that the dyes were covalent incorporated into the particles. Particles showed minimum dye leaching or fluorescence quenching. Thus, the strategy of using a silicon alkoxide derivative (APTES) for incorporate organic molecules covalently into the polycondensed network, is an effective strategy to prevent molecular leaching.

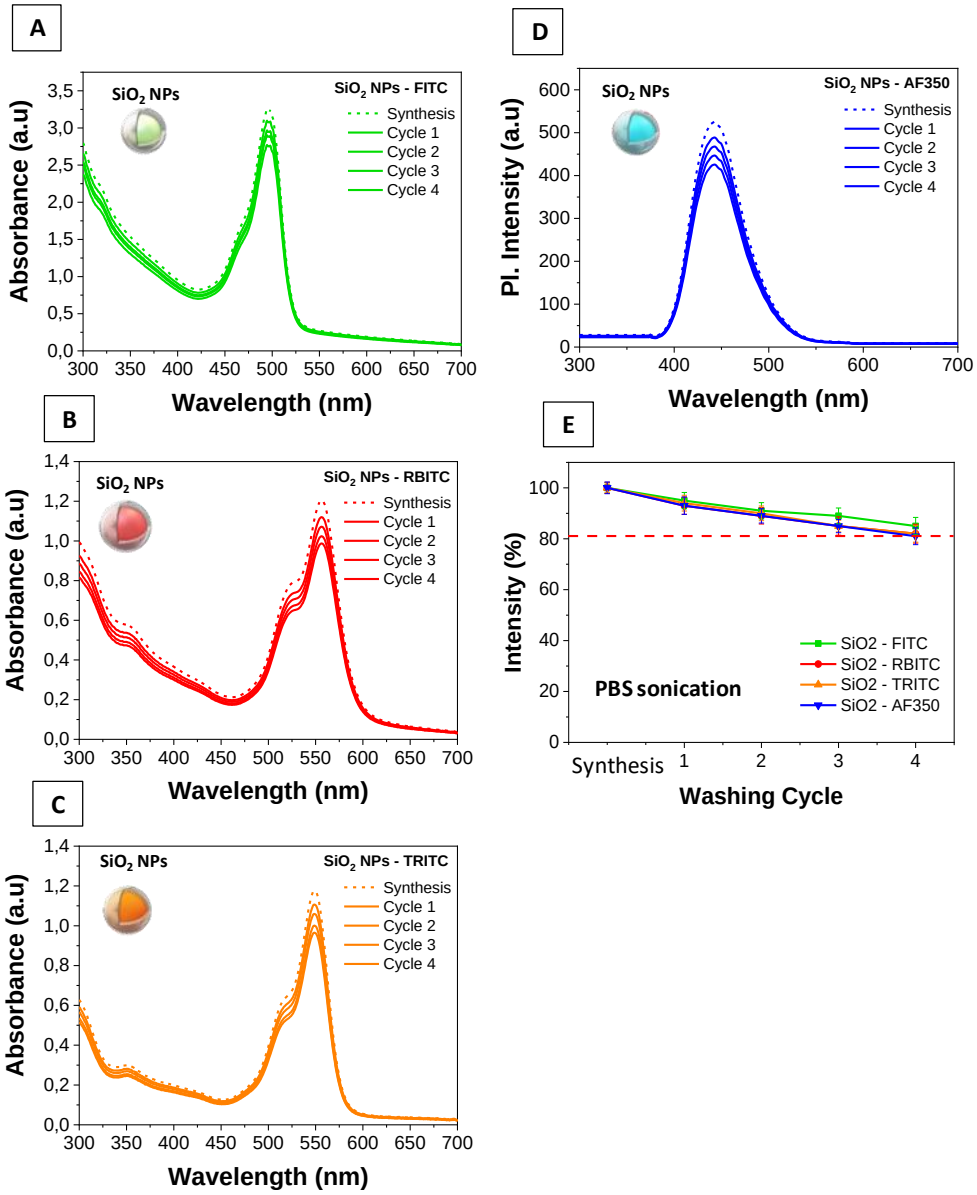

Figure 3.12 Dye leaching and stability evaluation of the core-doped SiO_2 NPs with different organic dyes, after 4 cycles of washing by centrifugation (10 min, 10.000g). SiO_2 NPs were incubated in PBS for 2 hours and were subjected to 1 minute of sonication in every cycle. (A) Uv-Vis absorption spectra of the core-shell SiO_2 NP with FITC. (B) SiO_2 NP with RBITC. (C) SiO_2 NP with TRITC. (D) SiO_2 NP with AF350 were recorded the fluorescence intensity with an excitation energy of 346nm. (E) Graphical representation of the optical intensity as a function of washing cycles of the different fluorescents SiO_2 NPs. The red dotted line indicates that after 4 cycles, NPs only lose 18% of their signal.

3.5 Development of a Multilayer Dual-Emission Responsive Core-Shell SiO_2 Nanoparticle as a Biological Probe for Imaging

In order to demonstrate the potential application of our original dual-emission functionalized silica nanoparticles with optical properties, for instance, as a fluorescent

probe, we decided to develop and hybrid dual-emission core-shell fluorescent SiO_2 NPs, composed of two different dyes, in two different layers of the NPs. The core–shell architecture is ideally suited for the development of fluorescent sensors on the nanoscale. This strategy is specifically versatile, because allow the separation of two incorporated fluorophores, either in the core or in the silica shell of NPs, and thus to avoid possible interactions between two dyes reducing their fluorescence intensity. Using the SiO_2 shell thickness as spacer, effectively separated the dyes from its neighbors, without permitting energy transfer between neighboring fluorophores. In addition, the growth of a final silica external layer, after the dual-dye doping, will allow the protection from external influences, such as solvent, high-ionic-environment and other large molecules, both: the internal reference dyes isolated in the particle core, and the second reference dye coupled in the matrix of the second silica layer, providing a stable reference dual signal. The core–shell architecture not only provides a means to engineer the photophysical properties of the encapsulated fluorophores, but also creates a means to tailor their collective behaviour. The advantage of our synthetic strategy, is that the sensor dyes can then be integrated covalently into the particle core and shell, using APTES as cross-linker, protecting the reference dyes, as well as the dye leaching, in order to create stable sensors with low background signal.

3.5.1 Multilayer Dual-Emission Core-Shell SiO_2 Nanoparticle Synthesis

In this regard, as proof-of-principle we developed a multilayer dual-emission core–shell silica nanoparticles SiO_2-RBITC@FITC@SiO_2 NPs, for in vitro chemical imaging and spectrofluorometric analysis. Fluorescein isothiocyanate (FITC) was chosen as a pH sensor dye for its significant change in quantum yield upon protonation/ deprotonation of the hydroxyl groups on the xanthene backbone of the dye. In the protonated, mono-anionic form, the dye exhibits a relatively low quantum yield of 36%, whereas upon deprotonation the quantum yield increases to 93% for the dianion form. With a pKa of 6.4, this transition makes fluorescein an excellent sensor for pH in the biologically relevant range from pH 5–8.5. Rhodamine isothiocyanate (RBITC) was chosen as the internal standard (core) because

its quantum yield is unaffected by pH changes. The synthetic strategy to synthetize this dual-emission particle is shown in **figure 3.13**, as follows:

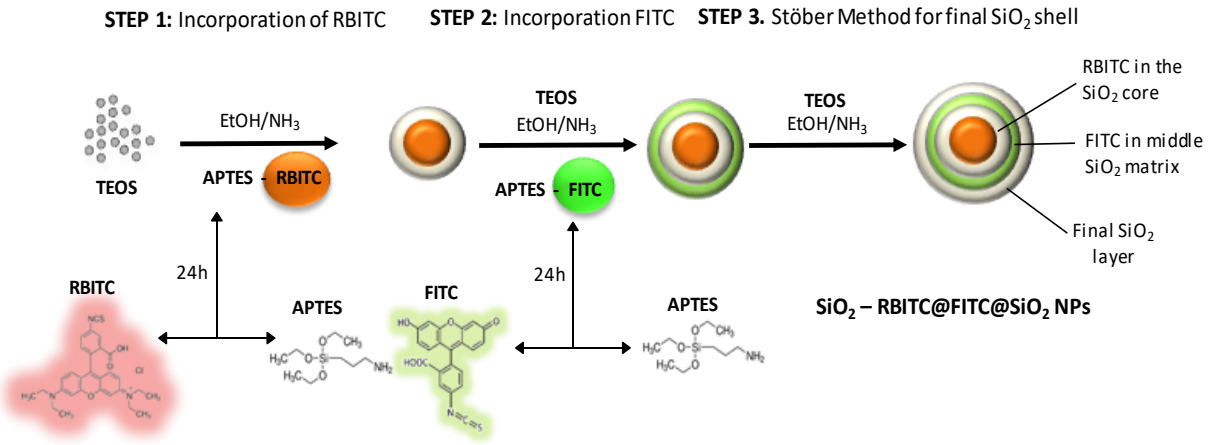

Figure 3.13 Graphical representation of the synthetic process for preparation the dual-emission core-shell SiO_2 NPs (SiO_2-RBITC@FITC@SiO_2 NPs) using a multi-step modified Stöber method. The APTES-RBITC and APTES-FITC were prior incubated for 24h for complex formation.

First, the dye RBITC were incorporated in the silica particle core as internal standard by copolymerization between the APTES-RBITC complex with the TEOS and ammonia following our modified Stöber method. As shown in **figure 3.14**, the RBITC doped SiO_2–RBITC NPs, revealed a mean size distribution (71.7 ± 8.3 nm) by SEM. The absorbance spectra showed a characteristic absorbance peak at 551nm, corresponding to the absorbance peak of the RBITC and the increased signal at shorter wavelengths due the typical scattering of the SiO_2 NPs. Similarly, the photoluminescence spectrum of SiO_2-RBITC NPs showed the characteristic emission peak of RBITC at 580nm, confirming that the fluorescence of RBITC is preserved after being embedded in the SiO_2 core.

Once particles were cleaned, were used as seeds for the growth of a SiO_2 layer using a mixture of TEOS and APTES-FITC complex, in order to attach the FITC sensor dye molecules within the silica matrix, by a second alkaline Stöber hydrolysis and condensation.

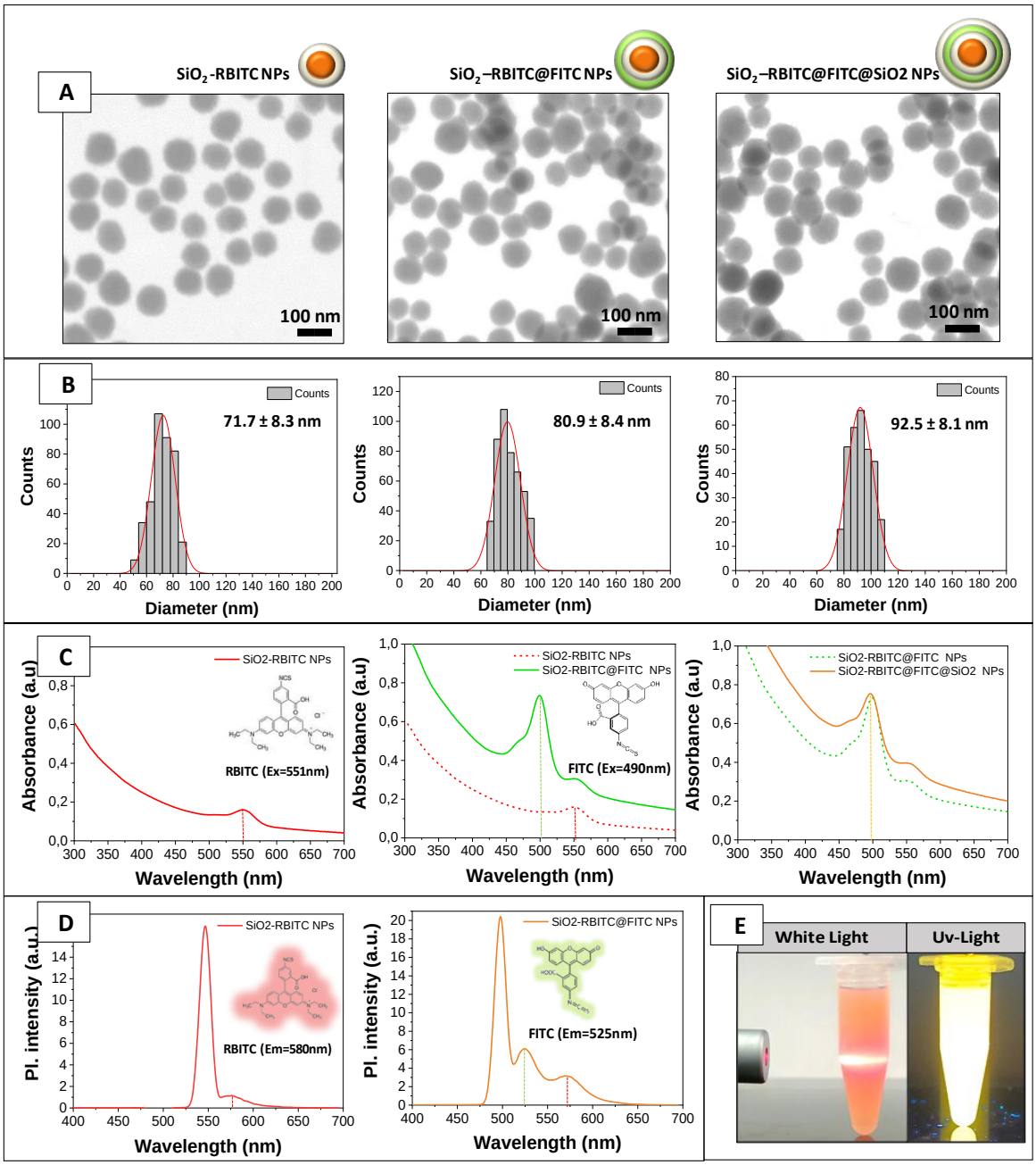

Figure 3.14 Characterization of the dual-emission core-shell SiO_2-RBITC@FITC@SiO_2 NP using a multi-step modified Stöber method. (A) Representative (STEM) images of NPs and its production process. From left to right: SiO_2-RBITC, SiO_2-RBITC@FITC@SiO_2 and SiO_2-RBITC@FITC@SiO_2 NPs. (B) Calculated size distribution profile of NPs. Mean size and Standard distribution was calculated at least counting 300 particles using software image J. (C) Absorbance spectra 1/10 dilution of the SiO_2-RBITC@FITC@SiO_2 NPs and its production process. From left to right, SiO_2-RBITC, SiO_2-RBITC@FITC@SiO_2 and SiO_2-RBITC@FITC@SiO_2 NPs. The characteristic RBITC and FITC absorbance peaks around 550nm and 495nm, respectively. (D) Photoluminescence spectra 1/10 dilution of SiO_2-RBITC NPs and SiO_2-RBITC@FITC@SiO_2 NPs showing the characteristic RBITC and FITC emission peaks at 580nm and 525nm, respectively. (E) Optical image of colloidal solution of SiO_2-RBITC@FITC@SiO_2 NPs under white light and UV-light, revealing the yellow fluorescent colour, by the combination of FITC and RBITC.

The seeds NPs loaded with FITC, were label as SiO_2–RBITC@FITC NPs, revealing a mean size distribution (80.9 ± 8.4 nm) by SEM. Approximately 10nm in SiO_2 shell were growth. The absorbance spectra showed both characteristic absorbance peaks at 495nm corresponding to the FITC and the second at 551nm peak of the RBITC, revealing the presence of both organic dyes in the SiO_2 particles. The increased signal was due the typical scattering of the SiO_2 NPs, that were bigger in size. Similarly, the photoluminescence spectrum of SiO2-RBITC@FITC NPs showed the characteristic emission peak of FITC at 525nm, and RBITC 580nm confirming that both fluorophores embedded in the SiO_2 particles.

For quantify the loading RBITC and FITC concentration inside the dual-emission NPs, first a calibration curve was built using standard FITC and RBITC solution in water, measuring the photoluminescence signal of their respective emission maximum intensity. Second, the dye concentration was calculated measuring the difference in fluorescence between the dye concentration added for the synthesis and the remaining dye in the supernatant. The calibration curve, as well as the detailed calculations are showed in the (**Appendix B7**). Therefore, the concentration of RBITC found inside the NPs was 0.011 mM (15.1% of loaded yield) and for FITC was 0.0064mM (12.8% of yield). Finally, once the dual-emission core–shell silica particles were cleaned, a final SiO_2 layer were growth, in order to protect the FITC from external interactions, following the same strategy of heterogeneous nucleation, using the particles a seed. The SiO_2-RBITC@FITC@SiO_2 NP revealed a final mean size distribution (92.4 ± 8.1 nm) by SEM, about 10nm in SiO_2 shell were growth. The absorbance and photoluminescence spectrum showed both characteristic absorbance of the RBITC and FTIC, with the increased signal was due the SiO_2 scattering. experimental described in detail, **Chapter 5, section 5.2.2.5**. Representative Scanning Transmission Electron microscopy (STEM) images of the synthetic process for preparation the SiO_2-RBITC@FITC@SiO_2 NPs, are shown in **figure 3.14-A**, the particles displayed a spherical monodisperse morphology. Finally, the optical images of colloidal solutions under white light and UV-light are shown in the last figure E. The complete characterization is showed in **figure 3.14**.

3.5.2 In vitro evaluation of the Multilayer Dual-Emission Core-Shell SiO_2 Nanoparticles after Incubation in Physiological Media.

After the dual-emission SiO_2-RBITC@FITC@SiO_2 NPs were prepared and characterized, as proof-of-concept, the NPs were incubated in physiological conditions for seven days, using fetal bovine serum (FBS) as proteins source in a physiological solution at pH 7.2 composed with Dulbecco's Modified Eagle Medium (DMEM) without phenol red, in order to observe the colloidal behaviour of the particles upon incubation. For the experiments, 0.2 mL of the SiO_2-RBITC@FITC@SiO_2 NPs were incubated in (10% FBS with 90%DMEM at 37°C), in a total volume of 2.0mL. The diameter of the NPs, the photoluminescence spectrums at excitation energy of 490nm and 540nm, were monitored as a function of time for seven days by electron microscopy (STEM) and by fluorescence using the calibration curve. Also, the colloidal solution of the NPs after incubation were exposed under UV-light, in order to observe changes any change in the fluorescent colour. The results are showed in **figure 3.15**.

Our results in **figure 3.15-A**, revealed that the SiO_2-RBITC@FITC@SiO_2 NPs were structural changing, surely by dissolution after incubation in physiological media for seven days. The calculated mean size of the NPs revealed only a slightly decreased from (92.5 ± 8.1 nm to 79.1 ± 17.3nm), but the morphology of the NPs by STEM, showed that they evolved decreasing the contrast of particles with increasing the surface roughness in the end.

This observation suggested that the NPs were losing mass by dissolution, from both core and surface, towards a hollow silica structure. Park et al [94] reported the same behaviour of size-dependent shape dissolution of silica nanoparticles. They explained that silica particles develop small pores inside the nanoparticles under slightly basic conditions as a result of base-catalyzed etching. The ammonium hydroxide or other base, can potentially act as an etchant for silica particles, causing these internal structural changes. The mechanism of dissolution is through a series of bond-breaking Si-O and bond-making processes by the hydroxide ions (OH^-), causing the small pores to collapse into larger voids to reduce the surface energy. These larger voids eventually merge and form a hollow core. Moreover, Yongxing Hu et al [95] reported a similar behaviour in hollow formation inside

the NPs, but were dispersed in water (in their water-based etching strategy) for converting solid silica into porous ones with controllable permeability. Therefore, the dissolution of the SiO_2 NPs can happen even in neutral conditions. This explains why the mean size of particles display a small change. In contrast, the standard distribution of the mean size of the NPs increased, suggesting an heterodipersity of the colloidal particles or aggregation. Same author explained this phenomenon demonstrating that larger silica particles are denser and more stable to chemical etching, as bulk silica.

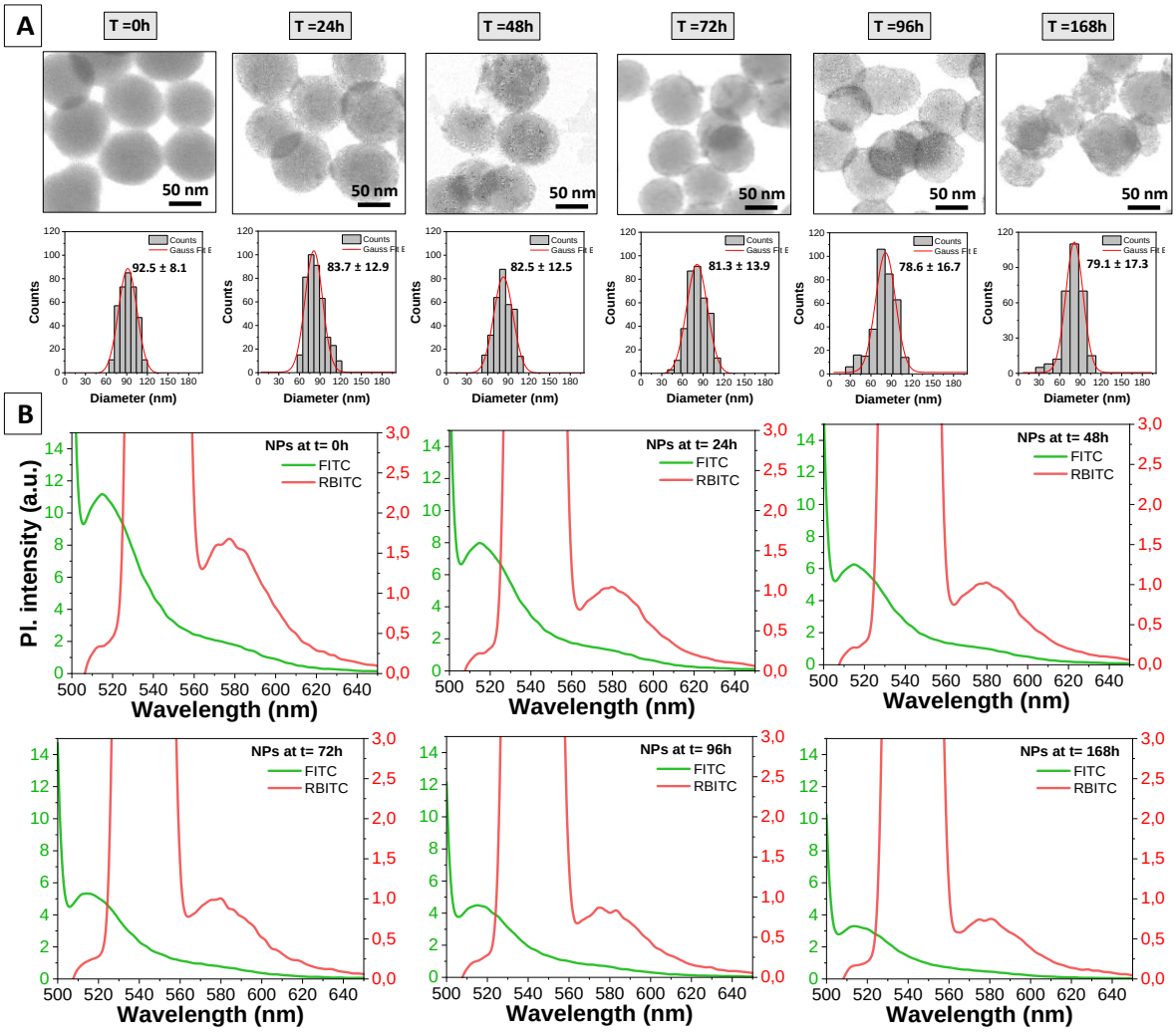

Figure 3.15 Characterization of the dual-emission core-shell SiO_2 NPs (SiO_2-RBITC@FITC@SiO_2 NPs) as a function of time, after seven days of incubation in physiological media. (A) Representative STEM images of SiO_2-RBITC@FITC@SiO_2 NPs and Calculated size distribution profile of NPs. Mean size and Standard distribution was calculated at least counting 300 particles using software image J. (B) Photoluminescence spectra 1/10 dilution of the SiO_2-RBITC@FITC@SiO_2 NPs showing the characteristic RBITC and FITC emission peaks at 580nm and 525nm, respectively.

Finally, the photoluminescence spectra of the NPs showed in **figure 3.15-B**, revealed a decreased signal of FITC (emission at 525nm) as a function of time, as well as the RBITC (emission 580nm) intensity. These results were not expected, because the main idea was a developed a controlled released of dye (the doped in the external layer first), but the formation of small pores inside the particles explain the liberation of both dyes simultaneously.

In this regard, in order to understand the released profile of the dyes in our hybrid dual-emission particles, the dyes in solution were quantified by photoluminescence spectroscopy and the final fluorescence of the NPs were recorded under UV-light. The obtained results are showed in **figure 3.16**, and the dye concentrations were calculated using photoluminescence spectrums of the supernatant (showed in **Appendix B8**).

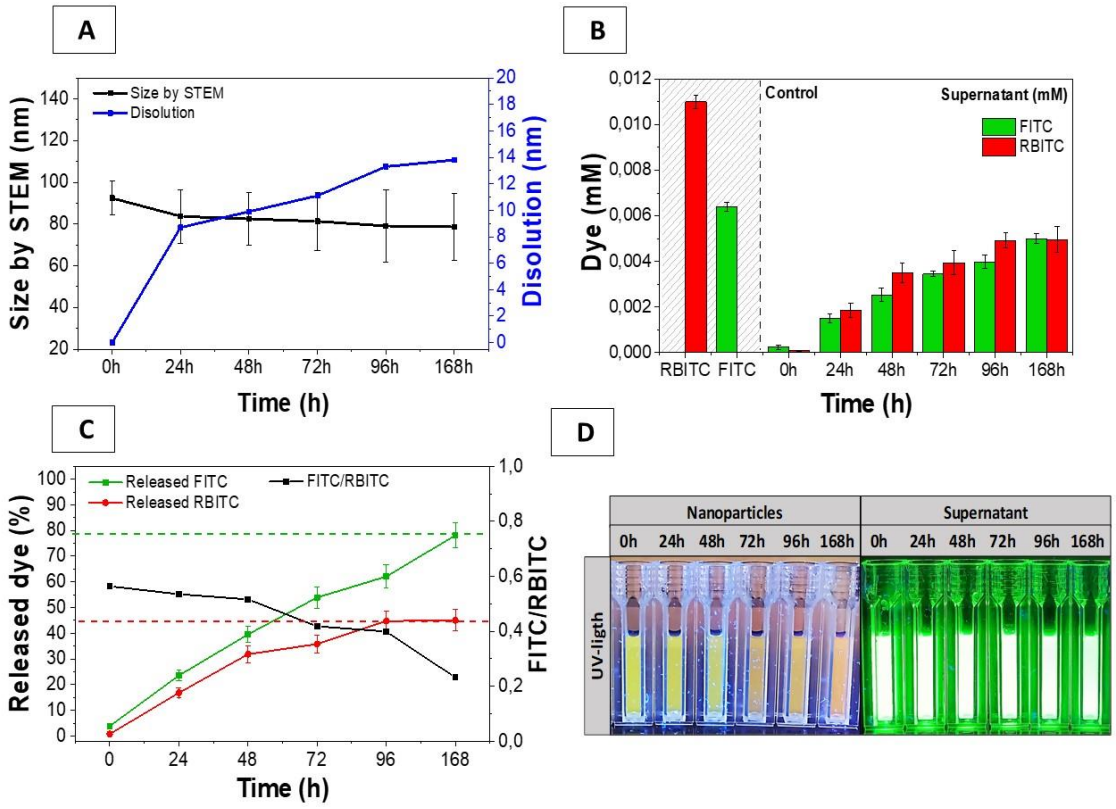

Figure 3.16 Graphical representation of the characterization of the SiO_2-RBITC@FITC@SiO_2 NPs after dissolution as a function of time. (A) Mean size and standard distribution as a function of particle dissolution. (B) Calculated released dye FITC and RBITC using calibration curve (**Appendix C8**). In shaded the incorporated concentration of dyes in the initial NPs as control. (C). Calculated released dyes RBITC and FTIC after particle dissolution as a function of FITC/RBIC concentration. (D)Optical image of colloidal solution of SiO_2-RBITC@FITC@SiO_2 NPs and supernatant under UV-light, revealing the different fluorescent colours upon dissolution.

As showed in **figure 3.16-A**, the mean size of the NPs decreased to 79.1 ± 17.3nm, revealing a size decrease of about 13nm after 7 days of incubation. This observation was commented previously that dissolution goes thorough pores formation, rather than surface etching. Although the etching reaction can also occur at the exterior of the nanoparticles, the surface energy of the exterior should be lower than that of small pores inside the nanoparticles, leading to site-dependent etching reactivity. Later, in **figure 3.16-B**, the released FTIC and RBITC from the NPs were calculated. The results showed a progressively released of both dyes over time. The liberation of the entrapped dyes was explained by the silica dissolution mechanism in aqueous conditions, in which, small molecules, such as dyes, can diffuse relatively easily out of the formed pores, after Si-O bond breaking, as demonstrated by Tierui Zhang et al [96] in the spontaneous dissolution and regrowth process of silica. Interestingly, as showed by the **figure 3.16-C**, the concentration of liberated dyes in the supernatant, increases over time for both fluorophores, until a released of almost 79% of FITC and 43% of RBITC, suggesting that both entrapped dyes were diffusing from the NPs structure at the same time.

However, because of the calculated relationship (FITC/RBIC) in concentration in the same interval, decreased from 0.5 to 0.2, indicate that the FITC were released faster than the RBITC, result in agreement with the fact that FITC were in the outer layer. However, because of the concentration of RBITC dyes in the SiO_2-RBITC@FITC@SiO_2 NPs were two times bigger than FITC, a further study in the size-depend diffusion of dyes need to be properly addressed and were out of the scope of this study. Finally, the different NPs obtained at different times after dissolution in the physiological media were suspended in water at neutral pH and after exposing them to UV-light, the different fluorescent colours were exhibited, from yellow to a pale red, indicating that upon dissolution the RBITC were in higher concentration than the green FITC dye, that can be seen on the supernatant.

3.5.3 In vitro evaluation of the Multilayer Dual-Emission Core-Shell SiO_2 Nanoparticles after Incubation in HEK Cell Lines

In addition, an in-vitro experiment was done, in which the dual-emission particles were incubated in a HEK cell lines, with the purpose of colocalization the presence of both dyes in a more realistic biological environment, using a high-resolution confocal microscopy, (Experimental described in detail, **Chapter 5, section 5.2.4)**.

The results of the in-vitro experiment of the SiO_2-RBITC@FITC@SiO_2 NPs, after incubating the NPs with HEK293 cell line, in order to localize the intensity of both fluorophore FITC and RBITC are showed in **figure 3.17**.

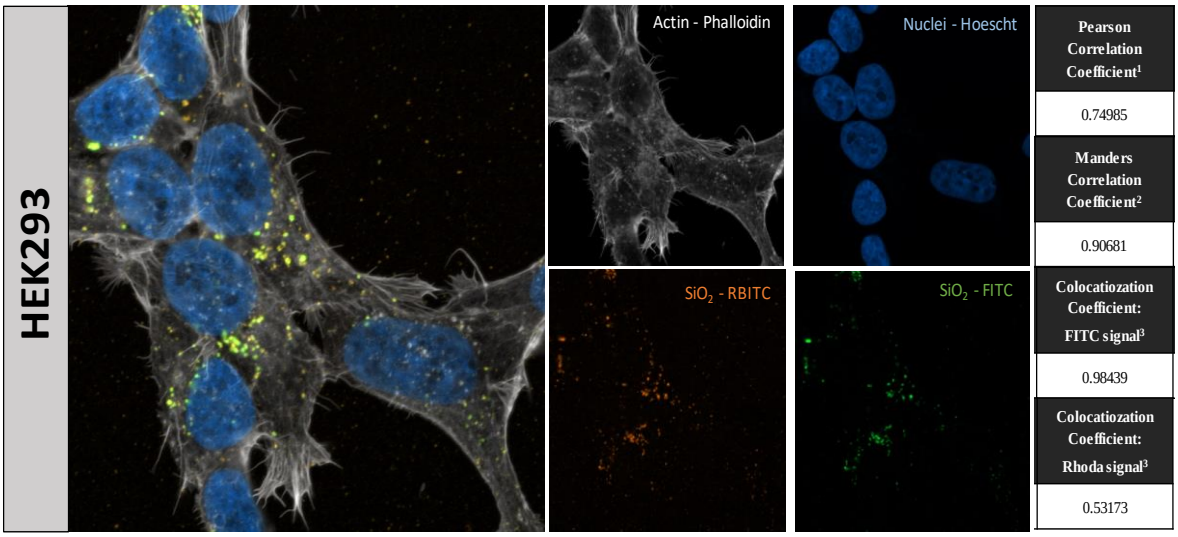

Figure 3.17 Graphical representation of the colocalization analysis of the SiO_2-RBITC@FITC@SiO_2 NPs when exposed to HEK290 cells for 24h under high-resolution laser confocal microscopy. Zen Blue 3.0 (Zeiss) software was used to perform the colocalization analysis. Pearson and Manders Correlation Coefficients shown a positive correlation between signals. RBITC (em558/ex575) and FITC (em490/ex525) were observed using the standard fluorescence mode and pre-defined settings. Colours from the images acquired are chosen arbitrarily in each case to better discriminate all the signals collected. Pearson and Manders Correlation Coefficients shown a positive correlation for Au:FITC signal. This value quantifies the degree to which two channels follow a simple linear relationship of intensity. Values can range from -1 (an inverse or "anti-colocalization" relationship), to 0 (a random cloud of no relationship), or +1 (a perfect linear slope). This measurement is similar to Pearson's above but ranges from 0 to +1. It does not incorporate a relationship to mean intensity (as with Pearson's), so it largely just looks for spatial overlap alone above the fixed threshold. 3These values are reported as pairs that range from 0 to 1. The metric simply calculates the fraction of pixels colocalized to the total number of pixels from the specified channel.

These experiments were done under the direction and collaboration with the PhD student, Muriel Freixanet Gusta, from the Vall d'Hebron Institute of Research (VHIR), in the Research Group Pharmacokinetic Nanoparticles. Before the exposure to cultured cells, NPs were stabilized with BSA in order to avoid NP aggregation upon dispersion in the culture media.

Later, the HEK cells were incubated the SiO_2-RBITC@FITC@SiO_2 NPs and imaged using the confocal microscope. After 24h, particles were fixed and stained for their visualization on the confocal microscope. NPs were simultaneously imaged by the FITC (green) and the Rhodamine (orange) dyes present on the particles using the conventional fluorescence mode with the super-resolution Airyscan detector. the multiplex staining with the Phalloidin and the Hoechst allows us to locate the NPs in the sample, either in the extracellular space, intracellularly or bound to the cell membrane, from a certain z-section of the sample. As shown in **figure 3.17**, the cells show a good morphology with no signs of necrosis after 24h of NPs exposure. NPs appear to be mostly internalized in the cytoplasmic space. The signal from FITC and Rhodamine present in the NPs could be specifically collected without any signal overlap from the other emission tracks. Additionally, a colocalization analysis of the FITC and Rhodamine signals was performed. The colocalization coefficient was measured as a function of the pixel intensity (Pearson Correlation Coefficient) and as function of the spatial overlap (Manders Correlation Coefficient). In both cases, it shows a positive correlation between the FITC and Rhodamine signal, suggesting that both dyes are located in the same space, indicating that the dual-emission NPs can be used in further biological studies as fluorescent sensors probe on the nanoscale.

3.6 References

[1] M. C. Gomes, Â. Cunha, T. Trindade, and J. P. C. Tomé, "The role of surface functionalization of silica nanoparticles for bioimaging," *J. Innov. Opt. Health Sci.*, vol. 9, no. 4, p. 1630005, Mar. 2016, doi: 10.1142/S1793545816300056.

[2] N. Desai, "Challenges in development of nanoparticle-based therapeutics," *AAPS J.*, vol. 14, no. 2, pp. 282–295, Jun. 2012, doi: 10.1208/s12248-012-9339-4.

[3] E. Phillips *et al.*, "Clinical translation of an ultrasmall inorganic optical-PET imaging

nanoparticle probe," *Sci. Transl. Med.*, vol. 6, no. 260, p. 260ra149-260ra149, Oct. 2014, doi: 10.1126/scitranslmed.3009524.

[4] L. Wang, W. Zhao, and W. Tan, "Bioconjugated silica nanoparticles: Development and applications," *Nano Res.*, vol. 1, no. 2, pp. 99–115, 2008, doi: 10.1007/s12274-008-8018-3.

[5] L. Guerrini, R. A. Alvarez-Puebla, and N. Pazos-Perez, "Surface Modifications of Nanoparticles for Stability in Biological Fluids," *Mater. (Basel, Switzerland)*, vol. 11, no. 7, p. 1154, Jul. 2018, doi: 10.3390/ma11071154.

[6] M. Catauro and S. V Ciprioti, "Characterization of Hybrid Materials Prepared by Sol-Gel Method for Biomedical Implementations. A Critical Review," *Materials* , vol. 14, no. 7. 2021, doi: 10.3390/ma14071788.

[7] S. Pandey and S. B. Mishra, "Sol–gel derived organic–inorganic hybrid materials: synthesis, characterizations and applications," *J. Sol-Gel Sci. Technol.*, vol. 59, no. 1, pp. 73–94, 2011, doi: 10.1007/s10971-011-2465-0.

[8] P. Judeinstein and C. Sanchez, "Hybrid organic–inorganic materials: a land of multidisciplinarity," *J. Mater. Chem.*, vol. 6, no. 4, pp. 511–525, 1996, doi: 10.1039/JM9960600511.

[9] M. Ochi and R. Takahashi, "Phase structure and thermomechanical properties of primary and tertiary amine-cured epoxy/silica hybrids," *J. Polym. Sci. Part B Polym. Phys.*, vol. 39, no. 11, pp. 1071–1084, Jun. 2001, doi: https://doi.org/10.1002/polb.1084.

[10] P. Yang, S. Gai, and J. Lin, "ChemInform Abstract: Functionalized Mesoporous Silica Materials for Controlled Drug Delivery," *Chem. Soc. Rev.*, vol. 41, pp. 3679–3698, Mar. 2012, doi: 10.1039/c2cs15308d.

[11] Y. Yang, M. Zhang, H. Song, and C. Yu, "Silica-Based Nanoparticles for Biomedical Applications: From Nanocarriers to Biomodulators," *Acc. Chem. Res.*, vol. 53, no. 8, pp. 1545–1556, Aug. 2020, doi: 10.1021/acs.accounts.0c00280.

[12] A. Liberman, N. Mendez, W. C. Trogler, and A. C. Kummel, "Synthesis and surface functionalization of silica nanoparticles for nanomedicine," *Surf. Sci. Rep.*, vol. 69, no. 2, pp. 132–158, 2014, doi: https://doi.org/10.1016/j.surfrep.2014.07.001.

[13] I. Slowing, B. G. Trewyn, and V. S.-Y. Lin, "Effect of Surface Functionalization of MCM-41-Type Mesoporous Silica Nanoparticles on the Endocytosis by Human Cancer Cells," *J. Am. Chem. Soc.*, vol. 128, no. 46, pp. 14792–14793, Nov. 2006, doi: 10.1021/ja0645943.

[14] T. Yu, D. Hubbard, A. Ray, and H. Ghandehari, "In vivo biodistribution and pharmacokinetics of silica nanoparticles as a function of geometry, porosity and surface characteristics," *J. Control. Release*, vol. 163, no. 1, pp. 46–54, 2012, doi: https://doi.org/10.1016/j.jconrel.2012.05.046.

[15] B. Qiao, T.-J. Wang, H. Gao, and Y. Jin, "High density silanization of nano-silica particles using γ-aminopropyltriethoxysilane (APTES)," *Appl. Surf. Sci.*, vol. 351, pp. 646–654, 2015, doi: https://doi.org/10.1016/j.apsusc.2015.05.174.

[16] B. M. Estevão, I. Miletto, N. Hioka, L. Marchese, and E. Gianotti, "Mesoporous Silica Nanoparticles Functionalized with Amino Groups for Biomedical Applications," *ChemistryOpen*, vol. 10, no. 12, pp. 1251–1259, Dec. 2021, doi: 10.1002/open.202100227.

[17] A.-M. Putz, L. Almásy, A. Len, and C. Ianasi, "Functionalized silica materials

synthesized via co-condensation and post-grafting methods," *Fullerenes, Nanotub. Carbon Nanostructures*, vol. 27, pp. 1–14, Mar. 2019, doi: 10.1080/1536383X.2019.1593154.

[18] G. Wang, A. N. Otuonye, E. A. Blair, K. Denton, Z. Tao, and T. Asefa, "Functionalized mesoporous materials for adsorption and release of different drug molecules: A comparative study," *J. Solid State Chem.*, vol. 182, no. 7, pp. 1649–1660, 2009, doi: https://doi.org/10.1016/j.jssc.2009.03.034.

[19] C. Delacôte, F. O. M. Gaslain, B. Lebeau, and A. Walcarius, "Factors affecting the reactivity of thiol-functionalized mesoporous silica adsorbents toward mercury(II)," *Talanta*, vol. 79, no. 3, pp. 877–886, 2009, doi: https://doi.org/10.1016/j.talanta.2009.05.020.

[20] M. Sharifi, R. Marschall, M. Wilhelm, D. Wallacher, and M. Wark, "Detection of Homogeneous Distribution of Functional Groups in Mesoporous Silica by Small Angle Neutron Scattering and in Situ Adsorption of Nitrogen or Water," *Langmuir*, vol. 27, no. 9, pp. 5516–5522, May 2011, doi: 10.1021/la2000188.

[21] I. A. Rahman and V. Padavettan, "Synthesis of silica nanoparticles by sol-gel: size-dependent properties, surface modification, and applications in silica-polymer nanocomposites — a review," *J. Nanomater.*, vol. 2012, p. 8, 2012, doi: 10.1155/2012/132424.

[22] K.-M. Kim *et al.*, "Colloidal Properties of Surface Coated Colloidal Silica Nanoparticles in Aqueous and Physiological Solutions," *Sci. Adv. Mater.*, vol. 6, no. 7, pp. 1573–1581, 2014, doi: 10.1166/sam.2014.1837.

[23] K.-M. Kim *et al.*, "Colloidal behaviors of ZnO nanoparticles in various aqueous media," *Toxicol. Environ. Health Sci.*, vol. 4, no. 2, pp. 121–131, 2012, doi: 10.1007/s13530-012-0126-5.

[24] K.-M. Kim *et al.*, *Surface treatment of silica nanoparticles for stable and charge-controlled colloidal silica*, vol. 9. 2014.

[25] F. Vatansever and M. R. Hamblin, "Surface-initiated polymerization with poly(n-hexylisocyanate) to covalently functionalize silica nanoparticles," *Macromol. Res.*, vol. 25, no. 2, pp. 97–107, 2017, doi: 10.1007/s13233-017-5009-9.

[26] I.-L. Hsiao *et al.*, "Biocompatibility of Amine-Functionalized Silica Nanoparticles: The Role of Surface Coverage," *Small*, vol. 0, no. 0, p. 1805400, doi: doi:10.1002/smll.201805400.

[27] K. N. Pham, D. Fullston, and K. Sagoe-Crentsil, "Surface Charge Modification of Nano-Sized Silica Colloid," *Aust. J. Chem.*, vol. 60, no. 9, pp. 662–666, 2007, doi: https://doi.org/10.1071/CH07138.

[28] C. Yi, W. Qingqiao, P. Hongkun, and L. C. M., "Nanowire Nanosensors for Highly Sensitive and Selective Detection of Biological and Chemical Species," *Science (80-.).*, vol. 293, no. 5533, pp. 1289–1292, Aug. 2001, doi: 10.1126/science.1062711.

[29] D. E. Leyden, "Characterization and Chemical Modification of the Silica Surface By E. F. Vansant, P. Van Der Voort, and K. C. Vrancken (University of Antwerp, Belgium). Elsevier: The Netherlands. 1995. xv + 556. $241.25. ISBN 0-444-81928-2," *J. Am. Chem. Soc.*, vol. 118, no. 12, p. 3071, 1996, doi: 10.1021/ja955247o.

[30] B. M. Cash, L. Wang, and B. C. Benicewicz, "The preparation and characterization of carboxylic acid-coated silica nanoparticles," *J. Polym. Sci. Part A Polym. Chem.*, vol. 50, no. 13, pp. 2533–2540, 2012, doi: 10.1002/pola.26029.

[31] A. Burns, H. Ow, and U. Wiesner, “Fluorescent core–shell silica nanoparticles: towards ‘Lab on a Particle’ architectures for nanobiotechnology,” *Chem. Soc. Rev.*, vol. 35, no. 11, pp. 1028–1042, 2006, doi: 10.1039/B600562B.

[32] H. Ow, D. R. Larson, M. Srivastava, B. A. Baird, W. W. Webb, and U. Wiesner, “Bright and Stable Core−Shell Fluorescent Silica Nanoparticles,” *Nano Lett.*, vol. 5, no. 1, pp. 113–117, Jan. 2005, doi: 10.1021/nl0482478.

[33] S. Bonacchi *et al.*, “Luminescent Silica Nanoparticles: Extending the Frontiers of Brightness,” *Angew. Chemie Int. Ed.*, vol. 50, no. 18, pp. 4056–4066, Apr. 2011, doi: https://doi.org/10.1002/anie.201004996.

[34] R. P. Bagwe, C. Yang, L. R. Hilliard, and W. Tan, “Optimization of Dye-Doped Silica Nanoparticles Prepared Using a Reverse Microemulsion Method,” *Langmuir*, vol. 20, no. 19, pp. 8336–8342, Sep. 2004, doi: 10.1021/la049137j.

[35] R. Riccò, S. Nizzero, E. Penna, A. Meneghello, E. Cretaio, and F. Enrichi, “Ultra-small dye-doped silica nanoparticles via modified sol-gel technique,” *J. Nanoparticle Res.*, vol. 20, no. 5, p. 117, 2018, doi: 10.1007/s11051-018-4227-1.

[36] F. J. Arriagada and K. Osseo-Asare, “Synthesis of Nanosize Silica in Aerosol OT Reverse Microemulsions,” *J. Colloid Interface Sci.*, vol. 170, no. 1, pp. 8–17, 1995, doi: https://doi.org/10.1006/jcis.1995.1064.

[37] A. Van Blaaderen and A. Vrij, “Synthesis and characterization of colloidal dispersions of fluorescent, monodisperse silica spheres,” *Langmuir*, vol. 8, no. 12, pp. 2921–2931, 1992, doi: 10.1021/la00048a013.

[38] R. A. Sperling and W. J. Parak, “Surface modification, functionalization and bioconjugation of colloidal inorganic nanoparticles,” *Philos. Trans. R. Soc. A Math. Phys. Eng. Sci.*, vol. 368, no. 1915, pp. 1333–1383, Mar. 2010, doi: 10.1098/rsta.2009.0273.

[39] K. M. R. Kallury, P. M. Macdonald, and M. Thompson, “Effect of Surface Water and Base Catalysis on the Silanization of Silica by (Aminopropyl)alkoxysilanes Studied by X-ray Photoelectron Spectroscopy and 13C Cross-Polarization/Magic Angle Spinning Nuclear Magnetic Resonance,” *Langmuir*, vol. 10, no. 2, pp. 492–499, 1994, doi: 10.1021/la00014a025.

[40] A. M. Carvalho, R. A. Cordeiro, and H. Faneca, “Silica-Based Gene Delivery Systems: From Design to Therapeutic Applications,” *Pharmaceutics*, vol. 12, no. 7, p. 649, Jul. 2020, doi: 10.3390/pharmaceutics12070649.

[41] M. Friedman, “Applications of the Ninhydrin Reaction for Analysis of Amino Acids, Peptides, and Proteins to Agricultural and Biomedical Sciences,” *J. Agric. Food Chem.*, vol. 52, no. 3, pp. 385–406, 2004, doi: 10.1021/jf030490p.

[42] C.-Y. Wen and J.-Y. Sun, “Quantitative Determination of the Carboxyl Groups on Individual Nanoparticles by Acid-Base Titrimetry,” *ChemistrySelect*, vol. 2, no. 33, pp. 10885–10888, 2017, doi: 10.1002/slct.201702242.

[43] C. Weiss and S. Diabaté, “A special issue on nanotoxicology,” *Arch. Toxicol.*, vol. 85, pp. 705–706, Jul. 2011, doi: 10.1007/s00204-011-0707-0.

[44] F. S. Bierkandt, L. Leibrock, S. Wagener, P. Laux, and A. Luch, “The impact of nanomaterial characteristics on inhalation toxicity,” *Toxicol. Res. (Camb).*, vol. 7, no. 3, pp. 321–346, Feb. 2018, doi: 10.1039/c7tx00242d.

[45] I. Lynch, C. Weiss, and E. Valsami-Jones, “A strategy for grouping of nanomaterials based on key physico-chemical descriptors as a basis for safer-by-design NMs,” *Nano*

Today, vol. 9, no. 3, pp. 266–270, 2014, doi: https://doi.org/10.1016/j.nantod.2014.05.001.

[46] I. I. Slowing, C.-W. Wu, J. L. Vivero-Escoto, and V. S.-Y. Lin, "Mesoporous Silica Nanoparticles for Reducing Hemolytic Activity Towards Mammalian Red Blood Cells," *Small*, vol. 5, no. 1, pp. 57–62, Jan. 2009, doi: https://doi.org/10.1002/smll.200800926.

[47] E.-J. Park and K. Park, "Oxidative stress and pro-inflammatory responses induced by silica nanoparticles in vivo and in vitro," *Toxicol. Lett.*, vol. 184, no. 1, pp. 18–25, 2009, doi: https://doi.org/10.1016/j.toxlet.2008.10.012.

[48] M. Al-Rawi, S. Diabaté, and C. Weiss, "Uptake and intracellular localization of submicron and nano-sized SiO2 particles in HeLa cells," *Arch. Toxicol.*, vol. 85, no. 7, pp. 813–826, 2011, doi: 10.1007/s00204-010-0642-5.

[49] A. Panas *et al.*, "Screening of different metal oxide nanoparticles reveals selective toxicity and inflammatory potential of silica nanoparticles in lung epithelial cells and macrophages," *Nanotoxicology*, vol. 7, Jan. 2012, doi: 10.3109/17435390.2011.652206.

[50] H. Nabeshi *et al.*, "Amorphous nanosilica induce endocytosis-dependent ROS generation and DNA damage in human keratinocytes," *Part. Fibre Toxicol.*, vol. 8, p. 1, Jan. 2011, doi: 10.1186/1743-8977-8-1.

[51] V. Marzaioli *et al.*, "Surface modifications of silica nanoparticles are crucial for their inert versus proinflammatory and immunomodulatory properties," *Int. J. Nanomedicine*, vol. 9, pp. 2815–2832, Jun. 2014, doi: 10.2147/IJN.S57396.

[52] A. Kurtz-Chalot *et al.*, "Adsorption at cell surface and cellular uptake of silica nanoparticles with different surface chemical functionalizations: impact on cytotoxicity," *J. Nanoparticle Res.*, vol. 16, no. 11, p. 2738, 2014, doi: 10.1007/s11051-014-2738-y.

[53] T. Yu, A. Malugin, and H. Ghandehari, "Impact of Silica Nanoparticle Design on Cellular Toxicity and Hemolytic Activity," *ACS Nano*, vol. 5, no. 7, pp. 5717–5728, Jul. 2011, doi: 10.1021/nn2013904.

[54] X. Wei *et al.*, "Cationic nanocarriers induce cell necrosis through impairment of Na+/K+-ATPase and cause subsequent inflammatory response," *Cell Res.*, vol. 25, no. 2, pp. 237–253, 2015, doi: 10.1038/cr.2015.9.

[55] S. T. Moerz and P. Huber, "pH-Dependent Selective Protein Adsorption into Mesoporous Silica," *J. Phys. Chem. C*, vol. 119, no. 48, pp. 27072–27079, 2015, doi: 10.1021/acs.jpcc.5b09606.

[56] Z. Abbas, C. Labbez, S. Nordholm, and E. Ahlberg, "Size-Dependent Surface Charging of Nanoparticles," *J. Phys. Chem. C*, vol. 112, no. 15, pp. 5715–5723, 2008, doi: 10.1021/jp709667u.

[57] R. J. Hunter, "Chapter 2 - Charge and Potential Distribution at Interfaces," in *Zeta Potential in Colloid Science*, R. J. Hunter, Ed. Academic Press, 1981, pp. 11–58.

[58] P. Actis *et al.*, "Voltage-Controlled Metal Binding on Polyelectrolyte-Functionalized Nanopores," *Langmuir*, vol. 27, no. 10, pp. 6528–6533, 2011, doi: 10.1021/la2005612.

[59] Y. Ai, M. Zhang, S. W. Joo, M. A. Cheney, and S. Qian, "Effects of Electroosmotic Flow on Ionic Current Rectification in Conical Nanopores," *J. Phys. Chem. C*, vol. 114, no. 9, pp. 3883–3890, 2010, doi: 10.1021/jp911773m.

[60] M. Ali *et al.*, “Layer-by-Layer Assembly of Polyelectrolytes into Ionic Current Rectifying Solid-State Nanopores: Insights from Theory and Experiment,” *J. Am. Chem. Soc.*, vol. 132, no. 24, pp. 8338–8348, 2010, doi: 10.1021/ja101014y.

[61] M. Niknam Hamidabad, S. Asgari, and R. Haji Abdolvahab, “Nanoparticle-assisted polymer translocation through a nanopore,” *Polymer (Guildf).*, vol. 204, p. 122847, 2020, doi: https://doi.org/10.1016/j.polymer.2020.122847.

[62] A. Lazaro, N. Vilanova, L. Barreto Torres, G. Resoort, I. Voets, and H. J. H. Brouwers, “Synthesis, Polymerization, and Assembly of Nanosilica Particles below the Isoelectric Point,” *Langmuir*, vol. 33, Nov. 2017, doi: 10.1021/acs.langmuir.7b01498.

[63] P. G. Hartley, I. Larson, and P. J. Scales, “Electrokinetic and Direct Force Measurements between Silica and Mica Surfaces in Dilute Electrolyte Solutions,” *Langmuir*, vol. 13, no. 8, pp. 2207–2214, Apr. 1997, doi: 10.1021/la960997c.

[64] K. Mittal, *Silanes and Other Coupling Agents, Volume 4*. 2007.

[65] Y. Pei *et al.*, “Tuning surface properties of amino-functionalized silica for metal nanoparticle loading: The vital role of an annealing process,” *Surf. Sci.*, vol. 648, pp. 299–306, 2016, doi: https://doi.org/10.1016/j.susc.2015.10.019.

[66] Y. Sun *et al.*, “Quantification of amine functional groups on silica nanoparticles: a multi-method approach,” *Nanoscale Adv.*, 2019, doi: 10.1039/c9na00016j.

[67] L. C. Mugica, B. Rodríguez-Molina, S. Ramos, and A. Kozina, “Surface functionalization of silica particles for their efficient fluorescence and stereo selective modification,” *Colloids Surfaces A Physicochem. Eng. Asp.*, vol. 500, pp. 79–87, 2016, doi: https://doi.org/10.1016/j.colsurfa.2016.04.002.

[68] H.-T. Lu, “Synthesis and characterization of amino-functionalized silica nanoparticles,” *Colloid J.*, vol. 75, no. 3, pp. 311–318, 2013, doi: 10.1134/s1061933x13030125.

[69] E. Soto-Cantu, R. Cueto, J. Koch, and P. S. Russo, “Synthesis and Rapid Characterization of Amine-Functionalized Silica,” *Langmuir*, vol. 28, no. 13, pp. 5562–5569, 2012, doi: 10.1021/la204981b.

[70] A. Y. Fadeev and T. J. McCarthy, “Trialkylsilane Monolayers Covalently Attached to Silicon Surfaces: Wettability Studies Indicating that Molecular Topography Contributes to Contact Angle Hysteresis,” *Langmuir*, vol. 15, no. 11, pp. 3759–3766, 1999, doi: 10.1021/la981486o.

[71] T. Schiestel, H. Brunner, and G. Tovar, *Controlled Surface Functionalization of Silica Nanospheres by Covalent Conjugation Reactions and Preparation of High Density Streptavidin Nanoparticles*, vol. 4. 2004.

[72] H.-S. Jung, D.-S. Moon, and J.-K. Lee, “Quantitative Analysis and Efficient Surface Modification of Silica Nanoparticles,” *J. Nanomater.*, vol. 2012, p. 8, 2012, doi: 10.1155/2012/593471.

[73] E. Asenath Smith and W. Chen, “How To Prevent the Loss of Surface Functionality Derived from Aminosilanes,” *Langmuir*, vol. 24, no. 21, pp. 12405–12409, 2008, doi: 10.1021/la802234x.

[74] S. M. Kanan, W. T. Y. Tze, and C. P. Tripp, “Method to Double the Surface Concentration and Control the Orientation of Adsorbed (3-Aminopropyl)dimethylethoxysilane on Silica Powders and Glass Slides,” *Langmuir*, vol. 18, no. 17, pp. 6623–6627, 2002, doi: 10.1021/la0203133.

[75] F. Kunc, V. Balhara, A. Brinkmann, Y. Sun, D. M. Leek, and L. J. Johnston,

"Quantification and Stability Determination of Surface Amine Groups on Silica Nanoparticles Using Solution NMR," *Anal. Chem.*, vol. 90, no. 22, pp. 13322–13330, 2018, doi: 10.1021/acs.analchem.8b02803.

[76] S. Li, Q. Wan, Z. Qin, Y. Fu, and Y. Gu, "Understanding Stöber Silica's Pore Characteristics Measured by Gas Adsorption," *Langmuir*, vol. 31, no. 2, pp. 824–832, 2015, doi: 10.1021/la5042103.

[77] S. Azarshin, J. Moghadasi, and Z. A Aboosadi, "Surface functionalization of silica nanoparticles to improve the performance of water flooding in oil wet reservoirs," *Energy Explor. Exploit.*, vol. 35, no. 6, pp. 685–697, Jun. 2017, doi: 10.1177/0144598717716281.

[78] S. S. Shafqat *et al.*, "Development of amino-functionalized silica nanoparticles for efficient and rapid removal of COD from pre-treated palm oil effluent," *J. Mater. Res. Technol.*, vol. 8, no. 1, pp. 385–395, 2019, doi: https://doi.org/10.1016/j.jmrt.2018.03.002.

[79] B. A. Holm *et al.*, "Nanotechnology in BioMedical Applications," *Mol. Cryst. Liq. Cryst.*, vol. 374, no. 1, pp. 589–598, Jan. 2002, doi: 10.1080/713738279.

[80] B. Kairdolf, A. Smith, T. Stokes, M. Wang, A. Young, and S. Nie, "Semiconductor Quantum Dots for Bioimaging and Biodiagnostic Applications," *Annu. Rev. Anal. Chem. (Palo Alto. Calif).*, vol. 6, Mar. 2013, doi: 10.1146/annurev-anchem-060908-155136.

[81] A. M. Derfus, W. C. W. Chan, and S. N. Bhatia, "Probing the Cytotoxicity Of Semiconductor Quantum Dots," *Nano Lett.*, vol. 4, no. 1, pp. 11–18, Jan. 2004, doi: 10.1021/nl0347334.

[82] C. Walkey, E. A. Sykes, and W. C. W. Chan, "Application of semiconductor and metal nanostructures in biology and medicine," *Hematology*, vol. 2009, no. 1, pp. 701–707, Jan. 2009, doi: 10.1182/asheducation-2009.1.701.

[83] W. Tan *et al.*, "Bionanotechnology based on silica nanoparticles," *Med. Res. Rev.*, vol. 24, no. 5, pp. 621–638, Sep. 2004, doi: https://doi.org/10.1002/med.20003.

[84] J. K. Jaiswal, H. Mattoussi, J. M. Mauro, and S. M. Simon, "Long-term multiple color imaging of live cells using quantum dot bioconjugates," *Nat. Biotechnol.*, vol. 21, no. 1, pp. 47–51, 2003, doi: 10.1038/nbt767.

[85] M. Nakamura, M. Shono, and K. Ishimura, "Synthesis, Characterization, and Biological Applications of Multifluorescent Silica Nanoparticles," *Anal. Chem.*, vol. 79, no. 17, pp. 6507–6514, Sep. 2007, doi: 10.1021/ac070394d.

[86] S. Santra, D. Dutta, and B. M. Moudgil, "Functional Dye-Doped Silica Nanoparticles for Bioimaging, Diagnostics and Therapeutics," *Food Bioprod. Process.*, vol. 83, no. 2, pp. 136–140, 2005, doi: https://doi.org/10.1205/fbp.04400.

[87] H. Yoo and J. Pak, "Synthesis of highly fluorescent silica nanoparticles in a reverse microemulsion through double-layered doping of organic fluorophores," *J. Nanoparticle Res.*, vol. 15, May 2013, doi: 10.1007/s11051-013-1609-2.

[88] X. Mu *et al.*, "A facile and general approach for the synthesis of fluorescent silica nanoparticles doped with inert dyes," *Chinese Sci. Bull.*, vol. 56, no. 31, p. 3242, 2011, doi: 10.1007/s11434-011-4727-1.

[89] J. B. Wacker, I. Lignos, V. K. Parashar, and M. A. M. Gijs, "Controlled synthesis of fluorescent silica nanoparticles inside microfluidic droplets," *Lab Chip*, vol. 12, no. 17, pp. 3111–3116, 2012, doi: 10.1039/C2LC40300E.

[90] W. D. L. van Raamsdonk *et al.*, “Current Insights into Monitoring, Bioaccumulation, and Potential Health Effects of Microplastics Present in the Food Chain,” *Foods* , vol. 9, no. 1. 2020, doi: 10.3390/foods9010072.

[91] A. Imhof, M. Megens, J. J. Engelberts, D. T. N. de Lang, R. Sprik, and W. L. Vos, “Spectroscopy of Fluorescein (FITC) Dyed Colloidal Silica Spheres,” *J. Phys. Chem. B*, vol. 103, no. 9, pp. 1408–1415, Mar. 1999, doi: 10.1021/jp983241q.

[92] S. Shahabi, L. Treccani, R. Dringen, and K. Rezwan, “Dual fluorophore doped silica nanoparticles for cellular localization studies in multiple stained cells,” *Acta Biomater.*, vol. 14, pp. 208–216, 2015, doi: https://doi.org/10.1016/j.actbio.2014.11.037.

[93] M. Kasha, “Energy Transfer Mechanisms and the Molecular Exciton Model for Molecular Aggregates,” *Radiat. Res.*, vol. 20, no. 1, pp. 55–70, Jul. 1963, doi: 10.2307/3571331.

[94] S.-J. Park, Y.-J. Kim, and S.-J. Park, “Size-Dependent Shape Evolution of Silica Nanoparticles into Hollow Structures,” *Langmuir*, vol. 24, no. 21, pp. 12134–12137, Nov. 2008, doi: 10.1021/la8028885.

[95] Y. Hu, Q. Zhang, J. Goebl, T. Zhang, and Y. Yin, “Control over the permeation of silica nanoshells by surface-protected etching with water,” *Phys. Chem. Chem. Phys.*, vol. 12, pp. 11836–11842, Oct. 2010, doi: 10.1039/c0cp00031k.

[96] T. Zhang, J. Ge, Y. Hu, Q. Zhang, S. Aloni, and Y. Yin, “Formation of Hollow Silica Colloids through a Spontaneous Dissolution–Regrowth Process,” *Angew. Chemie Int. Ed.*, vol. 47, no. 31, pp. 5806–5811, Jul. 2008, doi: https://doi.org/10.1002/anie.200800927.

IV. Silica-Based Hybrid Nanostructures with Advanced Optical Properties as a Multimodal Contrast Agent

“I would rather have a mind opened by

wonder than one closed by belief”

Gerry Spence

Chapter 4

Development of an Inorganic-Polymer Hybrid Nanostructure with Multimodal Imaging Capabilities as a model for In vitro and In vivo Identification of Microplastics

Nowadays, there has been an increasing global concerns about the impact of micro/nano sized plastics, by reason of the cumulative production and the fragmentation into smaller particles, suggesting a plausible yet unclear hazard in the natural environment [1]. One of the major issues, is whether microplastics (MPs) can be absorbed and enter the systemic circulation via phagocytosis and endocytosis [2]. At present, the MPs analysis consists in physical characterization (e.g., microscopy), followed by a chemical characterization (e.g., spectroscopy techniques) [3]. The first, relies on isolation of MPs by visual sorting or by some techniques (e.g., filtration, sieving, flotation, elutriation) for further use a microscope. On the other hand, chemical characterization relies on the use of techniques, such as, attenuated total reflection-Fourier transform infrared FTIR (ATR-FTIR), Raman spectroscopy and pyrolysis-gas chromatography–mass spectrometry (Pyro-GC-MS)[4]. Despite the useful combination of both strategies, the identification is based on isolated particles using complex extraction clean-up steps. Therefore, the possibility of observe MPs in manipulative laboratory experiments, is of paramount importance for understanding the fate of these materials. On one hand, electron microscopy, are the most used technique to track particles on the cellular level. Nevertheless, is not chemically specific for MPs detection and not suitable for *in situ* analysis. On the other hand, the use of confocal fluorescence microscopy, suggest more clear advantages. The cell nucleus and other organelles can be stained and the use of tagged particles with florescent dyes, can be used for monitor penetration and localization within cells [5]. However, disadvantages, such as, photobleaching, altering the cellular environment by surface dyes, and dye-leaching, may lead to erroneous interpretation. In addition, limitations in the penetration

depth in biological systems, may also be present [6]. Thus, reliable chemically/optically-specific labels for study the uptake of MPs is highly needed.

Besides the well-established synthetic polymers, polyethylene (PET), polypropylene (PP), polyvinylchloride (PVC), polyurethane (PUR), and poly(methylmetacrylate) (PMMA), polystyrene (PS) is one of the most extensively used type of plastic. It may cause growth inhibition, reproductive dysfunction, and reduced viability in marine organisms [7]. PS particles are synthetized following a free radical chain polymerization [8]. The mechanism involves, the break of a molecules called, radical initiator, to subsequently attack the carbon-carbon double bond of the vinyl monomer, to ultimately prepare polystyrene spheres. Although the synthesis of PS is well described in the literature, can be hardly identified once brought into biological systems [9]. Therefore, incorporating easy labels are highly convenient for tracking them in laboratory experiments. Despite the interest in labelling polymeric particles, there are a few studies addressing the point of incorporating markers. Those were limited to an optical label which is the incorporation of fluorescent molecules. Among the different methodologies for doping fluorophores to polymers, physical adsorption onto the particle surface [10]–[12], covalent attachment [13] or copolymerization of a fluorescent monomer [14]–[18] are the most used. On one hand, labelling particles with fluorescent dyes by physical adsorption may suggest drawbacks, such as, dye leaching from the matrix, since the fluorophores are not covalently linked to the particle. Similarly, the photostability of the fluorophores, may affect the quantum yield of the dye, several dye are pH dependent, (biological studies normally use, different pH and high ionic physiological buffers). On the other hand, covalent attachment, may cause uniformity distribution of the dye into the polymer matrix, which will depend on the experimental conditions for polymerization, such as initiator concentration and the presence of surfactant. For both methodologies, the behaviour of the particle in biological studies, may lead to different biological impact, due to, fluorophores are grafted on the surface. Lastly, copolymerization of the dye, may results in low dye incorporation into the polymer matrix, because of, some of the fluorescent co-monomers, may present a hydrophobic nature, which affect the homogeneous diffusion of the dye trough the water-phase, due to the low water solubility. Furthermore, when dyes and the other monomers

are added to the reaction at once, unstable emulsions, heterogeneous polymers and coagulation are obtained, due to, the different polarities and solubility of the different components. In addition, the use of aromatic co-solvents, such as, bromobenzene for transport the dye through the aqueous phase, hamper the use in biological studies, making it necessary, for most applications to remove it. Therefore, methods for labelling polymeric particles that are not only limited onto the adsorption of fluorescent molecules, are promptly needed. To address this matter, one approach, may comprise the incorporation of label markers in the core of the PS, using compatible materials with high chemical affinity, as a scaffold, to further growth the polymer shell. One strategy could involve the use nanocomposites having a core-shell structure made of an of inorganic-organic materials [19]. This strategy has attracted a great attention since they cover a wide range of properties by combining the contrasting properties of the components. For instance, iron oxide (maghemite (γ-Fe_2O_3), titanium dioxide (TiO_2) or gold (Au), may exhibit properties to respond to magnetic fields or to perform catalysis, or generate heat via surface plasmon resonance (SPR) upon irradiation [20]. In addition, silica (SiO_2) particles, have been used as fluorescent probes, for imaging, sensing and diagnostics applications [21]–[23] and for improving the thermal and mechanical properties of polymeric systems as fillers [24]. Therefore, core-label the polystyrene (PS) nanoparticles with chemically or fluorescently -tagged NCs, used as a core, represent an interesting alternative. However, the low chemical compatibility of these materials with the hydrophobic nature of the PS, hinder the use of these NC, as a *Trojan horse*. Thus, the existence of a chemical bond in the interface, that promotes the strong adhesion between the two phases, is highly required.

In this regard, the use of a silica (SiO_2) as an interphase material between the metal NCs or an organic molecule used as tag reporter with the hydrophobic vinyl polymer, can be an interesting approach for combining these two incompatible materials. Despite of their hydrophilic surface, that displays limited affinity for the hydrocarbon polymer matrix, the well use of suitable organosilanes molecules (silane coupling agents), for functionalize the silica surface, suggest a good alternative, decreasing the surface energy and promoting adhesion between phases [25], [26]. It has been reported that the use of these molecules, increase the surface-free energy and improve the interfacial interaction with other

matrices [27]. In addition, the hydroxyl groups (Si-OH) on the SiO_2 can be easily tailored via siloxane bridging, using this silane coupling agents, to covalently graft polymerizable vinyl groups on the surface [28]. On the other hand, metal nanoparticles, such as gold (Au) nanoparticles, also exhibit low compatibility an agglomeration tendency in polymer matrices due to high surface energy [29]. The chemical interaction between the Au and the polymer must be tailored to form a controllable shell. The use of specific ligands with thiol, disulfide, and trithiocarbonate groups, have been grafted onto Au NPs to improve their stability [30], allowing to reduce the interfacial tension and to stabilize emulsion [31]. Nevertheless, grafting polymerizable mono-vinyl groups onto Au NPs surface, suggest the use of complex ligand-exchange strategies [32]–[34], that make these routes challenging. Therefore, a good approach to introduce the Au colloids in the hydrophobic hydrocarbon matrix, without affecting their optical properties, is to grow a thin layer of SiO_2, to further graft a silane-linker with polymerizable groups as previously mentioned. The silica-coating of gold colloids is well reported in the literature [35], [36], and direct silica coating by Stöber method with any surface modification is described [37], [38]. Thus, the core-shell strategy using other NCs as seed for later growth a polymer shell on the NPs, is a suitable strategy to label the PS nanoparticles. One fashion route to synthetize inorganic-organic core-shell polystyrene nanocomposites is via radical seeded emulsion polymerization. This method use inorganic particles as seeds during the polymerization [39]–[42], and has the advantage to produce systems characterized by an inorganic core surrounded by a polymer shell.

Considering these aspects, in the following chapter, first we study the emulsion polymerization reaction in order to understand the critical parameters for preparing polystyrene particles (PS NPs) using and homogenous nucleation process. The main objective is to understand the synthetic parameters that allow us to control the nucleation and growth of these polymer NPs. Once we understand the homogeneous radical emulsion polymerization for production PS particles, we performed the emulsion polymerization synthesis, but in the presence of inorganic NCs, such as fluorescent core-doped SiO_2 with FITC and metal gold (Au NPs), following and heterogeneous nucleation by the radical seeded emulsion polymerization, in order find the best synthetic conditions for producing core-shell PS particles, having chemically and optical NCs in the core. Thereafter, we

developed a flexible synthetic protocol to produce chemically and/or optically-labelled PS nanoparticles for engineer a polymeric model that allows the risk assessment the biological and ecological impact of the MPs. Our method, based on the controlled growth of PS onto labelled NCs used as a core, relies on the control of chemical affinity between both components. Tagged-NCs were chosen on the basis of their properties; Au NPs were used due to their unique chemical traceability and optical properties, fluorescently-labelled SiO_2 NCs due to their well-known use as biological probes. Since the chemical affinity of the chosen NCs for PS is very low, a thin layer of SiO_2 was grown onto the selected NCs. This allows decreasing the surface energy between both materials, thereby allowing to growth a concentrically PS shell onto the NCs used as a tag. In a second step, the size of the PS shell was controlled by adjusting reaction parameters. The fine adjustment allows to the proper balance of nucleation and growth processes.

Finally, the physiochemical transformation of multimodal contrast agent PS nanoparticles was evaluated in artificial physiological conditions (intravenous, gastric and intestinal simulated fluids) in order to assess their colloidal stability behaviour in biological conditions, as well as, the integrity of the PS shell. Additionally, as a proof-of-concept, the feasibility of the multimodal capabilities of the PEF-labelled PS NPs as contrast agent were demonstrated in vitro with confocal microscopy and in vivo/in situ through CT. The presence of Au allowed the elemental detection of the structure with high sensitivity spectroscopy methods such as, inductively coupled plasma mass spectrometry (ICP-MS). The approach is versatile and straightforward and can be customized to users' needs with a complete set of optical and chemical labels. Furthermore, it can be adapted to a wide range of potential plastic sizes, types and shapes, so we hope that others will use and adapt this method to increase our understanding of microplastics and their interactions with organisms in the environment

4.1 Understanding The Synthesis of Polystyrene (PS) Nanoparticles by Radical Emulsion Polymerization

Emulsion polymerization involves the propagation of relatively water-insoluble vinyl monomer in a latex system (Latex is known to be polymer particles dispersed in an

aqueous phase). These polymer particles can be stabilized by adsorption of surfactant species on the particle surface and polymerization can be generally initiated by a water-soluble or organic-miscible initiator, leading to unique free radical reactions [43]. This mechanism is one of the most common and useful for making polymers and is called free radical chain polymerization [8]. This kind of reaction It is used to make polymers from vinyl monomers; small molecules containing carbon-carbon double bonds, such as, styrene and the reaction also use small molecules called initiators [44]. These initiator molecules present the natural ability to fall apart, having a unpair of electrons in the bond which is broken, generating the so-called free radicals. These radical's fragments are unstable, therefore, they attack the carbon-carbon double bond of the vinyl monomer which has a pair of electrons, generating a new chemical bond between the initiator fragment and the monomer molecule, and at the same time, a migration of one of the electrons of the double bonds, to other carbon atom, generating a new free radical. The reaction is showed in **figure 4.1**.

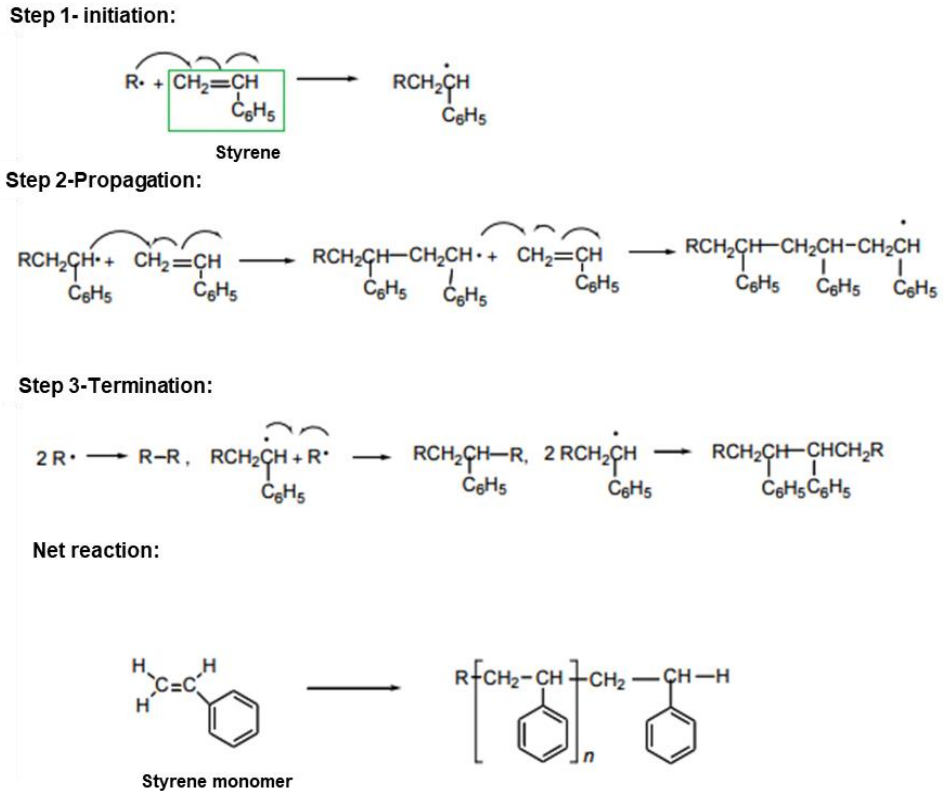

Figure 4.1 Free radical chain polymerization mechanism for production Polystyrene using styrene as vinyl monomer. Adapted from reference [44].

As shown in **figure 4.1**, the mechanism in the free radical chain polymerization involves three main reactions: step 1 (initiation), which involves the formation of radicals by the hemolytic dissociation of an initiator species to yield a pair of radicals R·, followed by the radical's reaction with a vinyl monomer, involving the addition of this radical to the first styrene monomer. Later, the step 2 (propagation), consist in the rapid and progressive addition of monomers to the growing polymer chain without a change of the active centre generating a new radical that has the same identity as the one previously, except that it is larger by one monomer unit. Finally, step 3 (termination), with the destruction of the growth active centre, usually by combination or coupling of the radicals of two growing polymer chains (two growing polymer chains react with each other forming a single nonreactive polymer chain) or by disproportionation (a hydrogen atom is transferred from one radical to the other resulting in two polymers (one with a saturated end and the other with an unsaturated) [45]. One thing to take into account is the polymerization initiators, can be organic or inorganic. The characteristics to the synthesized polymeric materials, may be influenced by the initiator used. The water-soluble initiators (inorganic) produce almost all of the free radicals in the aqueous phase, while the initiators soluble in organic solvents distribute their radicals among four phases, monomer-micelle, monomer-polymer particles, monomer droplets and aqueous phase. The initiator is responsible for functional groups on the particles surfaces. During polymerization, free radicals from the initiator become incorporated into the end groups of the polymer chains and hence any functional or polar groups on the initiators will lead to functionalized or polar particles. Particles using, 4,4 ′-azobis(4-cyanovaleric acid) (ACVA) or 2,2-azobis(isobutyronitrile) (AIBN) as initiator could be redispersed in low polarity solvents, whereas particles using potassium persulfate (KPS), could only be dispersed in higher polarity solvents. They attributed this to the weakly acidic surfaces and low surface charge densities of ACVA particles compared to the strongly acidic surfaces and high surface charge densities of the KPS particles [46].

In this regard, one of the first report (1965) for producing polystyrene particles were done by Matsumoto et al [47]. They performed a radical polymerization of styrene in aqueous solution in the absence of any emulsifier, using styrene as monomer and potassium persulfate (KPS) as initiator. They were able to tuned the size of the polymer

particles between 260-1000nm, having the narrowest particle size distribution at a concentration of KPS (0.00062 mol/l), monomer concentration (0.871 mol/l), speed of agitation 250 rpm, temperature 70°C and polymerization time of 28.5 hours. They reported that the polymer particles were stabilized by electrical repulsion force by the ($\bullet SO4^-$) groups on the surface which are covalently linked to the polymer molecules. In addition, they found that the particle size and the degree of polymerization decrease as the speed of agitation increases. Later extended characterization works were done by Kotera et al in 1970 [46], in which polystyrene particles were polymerized as well by a surfactant-free solution, using potassium persulphate as an initiator. They obtained polymer dispersions of particles having high monodispersity and their diameters could be varied within a wide range (350 to 1400 nm). Recently, M.N. Gords et al [48] (2012); synthesize polymer spheres with controlled diameter and very narrow size distribution by emulsion polymerization, using two different initiators (ACVA and KPS) and the use of (PVP) as stabilizer agent. They discovered that the use of PVP prevented the aggregation of colloidal PS particles during the polymerization. The polystyrene particles were in size between 500-3000 nm. They conclude that increasing initiator concentrations, lead to a higher rate of polymerization, therefore, the smaller PS particles were obtained. They attributed this size difference to the different diffusion rates of the initiators. The KPS, soluble in aqueous phase, diffuses at a fast rate to the monomer where polymerization takes place, resulting in particles of smaller diameter. In contrast, the organic initiator (ACVA), had a diffusion rate slower in aqueous phase, slowing down the polymerization process and, therefore, obtaining larger size particle. However smaller PS NPs in the sub-100nm regime with narrow size distribution were not achieved.

As previously discussed, the synthesis of sub-100 nm polymeric PS nanoparticles in a surfactant-free form is currently very challenging due to the oil nanoemulsion instability in polar solvents and in the absence of ligands stabilizers. Therefore, in order to synthesize colloidal polymer particles at the nanoscale size regime with tunable functionality, emulsion or dispersion polymerization techniques aided with a surfactant stabilizer may be employed. In this regard, the study and synthesis of polystyrene (PS) nanoparticles (NPs) were done modifying the emulsion polymerization method [49]. Styrene (Sty) were use as

precursor, potassium persulfate salt (KPS) as polymer initiator and sodium dodecyl sulphate (SDS) as stabilizing agent. The reaction was conducted in a water (depending ethanol as co-solvent) and the temperature was fixed at 80°C under magnetic agitation.

4.1.1 Tailoring the Particle Size of Monodisperse Colloidal Polystyrene NPs

The emulsion polymerization reaction of polystyrene NPs, involves the polymerisation of the immiscible styrene vinyl monomer in aqueous media in the presence of a water-soluble initiator (KPS) and a surfactant (SDS) to stabilise the growing polymer particle. Usually the process is divided into three distinct stages, as showed in **figure 4.2**.

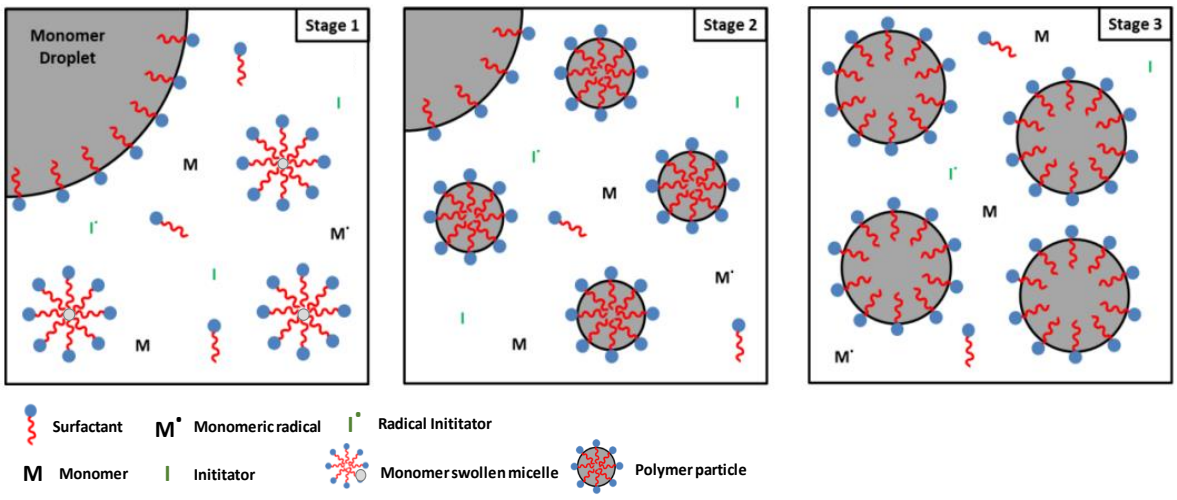

Figure 4.2 Schematic representation of the emulsion polymerization process, divided in three main stages. Stage 1, nucleation of particle nuclei by capture of radicals by monomer-swollen micelles, stage 2, growth of polymer particles by recruiting monomer and surfactant from the emulsified monomer droplets, and Stage 3, depletion of residual monomer in polymer particles. The Monomer droplets act as reservoirs to supply the growing particles with monomer and surfactant species. Adapted from reference [50].

The mechanism of formation begins with the production of the micrometre-sized surfactant-stabilised styrene monomer droplets, smaller soluble monomer-swollen surfactant micelles and a relatively small amount of molecularly-dissolved styrene monomer. Later, the thermal decomposition of the radical initiator molecules (KPS) generates radical species (sulphate radical $SO_4^{-\bullet}$) that in principle, on one hand can react with the dissolved monomer (homogeneous nucleation) to generate surface-active oligomers that then form micelles in situ. On the other hand, if the aqueous monomer

solubility is relatively low, these sulphate radicals can diffuse into the monomer-swollen styrene surfactant micelles, leading to heterogeneous nucleation with the appearance of particles nuclei. In either scenario, the micelles provide the main place for the radical polymerisation. Thereafter, given the relatively high styrene monomer concentration, polymer radicals propagate rapidly within such nuclei micelles, to form a polymer particle. As the supply of monomer becomes depleted, monomer diffusion from the micrometre-sized surfactant-stabilised droplets into the growing nascent polymer particles occurs. Thus, termination is suppressed relative to propagation and relatively high molecular weight polymer chains can be obtained, until the monomer droplet reservoirs are consumed, producing colloidal stable polymer particles are the final product [50].

In this regard, in order to understand the role of each reactant specie during the PS radical emulsion synthesis, our strategy followed the synthesis of PS nanoparticles by a modified emulsion process [49], adjusting only one parameter at time, while others remained constant, as shown in **figure 4.3**. In detail, the experimental conditions (Styrene concentration, KPS initiator concentration and rate and solvent polarity) were systematically varied, while using as initial conditions: 40mL of water as initial solvent, stirring at 800 rpm, 0.5 mL of styrene (final concentration (100mM), SDS (final concentration 2mM), 2mL of a KPS solution (final concentration 2.00mM) at 80°C in reflux conditions for 24h (experimental described in **Chapter 5, section 5.3.2.1**). The final mean particle size and size distribution were analysed by STEM microscopy and the yield of the reaction was calculated by the monomer conversion with the gravimetric method [51], with the difference between the mass of the monomer added and the obtained purified weight of solid PS polymer content after 24h. **table 4.1** showed the summary of the characterization.

As showed in **figure 4.3**, polystyrene nanoparticles with different sizes and yields can be prepared in a wide variety of different combinations by emulsion polymerization, as demonstrated by the different tested experimental conditions. The final PS particle size is therefore a function of several kinetic factors including: (I) monomer solubility, (2) reactant composition, (3) rate of addition and (4) solvent medium. Therefore, the emulsion polymerization is a complex process because the nucleation and growth mechanism was

controlled by the radical polymerization process in combination with various colloidal phenomena (eg; particle stabilization, micelles formation and conductivity).

Table 4.1 Summary of detailed experimental conditions and physicochemical characterization of the PS Nanoparticles.

Effect of Solvent								
Styrene (mM)	**Solvent (Water:ethanol)**	**KPS (mM)**	**KPS rate (µL/min)**	**SDS (mM)**	**TEM diameter (nm)**	**SD (%)**	**Solid polymer (mg)**	**Yield (%)**
100	100:0	2.0	D.A	2.0	68.4 ± 6.5	9.5	3.10	29.8
	80:20				130.0 ± 8.9	6.8	5.80	55.7
	30:70				574.4 ± 35.4	6.2	9.20	88.5
	20:80				1519 ± 43	2.8	9.70	93.3
Effect of Monomer								
Styrene (mM)	**Solvent (Water:ethanol)**	**KPS (mM)**	**KPS rate (µL/min)**	**SDS (mM)**	**TEM diameter (nm)**	**SD (%)**	**Solid polymer (mg)**	**Yield (%)**
100	40:60	2.0	D.A	2.0	256.6 ± 9.5	3.7	8.50	85.0
200					312.2 ± 8.3	2.6	17.8	89.0
600					318.0 ± 15.7	4.9	53.2	88.7
1200					341.9 ± 10.5	3.1	98.6	82.2
Effect of Initiator								
Styrene (mM)	**Solvent (Water:ethanol)**	**KPS (mM)**	**KPS rate (µL/min)**	**SDS (mM)**	**TEM diameter (nm)**	**SD (%)**	**Solid polymer (mg)**	**Yield (%)**
100	40:60	0	D.A	2.0	N.P	0	0	0
		2.87			304.1 ± 11.7	3.8	8.63	86.3
		5.75			264.4 ± 6.9	2.6	8.51	85.1
		11.5			A.P	0	0	0
Effect of Initiator rate								
Styrene (mM)	**Solvent (Water:ethanol)**	**KPS (mM)**	**KPS rate (µL/min)**	**SDS (mM)**	**TEM diameter (nm)**	**SD (%)**	**Solid polymer (mg)**	**Yield (%)**
100	40:60	5.75	60	2.0	329.6 ± 6.9	2.1	8.61	82.7
			120		316.9 ± 7.2	2.3	8.80	84.6
			360		315.5 ± 8.1	2.6	8.62	82.9
			520		329.6 ± 7.0	2.2	8.72	83.8
Effect of Surfactant								
Styrene (mM)	**Solvent (Water:ethanol)**	**KPS (mM)**	**KPS rate (µL/min)**	**SDS (mM)**	**TEM diameter (nm)**	**SD (%)**	**Solid polymer (mg)**	**Yield (%)**
100	40:60	5.75	120	0	312.2 ± 9.3	3.0	7.60	76.0
				1	252.1 ± 9.8	3.8	8.00	80.1
				3.85	219.5 ± 6.8	3.1	8.60	86.0
				10	217.3 ± 5.6	2.6	9.50	95.0

D.A = directly added; N.P= no particles; A.P= aggregated particles.

Effect of solvent and monomer in the synthesis of Size Colloidal Polystyrene NPs

As can be seen in **figure 4.3-A**, the size of the PS NPs increased, when the ethanol as co-solvent was increased in the solvent mixture. These results suggest that the initial medium solvency (capability of dissolving other material) was strongly sensitive in

determining the final PS particle size. Using water as the initial medium solvent, the mean size of the PS NPs was 60nm (conversion yield 30%) in comparison when high ethanol (20:80) in the solvent mixture was used, leading to 1.5 µm particles (conversion yield 93%). These results indicate that the solubility of the reactant species strongly affected the particle formation, that usually is restricted to the early stages of the polymerization reaction due to the formation of the monomer-micelles.

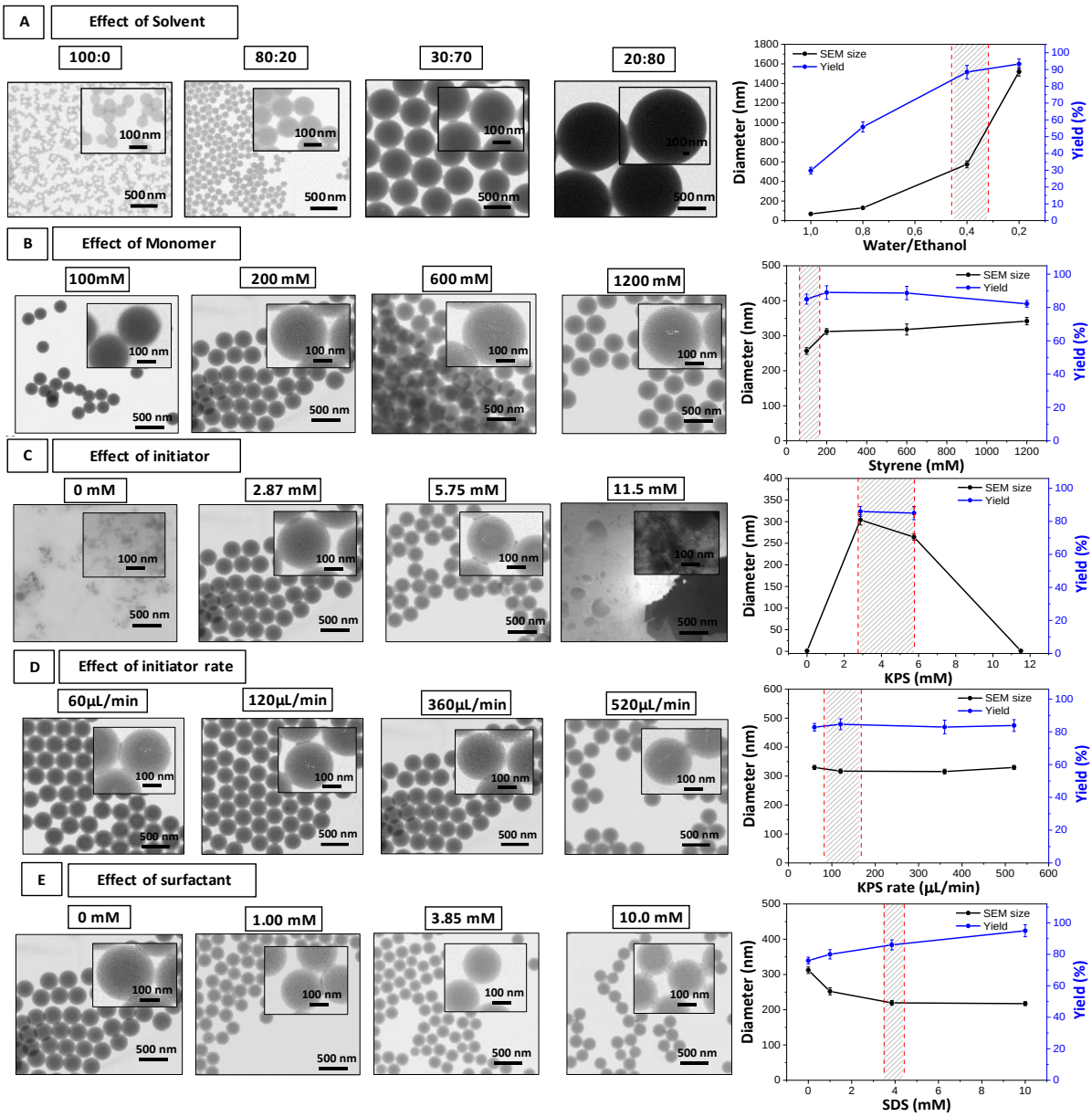

Figure 4.3 Representative STEM images of the different synthetic parameters for the synthesis of PS NPs by radical emulsion polymerization. (A) Evaluation the effect of solvent (H_2O: Ethanol). (B) Evaluation the effect of monomer styrene. (C) Evaluation the effect of radical initiator (KPS). (D) Evaluation the effect of addition rate of the radical initiator (KPS). (E) Evaluation the effect of surfactant (SDS). From left to right, the concentrations were systematically varied. The

size distribution was calculated measuring at least 300 particles by image J software and error bars are indicative of the standard distribution (showed in **Appendix C1**). The red dotted lines and the shaded area highlight the chosen optimal concentration for every parameter.

These results can be explained by analysing two important mechanistically facts during the synthesis. First, 2.0mM of SDS were used for styrene (100mM) polymerization. This initial surfactant concentration was below the critical micellar concentration (CMC). The SDS have a reported CMC of about (8.50 mM in water at 303.15 K). Therefore, less styrene precursor in form of soluble monomer-micelles were diffused to the medium. As a consequence, the water-soluble sulphate radicals from the initiator KPS, were unable to diffuse into the organic phase, therefore only a small portion of the soluble monomer/micelles were polymerized. This explain why the conversion yield of the reaction, was around 30% using water as continuous phase, while using the high ethanol mixture (20:80) were almost complete, around 93%. Second, the modification of the polarity of the continuous phase, by increasing the ethanol content in the water, highly affects the reactant species. Despite both (water and ethanol) are considered polar solvents, the relative polarity differences altered the solubility of the monomer styrene, causing different kinetic behaviours during the nucleation and growth, as reported in literature [52]. Using ethanol as co-solvent, the size of the PS NPs was expected to increased, because the monomer (Sty) is highly soluble in ethanol and limited in water. Therefore, increasing the monomer solubility leaded to the production of larger particles, but also to a higher monomer consumption. Furthermore, the ethanol also increased the solubility of the propagating monomeric radical, thereby increasing size and decreasing the nucleation time. Thus, this suggest that after induction time, lower number of monomer-micelles nuclei`s were formed. Hence, a fewer nucleation led to bigger sizes, as explained by LaMer-Dinegar model of homogeneous burst nucleation.

In the literature, emulsion polymerization is reported to present two reaction mechanism [53]. On one hand, the “limited coagulation” mechanism, in which the polymerization occurred below the (CMC) of the surfactant (limited or any number of formed micelles), hence, particles are formed preferentially by homogenous nucleation [54]–[56]. Depending on the availability of surfactant, these new-born particles (also known as primary) can undergo coagulation. Thus, particle coagulation occurs to the point,

where the surface charge density is enough to impart colloidal stability to the particles. On the other hand, the "micellar nucleation" mechanism (explained in **figure 4.2**), is when the polymerizations reactions are occurring above the (CMC). The monomer (styrene) and radical species (KPS sulphate radicals) formed in the aqueous phase, diffuse into the monomer-swollen surfactant micelles, giving place to a new polymer PS particle [57], [58]. Thus, changing the relative solubility in the media, revealed that the micellar mechanism of PS competes with the homogenous coagulation mechanism [59]. When the surfactant concentration is close and above the CMC, micellar nucleation dominates the reaction mechanism. Interestingly, once the medium polarity was fixed (water: ethanol, 40:60), as showed in **figure 4.3-B**, the mean size distribution and yield of the PS NPs remained comparable, when the monomer concentration was increased. These results suggest that the size of the polymer particles is then regulated by other factors than monomer availability, such as number of reactive sites controlled by the number of monomer-micelles in solution, conductivity and radical initiator concentration.

Effect of initiator in the synthesis of Size Colloidal Polystyrene NPs

As expected, **figure 4.3-C** showed any nucleation event when the polymerization was done without the KPS. These results revealed the need of radicals to start the styrene polymerization. The KPS generate the sulphate radicals by thermal decomposition. On the other hand, using a concentration of KPS between 2.87-5.5 mM, allowed us to produce PS particles, but slightly smaller in size as KPS was increased. These results were in agreement with the literature, that state that the PS size decrease along with the initiator concentration [60]. This observed trend to a smaller size using 5.75mM KPS, can be explained by the increased particle surface electrostatic stabilization. Increasing KPS in media, may enhance particle surface charge density, originated from the KPS sulphate end groups ($SO_4^{-\bullet}$), which stabilized earlier the growing PS particle. Therefore, the surface charge density and the colloidal stability is improved due to increased electrostatic repulsion force between two approaching particles. As a result, a higher number of monomer-micelles were formed in the initial stage of the reaction, thereby decreasing the size. M. N. Gorsd et al. [49] state that increasing the KPS concentration, lead to a faster polymerization process, in which smaller PS particles were obtained. He explained the

decrease in the particle size as a result of the formation of a higher fraction of small monomer droplets during the nucleation. Goodwin et al.[61], showed that the final PS particle size decreased as the initial concentration of KPS was increased, when the ionic strength was fixed. He attributed that the stabilizing sulphate groups originated from the thermal decomposition, early stabilized the PS particle. In contrast, using a higher KPS concentration (11.5mM), the system was coagulated and polymer aggregation was observed. This can be explained by the increased presence of counter ions in solution (increased ionic strength). The potassium cation K^+ derived from the KPS salt, can electrostatically destabilize the monomer-micelles formed as nuclei`s during the polymerization. According to DVLO theory, the ionic strength of the aqueous phase controls the thickness of the electric double layer. The thickness of the double layer and the total potential energy govern the stability of the polymer particles [62]. As the ionic strength of the solvent phase increases, the electrostatic barrier to coagulation (total potential energy curve), decreases, as a result, coagulated PS particles were generated. Thus, the initiator KPS concentration is, in effect, a double variable.

Effect of surfactant in the synthesis of Size Colloidal Polystyrene NPs

Finally, as showed by **figure 4.3-E**, the PS particle mean diameter was decreased, when the SDS concentration was increased. However, the polymer conversion yield followed an opposite trend, increasing along with the surfactant concentration. These results revealed that the number of initial micelles in solution were increased with SDS, affecting the nucleation and further growth of the PS particles. Using a higher SDS concentration, the final number of growing polymer particles were higher, consuming more monomer, thereby leading to smaller sizes. This can be state because the yield of the reaction was increased in a similar trend with SDS. This suggested that higher monomer concentration was consumed to form more monomeric-micelles, thus increasing the yield of the reaction. The addition of SDS in the media allowed to reduce the surface tension of the aqueous phase and the adsorption in the dispersion phases. When SDS concentration exceeds the (CMC), it aggregates in form of spherical micelles, so surface tension at the particle surface decrease, as a result more hydrophobic monomers can enter in to the vicinity of micelle and reaction continue until all monomer droplets are exhausted,

increasing the size. This behaviour occurred because monomer-micelles (droplets) are not as effective in capturing free radicals generated in the aqueous phase due to their relatively small surface area, as the micelles [63]. Therefore, particle nucleation process is greatly affected by surfactant concentration, which in turn affect particle mean size and size distribution. The SDS promote the emulsification of monomers' droplets, solubilisation of the monomers inside the micelles and for controlling the number of nucleated particles.

4.2 Seeded Emulsion Polymerization for Growing a PS shell into Fluorescent SiO_2 and Noble-Metal Au NPs

Nowadays, metal-polymer hybrid colloidal particles have engrossed considerable attention in recent years, because the synergistic combination of polymers with inorganic components, offers the promise of merging interesting properties that are not possible from either material alone [64]. Especially, the inorganic-polymer hybrids particles with different morphological and/or compositional anisotropies have been attracted more and more attentions, due to the development of synergistic combination of unique properties (such as magnetic, optical and electrical properties), when coupling both materials, using NCs, such as noble-metals and metal-oxides [65]. The encapsulation of metal nanoparticles with polymers have showed several potential applications in scientific research and technology, such as drug delivery, nanosensors, catalyst support, colloidal stabilizer, self-assembly, photonic crystals and optical switches [66].

As previously commented in the introduction of this chapter, the seeded emulsion polymerization is one of the most common routes for the preparation hybrid inorganic-polymer particles. For instance, silica and gold NPs have been polymerized with styrene, for producing polystyrene hybrids with NPs with different anisotropies, as shown in **figure 4.4**. These synthetic strategies followed a radical emulsion heterogeneous polymerization of styrene. In a typical reaction, the styrene monomer is polymerized on the surface of the inorganic silica and gold NPs, used as seeds, leading to different SiO_2/Au-polystyrene hybrids and heterodimers. However, the chemical compatibility of both inorganic materials need to be properly addressed in order to avoid phase segregation or particle aggregation [69], [70]. Therefore, the preparation of these inorganic/polymer particles usually requires efforts to establish the favourable interactions between the inorganic core and the polymer

shell. One strategy to overcome this challenge is to graft the inorganic particle surface with "coupling agents or specific ligands", for improving chemical affinity and promoting the formation of a fine polymer layer on top of the inorganic domain. For instance, Z. Zhang et al [64], prepare silica/polymer composite particles with different anisotropies by covalently functionalized the silica surface with polymerizable vinyl groups by siloxane bonding, using the 3-(Trimethoxysilyl)propyl methacrylate (TMSPMA), for further grow the polymer shell, **figure 4.4-A**.

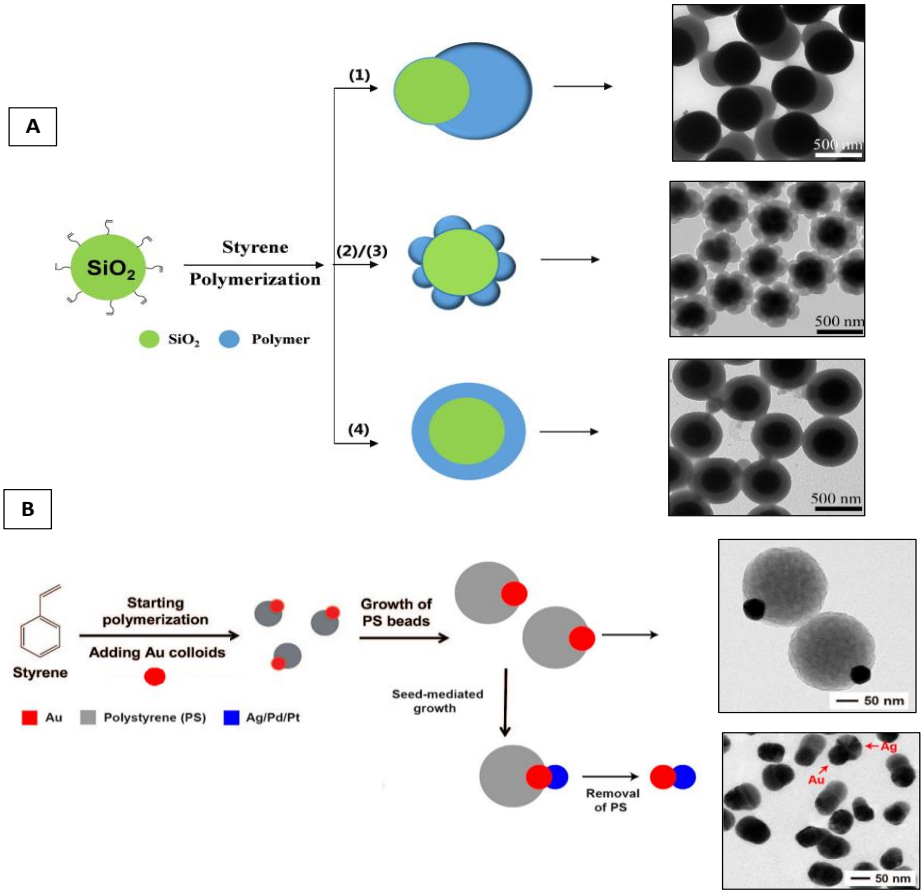

Figure 4.4 Graphic representation of anisotropic composites particles by radical emulsion polymerization with polystyrene. (**A**) Silica/polystyrene core-shell (SiO_2/PS) particles with different anisotropies using different experimental conditions. Taken from reference [64]. (**B**) Gold/polymer Janus-type gold/PS structures for preparation of metal heterodimers. Taken from reference [64], [68].

On the other hand, the hydrophilic sodium citrate surface of the gold NPs, can be grafted with functional molecules, using a two-steps ligand exchange strategy, using 11-mercaptoundecyl methacrylate (MUMA) or N-vinyl pyrrolidone, for further polymerized with styrene via reversible addition–fragmentation chain transfer (RAFT) polymerization. However, this synthetic strategy is rather complex and time consuming. In the literature,

Younan Xia et al. [64], [68], used citrate stabilized Au NPs, as seeds, in the emulsion polymerization with styrene for the preparation of heterodimers, as showed in **figure 4.4-B**. Their synthetic approach was based on the controlled accurate timed-addition of the SC-Au NPs, once the styrene began to polymerize in the reaction media. It was an interesting approach for the preparation of PS-Au nanocomposites. However, because of the surface of the Au NPs were not functionalized with a suitable molecule, the colloidal stabilization of the Au was compromised in the polymerisation media with hydrophobic monomers and the organic initiator (AIBN). Thus, their strategy is challenging to reproduce and eccentric or Janus structures usually were prepared.

Other studies performing the seeded emulsion polymerization of styrene as vinyl monomer in presence of functionalized SiO_2 NPs with TMSPMA have been reported. However polymerization using toxic organic solvents (toluene, THF), that require further purification techniques have been used [40], [72], secondary polymer nucleation were observed [73], core-shell silica/polystyrene NPs having silica multicores morphologies [74]–[76] or silica NPs with eccentric core-shell structures [77], large core-shell polymer-encapsulated silica particles (500nm) using organic radical AIBN initiator [78] and submicron-sized anisotropic SiO_2/PS composite particles (raspberry and snowman-like structures) have been reported [69]. On the other hand, for preparing metal-polymer hybrid particles, using noble-metals, such as gold (Au NPs) have been also described. However, the multiple Au colloids NPs were attached on the PS surface (polystyrene was used as core) [79], [80], or emulsion polymerization of unmodified metal Au colloids having an asymmetric Au-PS hybrid NPs have been produced [81], [82], with a lack in the control of the PS shell [64] and a Janus-type gold/PS structures for prepare heterodimers [33], [68], [83], were also reported. Curiously, to the best of our knowledge, only one report was found in which silica and gold were used in combination for preparing a multilayer gold@silica@polystyrene core–shell composite particles. Shunchao Gu. Et al. [84], used the seeded polymerization technique, in which the Au NPs were first coated with a SiO_2 shell, functionalized with TMSPA before the polymer coating. However, the composite polymer NPs were in the micron size (800nm), lacked of characterization in detail. The experimental variables for controlling the PS shells were not properly resolved.

4.2.1 Tailoring the Seeded Emulsion Polymerization Reaction for Growing a PS Shell into Silica (SiO_2) and Gold (Au) Nanoparticles

First, the colloidal NCs that were used as seeds in the seeded radical emulsion polymerization were prepared. For this purpose, fluorescent silica nanoparticles loaded with FITC in the core and core-shell gold NPs with a silica layer, were synthetized by a modified Stöber method [21] and sodium citrate reduction method [85]. Experimental described at (**Chapter 5, section 5.3.2.2**). The hybrids NPs were further characterized by STEM and UV-Vis spectroscopy, as showed **table 4.2** and **figure 4.5**. The surface of both NPs was functionalized with the silane-coupling agent TMSPMA, for attaching the polymerizable vinyl groups on surface. Thereby, the chemical compatibility with hydrophobic vinyl monomers were increased.

Table 4.2 Physicochemical characterization of the SiO_2-FITC and Au NPs as seed for the emulsion polymerization with styrene.

NPs	Absorbance/$LSPR_{peak}$ (nm)	TEM size (nm)	SD (%)	DLS_{number} (nm)	PdI	ζ-potential (mV)	Media / pH	Cond. (mS/cm)
Au-SC	518.5	11.6 ± 1.3	11.2	40.2 ± 4.1	0.118	-20.7 ± 1.1	Water/ 5.6	0.16000
Au@SiO_2	530.4	28.6 ± 3.8	13.2	94.6 ± 3.1	0.096	-27.0 ± 2.2	Ethanol/ 8.1	0.00484
SiO_2-FITC	495	55.3 ± 5.9	10.7	87.0 ± 4.6	0.049	-33.3 ± 2.6	Ethanol/ 8.2	0.00990

	Concentration (mg/mL)	Particles number (NPs/mL)[a]	Concentration (FITC/NP)[b]
Au-SC	0.033	$2.21x10^{12}$	
Au@SiO_2	0.099	$6.63 x10^{12}$	
SiO_2-FITC	5.26	$4.25x10^{13}$	115.4

a=theoretically calculated; b= calculated using calibration curve for FITC.

As shown in **figure 4.5**, the FITC core-labelled SiO_2 NPs presented a spherical morphology with a mean size distribution of 55.3 ± 5.9 nm. The Uv-Vis spectra displayed the characteristic FITC absorbance peak at 495nm after purification and the increased signal at short wavelengths due to the silica scattering, suggesting that the dye were entrapped within the silica matrix in the core. On the other hand, the gold nanoparticles after the sodium citrate reduction, presented a mean size distribution of 11.6 ±1.3 nm. The microscopy characterization by STEM, revealed that a silica shell of approximately ~10nm was growth on top of the gold, for producing a core-shell Au@SiO_2 NPs, having mean size distribution 28.6 ± 3.43 nm.

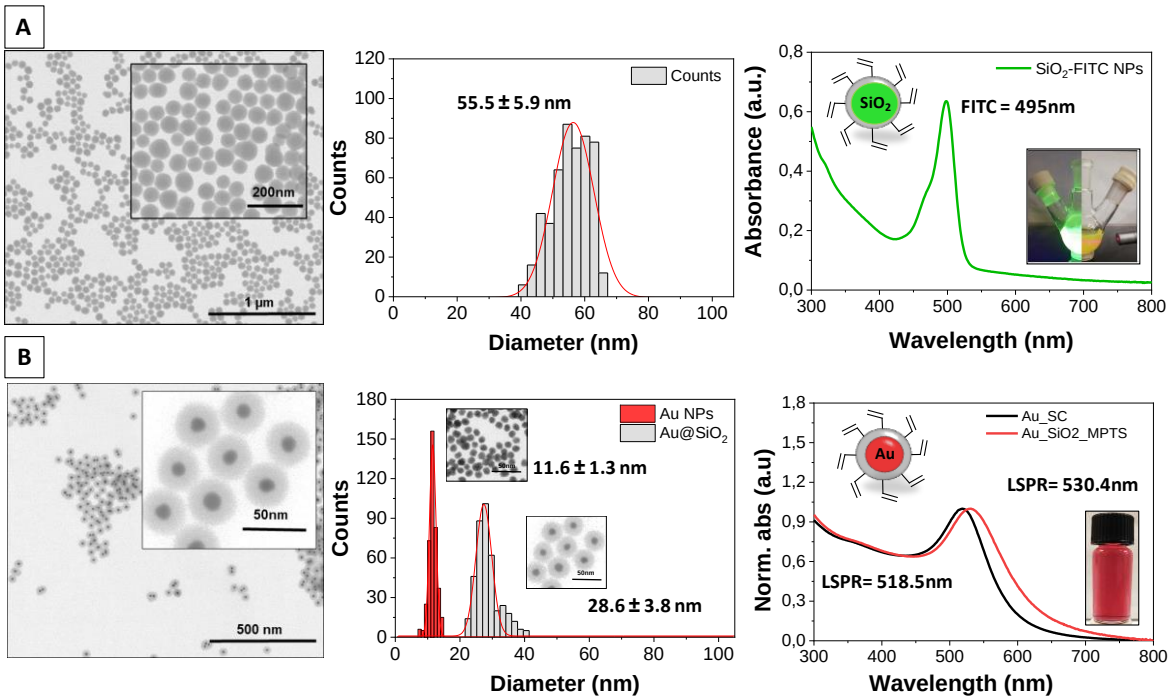

Figure 4.5 Characterization of the inorganic NPs before the seeded radical emulsion polymerization for growing a PS shell. (A) Fluorescent SiO_2-FITC NPs core-labeled with FITC synthetized by the modified Stöber method. From left to right, electron microscopy image by STEM mode, Calculated mean size and size distribution by Image J software and the recorded Uv-Vis absorption spectra after purification 1/10 dilution in ethanol. (B) Core-shell Au@SiO_2 NPs. The Au core were synthetized by the sodium-citrate reduction method]and the silica layer were done by the modified Stöber method.

The Uv-Vis spectra of the Au core-shell particles displayed the characteristic LSPR band of the sodium citrate gold at 518.5nm, that red-shifted towards longer wavelength after the silica coating to 530.4nm, due to the change in the refractive index (RI) on the surface. Aggregation was not evidenced for any NPs after purification. Finally, both NPS were dispersed in ethanol for further functionalization with vinyl groups adding a 20mM solution of the silane-linker TMSPMA, for incubation overnight. (Emulsion seeded polymerization of the SiO_2-FITC NPs with and without TMSPMA is showed in **Appendix C2**). The vinyl groups on surface were needed in order to growth the PS shell on top of the NPs. Otherwise, the PS particles nucleated separated from the silica in the solution.

Once the SiO_2–FITC NPs and the Au@SiO_2 NPs were functionalized and characterized, the NPs were used as seeds in the radial emulsion polymerization with styrene, in order to grow a PS shell.

4.2.1.1 Controlling the Seeded Emulsion Polymerization Reaction into Silica (SiO_2) and Gold (Au) Nanoparticles

Because of the polymerization process were done under the presence of NPs in solution (heterogeneous nucleation), first, an optimization of two experimental conditions, the KPS addition rate and the use of a co-monomer called 1,4-divinylbenzene (DVB), were evaluated during the polymerization in order to produce concentric single core-shell particles in the seeded emulsion reaction, as shown by the **figure 4.6**. The synthetic conditions, briefly, 40mL of solvent (water or water: ethanol 40:60), 100µL Styrene (100mM) and DVB (2.5, 3.0, 5.0 and 10 µL), SDS (3.85mM), 2mL of the SiO_2–FITC NPs at a concentration ($4.25x10^{13}$ NPs/mL) or Au@SiO_2 NPs ($6.63x10^{12}$ NPs/mL) and 2mL of KPS (5.75mM at different rates) were added in the bottom flask and heated to 80°C in reflux conditions while stirring at 800 rpm for 24h. The final mean particle size and size distribution were analysed by STEM microscopy. Experimental is described in (**Chapter 5, section 5.3.2.3**).

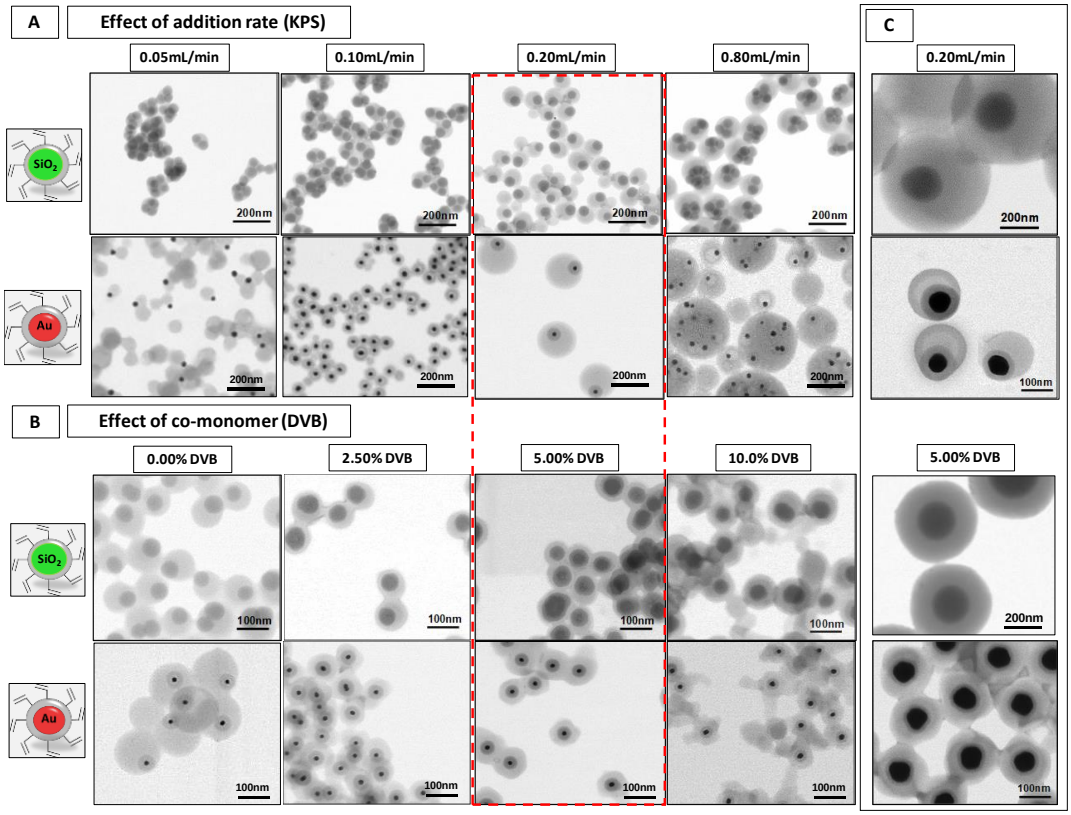

Figure 4.6 Representative STEM images of the TMSPMA grafted SiO_2–FITC and Au@SiO_2 NPs after the PS shell by seeded radical emulsion polymerization. (A) Effect of the addition rate of the KPS initiator 5.75mM. From left to right the speed of addition were increased. (B) Effect of a co-monomer (DVB) addition. From left to right, the concentration of DVB in

the monomer mixture (styrene/DVB) were increased. A total styrene 100µL (100mM) were used. Optimal conditions in red-dotted lines. (C) Large SiO_2–FITC (200nm) and Au@SiO_2 (60nm Au NPs) were also evaluated using the optimal conditions. (Characterization showed in table D1, **Appendix C3**).

Evaluation of the Initiator (KPS) Addition Rate

As can be seen in **figure 4.6-A**, the rate of addition of the KPS, greatly affected the formation of a PS shell on top of the SiO_2–FITC and Au@SiO_2 NPs. A slower addition of the radical initiator (0.05mL/min), leaded to a particle aggregation and the formation of polymer substructures. In contrast, at higher rate of addition (0.8mL/min), the formation of core-shell polystyrene NPs having multicores were observed. Using a constant rate of (0.20mL/min) achieved the production of single core-shell metal-PS particles, but with eccentric morphology. These results can be explained in terms of two factors: i) a slower KPS rate was affecting the colloidal stability of the functionalized seed particles. The silica surface was grafted with vinyl groups on surface with TMSPMA by covalent siloxane bond (Si-O-Si). Therefore, when the NPs were heated in aqueous solution, the silica surface may experience dissolution through a series of Si-O bond-breaking [86], releasing the vinyl groups on surface. Hence, the styrene cannot polymerize on top of the NPs.

In addition, the thermal decomposition of KPS, decreased the pH of the reaction by the generation of sulphuric acid as sub-product [87]. As a consequence, at the end of the reaction the pH was close to 3 and the silica (IEP) is close to pH 2. This induced particle aggregation due to decreased surface charge stabilization. On the other hand, ii) the faster KPS addition is affecting the coalescence between the growing polymer over silica particles due to higher mobility of PS. Therefore, in a faster KPS addition, the generation of highly radical species was increased, thus, the faster kinetics of coalescence between the growing polymer micelles become bigger and with a closer contact due to higher monomer conversion, caused the coalescence of multiple particles, leading to a multicore system. These results suggest that during the polymerization, the rapid but controlled formation of a stable PS shell on top of the NPs is critical for stabilization. The sulphate groups on the surface of the PS particles present a (pKa <2), remaining negatively charge with highly electrostatic repulsion, even at lower pH [87]. This is why other authors used a higher PVP

55.00 kDa concentrations to confer and additional steric stabilization to the growing seed particles [49].

Evaluation of the Co-monomer DVB Concentration

For controlling the position of the core SiO_2-FITC and Au@SiO_2 NPs in the hybrid-PS particles, from eccentric to a concentric position, the use of the 1,4-divinylbenzene as cross-linker as co-monomer was evaluated. The DBV molecule differs from styrene, for having a two separate vinyl groups bonded in the benzene ring, instead of one. In 1998 Masayoshi Okubo et al. [87], was the first author who reported the use of DVB as crosslinker polymer agent, for controlling the PS particles formation and their cross-linking densities (higher DVB, higher molecular weight of polymer particles were obtained).

As can be seen in **figure 4.6-B**, increasing the concentration of DVB tended to promote shell formation, leading to a concentric morphology on both, SiO_2-FITC and Au@SiO_2 particles. The optimal found concentration was 5.00%. Higher DVB concentration (10.0%), leaded to a higher interparticle polymer crosslinking, as showed by the STEM images. Mechanistically speaking, it is believed that this difference in position was perhaps caused by the difference in viscosity of the monomer-swollen polymer phase, during the polymerization process, thus affecting the coalescence of polymer nodules over silica and Au with silica. In the initial stage of polymerization, a thin layer of the PS shell should be deposited on the SiO_2 surface. The PS shell tends to contract and reduce the surface area as a result of interfacial tension between the seed particle and the hydrophobic monomer. The relatively high viscosity, achieved by increasing the cross-linker concentration, could limit the degree of PS contraction and thus lead to the formation of a concentric core-shell structure [89]. Finally, the **figure 4.6-C**, show that the production process of the hybrids core-shell PS NPs can also be applied to bigger NPs sizes, using the same reaction conditions.

Controlling the PS Shell Size into SiO_2 and Au NPs

Once we stablished the optimal reaction conditions (fixing DVB content and KPS rate) for growing a concentrically PS shell on top of the NPs, the size of the PS shell was controlled by increasing the styrene concentration (with 5.0% DVB). The size of the PS shell and mean size distribution of the hybrid PS particles were evaluated by electron microscopy in STEM mode, UV-Vis spectroscopy, and their characterization is showed in **figure 4.7** and **4.8** and the summary of the physicochemical characterization in **table 4.3**.

Table 4.3 Physicochemical characterization of the PS shell on top of the SiO_2-FITC and Au NPs after the emulsion polymerization with optimized conditions

SiO_2-FITC	Absorbance (nm)	TEM size (nm)	SD (%)	PS shell (nm)	SD ± (nm)
As-synthesized	495	55.3 ± 5.9	10.7	0	0
25 mM	495	62.2 ± 8.7	13.9	3.5	1.3
50 mM	495	98.8 ± 8.8	8.9	22.3	2.9
100 mM	Suppressed	123.3 ± 22.0	17.8	33.2	10.2
150mM	Suppressed	207.0 ± 21.1	10.2	75.7	9.63
$Au@SiO_2$	**$LSPR_{peak}$ (nm)**	**TEM size (nm)**	**SD (%)**	**PS shell (nm)**	**SD ± (nm)**
As-synthesized	530.4	28.6 ± 3.8	13.2	0	0
25 mM	522.5	80.5 ± 5.7	7.1	25.9	1.1
50 mM	522.5	95.7 ± 6.4	6.7	33.5	1.4
100 mM	Suppressed	121.6 ± 9.1	7.5	46.3	2.7
150mM	Suppressed	142.3 ± 7.1	5.0	56.8	3.8

As can be seen in **figure 4.7**, increasing the styrene monomer concentration during the emulsion polymerization process, leaded to the formation of a bigger PS shell as expected. The mean size and distribution of the SiO_2-FITC@PS NPs increased from 55.3 ± 5.9 nm to 207.0 ± 21.2 nm when the styrene monomer was changed from 25 to 150mM. The PS shell size was varied from 23 to 80nm. However, using 25mM of styrene lead to an incomplete PS shell, due to the higher number of seed in solution. On the other, the $Au@SiO_2$@PS NPs mean size was increased from 28.6 ± 3.8nm to 142.3 ± 7.7nm, having a PS shell variation from 26 to 57nm. The differences in size of the PS shell can be related to the number of seed particles used for the seeded emulsion and the diameter of the particle. The SiO_2-FITC ($4.25x10^{13}$ NPs/mL) were one order of magnitude higher in concentration, in comparison with the $Au@SiO_2$ ($6.63x10^{12}$ NPs/mL) and the fluorescent silica particles were bigger in size.

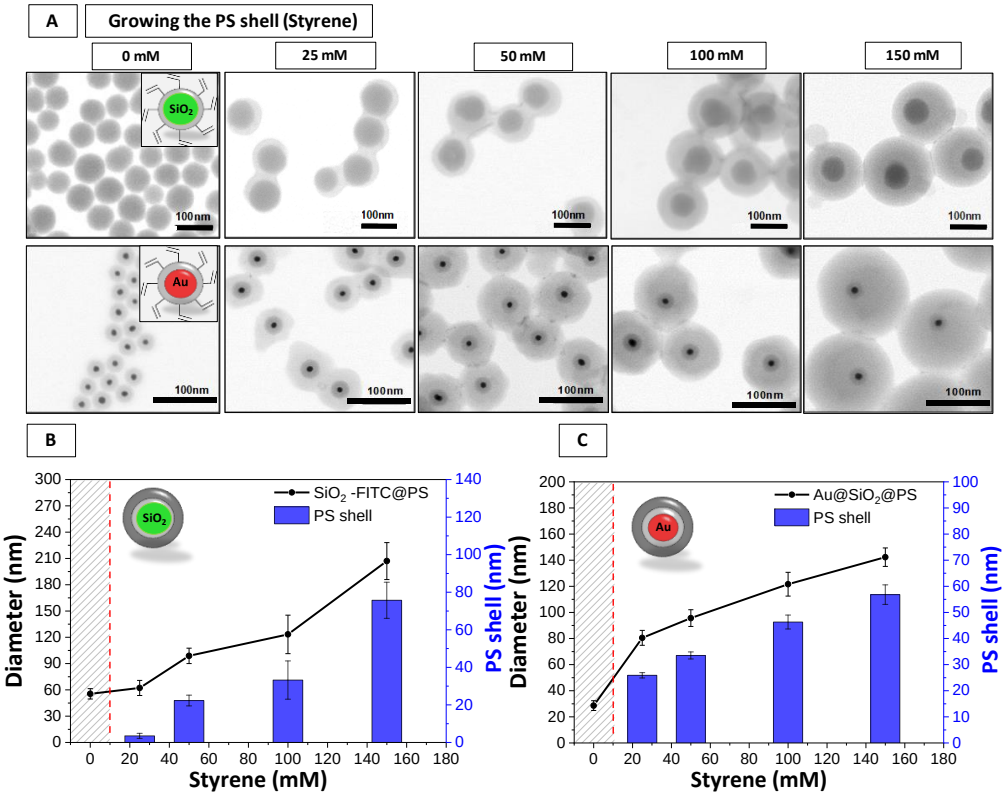

Figure 4.7 Characterization of the growing PS shell on top of the TMSPMA grafted SiO_2–FITC and Au@SiO_2 NPs using styrene (with 5% DVB) after emulsion polymerization. (A) Representative STEM images increasing the styrene content. From left to right the concentration were increased from 25mM to 150mM. (B) Graphical representation of the mean size distribution as a function of PS shell for SiO_2–FITC@PS and (C) for Au@SiO_2@PS NPs. The mean size distribution was calculated measuring at least 300 particles by image J software (showed in **Appendix C4**). The red dotted line with shaded region indicates the size and morphology of the NPs, before PS coating as-synthesized.

Further characterization of the optical properties by UV-Vis spectroscopy of these aqueous dispersions of SiO_2–FITC@PS and Au@SiO_2@PS hybrids particles with different PS shells were done, as showed in **figure 4.8**. As can be observed in **figure 4.8-A**, the UV-Vis absorption spectra of the SiO_2–FITC particles reveal the characteristic FTIC absorption band at 490nm without a PS coating. Interestingly, as the PS shell was increased on top of the particles, the absorption band of the FITC were progressively decreased, until the high scattering contribution of the shell PS was high enough to scattered the incoming beam light and suppressed the FITC signal. In addition, **figure 4.8-B** showed the optical images of the colloidal solutions of the SiO_2–FITC@PS, revealing the increased opalescent white colour as the PS shell was bigger under white Light (from left to right), in comparison with

the uncoated SiO_2–FITC NPs. Moreover, when the colloidal solutions were exposed under UV-light, the decreased in fluorescent intensity (green colour) were also observed.

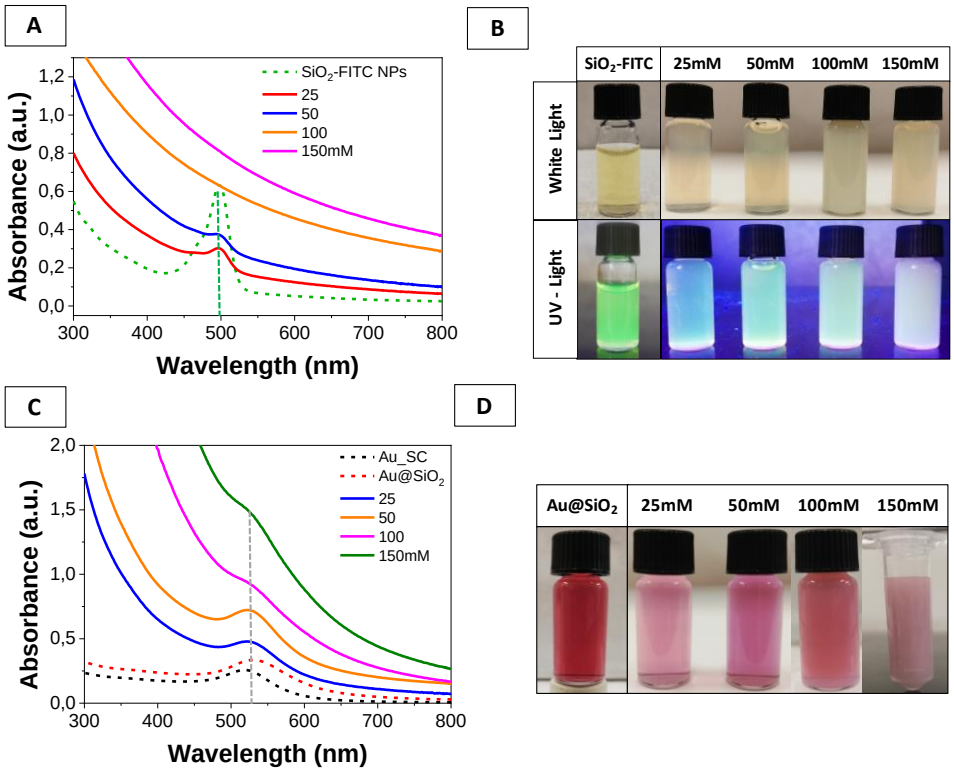

Figure 4.8 Optical characterization of the core-shell SiO_2–FITC and Au@SiO_2 polystyrene NPs after the coating with styrene by the emulsion polymerization. (A) Absorbance spectra of the different core-shell SiO_2-FITC@PS NPs, after the PS coating with increasing styrene concentrations in water. The characteristic FITC absorbance peak at 490nm is attenuated by the polystyrene high scattering. (B) Optical images of colloidal solutions SiO_2-FITC@PS NPs under white light and UV-light from left to right. The SiO_2–FITC NPs were showed for comparison. (C) Absorbance spectra of the different core-shell Au@SiO_2@PS NPs, after the PS coating. The characteristic LSPR peak (530.4nm) of the Au@SiO_2 is gradually attenuated by PS shell due to the high scattering. (D) Optical images of colloidal solutions Au@SiO_2@PS NPs under white light. The Au@SiO_2 were showed for comparison.

On the other hand, **figure 4.8-C**, showed the UV-Vis extinction spectra of the SC-stabilized Au NPs displaying their the characteristic LSPR band at 518.5nm, which red-shifted to a longer wavelength after the SiO_2 coating to 530.4nm, due to the refractive index change. Interestingly, after the PS coating, the high scattering contribution of the shell PS progressively suppressed the LSPR signal of the gold. However, the LSPR blue-shifted to shorter wavelength to 522.5nm, remaining unchanged even when the PS shell was increased. It is well known that the position of the LSPR band is very sensitive to local changes of the refractive index (RI) and can be correlated to the changes in chemical and/or

physical environment near the NPs surface. This change in blue-shift of the LSPR peak can be attributed to the change in solvent polarity and dielectric constant of the materials. The LSPR peak of the Au@SiO_2 were measured in ethanol due to the solubility of the vinyl groups on surface. In contrast, the optical properties of the Au@SiO_2@PS NPs were in pure water. Curiously, the RI of PS (n=1.600) is higher than SiO_2 (n=1.4585), therefore is expected a red-shift of the LSPR towards longer wavelength, when the PS shell was increased. Perhaps a quantum behaviour affecting the SPR frequency of the Au by the dielectric properties of the surrounding materials (SiO_2 and PS) or inter-nanoparticle coupling interactions cause a classical size-dependent SPR effect and strong quantum transitions of the conduction electrons, as is reported [89]. Finally, **figure 4.8-C**, displayed the optical images of the Au@SiO_2@PS after emulsion, revealing the change of colour from wine-red to opalescent white, when the PS shell was increased by the monomer.

4.3 Development of a Multimodal Contrast Agent with Advanced Optical Properties for Microplastics Evaluation: The case of Polystyrene NPs

Nowadays, microplastics (MPs) are considered an emerging global pollutants that have been gathered enormous attention due to their potential threat to the ecosystem in virtue of their persistence, accumulation and resistance to degradation [90]. In addition, the inevitable distribution in water environments and terrestrial land-based sources, including oceans, lakes, rivers and particularly runoff, make the plastic pollution to be found ubiquitously, becoming a major global environmental issue in the recent decade [9]. The MPs are non-degradable, biologically incompatible, and their presence in the air, soil, water and food can induce ecotoxicological issues [91]. Once inside the body, MPs can release toxins, additives, and monomers that trigger carcinogenic behaviour [92]. Moreover, the human intake of MPs can cause lung damage and liver function changes [93]. Several studies have suggested that microplastics can induce microbiota dysbiosis, intestinal barrier dysfunction, inflammation, and metabolic disorders in mice [94]. At present, MPs' detection relies on visual-based approaches (pre-sorting identification of larger MPs), fluorescent staining techniques, Fourier transform infrared (FTIR), Raman spectroscopy and pyrolysis gas chromatography - mass spectrometry (Py-GC-MS) [95].

However, these techniques rely on the extensive and complex preparation procedures and sample separation beyond removal of organic matter via digestion with acids, hydroxides, enzymes or oxidizing agents for chemical identification. Therefore, an accurate and reliable detection of MPs in live cells and organisms is an essential problem that requires the development of accurate in vivo and in vivo detection methods [96]. Their broad size range, chemical heterogeneity, low concentration and naturally occurring transformations (e.g., ageing, fragmentation, and aggregation) make the label-free detection of MPs in cells, tissues and organisms very challenging.

Labelling MPs is a valuable tool for their tracking by a wide variety of imaging techniques, each with a trade-off between imaging resolution and penetration depth. In vitro techniques such as confocal and electron microscopy are generally the method to detect optically-labelled MPs at the cellular and sub-cellular levels [97], [98]. With the ability to resolve cellular and subcellular features, these techniques allow to elucidate MP-cell interactions and, with it, underlying mechanisms of action. However, biological organisms are complex 3D structures arranged hierarchically from cells to organs. The complementary features of traditional clinical techniques such as positron emission tomography (PET) and X-ray computed tomography (CT) enable MPs visualization in living organisms after labelling with specific contrast agents [99].

By combining the advantages of complementary imaging modalities, it is possible to detect MPs at different biological levels, from individual cells up to the scale of the intact organ. This provides information about the mechanism of MPs interaction with cells, tissues and organs, their biodistribution, accumulation, fate and secretion pathways [100]. For that, the development of multimodal MP models comprising labels for different imaging modalities is needed. Various studies have widely demonstrated the importance of multimodal contrast agents for bioimaging [101]. However, none of them have applied the principle to detecting MPs due to the low chemical compatibility of the materials involved. In this sense, there has been substantial interest in nanoparticle-based contrast agents for in vivo and in vitro imaging [102]. Unlike small molecule imaging agents, multimodal imaging hybrids NPs can: i) easily integrate more than one kind of imaging or therapeutic agents, which makes them potential multifunctional nanoplatforms for both

diagnosis and therapy; ii) considerable amounts of imaging agents or pharmaceuticals can be introduced into NPs through simple loading and chemical conjugation, due to their large compartments (e.g. large surface area or interior cargo volume); (iii) can be combined different incompatible materials into one hybrid structure, with specific targeting moieties or physicochemical optimization of size and surface properties. These features provide multifunctional NPs with great potential as innovative multimodal bioimaging and diagnostic systems for the clinical and environmental field [103].

In this context, we approached this serious dilemma with a novel solution by developing a new class of multimodal contrast agent of polystyrene (PS) NPs for the evaluation of MPs. This model particle presented interesting multimodal imaging capabilities for optical fluorescence (LCM), electron microscopy (SEM/TEM), X-ray imaging (CT) and the possibility of performing biodistribution studies by elemental analysis (ICP-MS). The multimodal contrast NPs presented a multilayer single-core architecture, comprising an Au NP surrounded by a SiO_2 shell containing a FTIC fluorophore onto which a concentric PS shell has grown. By controlling fluorophore location within the SiO_2 shell, the brightness of the organic fluorophore is increased up to 3.0 folds, which allows the efficient optical detection of the MPs. We select PS as a model microplastics due to their abundance [104] and environmental impact [105]. The tagged-NCs were chosen on the basis of their properties; gold (Au) nanoparticles were used due to their remarkable properties including, high X-ray absorption coefficient (at 100 keV the coefficients of gold and iodine are 5.16 and 1.94 respectively), X-ray attenuation coefficient profile and electron density (Gold (Z = 79) has a higher atomic number compared with iodine (Z = 53) or barium (Z = 56), low cytotoxicity, tailored surface chemistry, excellent biocompatibility, and unique chemical traceability and optical properties [106]. On the other hand, fluorescently-labelled Silica (SiO_2) NPs due to their extraordinarily features, including tuneable structures in term of size and morphology, good biocompatibility, (eg; the surface can be easily modified with silanes for obtain tumor-targeting nanomaterials), high surface area, chemical inertness, water solubility, optically transparent, ease of preparation and free of interference with magnetic radiation and their well-known use as biological probes [101] .

4.3.1 Multimodal Contrast Agent for Microplastics Evaluation by the Seeded Emulsion Polymerization Reaction

The synthesis of the engineered multimodal contrast agent of polystyrene (PS) NPs (from now on called: *PEF-labelled PS NPs*) were done modifying the seeded emulsion polymerization method [49]. Experimental described at (**Chapter 5, section 5.3.2.4**). The multimodal imaging NPs involved the controlled growth of polystyrene (PS) shell onto a Plasmon enhance fluorescence (PEF) core particle. The PEF core comprises an Au NP surrounded by two concentrically layers of SiO_2, the inner of approximately 30nm of SiO_2 shell acting as a spacer and the outer containing the FITC fluorophore (PEF-core detailed characterization is showed in **Appendix C5**). The 50nm Au NPs size were selected to enhance the fluorescence intensity of the fluorophore. The spectral overlapping between the LSPR and the fluorophores absorption band near or over the surface of the metallic nanostructure. Fluorescein isothiocyanate (FITC) dye molecule -emission wavelength at 525nm- was chosen for fluorescence measurements of biological samples. Their excitation peak (495nm) significantly overlaps with the absorption spectra of the Au NPs (545nm), which is beneficial for PEF. The schematic of the production process of the PEF-labelled PS NPs is showed in **figure 4.9** and their physicochemical characterization in **table 4.4**

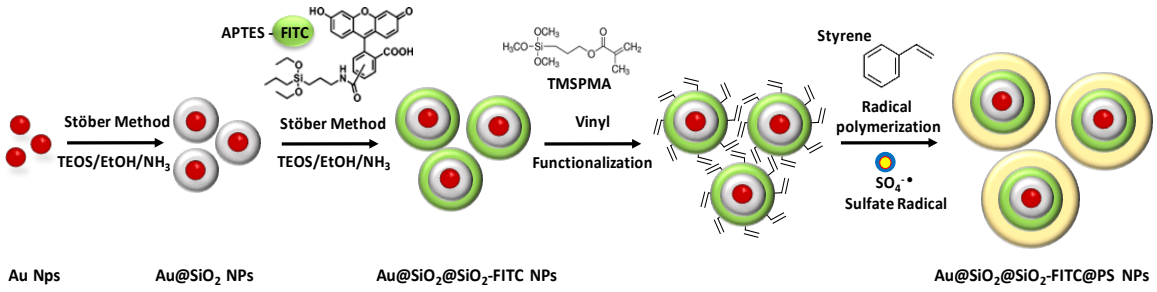

Figure 4.9 Schematic procedure of the production process of the PEF-labelled PS NPs.

The schematic production of PEF-labelled PS NPs is shown in **Figure 4.9**. In detail, Au NP of size (66.7 ± 8.3 nm) were prepared using the seeded growth citrate-reduction method [85] and further used as seeds for the growth of a uniform shell of ~30 nm of amorphous silica derived from hydrolysis/condensation of the tetraethylorthosilicate (TEOS) precursor by the modified Stöber method [107], to achieve the Au@SiO_2 NPs of size (127.8 ± 8.7 nm). (Characterization shown in **table 4.4** and **Figure 4.10**). The silica layer acts

as a spacer because if the distance between the dye molecules and the Au NP is too close, the fluorescence energy transfer quenches the fluorescence signal of dye molecules instead of achieving an enhancement in the dye signal (showed in Table D2, **Appendix C5**). Representative Scanning Transmission Electron microscopy (STEM) images of Au NPs before and after coating with SiO_2 are shown in **figure 4.10**, where the monodispersity of the Au NPs used as cores is retained after the growth of the SiO_2 shell. Absorbance spectra show the characteristic LSPR peak of Au NPs at 545.6nm, which red-shifts to 562 nm after the coating with SiO_2, which can be ascribed to the increase in the dielectric constant of the particle environment. Remarkably, no spectral changes were noted that could be associated with aggregation. Consistent with the growth of a SiO_2 shell around the Au NPs, the hydrodynamic diameter of the NPs increases from 40.2 ± 13.1 nm (Au NPs) to 144.3 ± 2.3 nm (Au@SiO_2 NPs), as summarized in **table 4.4**.

Table 4.4 Physicochemical characterization of the NPs for the production process of the PEF-labelled PS NPs.

NPs	$LSPR_{peak}$ (nm)	TEM diameter (nm)	SD (%)	DLS_{number} (nm)	PdI	ζ-potential (mV)	Media / pH	Cond. (mS/cm)
Au NPs	545.6	66.7 ± 8.3	12.2	40.2 ± 13.1	0.238	-21.5 ± 4.30	Water/ 5.0	0.7944
Au@SiO_2	561.9	127.8 ± 8.7	6.8	144.3 ± 2.3	0.038	-31.7 ± 1.6	Ethanol	0.0018
Au@SiO_2@SiO_2-FITC	569.4	201.3 ± 10.5	5.2	219.9 ± 5.3	0.068	-22.2 ± 1.6	Ethanol	0.0042
Au@SiO_2@SiO_2-FITC@PS	N/A	536.5 ± 22.8	4.2	570.1 ± 10.9	0.047	-41.2 ± 0.9	Water/ 7.0	0.3317

For the Au@SiO_2 NPs to be used as PEF labels, a second layer of SiO_2 containing the fluorescein isothiocyanate (FITC) fluorophore was grown, to achieve the PEF particles (Au@SiO_2@SiO_2-FITC). The FITC was integrated into the SiO_2 shell after conjugation with the APTES, as previously discussed in **chapter 3**. Remarkably, the integration process of FITC fluorophore in the SiO_2 shell is not just a physical entrapment of the dye into the pores of SiO_2 but a covalent incorporation into the shell through condensation, preventing the leaking of dye molecules. Both absorption and fluorescence spectra of the FITC-APTES complex revealed that the reaction process did not alter the nature of the dye (showed in **Appendix C6**).

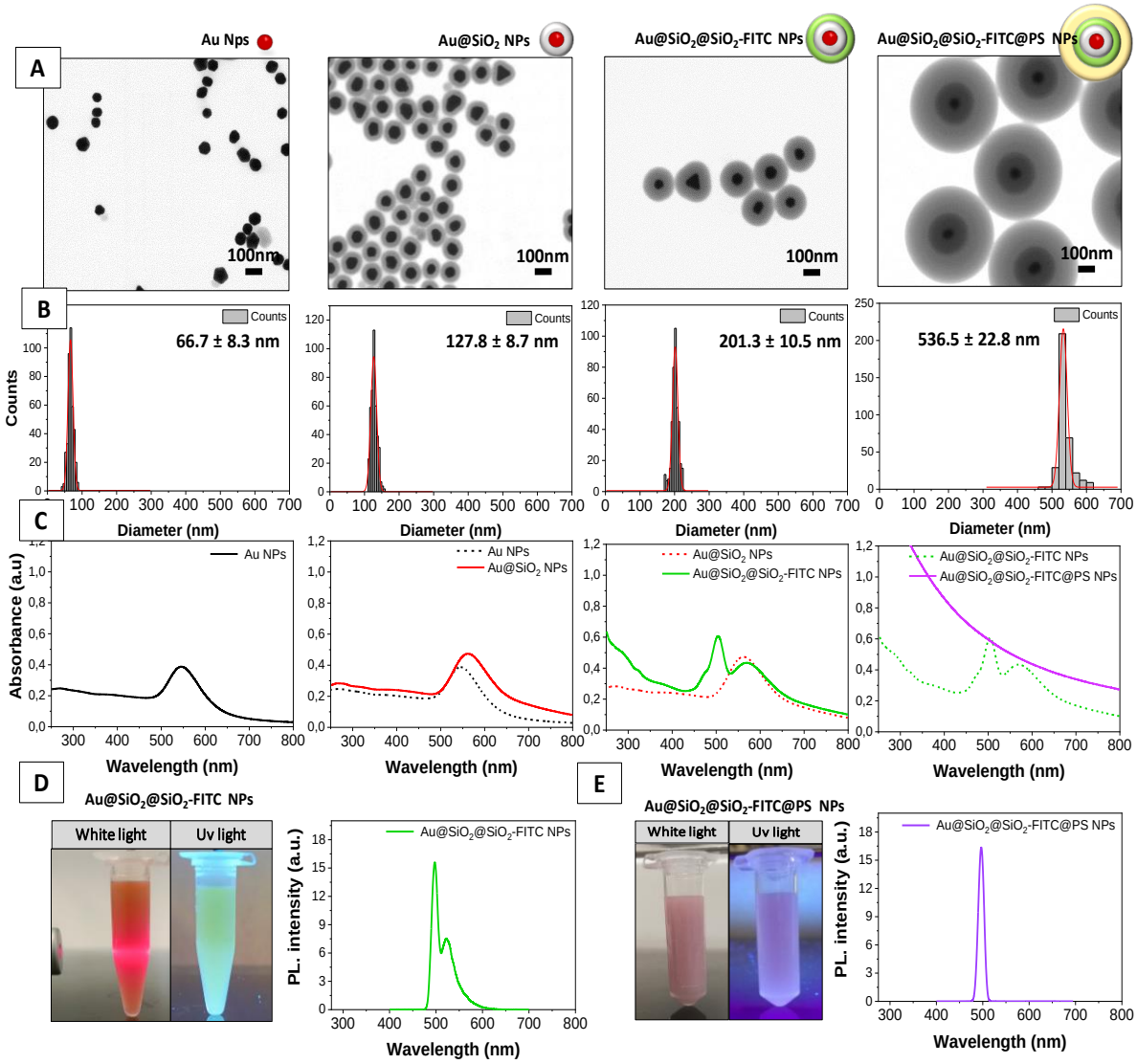

Figure 4.10 Characterization of the PEF-labelled PS NPs and its production process. From left to right Au cores, Au@SiO_2, Au@SiO_2@SiO_2-FITC and Au@SiO_2@SiO_2-FITC@PS NPs. (A) Representative (STEM) images. (B) Calculated size distribution profile of NPs. Mean size and Standard distribution was calculated at least counting 300 particles using software image J. (C) Absorbance spectra of the different NPs in 1/10 dilution. The characteristic LSPR peak of Au NPs is red shifted to longer wavelength after SiO_2 coating processes. The Au@SiO_2@SiO_2-FITC NPs shows the characteristic FITC absorbance peak at 495nm. For Au@SiO_2@SiO_2-FITC@PS, the characteristic LSPR of the Au and FITC were attenuated by the high scattering contribution of PS. Photoluminescence spectra in 1/10 dilution of (D) Au@SiO_2@SiO_2.FITC NPs showing the characteristic FITC emission peak at 525nm and (E) Au@SiO_2@SiO_2-FITC@PS NPs. Inset optical images of colloidal solutions under white light and UV-light.

A mixture of the FITC-APTES complex and TEOS was used as Si precursor for the growth of an additional second layer of SiO_2 of ~37 nm onto the Au@SiO_2 to increase the loading capacity of the NPs while preserving the integrity of the FITC dye from the environment. The presence of the dye in the outer SiO_2 shell results in the appearance of

an additional band in the absorbance spectrum of Au@SiO_2@SiO_2-FITC at 495 nm, corresponding to the absorbance peak of the FITC fluorophore, **figure 4.10-C**. Similarly, emission spectrum of Au@SiO_2@SiO_2-FITC shows the characteristic emission peak at 525nm **figure 4.10-D**, confirming that the fluorescence of FITC is preserved after being embedded in the SiO_2 shell. Hydrodynamic diameter of NPs increases from 144.3 ± 2.3nm (Au@SiO_2) to 219.9 ± 5.3nm (Au@SiO_2@SiO_2-FITC). Moreover, the presence of the dye in the outer SiO_2 shell provides a less negative surface charge to the NPs (-22.2 ± 1.6 mV) compared to the Au@SiO_2 NPs (-31.7± 1.6 mV), indicating that the presence of positively charged amine groups of APTES partially lowers the magnitude of the charge provided by the SiO_2-coating.

The final step involves the growth of a polystyrene (PS) shell onto the Au@SiO_2@SiO_2-FITC NPs, by the radical emulsion polymerization. For that, the surface of the NPs was chemically modified with methacryloxypropyltrimethoxysilane (TMSPMA). This functionalization process is necessary to adjust the reactivity of the NPs and obtain uniform polymer shells with controllable thickness by the controlled addition of styrene (St) as precursor and divinylbenzene (DVB) as co-monomer crosslinker. In addition, the polymer initiator potassium persulfate salt (KPS), acts as strong oxidant for the generation of sulphate SO_4^- radical species by thermal decomposition, which initiates the polymerization process. The obtained Au@SiO_2@SiO_2-FITC@PS NPs with a mean size and size distribution (536.5 ± 22.8 nm) present a quasi-concentric core-shell morphology, with single Au core inclusion per particle. The presence of the PS appears as a white layer surrounding the dark Au core. The growth of the polymer layer caused a complete attenuation of the UV-Vis profile due to the high absorption of the PS shell. ζ-potential values (-41.2 ± 0.90 mV) confirmed the colloidal stability of NPs due to the negative charge of the sulphate groups at the particle surface. Polymer-coated particles can be precipitated by centrifugation and re-suspended in deionized water, various buffers, and short-chain alcohols. This procedure can be repeated an unlimited number of times without losing colloidal stability. Finally, the mass of PS in the PEF-labelled PS NPs was calculated. For this purpose, first the concentration of Au was determined. The concentration found was (124µg/mL). This procedure was done by elemental spectroscopy analysis (ICP-MS), in collaboration with the Chemical Analysis Service (SAQ) of the Scientific and technical

services of the University Autonomous of Barcelona (UAB). Second, the PS content of the NPs was determined by theoretical calculation of the relationship in concentration between Au gold to Polystyrene, in where PS (µg/mL) = 3.89 x $Au(\mu g/mL)_{ICP\text{-}MS}$, thus, the PS content calculated on the NPs was *482.4 µgPS/mL.* For calculations, were used the weight loss by thermogravimetric analysis (TGA), the molecular weight (MW) and density (ρ), for colloidal silica and the gold particles, the $\bar{V}_{NP}$ is the volume occupied for NP in nm^3, calculated using the sphere volume formula ($4/3\pi r^3$), in which diameter were calculated by STEM. The detailed calculations showed in **Appendix C7**.

4.4 In Vivo and In Vitro Correlation of the Multimodal Contrast Agent Polystyrene NPs Using Different Imaging Modalities

The faculty of the PEF-labelled PS NPs for biological identification and tracking as a multimodal contrast agent, were evaluated in this section. For this purpose, a cell line (for evaluation of the cellular and sub-cellular levels) and in animal model (for assessment tissues and organs and their biodistribution, accumulation, fate and secretion pathways) were demonstrated by the combination of a wide variety of physicochemical characterization techniques, such as laser confocal microscopy (LCM), X-ray imaging (CT) and elemental analysis (ICP-MS), each with a trade-off between imaging resolution and penetration depth. The synergistic imaging and chemical analysis of the PEF-labelled NPs, allowed us the optimal visualization of across the different techniques in a biological model. The NPs were incubated for 24h in human embryonic kidney HEK293 cells for in vitro assessment and for the in vivo biodistribution oral administration were done, where the NPs were administered as synthesized via (gavage/mouse) and intravenous administration via (tail-vein injection). However, before the biological imaging analysis of the particles, the integrity and colloidal stability of the PEF-labelled PS NPs were evaluated by exposing them on simulated biological in vivo and in vitro mediums.

4.4.1 Exposition of The Multimodal Contrast Agent Polystyrene NPs to Biological Media

In this part, we studied the physical stability (agglomeration, dissolution or aggregation) of the PEF-labelled PS NPs, as multimodal contrast agent, after their exposure to simulated body fluid (SBF) intravenous and oral physiological conditions, (SBF conditions in **Chapter 5, section 5.3.3.1**). In brief, the SBF medias were: for albuminization, 10mM Phosphate Buffer solution (PB) and (2.0 mg/mL) Bovine Serum Albumin (BSA). For intravenous conditions, using complete Cell Culture Media (cCCM) composed of (10%) Fetal Human Serum (FBS) and (90%) Dulbecco's Modified Eagle Medium (DMEM) and for oral administration, artificial simulated physiological intestinal (I.F) and gastric fluids (G.F), composed of lecithin, pepsin, mucin gastric, maleic acid and sodium taurocholate at pH 6.50 and 1.50, respectively. This experiments were done, in order to assess the integrity of the PS layer once exposed to biological medias for 24h. However, a PS NPs without the PEF-core (without FITC) but with the same Au NPs size having a comparable 30nm of SiO_2 shell was prepared for practical evaluation of the integrity of the PS shell in the biological conditions. The physicochemical characterization of the synthetized particle was done by UV-Vis spectroscopy, DLS and STEM microscopy and is showed in the **table 4.5** and **figure 4.11**, as follows:

Table 4.5 Physicochemical characterization of the Au@SiO_2@PS NPs for the biological evaluation

NPs	$LSPR_{peak}$ (nm)	TEM diameter (nm)	SD (%)	DLS_{number} (nm)	PdI	ζ-potential (mV)	Media / pH	Cond. (mS/cm)
Au NPs	545.3	64.7 ± 7.4	11.4	55.8 ± 4.2	0.196	-28.9 ± 0.2	Water/6.9	0.7822
Au@SiO_2	561.4	144.3 ± 10.7	7.4	192.1 ± 4.5	0.046	-34.1 ± 1.3	Ethanol	0.0052
Au@SiO_2 @PS	571.8	210.8 ± 11.9	5.6	287.5 ± 10.4	0.115	-30.5 ± 1.2	Water/7.8	0.0327

DLS and ZP were done calculated by three independent measurements.

In brief, gold Au NPs of size (64.7 ± 7.4 nm) were synthesized following a well reported kinetically controlled seeded growth method via the reduction of HAuCl4 by sodium citrate, until preferred size [85]. Then, were used as seeds for growing of an uniform SiO_2 shell of ~39 nm (Au@SiO_2 NPs) derived from hydrolysis/condensation of the TEOS by a modified Stöber [107], leading to mean size and SD of (144.3 ± 10.7 nm). Representative STEM images of Au NPs before and after coating with SiO_2 are shown in **figure 4.11-A**,

where the monodispersity of the Au NPs cores were retained after the SiO_2 shell growth of the SiO_2 shell. The extinction spectra show their characteristic LSPR peak of Au NPs at 545.3nm, for-which red-shifted to 561.4 nm after the SiO_2 coating which, ascribed to the increase in the dielectric constant of the particle surroundings. In agreement with the increase in STEM diameter, the Au NPs displayed a hydrodynamic diameter increased from 55.8 ± 4.2 nm (Au NPs) to 192.1 ± 4.5 nm (Au@SiO_2 NPs). In addition, the ZP decreases from -28.9 ± 0.2 to -34.1± 1.3 mV, confirming the generating of highly negative silanol groups (Si-OH) on the surface.

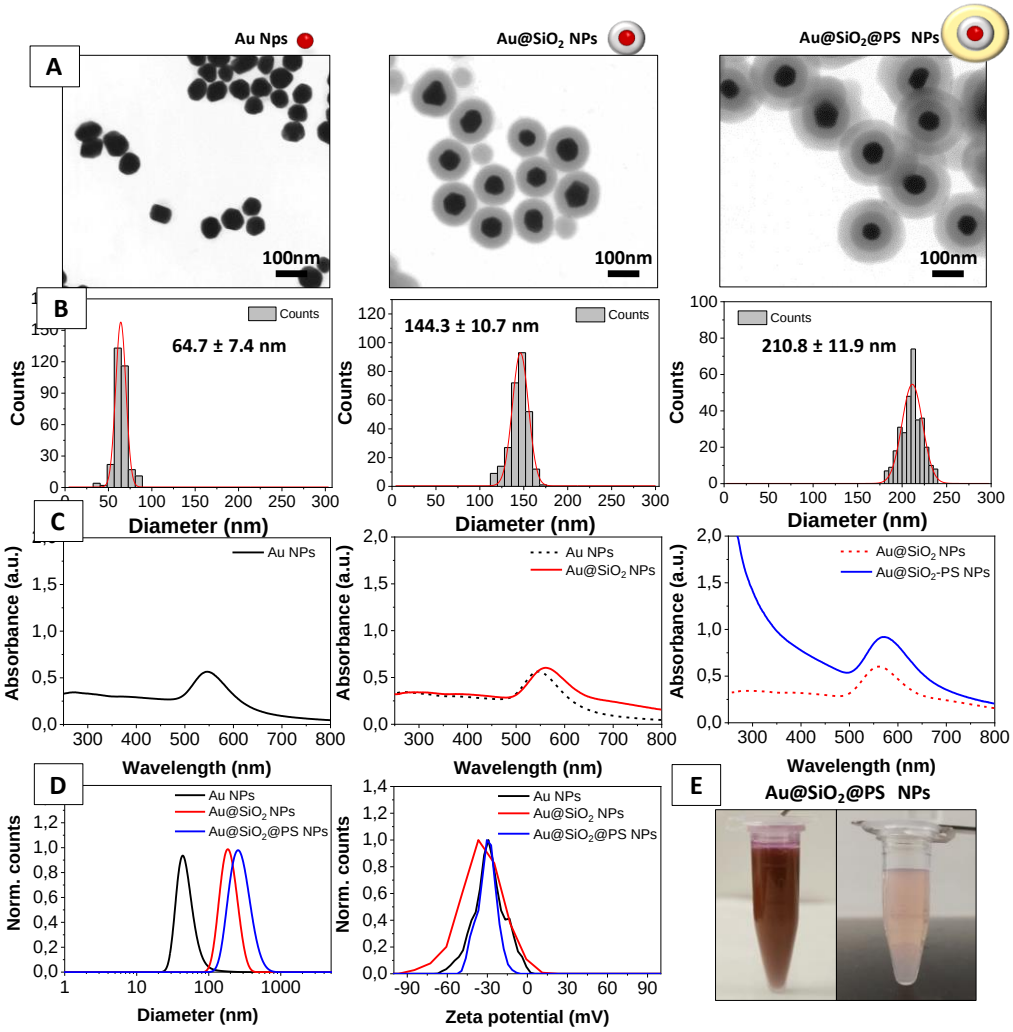

Figure 4.11 Characterization of the Au@SiO_2@PS NPs and its production process. From left to right Au cores, Au@SiO_2 and Au@SiO_2@PS NPs. (A) Representative (STEM) images. (B) Calculated size distribution profile of NPs. Mean size and Standard distribution was calculated at least counting 300 particles using software image J. (C) Absorbance spectra of the different NPs in 1/10 dilution. The characteristic LSPR peak of Au NPs is red shifted to longer wavelength after SiO_2 coating and PS shell processes. Inset optical images of colloidal solutions under white light as-synthetized and 1/10 dilution.

Once the Au@SiO_2 NPs particles were coated with the silica layer, the NPs were purified by centrifugation (3.000g for 15 min) and were directly surface-modified with 150mM of (TMSPMA), to introduce vinyl groups onto the particle surface. Finally, the PS shell (~33 nm) was grown on the surface of the NPs (Au@SiO_2@PS NPs) by adapting the emulsion polymerization, in which radicals were generated by thermal decomposition of potassium persulfate to polymerize the styrene precursor on the particle surface. The results were in agreement with an increased in the hydrodynamic size to 287.5 ± 10.4 nm. In addition, the LSPR of the NPs ref-shifted to 571.8nm and the particles were colloidal stable in water at neutral pH, with a negative ZP value of (-30.5 ± 1.2 mV), indicating good colloidal stability due to the sulphate (−SO_3H) negative groups on particle surface.

To study the physical stability of the particles and evaluate the integrity of the PS shell, the NPs were incubated in intravenous (I.V.) and in oral (O.A) conditions (experimental in **Chapter 5, section 5.3.3.1**). First, for (I.V) 10% of the Au@SiO_2@PS NPs were conjugated with a solution of (PB 10mM + BSA 2mg / mL) of final concentration, for 24 hours at 4 degrees. (Albuminization). Second, the 10% of the albuminized NPs of the previous step were incubated in a solution (DMEM 90% + FBS 10%), for 24 hours at 37 degrees. Then, For the (O.A.), 200uL of NPs as-synthetized were exposed directly to the gastric and intestinal media, and were incubated for about 24 hours at 37 degrees. Finally, for all the conditions, the NPs unpurified and purified were characterized by DLS recording the ZP and hydrodynamic size, UV-VIS spectroscopy and microscopy by STEM. Results summarized in **table 4.6** and **figure 4.12**

Table 4.6 Physicochemical characterization of the Au@SiO_2@PS NPs after exposure to the different biological media

NPs	LSPR $_{peak}$ (nm)	TEM diameter (nm)	SD (%)	DLS_{number} (nm)	PdI	ζ-potential (mV)	Media / pH	ζ-potential (mV)[a]	Cond. (mS/cm)[b]
Au@SiO_2 @PS	571.8	210.8 ± 11.9	5.6	262.5 ± 2.7	0.060	-29.4 ± 0.9	Water pH 7.00	-30.5 ± 1.2	0.0326
Albuminization (PB + BSA)	575.7			271.4 ± 3.5	0.015	-25.4± 0.4	PB 10 mM pH 7.20	-41.3± 0.7	0.0894
cCCM (DMEM + FBS)	573.3			297.3 ± 2.07	0.042	-9.7 ± 2.1	cCCM 7.20	-34.3 ± 0.6	0.0364
Intestinal Fluid	575.6			361.5 ± 16.6	0.220	-29.9 ± 2.2	Mild Acid pH 6.5	-37.1 ± 0.7	0.0107

Gastric fluid	571.8			687.5 ± 20.6	0.397	0.95 ± 1.5	Acid pH 1.5	-22.3 ± 1.0	0.0374

DLS analysis were done by triplicate, a=Zeta potential after sample purification. b= conductivity after purification.

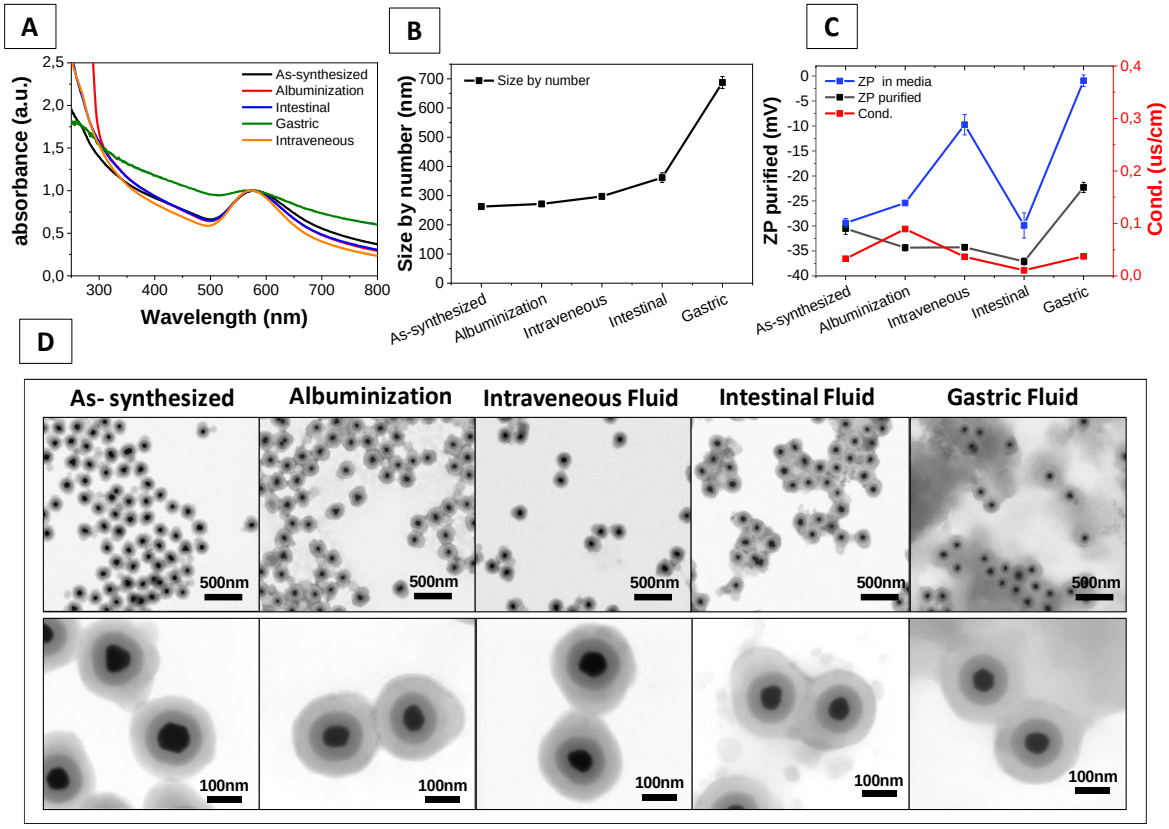

Figure 4.12 Characterization of the Au@SiO_2@PS NPs after their exposure to the different physiological media. (A) UV-Vis spectra of the NPs after their exposure for24h to the different physiological media. The spectra were taken in a 1_10 dilutions in pure water at neutral pH. Dynamic light scattering (DLS) analysis of the purified NPs recording, (B) Hydrodynamic size by number after 24h and (C) Zeta potential (ZP) distribution after 24h. ZP of the not purified NPs in media is showed (in blue) for comparison. (D) Electron microscopy images by STEM of the NPs after the exposure to the different physiological conditions and incubated for 24h. The as-synthesized column is the control which is the incubated NPs in water at 37°C for 24h for comparison.

Physicochemical transformations of NPs were analysed by UV-Vis spectroscopy, hydrodynamic size and ZP by DLS of the unpurified and purified samples, as showed in figure **4.12-A-C**. The combination of these characterization techniques has been proved to provide a remarkably robust analysis of the colloidal state of NPs in complex biological media. As it can be observed, the results from the Uv-Vis spectrums showed that the colloidal stability of the NPs were maintained in the majority of the biological mediums, with the exception of the gastric condition (G.F). The Uv-Vis spectra showed both an

increase in the absorbance signal at higher wavelengths and peak broadening, a clear evidences of a decrease in the colloidal stability of the NPs. Thus, in the G.F media, the LSPR band of the Au particles started to vanishes, due to the absence of serum proteins than can stabilize the NPs. On the other hand, the LSPR peak of the NPs in the other mediums (albuminization, cCCM and I.F) red shifted from 571.8nm (Au@SiO_2@PS) to 573.3nm and 575.7nm after incubation with proteins (cCCM and albuminization). This change in the LSPR of the NPs can be ascribed to the adsorption (by electrostatic, hydrophobic, van der Waals and dispersive forces) of proteins onto the NPs surfaces, forming a protein dense coating known as Protein Corona (PC) [108]. The PC shields the original surface properties of the NPs acting as a "complex" surfactant, increasing the colloidal stability and alters their size and composition providing the NPs with a new biological identity. Moreover, our obtained results were corroborated by DLS. Hydrodynamic diameter of the NPs remained comparable after being incubated in the (albuminization, cCCM and I.F), but increased dramatically towards larges sizes in G.F., suggesting the presence of larger objects in solution. The STEM images in **figure 4.12-D**, revealed any morphological change after 24 of incubation that could be associated to PS shell dissolution. However, the NPs exposed to G.F, presented a grey background, suggesting the presence of organic compounds composed (mucin, lecithin and pepsin), that were attached to the NPs, that explained the observation of larger size by DLS.

The unpurified ZP analysis showed a decreased in comparisons with the control (-30.5 ± 1.2mV) after the exposition of the NPs in the biological medias. The NPs exposed to BSA/PB buffer and I.V reported a ZP valued of -25.4± 0.4mV and -9.7 ± 2.1mV in the medium. These results support the previous observations that proteins form a dense layer on the surface NPs. The decreased in the surface charge of the NPs, were not low enough to prevent NPs from electrostatic aggregation (an absolute value of 30 mV is usually considered as a limit for particle stability), revealing that the stability of the NPs was mediated by steric repulsions provided by proteins. When the NPs were purified, the ZP of the NPs remained highly negative, suggesting that proteins were not covalently attached. In contrast, the NPs exposed to G.F, the ZP decreased close to 0mV. But after purification, the ZP increased to -22.3 ± 1.0 mV. This result is clear evidence that the presence of an organic mucus of proteins attached to the NPs. One explanation can be due to the low pH

of the media (1.50), that destabilized the NPs and decrease the electrostatic repulsion. Finally, we can conclude that the integrity of the PS shell was maintained in al biological conditions. Only aggregation can be observed in the G.F media.

4.4.2 In vitro Analysis of the Multimodal Contrast Agent Polystyrene NPs: HEK Model

Once we determined that the integrity of the PS shell of the Au@SiO_2@SiO_2 – FITC@PS NPs, was maintained after 24h of incubation in the both, in vivo and in vitro biological conditions. The multimodal imaging capabilities of the PEF-labelled PS NPs (characterized in **figure 4.10**), were evaluated using in vitro conditions using HEK cell lines as a model, as shown in **figure 4.13**. (Materials and Methods for the In vivo and in vitro analysis **Chapter 5, section 5.3.3.2**)

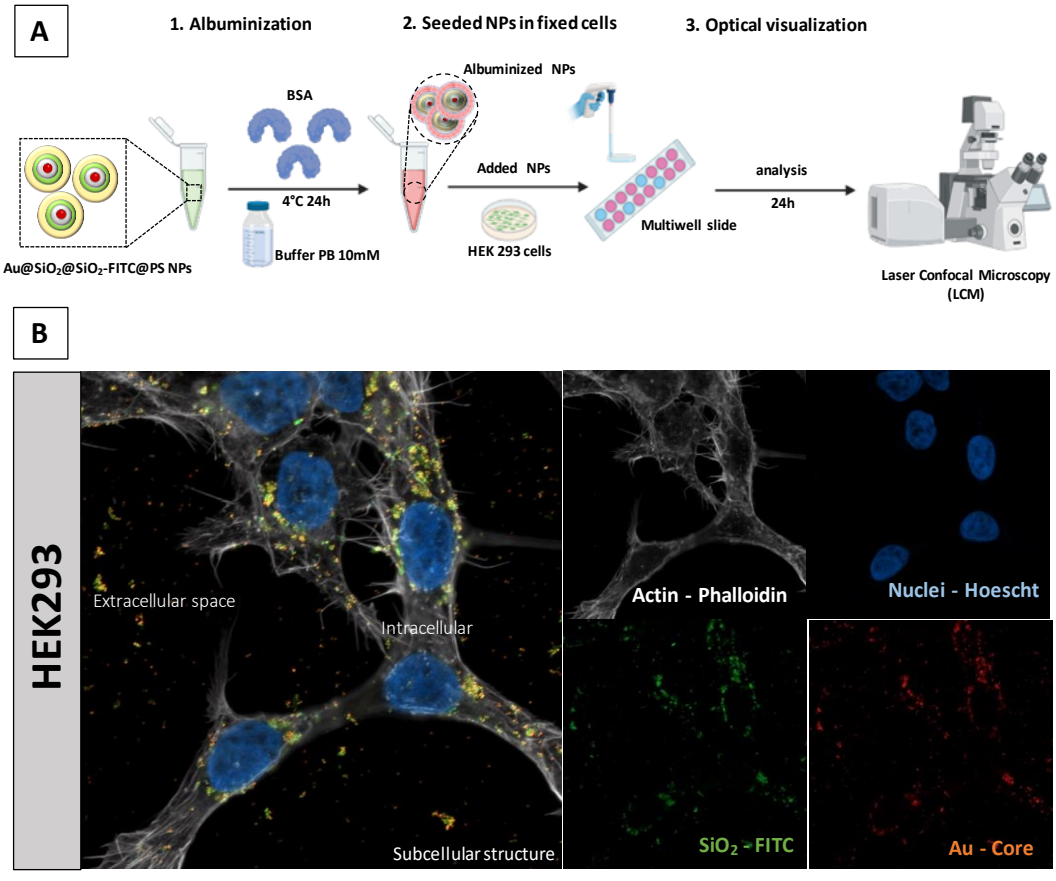

Figure 4.13 Graphical representation of the colocalization analysis of the Au@SiO_2@SiO_2-FITC@PS NPs when exposed to HEK290 cells for 24h. (A) Graphic illustration of the experimental procedure. NPs were prior albumenized before exposure. (B) High-resolution laser confocal microscopy analysis after 24h. It is possible to colocalizate into the HEK cell line the Au cores and the FITC dye into the SiO_2 shell. To image the Au core, the light scattered was collected by setting the Confocal microscope to reflectance mode. For this, the dichroic mirror was retracted, only a T80/20 beam splitter

was set instead. FITC (em490/ex525) were observed using the standard fluorescence mode and pre-defined settings. Colours from the images acquired are chosen arbitrarily in each case to better discriminate all the signals collected.

For this purpose, as showed by the figure **4.13-A**, first the NPs were albumenized with BSA (2.0mg/mL) for 24h at 4°C, for grafting the surface with proteins, thereby increasing their colloidal stability in physiological conditions. Later, the albumenized NPs, were added dropwise and homogenized onto cell cultures in multiwall slide with HEK293 cell lines for 24h. Finally, the incubated NPs were observed on the High-Confocal Laser Scanning Microscope (CLSM) Zeiss LSM 980 after 24, in order to localize the PS NPs, determining both the emission intensity of the fluorophore FITC and the scattering of the Au NPs, as shown in **figure 4.13-B.**

Studies on the interaction between PEF-labelled PS NPs nanoprobes and cells are helpful to better evaluate their potential applications in multimodal imaging. Therefore, the cellular uptake behavior of PEF-labelled PS NPs, was further examined by CLSM following the incubation of HEK293 cells in cell culture media for 24 h. As shown in **figure 4.13-B**, the confocal images of HEK cells were obtained after staining (blue) nuclei with Hoechst 33342. The HEK cells remained attached on the plate well and maintained their normal morphology after being incubated with PEF-labelled PS NPs, which further suggested no obvious cytotoxic effect on the cells. NPs were simultaneously imaged by the FITC (green) and Au (scattering in red) using the conventional fluorescence and reflectance modes. The multiplex staining with the Phalloidin and the Hoechst allows us to locate the NPs in the sample, either in the extracellular space, intracellularly or bound to the cell membrane, from a certain z-section of the sample. The significant internalization and colocalization of the NPs was demonstrated by the presence of spot-like green fluorescence and red spots scattering in the subcellular structure via, perhaps via endocytosis. The colocalization coefficient was measured as a function of the pixel intensity (Pearson Correlation Coefficient) and as function of the spatial overlap (Manders Correlation Coefficient). In both cases, it shows a positive correlation demonstrating that PEF-labelled PS NPs can be a promising candidate for multi contrast agent for in vitro cellular imaging for microplastics.

4.4.3 In vivo Analysis of the Multimodal Contrast Agent Polystyrene NPs: a Mice Model

Once we determined that the PEF-labelled PS NPs were suitable for in vitro analysis using cell lines, the feasibility of the multimodal imaging capabilities of the PEF-labelled PS NPs as contrast agent were assessed for in vivo conditions using an animal model. For this determination, as showed by experimental process in the **figure 4.14**, were done by oral (gavage) and intravenous (lateral tail-vein injection) administration, using a mice model. The Eight-week-old females Balb/C mice were facilitated and housed under pathogen-free conditions at the local animal facility (Vall d'Hebron Institute of Oncology, VHIO). All experimental procedures were carried out in compliance with the protocols approved by the local CEEA (Ethical Committee for the Use of Experimental Animals) (Generalitat Catalana, Territory and Sustainability Department, Barcelone, Spain, authorization number 11357). The acquisition and processing of computed tomography in vivo images were done in the Preclinical Imaging Platform (Cellux Lab Animal Service, VHIO, Barcelone, Spain). The Chemical Analysis Service were done at Autonomous University of Barcelone (SAQs, UAB, Barcelone, Spain). This in vivo analysis was done in collaboration with the PhD student Muriel Freixanet Gusta and Lena Montaña Ernst from the Vall d'Hebron Institute of Research (VHIR), in the Research Group Pharmacokinetic Nanoparticles and the Postdoctoral researcher Laura Mondragón Martinez, from the Josep Carreras Leukaemia Research Institute (IJC).

The animal uptake behavior and biodistribution of PEF-labelled PS NPs, was further examined by CLSM, X-ray (CT) scan and elemental analysis using ICP-MS spectrometry. The mice were randomly divided in three groups, control, intravenous I.V and oral O.A administration. As shown in figure the **figure 4.14**, for the I.V administration, NPs were first albuminized and further 200µL tail-vein injected in a concentration of (9 µg of Au, equivalent to approximately 22 µg of polystyrene; 2 mg/mL BSA final concentration was added which was equivalent to 20X the concentration needed to cover the surface of all NPs in the sample). Later, the CT scans was performed at different time (5 and 30 min, 1 and 24h post-treatment). The NPs biodistribution were assessed by elemental Au determination ICP-MS of the digested organs. The liver, kidney and spleen organs sections

were embedded in paraffin block and observed in the CLSM and finally once the treatment was administered. For the O.A administration, the NPs were administered directly in a saline solution 200µL by oral gavage (26 µg Au, equivalent to approximately 64 µg of polystyrene). The organs were collected for ICP-MS elemental analysis and later the mice were subjected to CT scans performed at different time (5 and 1,4,8 and 24h post-treatment). Imaging data were analysed by Preclinical Imaging Platform staff at VHIO. Image reconstruction was based on Feldkamp´s method. Data were represented as mean ± SEM. Control group was treated with the vehicles employed for the different treatments in a similar way to oral and intravenous treatment groups.

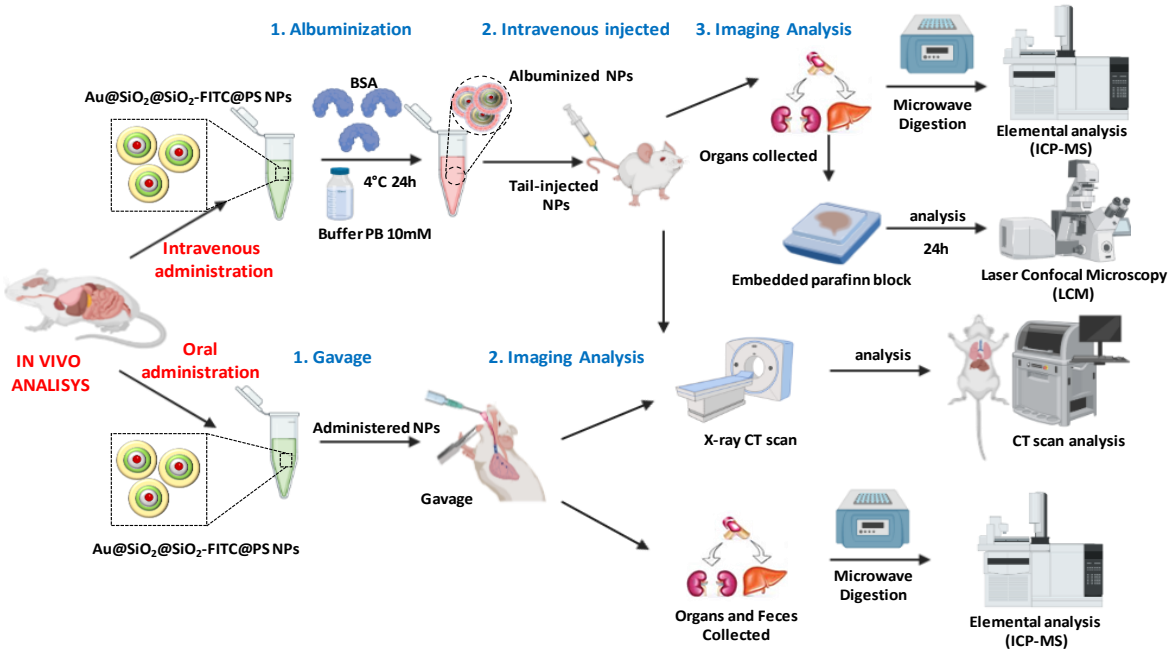

Figure 4.14 Graphical illustration of the experimental procedure for the in vivo analysis of the Au@SiO_2@SiO_2-FITC@PS NPs after the oral (gavage) and intravenous (lateral tail-vein injection) administration.

4.4.3.1 In vivo Analysis: Intravenous Administration (I.V)

Figure 4.15 demonstrate the utility of the Au@SiO_2-FITC@SiO_2@PS NPs as a contrast agent for in vivo imaging and tracking using a mice as animal model. This analysis revealed information about the mechanism of interaction with organs (liver, kidney, spleen), their biodistribution, accumulation, fate and secretion pathways after I.V. administration of the NPs.

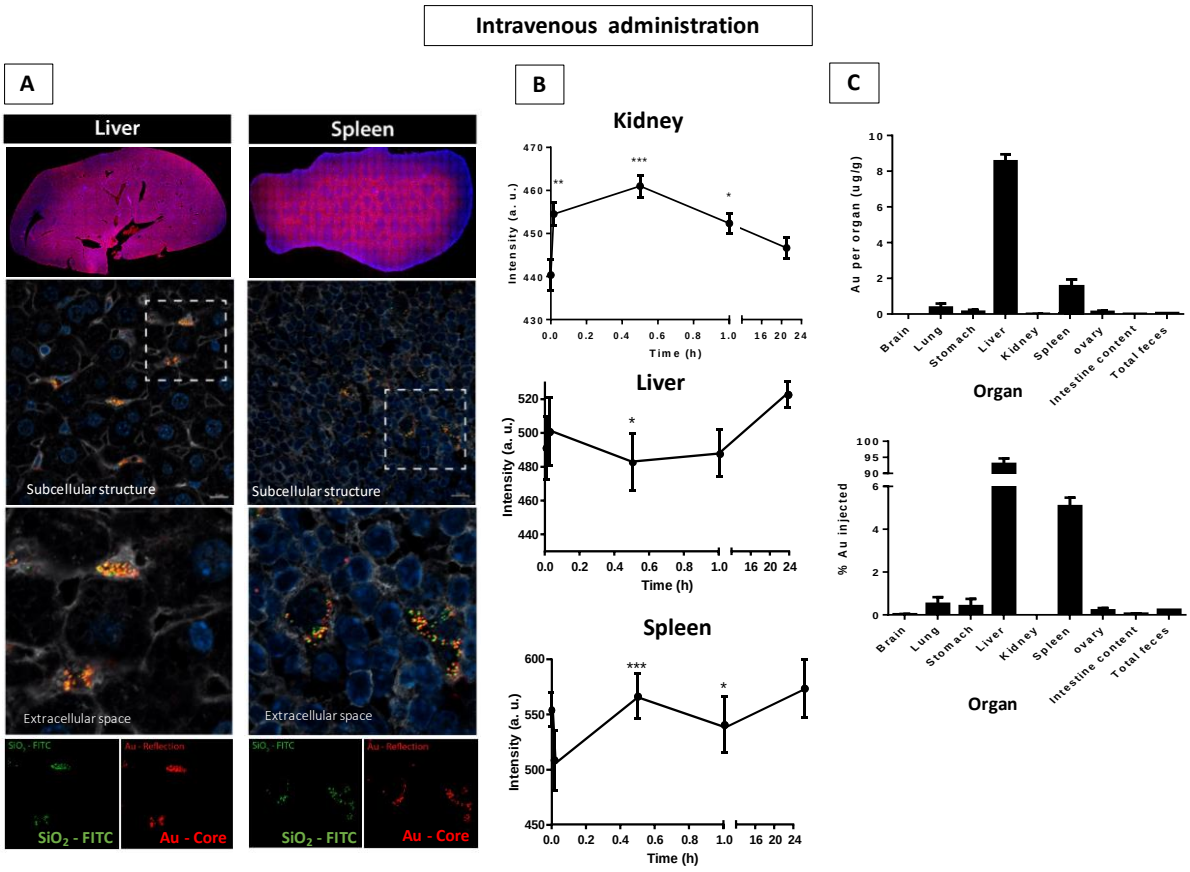

Figure 4.15 Graphic illustration of the biodistribution analysis of the Au@SiO_2-FITC@SiO_2@PS NPs after intravenous administration. (A) High-resolution laser confocal microscopy analysis of the liver and spleen sections. Colocalization analysis allowed the visualization of the Au cores and the FITC dye in both organs. To image the Au core, the light scattered was collected by reflectance mode. FITC (em490/ex525) were observed using the standard fluorescence mode and pre-defined settings. (B) Graphical representation of the computed tomography scan (CT) analysis of one of the five mice treated intravenously at different time-points. Quantification of the Au-Si-PS signal in Hounsfield units (HU) were done in different organs of the mice treated. (C) Graphical representation of the gold content (Au) of the collected organs and feces, after 24h of I.V administration by elemental analysis using ICP-MS. Organs and samples were treated prior analysis by microwaved digestion.

Confocal fluorescence images of the mouse liver and the spleen paraffin embedded tissue sections revealed the presence of orange dots, suggesting the presence of the PEF-Labelled PS NPs in both organs. NPs were simultaneously imaged by the FITC (green) and Au core (scattering in red) using the conventional fluorescence and reflectance modes. The multiplex staining allowed to co-localize the NPs in the liver hepatocytes and spleen mononuclear cells, either in the extracellular space, intracellularly or bound to the cell membrane, from a certain z-section of the sample. The internalization of the NPs was demonstrated by the separate collection of the FITC fluorescence spot-like green and Au

scattering red-spots signals. The co-localization coefficient was measured as a function of the pixel intensity (Pearson Correlation Coefficient) and as function of the spatial overlap (Manders Correlation Coefficient). Moreover, the haematoxylin & eosin image analysis of the rehydrated tissue sections was done, revealing any morphological damage of the tissues (showed in **Appendix C8**). For the X-ray (CT) scan, **figure 4.15-B** showed the attenuation values (HU) at different time-points of the I.V administered mice were measured by the CT equipment. The representative graphical (CT) scan intensities, revealed the increased contrast enhancement signal in the liver and spleen sections, revealing the fate and accumulation of the NPs after 24h. Results that were in agreement with the CLSM observations. In contrast, the kidney signal increased during the first hour but decreased after 24h, concomitant with the confocal results, that NPs were not observed in the Kidney section.

Finally, the biodistribution and accumulation of the PEF-labelled Ps NPs were done by elemental analysis by ICP-MS, determining the total Au content on the analysed organs, as shown in **figure 4.15-C**. Our results revealed that the Au content of the collected organs and feces after 24, were found in majority in the Liver section. The total Au content added were 9 µg Almost 90% (8.00µg Au/organ g) of the total Au content were found in this organ section. In contrast, around 6.0% were found in the spleen and <5.0% in the lungs and stomach. Interestingly, in the kidney section any content of gold was found. Results in agreement since, NPs remained longer circulation time in blood, which was well consistent with the results that the NPs could be gradually enriched in the organ such as liver.

4.4.3.2 In vivo Analysis: Oral Administration (O.A)

CT scan of the mouse was done after O.A to visualize the in vivo distribution of NPs by means of contrast enhancement. **Figure 4.16-A**, showed a representative computed tomography scan(CT) images in the coronal and axial axis at different time-points (5min, 1,4,8 and 24h). The Basal signal was taken as control. By following the white dots in to the images, it is possible to observed the presence of white dots (difference in scattering of the

Au NPs) in the CT scans. From the CT results, it can be concluded that the PEF-labelled PS NPs were seen in the stomach during the first 4 hours, but after 24h the white dots were mainly located in the large intestine zone.

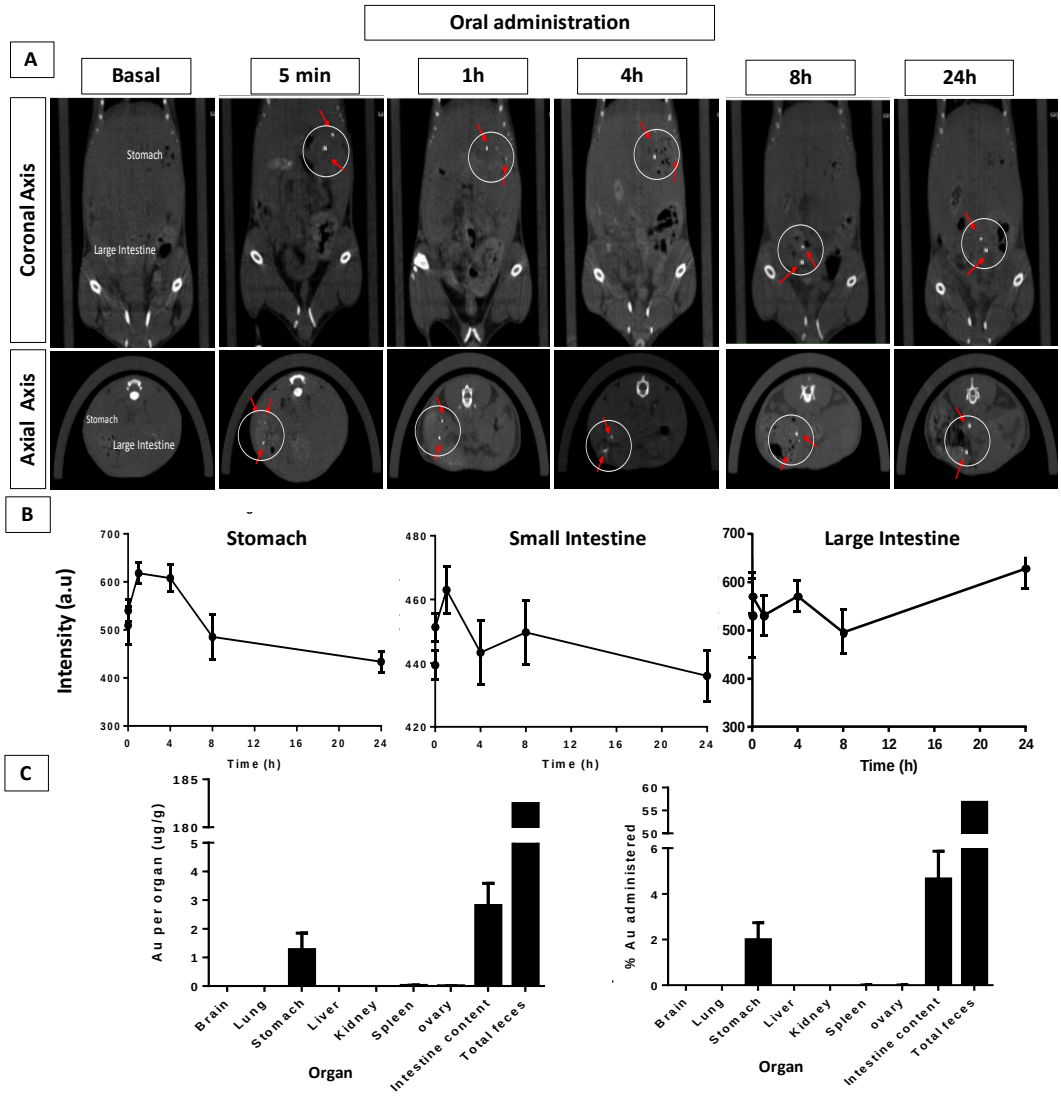

Figure 4.16 Graphic illustration of the biodistribution analysis of the Au@SiO_2-FITC@SiO_2@PS NPs after oral administration. (A) Representative computed tomography scan (CT) images of one of the five mice treated orally the NPs at different time-points. The presence of white dots, that evolved from the stomach to the large intestine can be observed due to the Au scattering signal. (B) Graphical representation of the CT scan analysis of one of the five mice treated orally with the NPs at different time-points. Quantification of the Au-Si-PS signal in Hounsfield units (HU) were done in different organs of the mice treated. (C) Graphical representation of the gold content (Au) of the collected organs and feces, after 24h of gavage administration by ICP-MS. Organs and samples were treated prior analysis by microwaved digestion. White circle indicates the site of NPs.

Concomitant with these observations, in **Figure 4.16-B,** the X-ray (CT) scan attenuation values (HU) intensities, revealed the increased contrast enhancement signals

in the stomach during the first 4 hours. In contrast, the intensity in signal was increased in the large intestine beyond 20h. Results that were in agreement with the scan images.

Finally, the fate and accumulation of the PEF-labelled PS NPs were followed by ICP-MS, as observed in **figure 4.16-C**. Our results showed that the Au content were mostly found stomach, intestine and feces. Interestingly, these observations were in agreement with the CT results, that increased the HU signal in the same organs. The Au content found were around 1.2 µg Au/g in the stomach, 2.8 µg Au/g and 182 µg Au/g in the total feces. These results indicate that around 55% of the total Au content were found in feces, thereby indicating that NPs were secreted. On the other hand, around 6.0% of the Au content were found in the stomach and intestines. It has to noted, that the recovery of the Au content was not higher, because we believed that experimentally, some samples of the feces may be lost or not properly collected for the elemental analysis. However, we can conclude that the PEF-labelled PS NPs can be followed by the combination of different imaging modalities, such as, CT, CLSM and ICP-MS, after O.A administration

4.7 References

[1] T. T. Awet *et al.*, "Effects of polystyrene nanoparticles on the microbiota and functional diversity of enzymes in soil," *Environ. Sci. Eur.*, vol. 30, no. 1, p. 11, 2018, doi: 10.1186/s12302-018-0140-6.

[2] S. A. for P. by E. Academies, "A Scientific Perspective on Microplastics in Nature and Society," Berlin, Jan. 2019.

[3] W. J. Shim, S. H. Hong, and S. E. Eo, "Identification methods in microplastic analysis: a review," *Anal. Methods*, vol. 9, no. 9, pp. 1384–1391, 2017, doi: 10.1039/C6AY02558G.

[4] J. C. Prata, J. P. da Costa, A. C. Duarte, and T. Rocha-Santos, "Methods for sampling and detection of microplastics in water and sediment: A critical review," *TrAC Trends Anal. Chem.*, vol. 110, pp. 150–159, 2019, doi: https://doi.org/10.1016/j.trac.2018.10.029.

[5] A. Müllertz, Y. Perrie, and T. Rades, *Analytical Techniques in the Pharmaceutical Sciences*. 2016.

[6] W. D. L. van Raamsdonk *et al.*, "Current Insights into Monitoring, Bioaccumulation, and Potential Health Effects of Microplastics Present in the Food Chain," *Foods* , vol. 9, no. 1. 2020, doi: 10.3390/foods9010072.

[7] C. Della Torre *et al.*, "Accumulation and Embryotoxicity of Polystyrene Nanoparticles at Early Stage of Development of Sea Urchin Embryos Paracentrotus lividus," *Environ. Sci. Technol.*, vol. 48, no. 20, pp. 12302–12311, Oct. 2014, doi: 10.1021/es502569w.

[8] A. Rudin and P. Choi, "Chapter 8 - Free-Radical Polymerization," A. Rudin and P. B.

T.-T. E. of P. S. & E. (Third E. Choi, Eds. Boston: Academic Press, 2013, pp. 341–389.
[9] B. R. Kiran, H. Kopperi, and S. Venkata Mohan, “Micro/nano-plastics occurrence, identification, risk analysis and mitigation: challenges and perspectives,” *Rev. Environ. Sci. Bio/Technology*, vol. 21, no. 1, pp. 169–203, 2022, doi: 10.1007/s11157-021-09609-6.
[10] K. Nakashima, J. Duhamel, and M. A. Winnik, “Photophysical processes on a latex surface: electronic energy transfer from rhodamine dyes to malachite green,” *J. Phys. Chem.*, vol. 97, no. 41, pp. 10702–10707, Oct. 1993, doi: 10.1021/j100143a029.
[11] M.-T. Charreyre, P. Zhang, M. A. Winnik, C. Pichot, and C. Graillat, “Adsorption of Rhodamine 6G onto Polystyrene Latex Particles with Sulfate Groups at the Surface,” *J. Colloid Interface Sci.*, vol. 170, no. 2, pp. 374–382, 1995, doi: https://doi.org/10.1006/jcis.1995.1115.
[12] E. Mubarekyan and M. Santore, “Characterization of Polystyrene Latex Surfaces by the Adsorption of Rhodamine 6G,” *Langmuir*, vol. 14, no. 7, pp. 1597–1603, Mar. 1998, doi: 10.1021/la970855y.
[13] A. M. Nuruzatulifah, A. A. Nizam, and N. M. N. Ain, “Synthesis and Characterization of Polystyrene Nanoparticles with Covalently Attached Fluorescent Dye,” *Mater. Today Proc.*, vol. 3, pp. S112–S119, 2016, doi: https://doi.org/10.1016/j.matpr.2016.01.015.
[14] S. Sosnowski, J. Feng, and M. A. Winnik, “Dye distribution in fluorescent-labeled latex prepared by emulsion polymerization,” *J. Polym. Sci. Part A Polym. Chem.*, vol. 32, no. 8, pp. 1497–1505, Jun. 1994, doi: 10.1002/pola.1994.080320810.
[15] F. Tronc, M. Li, J. Lu, M. A. Winnik, B. L. Kaul, and J.-C. Graciet, “Fluorescent polymer particles by emulsion and miniemulsion polymerization,” *J. Polym. Sci. Part A Polym. Chem.*, vol. 41, no. 6, pp. 766–778, Mar. 2003, doi: 10.1002/pola.10619.
[16] V. Holzapfel, A. Musyanovych, K. Landfester, M. R. Lorenz, and V. Mailänder, “Preparation of Fluorescent Carboxyl and Amino Functionalized Polystyrene Particles by Miniemulsion Polymerization as Markers for Cells,” *Macromol. Chem. Phys.*, vol. 206, no. 24, pp. 2440–2449, Dec. 2005, doi: 10.1002/macp.200500372.
[17] J. Desbiens, B. Bergeron, M. Patry, and A. M. Ritcey, “Polystyrene nanoparticles doped with a luminescent europium complex,” *J. Colloid Interface Sci.*, vol. 376, no. 1, pp. 12–19, 2012, doi: https://doi.org/10.1016/j.jcis.2012.02.020.
[18] A. L. Femia, V. D. G. Gonzalez, V. Garcia, and L. M. Gugliotta, “Polymerizable dye for colored particles synthesis with potential use in immunoassays,” *Int. J. Polym. Mater. Polym. Biomater.*, pp. 1–12, Jun. 2019, doi: 10.1080/00914037.2019.1616202.
[19] W. Benhadjala *et al.*, “Inorganic/organic nanocomposites: Reaching a high filler content without increasing viscosity using core-shell structured nanoparticles,” *Appl. Phys. Lett.*, vol. 107, no. 21, p. 211903, Nov. 2015, doi: 10.1063/1.4936339.
[20] W. Lee *et al.*, “Stimuli-responsive switchable organic-inorganic nanocomposite materials,” *Nano Today*, vol. 23, pp. 97–123, 2018, doi: https://doi.org/10.1016/j.nantod.2018.10.006.
[21] A. Van Blaaderen and A. Vrij, “Synthesis and characterization of colloidal dispersions of fluorescent, monodisperse silica spheres,” *Langmuir*, vol. 8, no. 12, pp. 2921–2931, 1992, doi: 10.1021/la00048a013.
[22] A. Imhof, M. Megens, J. J. Engelberts, D. T. N. de Lang, R. Sprik, and W. L. Vos, “Spectroscopy of Fluorescein (FITC) Dyed Colloidal Silica Spheres,” *J. Phys. Chem. B*,

vol. 103, no. 9, pp. 1408–1415, Mar. 1999, doi: 10.1021/jp983241q.
[23] M. Nakamura, M. Shono, and K. Ishimura, “Synthesis, Characterization, and Biological Applications of Multifluorescent Silica Nanoparticles,” *Anal. Chem.*, vol. 79, no. 17, pp. 6507–6514, Sep. 2007, doi: 10.1021/ac070394d.
[24] E. Bourgeat-Lami *et al.*, “Composite Polymer Colloid Nucleated by Functionalized Silica,” in *Hybrid Organic-Inorganic Composites*, vol. 585, American Chemical Society, 1995, pp. 10–112.
[25] M. S. Lee and N. J. Jo, “Coating of Methyltriethoxysilane—Modified Colloidal Silica on Polymer Substrates for Abrasion Resistance,” *J. Sol-Gel Sci. Technol.*, vol. 24, no. 2, pp. 175–180, 2002, doi: 10.1023/A:1015208328256.
[26] D. W. Lee and B. R. Yoo, “Advanced silica/polymer composites: Materials and applications,” *J. Ind. Eng. Chem.*, vol. 38, pp. 1–12, 2016, doi: https://doi.org/10.1016/j.jiec.2016.04.016.
[27] E.P. Plueddemann, *Silane Coupling Agents*. Springer US, 1991.
[28] E. Bourgeat-Lami, P. Espiard, and A. Guyot, “Poly(ethyl acrylate) latexes encapsulating nanoparticles of silica: 1. Functionalization and dispersion of silica,” *Polymer (Guildf).*, vol. 36, no. 23, pp. 4385–4389, 1995, doi: https://doi.org/10.1016/0032-3861(95)96843-W.
[29] E. Bourgeat-Lami, “Hybrid Organic/Inorganic Particles,” *Hybrid Materials*. pp. 87–149, 18-Dec-2006, doi: doi:10.1002/9783527610495.ch3.
[30] D. A. Giljohann, D. S. Seferos, W. L. Daniel, M. D. Massich, P. C. Patel, and C. A. Mirkin, “Gold Nanoparticles for Biology and Medicine,” *Angew. Chemie Int. Ed.*, vol. 49, no. 19, pp. 3280–3294, Apr. 2010, doi: 10.1002/anie.200904359.
[31] C. Boyer, M. R. Whittaker, M. Luzon, and T. P. Davis, “Design and Synthesis of Dual Thermoresponsive and Antifouling Hybrid Polymer/Gold Nanoparticles,” *Macromolecules*, vol. 42, no. 18, pp. 6917–6926, Sep. 2009, doi: 10.1021/ma9013127.
[32] J. Tian, F. Zheng, Q. Duan, and H. Zhao, “Self-assembly of polystyrene with pendant hydrophilic gold nanoparticles: the influence of the hydrophilicity of the hybrid polymers,” *J. Mater. Chem.*, vol. 21, no. 42, pp. 16928–16934, 2011, doi: 10.1039/C1JM11384D.
[33] X. Zhang, L. Liu, J. Tian, J. Zhang, and H. Zhao, “Copolymers of styrene and gold nanoparticles,” *Chem. Commun.*, no. 48, pp. 6549–6551, 2008, doi: 10.1039/B815778B.
[34] B. Wang, B. Li, B. Zhao, and C. Y. Li, “Amphiphilic Janus Gold Nanoparticles via Combining ‘Solid-State Grafting-to’ and ‘Grafting-from’ Methods,” *J. Am. Chem. Soc.*, vol. 130, no. 35, pp. 11594–11595, Sep. 2008, doi: 10.1021/ja804192e.
[35] L. M. Liz-Marzán, M. Giersig, and P. Mulvaney, “Synthesis of Nanosized Gold−Silica Core−Shell Particles,” *Langmuir*, vol. 12, no. 18, pp. 4329–4335, Jan. 1996, doi: 10.1021/la9601871.
[36] A. Guerrero-Martínez, J. Pérez-Juste, and L. M. Liz-Marzán, “Recent Progress on Silica Coating of Nanoparticles and Related Nanomaterials,” *Adv. Mater.*, vol. 22, no. 11, pp. 1182–1195, Mar. 2010, doi: 10.1002/adma.200901263.
[37] Y. Kobayashi, M. A. Correa-Duarte, and L. M. Liz-Marzán, “Sol−Gel Processing of Silica-Coated Gold Nanoparticles,” *Langmuir*, vol. 17, no. 20, pp. 6375–6379, Oct. 2001, doi: 10.1021/la010736p.

[38] E. Mine, A. Yamada, Y. Kobayashi, M. Konno, and L. M. Liz-Marzán, “Direct coating of gold nanoparticles with silica by a seeded polymerization technique,” *J. Colloid Interface Sci.*, vol. 264, no. 2, pp. 385–390, 2003, doi: https://doi.org/10.1016/S0021-9797(03)00422-3.

[39] T. Yamaguchi, T. Ono, and H. Ito, “I. Polymerization of vinyl monomers in the presence of inorganic substances,” *Die Angew. Makromol. Chemie*, vol. 32, no. 1, pp. 177–180, Aug. 1973, doi: 10.1002/apmc.1973.050320115.

[40] R. Laible and K. Hamann, “Formation of chemically bound polymer layers on oxide surfaces and their role in colloidal stability,” *Adv. Colloid Interface Sci.*, vol. 13, no. 1, pp. 65–99, 1980, doi: https://doi.org/10.1016/0001-8686(80)87002-3.

[41] M. Arai, K. Arai, and S. Saito, “Soapless emulsion polymerization of methyl methacrylate in water in the presence of calcium sulfite,” *J. Polym. Sci. Polym. Chem. Ed.*, vol. 20, no. 4, pp. 1021–1029, Apr. 1982, doi: 10.1002/pol.1982.170200411.

[42] M. Hasegawa, K. Arai, and S. Saito, “Uniform encapsulation of fine inorganic powder with soapless emulsion polymerization,” *J. Polym. Sci. Part A Polym. Chem.*, vol. 25, no. 11, pp. 3117–3125, Nov. 1987, doi: 10.1002/pola.1987.080251115.

[43] C.-S. Chern, S.-Y. Lin, and T. J. Hsu, “Effects of Temperature on Styrene Emulsion Polymerization Kinetics,” *Polym. J.*, vol. 31, no. 6, pp. 516–523, 1999, doi: 10.1295/polymj.31.516.

[44] W.-F. Su, “Radical Chain Polymerization BT - Principles of Polymer Design and Synthesis,” W.-F. Su, Ed. Berlin, Heidelberg: Springer Berlin Heidelberg, 2013, pp. 137–183.

[45] P. J. Flory, *Principles of polymer chemistry*. 1953.

[46] A. Kotera, K. Furusawa, and Y. Takeda, “Colloid chemical studies of polystyrene latices polymerized without any surfaceactive agents,” *Kolloid-Zeitschrift und Zeitschrift für Polym.*, vol. 239, no. 2, pp. 677–681, 1970, doi: 10.1007/BF02085916.

[47] T. Matsumoto and A. Ochi, “Polymerization of Styrene in Aqueous Solution,” *Kobunshi Kagaku*, vol. 22, no. 244, pp. 481–487, 1965, doi: 10.1295/koron1944.22.481.

[48] M. N. Gorsd, M. N. Blanco, and L. R. Pizzio, “Synthesis of Polystyrene Microspheres to be Used as Template in the Preparation of Hollow Spherical Materials: Study of the Operative Variables,” *Procedia Mater. Sci.*, vol. 1, pp. 432–438, Jan. 2012, doi: 10.1016/J.MSPRO.2012.06.058.

[49] M. N. Gorsd, M. N. Blanco, and L. R. Pizzio, “Synthesis of Polystyrene Microspheres to be Used as Template in the Preparation of Hollow Spherical Materials: Study of the Operative Variables,” *Procedia Mater. Sci.*, vol. 1, pp. 432–438, 2012, doi: https://doi.org/10.1016/j.mspro.2012.06.058.

[50] H. Warson, “Emulsion polymerization, a mechanistic approach. R. G. Gilbert. Academic Press, London, 1995. pp. xviii + 362, price £55.00. ISBN 0-12-283060-1,” *Polym. Int.*, vol. 41, no. 3, p. 352, Nov. 1996, doi: https://doi.org/10.1002/pi.1996.210410321.

[51] X. Liu and Y. Lu, “Tailoring Emulsion Polymerization for High-Yield Synthesis of Tween 80 Stabilized Magnetic Cross-Linked Polystyrene Nanocomposite Particles,” *Ind. Eng. Chem. Res.*, vol. 58, no. 19, pp. 8140–8147, May 2019, doi: 10.1021/acs.iecr.9b01103.

[52] K. P. Lok and C. K. Ober, “Particle size control in dispersion polymerization of

polystyrene," *Can. J. Chem.*, vol. 63, no. 1, pp. 209–216, Jan. 1985, doi: 10.1139/v85-033.

[53] S. Carro, J. Herrera-Ordonez, and J. Castillo-Tejas, "On the mechanism of particle formation above the CMC in emulsion polymerization," *Polym. Bull.*, vol. 75, no. 3, pp. 1027–1035, 2018, doi: 10.1007/s00289-017-2075-2.

[54] W. J. Priest, "Partice Growth in the Aqueous Polymerization of Vinyl Acetate," *J. Phys. Chem.*, vol. 56, no. 9, pp. 1077–1082, Sep. 1952, doi: 10.1021/j150501a010.

[55] R. M. Fitch and C. H. Tsai, "Particle Formation in Polymer Colloids, III: Prediction of the Number of Particles by a Homogeneous Nucleation Theory BT - Polymer Colloids," 1971, pp. 73–102.

[56] F. K. Hansen and J. Ugelstad, "Particle nucleation in emulsion polymerization. I. A theory for homogeneous nucleation," *J. Polym. Sci. Polym. Chem. Ed.*, vol. 16, no. 8, pp. 1953–1979, Aug. 1978, doi: https://doi.org/10.1002/pol.1978.170160814.

[57] W. D. Harkins, "A General Theory of the Mechanism of Emulsion Polymerization1," *J. Am. Chem. Soc.*, vol. 69, no. 6, pp. 1428–1444, Jun. 1947, doi: 10.1021/ja01198a053.

[58] W. V Smith and R. H. Ewart, "Kinetics of Emulsion Polymerization," *J. Chem. Phys.*, vol. 16, no. 6, pp. 592–599, Jun. 1948, doi: 10.1063/1.1746951.

[59] F. K. Hansen and J. Ugelstad, "Particle nucleation in emulsion polymerization. III. Nucleation in systems with anionic emulsifier investigated by seeded and unseeded polymerization," *J. Polym. Sci. Polym. Chem. Ed.*, vol. 17, no. 10, pp. 3047–3067, Oct. 1979, doi: https://doi.org/10.1002/pol.1979.170171002.

[60] H. Minami, K. Yoshida, and M. Okubo, "Preparation of Polystyrene Particles by Dispersion Polymerization in an Ionic Liquid," *Macromol. Rapid Commun.*, vol. 29, pp. 567–572, Apr. 2008, doi: 10.1002/marc.200700810.

[61] J. W. Goodwin, J. Hearn, C. C. Ho, and R. H. Ottewill, "The preparation and characterisation of polymer latices formed in the absence of surface active agents," *Br. Polym. J.*, vol. 5, no. 5, pp. 347–362, Sep. 1973, doi: https://doi.org/10.1002/pi.4980050503.

[62] G. T. D. Shouldice, G. A. Vandezande, and A. Rudin, "Practical aspects of the emulsifier-free emulsion polymerization of styrene," *Eur. Polym. J.*, vol. 30, no. 2, pp. 179–183, 1994, doi: https://doi.org/10.1016/0014-3057(94)90157-0.

[63] C. S. Chern, "Emulsion polymerization mechanisms and kinetics," *Prog. Polym. Sci.*, vol. 31, no. 5, pp. 443–486, 2006, doi: https://doi.org/10.1016/j.progpolymsci.2006.02.001.

[64] A. Ohnuma, E. C. Cho, M. Jiang, B. Ohtani, and Y. Xia, "Metal−Polymer Hybrid Colloidal Particles with an Eccentric Structure," *Langmuir*, vol. 25, no. 24, pp. 13880–13887, Dec. 2009, doi: 10.1021/la9015146.

[65] Z. Zhang *et al.*, "Controllable synthesis of anisotropic silica/polymer composite particles via seeded dispersion polymerization," *Mater. Chem. Phys.*, vol. 195, pp. 105–113, 2017, doi: https://doi.org/10.1016/j.matchemphys.2017.04.024.

[66] L. Scarabelli *et al.*, "Encapsulation of Noble Metal Nanoparticles through Seeded Emulsion Polymerization as Highly Stable Plasmonic Systems," *Adv. Funct. Mater.*, vol. 29, no. 14, p. 1809071, Apr. 2019, doi: https://doi.org/10.1002/adfm.201809071.

[67] M. Ishihara, T. Kaeda, and T. Sasaki, "Silica/polymer core–shell particles prepared via

soap-free emulsion polymerization," *e-Polymers*, vol. 20, no. 1, pp. 254–261, 2020, doi: doi:10.1515/epoly-2020-0028.

[68] J. Qiu, M. Xie, Z. Lyu, K. D. Gilroy, H. Liu, and Y. Xia, "General Approach to the Synthesis of Heterodimers of Metal Nanoparticles through Site-Selected Protection and Growth," *Nano Lett.*, vol. 19, no. 9, pp. 6703–6708, Sep. 2019, doi: 10.1021/acs.nanolett.9b03167.

[69] Y. D. Liu, F. F. Fang, and H. J. Choi, "Core−Shell Structured Semiconducting PMMA/Polyaniline Snowman-like Anisotropic Microparticles and Their Electrorheology," *Langmuir*, vol. 26, no. 15, pp. 12849–12854, Aug. 2010, doi: 10.1021/la101165k.

[70] E. B. Mock, H. De Bruyn, B. S. Hawkett, R. G. Gilbert, and C. F. Zukoski, "Synthesis of Anisotropic Nanoparticles by Seeded Emulsion Polymerization," *Langmuir*, vol. 22, no. 9, pp. 4037–4043, Apr. 2006, doi: 10.1021/la060003a.

[71] D. Wang, V. L. Dimonie, E. D. Sudol, and M. S. El-Aasser, "Seeded dispersion polymerization," *J. Appl. Polym. Sci.*, vol. 84, no. 14, pp. 2710–2720, Jun. 2002, doi: https://doi.org/10.1002/app.10593.

[72] N. Tsubokawa, T. Kimoto, and K. Koyama, "Polymerization of vinyl monomers in the presence of silica having surface functional groups," *Colloid Polym. Sci.*, vol. 271, no. 10, pp. 940–946, 1993, doi: 10.1007/BF00654853.

[73] K. Furusawa, Y. Kimura, and T. Tagawa, "Syntheses of composite polystyrene latices with silica particles in the core," *J. Colloid Interface Sci.*, vol. 109, no. 1, pp. 69–76, Jan. 1986, doi: 10.1016/0021-9797(86)90282-1.

[74] E. Bourgeat-Lami, P. Espiard, A. Guyot, C. Gauthier, L. David, and G. Vigier, "Emulsion polymerization in the presence of colloidal silica particles. Application to the reinforcement of poly(ethyl acrylate) films," *Die Angew. Makromol. Chemie*, vol. 242, no. 1, pp. 105–122, Nov. 1996, doi: 10.1002/apmc.1996.052420107.

[75] E. Bourgeat-Lami and J. Lang, "Encapsulation of Inorganic Particles by Dispersion Polymerization in Polar Media: 1. Silica Nanoparticles Encapsulated by Polystyrene," *J. Colloid Interface Sci.*, vol. 197, no. 2, pp. 293–308, Jan. 1998, doi: 10.1006/JCIS.1997.5265.

[76] E. Bourgeat-Lami and J. Lang, "Encapsulation of Inorganic Particles by Dispersion Polymerization in Polar Media: 2. Effect of Silica Size and Concentration on the Morphology of Silica–Polystyrene Composite Particles," *J. Colloid Interface Sci.*, vol. 210, no. 2, pp. 281–289, Feb. 1999, doi: 10.1006/JCIS.1998.5939.

[77] K. Zhang, H. Chen, X. Chen, Z. Chen, Z. Cui, and B. Yang, "Monodisperse Silica-Polymer Core-Shell Microspheres via Surface Grafting and Emulsion Polymerization," *Macromol. Mater. Eng.*, vol. 288, no. 4, pp. 380–385, Apr. 2003, doi: 10.1002/mame.200390031.

[78] S. Gu, T. Kondo, and M. Konno, "Preparation of silica–polystyrene core–shell particles up to micron sizes," *J. Colloid Interface Sci.*, vol. 272, no. 2, pp. 314–320, Apr. 2004, doi: 10.1016/J.JCIS.2004.01.056.

[79] J. Tian and P. Vana, "Polystyrene-Core–Silica-Shell Hybrid Particles Containing Gold and Magnetic Nanoparticles," *Chem. – An Asian J.*, vol. 11, no. 4, pp. 596–603, Feb. 2016, doi: 10.1002/asia.201501314.

[80] M. Zhang *et al.*, "Core–Shell and Asymmetric Polystyrene–Gold Composite Particles via One-Step Pickering Emulsion Polymerization," *Langmuir*, vol. 30, no. 1, pp. 75–

82, Jan. 2014, doi: 10.1021/la4041166.
[81] A. Ohnuma, E. C. Cho, P. H. C. Camargo, L. Au, B. Ohtani, and Y. Xia, “A Facile Synthesis of Asymmetric Hybrid Colloidal Particles,” *J. Am. Chem. Soc.*, vol. 131, no. 4, pp. 1352–1353, Feb. 2009, doi: 10.1021/ja8079934.
[82] N. Guarrotxena, O. García, and I. Quijada-Garrido, “Synthesis of Au@polymer nanohybrids with transited core-shell morphology from concentric to eccentric Emoji-N or Janus nanoparticles,” *Sci. Rep.*, vol. 8, no. 1, p. 5721, 2018, doi: 10.1038/s41598-018-24078-8.
[83] Y. Wang, T. Ding, J. J. Baumberg, and S. K. Smoukov, “Symmetry breaking polymerization: one-pot synthesis of plasmonic hybrid Janus nanoparticles,” *Nanoscale*, vol. 7, no. 23, pp. 10344–10349, 2015, doi: 10.1039/C5NR01999K.
[84] S. Gu, J. Onishi, E. Mine, Y. Kobayashi, and M. Konno, “Preparation of multilayered gold-silica-polystyrene core-shell particles by seeded polymerization,” *J. Colloid Interface Sci.*, vol. 279, pp. 284–287, Dec. 2004, doi: 10.1016/j.jcis.2004.06.065.
[85] N. G. Bastús, J. Comenge, and V. Puntes, “Kinetically Controlled Seeded Growth Synthesis of Citrate-Stabilized Gold Nanoparticles of up to 200 nm: Size Focusing versus Ostwald Ripening,” *Langmuir*, vol. 27, no. 17, pp. 11098–11105, 2011, doi: 10.1021/la201938u.
[86] S.-J. Park, Y.-J. Kim, and S.-J. Park, “Size-Dependent Shape Evolution of Silica Nanoparticles into Hollow Structures,” *Langmuir*, vol. 24, no. 21, pp. 12134–12137, Nov. 2008, doi: 10.1021/la8028885.
[87] M. Okubo, T. Suzuki, and S. Tasaki, “The acceleration behavior of decomposition of potassium persulfate in the dispersions of polystyrene particles stabilized with nonionic emulsifier,” *Stud. Surf. Sci. Catal. - STUD SURF SCI CATAL*, vol. 132, pp. 347–350, Dec. 2001, doi: 10.1016/S0167-2991(01)82103-0.
[88] M. Okubo, T. Yamashita, H. Minami, and Y. Konishi, “Preparation of micron-sized monodispersed highly monomer- ‘adsorbed’ polymer particles having snow-man shape by utilizing the dynamic swelling method with tightly cross- linked seed particles,” *Colloid Polym. Sci.*, vol. 276, no. 10, pp. 887–892, 1998, doi: 10.1007/s003960050325.
[89] H. Minami, Z. Wang, T. Yamashita, and M. Okubo, “Thermodynamic analysis of the morphology of monomer-adsorbed, cross-linked polymer particles prepared by the dynamic swelling method and seeded polymerization,” *Colloid Polym. Sci.*, vol. 281, no. 3, pp. 246–252, 2003, doi: 10.1007/s00396-002-0766-0.
[90] S. Mariano, S. Tacconi, M. Fidaleo, M. Rossi, and L. Dini, “Micro and Nanoplastics Identification: Classic Methods and Innovative Detection Techniques ,” *Frontiers in Toxicology* , vol. 3. 2021.
[91] Q. Zhang *et al.*, “A Review of Microplastics in Table Salt, Drinking Water, and Air: Direct Human Exposure,” *Environ. Sci. Technol.*, vol. XXXX, Mar. 2020, doi: 10.1021/acs.est.9b04535.
[92] J. C. Prata, “Airborne microplastics: Consequences to human health?,” *Environ. Pollut.*, vol. 234, pp. 115–126, 2018, doi: https://doi.org/10.1016/j.envpol.2017.11.043.
[93] L. C. Jenner, J. M. Rotchell, R. T. Bennett, M. Cowen, V. Tentzeris, and L. R. Sadofsky, “Detection of microplastics in human lung tissue using μFTIR spectroscopy,” *Sci. Total Environ.*, vol. 831, p. 154907, 2022, doi:

https://doi.org/10.1016/j.scitotenv.2022.154907.
[94] Y. Deng, Y. Zhang, B. Lemos, and H. Ren, “Tissue accumulation of microplastics in mice and biomarker responses suggest widespread health risks of exposure,” *Sci. Rep.*, vol. 7, no. 1, p. 46687, 2017, doi: 10.1038/srep46687.
[95] G. Everaert *et al.*, “Risk assessment of microplastics in the ocean: Modelling approach and first conclusions,” *Environ. Pollut.*, vol. 242, pp. 1930–1938, 2018, doi: https://doi.org/10.1016/j.envpol.2018.07.069.
[96] S. Noventa *et al.*, “Paradigms to assess the human health risks of nano- and microplastics,” *Microplastics and Nanoplastics*, vol. 1, no. 1, p. 9, 2021, doi: 10.1186/s43591-021-00011-1.
[97] W. Li, Y. Luo, and X. Pan, “Identification and Characterization Methods for Microplastics Basing on Spatial Imaging in Micro-/Nanoscales,” 2020.
[98] V. Wirnkor, E. Ebere, and V. Evelyn Ngozi, “Microplastics, an Emerging Concern: A Review of Analytical Techniques for Detecting and Quantifying Microplatics,” *Anal. Methods Environ. Chem. J.*, vol. 2, pp. 13–30, Jul. 2019, doi: 10.24200/amecj.v2.i2.57.
[99] C. Im *et al.*, “PET tracing of biodistribution for orally administered ⁶⁴Cu-labeled polystyrene in mice,” *J. Nucl. Med.*, p. jnumed.120.256982, Jul. 2021, doi: 10.2967/jnumed.120.256982.
[100] X. Zheng, S. Zeng, J. Hu, L. Wu, and X. Hou, “Applications of silica-based nanoparticles for multimodal bioimaging,” *Appl. Spectrosc. Rev.*, vol. 53, no. 5, pp. 377–394, May 2018, doi: 10.1080/05704928.2017.1355312.
[101] B. G. Cha and J. Kim, “Functional mesoporous silica nanoparticles for bio-imaging applications,” *WIREs Nanomedicine and Nanobiotechnology*, vol. 11, no. 1, p. e1515, Jan. 2019, doi: https://doi.org/10.1002/wnan.1515.
[102] J. K. Willmann, N. van Bruggen, L. M. Dinkelborg, and S. S. Gambhir, “Molecular imaging in drug development,” *Nat. Rev. Drug Discov.*, vol. 7, no. 7, pp. 591–607, 2008, doi: 10.1038/nrd2290.
[103] D.-E. Lee, H. Koo, I.-C. Sun, J. H. Ryu, K. Kim, and I. C. Kwon, “Multifunctional nanoparticles for multimodal imaging and theragnosis,” *Chem. Soc. Rev.*, vol. 41, no. 7, pp. 2656–2672, 2012, doi: 10.1039/C2CS15261D.
[104] S. H. Fauziah, M. Bhatti, N. Anuar, N. Anuar, P. Mohan, and A. Periathamby, “Worldwide distribution and abundance of microplastic: How dire is the situation?,” *Waste Manag. Res.*, vol. 36, p. 0734242X1878573, Aug. 2018, doi: 10.1177/0734242X18785730.
[105] J. Hwang, D. Choi, S. Han, S. Y. Jung, J. Choi, and J. Hong, “Potential toxicity of polystyrene microplastic particles,” *Sci. Rep.*, vol. 10, no. 1, p. 7391, 2020, doi: 10.1038/s41598-020-64464-9.
[106] M. M. Mahan and A. L. Doiron, “Gold Nanoparticles as X-Ray, CT, and Multimodal Imaging Contrast Agents: Formulation, Targeting, and Methodology,” *J. Nanomater.*, vol. 2018, p. 5837276, 2018, doi: 10.1155/2018/5837276.
[107] W. Stöber, A. Fink, and E. Bohn, “Controlled growth of monodisperse silica spheres in the micron size range,” *J. Colloid Interface Sci.*, vol. 26, no. 1, pp. 62–69, 1968, doi: https://doi.org/10.1016/0021-9797(68)90272-5.
[108] E. Casals and V. Puntes, *Inorganic nanoparticle biomolecular corona: Formation, evolution and biological impact*, vol. 7. 2012.

.

V. Experimental Section

“Be kind, for everyone you meet

is fighting a harder battle”

Plato

Chapter 5

Experimental Section:

Chemicals, Materials, Methods and Techniques

5.1. Experimental for Chapter 2: Kinetically Controlled Seeded Growth One-Pot Synthesis of Monodisperse SiO2 NPs

5.1.1. Chemicals

Tetraethyl orthosilicate (TEOS) of formula $Si(OC_2H_5)_4$ ≥99%, ammonia solution (ACS Reagent, p.a. 28-30%), ammonia solution 2.0 M in ethanol, sodium chloride (NaCl) BioXtra, ≥99.5% (AT), Ammonium molybdate tetrahydrate of formula $(NH_4)_6Mo_7O_{24} \cdot 4H_2O$ ACS reagent, 99.98%, Sulfuric acid ACS reagent, 95.0-98.0% and float-A-Lyzer® G2 dialysis device MWCO: 100 KDa were purchased from Sigma-Aldrich. Anhydride absolute ethanol (max. 0,003% H2O) ≥99.8% was purchased from VWR. All reagents were used as received without further purification and all glass material was sterilized and dehydrogenated in an oven prior to use. Milli-Q water was used in the preparation of all solutions.

5.1.2. Synthetic Procedures

5.1.2.1. Standard SiO_2 NPs Synthesis

Our standard methodology followed for the production of aqueous solutions of monodisperse silica nanoparticles with different sizes, ranging from (20 to 320 nm), were done using a Sol-gel process adapting the Stöber method. In detail, in a sealed flask with the help of a septum and under argon atmosphere, 32mL (14.1 M) of dry ethanol was added. Then, after 5 minutes of stirring at 800 r.p.m., 1.21mL (0.55M of NH_3) of ammonium hydroxide 28% and 1.05mL (0.15M) of tetraethylortosilicate (TEOS) were sequentially added in the ethanol solution and the reaction was left stirring overnight. The resulting NPs are coated negatively charged with silanol groups and thus were well suspended. In order

to modify the final size of the silica cores, a known amount of water was added at the end of the reaction, subtracting volume from the ethanol to have a reaction constant volume. To purify and transfer the silica cores from ethanol to pure water, first, the colloidal solution was heated at 30°C under a reduced pressure using a rotary evaporator to reduce the volume and then the solution was dialyzed against water. All the above experiments were conducted at room temperature. All the particles were used within 20 days after synthesis. The use of aged particles may result in increased experimental variability, since after a large period of time the stability of the particles may be compromised.

5.1.2.2. Variation of TEOS Concentration Synthesis

In a sealed flask with the help of a septum and under argon atmosphere, 32mL (14.1 M) of dry ethanol was added. Then, after 5 minutes of stirring at 800 r.p.m., 1.21mL (0.55M of NH_3) of ammonium hydroxide 28% and 2.50mL of H_2O (4.00M) were sequentially added in the ethanol solution. For evaluate the final size, a variation of TEOS (0.05M – 0.70M) were further added and the reaction were left overnight. The samples all are purified as the standard procedure and used within 20 days after synthesis.

5.1.2.3. Variation of Ammonia Concentration Synthesis

In a sealed flask with the help of a septum and under argon atmosphere, 32mL (14.1 M) of dry ethanol was added. Then, after 5 minutes of stirring at 800 r.p.m., scalar volumes of ammonia concentration (0.20M -1.50M of NH_3) using ammonia in ethanol 7.00M, subtracting volume from the ethanol to have a reaction constant volume and 1.05mL (0.15M) of tetraethylortosilicate (TEOS) with 2.50mL of H_2O (4.00M) were sequentially added in the ethanol solution the reaction were left overnight. The samples all are purified as the standard procedure and used within 20 days after synthesis.

5.1.2.4. Variation of water Concentration Synthesis

In a sealed flask with the help of a septum and under argon atmosphere, 32mL (14.1 M) of dry ethanol was added. Then, after 5 minutes of stirring at 800 r.p.m., 1.21mL (0.55M of NH_3) of ammonium hydroxide 28% and 1.05mL (0.15M) of tetraethylortosilicate

(TEOS) were sequentially added in the ethanol solution and the amount of water was added at the end of the reaction with a variation of (2.50M-13.0M), subtracting volume from the ethanol to have a reaction constant volume and the reaction was left stirring overnight. The samples all are purified as the standard procedure and used within 20 days after synthesis.

5.1.2.5. Monitoring Colloidal Particle Formation

In a sealed flask with the help of a septum and under argon atmosphere, 31mL (13.7 M) of dry ethanol was added. Then, after 5 minutes of stirring at 800 r.p.m., 2.67mL (0.55M of NH_3) of ammonium 7M in ethanol and 1.05mL (0.15M) of tetraethylortosilicate (TEOS) were sequentially added in the ethanol solution. The experiments were done simultaneously using 3 different reactions conditions with different water concentrations (2.00M,3.50M and 5.00M), subtracting volume from the ethanol to have a reaction constant volume. After the water were added in each synthesis, the evolution of the reaction was done extracting 1mL of the reaction and immediately measured by SEM/TEM, UV-Vis spectroscopy for monomer concentration, DLS recording the surface charge (mV), conductivity (mS/cm), hydrodynamic diameter, and number of particles (NPs/mL) in solution. The evolution was recorder at different intervals of time depending of the technique used.

5.1.2.6. Quantitative Monomer from TEOS Determination

The concentration of monomers molecules of the reaction medium was determined by means of the silicomolybdic acid (SMA) spectrophotometric method. To perform the quantification, first a solution containing 80mL of water and 4.1mL of concentrated H_2SO_4 (95.0-98.0%) was mixed, followed by dilution to a final volume of 100 mL with water. This yielded a solution called A. Second, 10 g of Ammonium heptamolybdate tetrahydrate $(NH_4)_6Mo_7O_{24}\cdot 4H_2O$ was dissolved in 90 mL of water having 4.7 mL of ammonia solution (28%), followed by dilution to a final volume of 100 mL with water. This yielded a solution called B. Later, a solution C was prepared mixing 20 mL of solution A and 10 mL of solution B, homogenized and further diluted with water to a final volume of 80mL. Finally, in order

to assess the TEOS concentration, an aliquot of (60 μL) was taken out of the reaction medium after a given time and subsequently mixed with 5 mL of solution C and further diluted with water to a total volume of 10 mL. Later, the mixture was stirred for 5 minutes at 600 r.p.m. and the yellow colour was left to develop over 10 min at room temperature, before measuring the optical density at λ = 400 ± 10 nm to determine the amount molybdosilicate, which one could determine the number of monomers molecules in the reaction medium using a calibration curve.

5.1.2.7 Standard SiO_2 NPs Synthesis Using 3.50M of H_2O

In detail, in a sealed flask with the help of a septum and under argon atmosphere, 32mL (14.1 M) of dry ethanol was added. Then, after 5 minutes of stirring at 800 r.p.m., 2.67mL (0.55M of NH_3) of ammonium 7.0M in ethanol, 1.05mL (0.15M) of tetraethylortosilicate (TEOS) and 2.2mL (3.50M) of H_2O were sequentially added in the ethanol solution, subtracting volume from the ethanol to have a reaction constant volume and the reaction was left stirring overnight. All the above experiments were conducted at room temperature.

5.1.2.8 Standard SiO_2 NPs Synthesis Adding a Fixed an Extra 3.00M Amount of Water in Different Intervals

In detail, in a sealed flask with the help of a septum and under argon atmosphere, 32mL (14.1 M) of dry ethanol was added. Then, after 5 minutes of stirring at 800 r.p.m., 2.67mL (0.55M of NH_3) of ammonium 7.0M in ethanol, 1.05mL (0.15M) of tetraethylortosilicate (TEOS) and 1.26mL (2.00M) of H_2O were sequentially added in the ethanol solution, subtracting volume from the ethanol to have a reaction constant volume. Later, in different intervals of time (5, 10, 15, 30, 60, 120, 240 minutes) were added 2.00mL of water (3.00M), and the reaction was left stirring overnight. All the above experiments were conducted at room temperature.

5.1.2.9 Standard SiO_2 NPs Synthesis Adding Different NaCl Concentrations

In detail, in a sealed flask with the help of a septum and under argon atmosphere, 32mL (14.1 M) of dry ethanol was added. Then, after 5 minutes of stirring at 800 r.p.m., 2.67mL (0.55M of NH3) of ammonium 7.0M in ethanol, 1.05mL (0.15M) of tetraethylortosilicate (TEOS) and 1.26mL (2.00M) of H_2O and different NaCl concentrations (0.10, 0.30, 0.50, 0.80, 1.00, 1.50, 3.00M) were sequentially added in the ethanol solution, subtracting volume from the ethanol to have a reaction constant volume) and the reaction was left stirring overnight. All the above experiments were conducted at room temperature.

5.1.2.10. Size tuning from 20 to 320 nm the SiO_2 NPs Beyond Stöber Method

In detail, in a sealed flask with the help of a septum and under argon atmosphere, 32mL (14.1 M) of dry ethanol was added. Then, after 5 minutes of stirring at 800 r.p.m., 2.67mL (0.55M of NH_3) of ammonium 7.0M in ethanol, 1.05mL (0.15M) of tetraethylortosilicate (TEOS) and a known amount of H_2O were sequentially added in the ethanol solution, subtracting volume from the ethanol to have a reaction constant volume, and the reaction was left stirring overnight. The water concentration in the media were varied from (1.80M - 13.0M). All the above experiments were conducted at room temperature. The samples all are purified as the standard procedure and used within 20 days after synthesis.

5.1.2.11. Process to calculate the yield of the Reaction

For the yield of the silica nanoparticles, after the modified Stöber synthesis of colloidal amorphous silica, the NP were carefully cleaned under a reduced pressure using a rotary evaporator to eliminate ammonia and solvent and then was dialyzed against milli-q water to finally dried at 650°C for 4 hours to obtained a solid white dried powder, which were calculated with the following formula:

$$\text{Yield (\%)} = W_{as}/W_t \cdot 100 \qquad \text{Equation 2}$$

Where W_{as} is the weight of silica nanoparticles after the cleaning process and W_t is the theoretical weight of the silica nanoparticles base on the assumption of complete condensation of total alkoxysiloxanes [1], [2].

5.2. Experimental for Chapter 3: Synthetic Strategy for Preparing Silica-Based Nanoparticles with Functional Properties for Biological Imaging

5.2.1. Chemicals

Tetraethyl orthosilicate (TEOS) ≥98%, 3-(aminopropyl)triethoxysilane (APTES, ≥98%), ninhydrin ACS reagent (1,2,3-Indantrione monohydrate, 2,2-Dihydroxy-1,3-indanedione), sodium chloride (NaCl) BioXtra, ≥99.5% (AT), Phosphate buffered saline (PBS) (0.01 M phosphate buffer, 0.0027 M potassium chloride and 0.137 M sodium chloride, pH 7.4 at 25 °C), and Float-A-Lyzer® G2 dialysis device MWCO: 100 KDa were purchased from Sigma-Aldrich. Ammonia solution (ACS Reagent, p.a. 28-30%) and dried ethanol (seccoSolv® max 0.01% H2O) were purchased from Merck. Fluorescein-5-isothiocyanate (FITC) ≥95%, Rhodamine B isothiocyanate (RBITC) mixed isomers, Fetal Bovine Serum, FBS (research grade, sterile filtered, EU approved, South American origin), Bovine Serum Albumin (BSA), DMEM (1x) + Glutamax TM (Dulbecco's Modified Eagle's Medium) with (4.500 mg/mL glucose and sodium bicarbonate, with L glutamine, sodium pyruvate, wihtout phenol red, liquid, were purchased from Gibco. HEK 293 cells (DSMZ), Poly-L-Lysine (40µg/cm2), Triton-X, Phalloidin-iFluor 647 Reagent (ab176759) and Alexa Fluor 647- ab176759 were adquired at Abcam. TRITC (5/6-tetramethyl-rhodamine isothiocyanate), mixed isomer, Molecular Probes™ Alexa Fluor™ 350 NHS Ester (Succinimidyl Ester) and Hoechst 3342 (H1399) were acquired in Thermo Fisher Scientific™. All reagents were used as received without further purification and all glass material was sterilized and dehydrogenated in an oven prior to use. Milli-Q water was used in the preparation of all solutions.

5.2.2. Synthetic Procedures

5.2.2.1. Synthesis of the surface functionalized SiO_2 NPs with amino groups

In detail, in a sealed flask with the help of a septum and under argon atmosphere, 32mL (14.1 M) of dry ethanol was added. Then, after 5 minutes of stirring at 800 r.p.m., 1.21mL (0.55M of NH_3) of ammonium hydroxide 28% and 1.05mL (0.15M) of tetraethylortosilicate (TEOS) were sequentially added in the ethanol solution and the reaction was left stirring overnight. The resulting NPs are coated negatively charged with silanol groups and thus were well suspended. In order to modify the final size of the silica cores, a known amount of water was added at the end of the reaction- (1.80M for 30nm and 2.50M for 50nm). Subsequently, corresponding amount of 3-(aminopropyl)triethoxysilane (APTES) was added directly to the mixture and was left stirring for another 24 h at room temperature. The aminated silica nanoparticles were purify under a reduced pressure using a rotary evaporator at 30°C and then the solution was dialyzed against ethanol in order to preserve the integrity of the amine functional groups on the surface. To transfer the particles into pure water, three cycles of centrifugation (3000g, 20 min T=20°C, centrifuge tubes-SuperClear PP, VWR collection in water) were done to ensure that the ethanol content in the samples was negligible and finally the solution was dispersed and sonicated for 10 minutes in acidified acetate buffer at pH 5 or water at same pH.

5.2.2.2. Synthesis of the core-shell SiO_2 NPs loaded with FTIC

First, the silane-dye complex was prepared. For this purpose, in a 10 mL flask, the dye FITC was measured (7.8mg) accurately and dissolved in 10 mL of dry ethanol. Subsequently, 4.8uL of 3-aminopropiltriethoxysilane (APTES) was added under stirring and the flask was sealed using septum and left for 15 minutes under argon atmosphere in dark conditions. The concentration of the APTES-FITC complex was (2mM:2mM). Finally, the reaction was left for 24 hours under magnetic agitation. Once the APTES-FITC complex was prepared, in a flask sealed with the help of a septum and under argon atmosphere, (50-X) mL of dry ethanol was added. Then, after 10 minutes of stirring, was added 2.02mL (50,7mmol) of ammonium hydroxide 28% and was left for 5 minutes with continuously stirring. Finally, 1.7mL (7,6mmol) of tetraethylortosilicate (TEOS) and X mL of APTES-FITC 2mM complex were sequentially added in the ethanol anhydride solution. The reaction was left for 24 hours stirring in dark conditions. Dialysis against pure water and centrifugation

(10.000g and 15minutes) was done for the purification of the unreacted dye and precursor, and the core-doped NPs were dispersed in water or ethanol depending of its use. All the above experiments were conducted at room temperature.

5.2.2.3. Synthesis of the core-shell SiO_2 NPs loaded with RBITC, TRITC and AF350

First, the silane-dye complex was prepared. For this purpose, in a 10 mL flask, the dye RBITC was measured (10.7mg) accurately and dissolved in 10 mL of dry ethanol. Subsequently, 4.8uL of 3-aminopropiltriethoxysilane (APTES) was added under stirring and the flask was sealed using septum and left for 15 minutes under argon atmosphere in dark conditions. For the TRITC was measured (8.88mg) the concentration of the APTES-RBITC and APTES-TRITC complex was (2mM:2mM). In the case of the AF350 was measured (5.0mg), in 50 mL of dry ethanol and subsequently 2.80uL of 3-aminopropiltriethoxysilane (APTES). The concentration of the APTES-AF350 was (0.24mM:0.24mM). Finally, the reaction was left for 24 hours under magnetic agitation. Once the APTES-RBITC/TRITC/AF350 complexes were prepared, in a flask sealed with the help of a septum and under argon atmosphere, (50-X) mL of dry ethanol was added. Then, after 10 minutes of stirring, was added 2.02mL (50,7mmol) of ammonium hydroxide 28% and was left for 5 minutes with continuously stirring. Finally, 1.7mL (7,6mmol) of tetraethylortosilicate (TEOS) and X mL of APTES-RBITC/TRITC/AF350 complexes were sequentially added in different vials with the ethanol anhydride solution. The reaction was left for 24 hours stirring in dark conditions. Dialysis against pure water and centrifugation (10.000g and 15minutes) was done for the purification of the unreacted dye and precursor, and the core-doped NPs were dispersed in water or ethanol depending of its use. All the above experiments were conducted at room temperature.

5.2.2.4. Synthesis of the dual emission core-shell SiO_2 NPs loaded with different APTES-Dyes mixtures.

SiO_2 NPs with FITC-RBITC mixture:

In order to obtain a different fluorescent color of silica (SiO_2) nanoparticles, a mixture of Silane-dye complex was done using, Rhodamine B isothiocyanate (RBITC) and Fluorescein isothiocyanate (FITC). First, the silane-dye precursor was prepared as follows:

a mixture of RBITC 0.2mM (3.18mg) and FITC 1.8mM (21.0mg) were measured accurately and dissolved in 30 mL of dry ethanol. Then, the 3-aminopropiltriethoxysilane (APTES) 0.2mM (15µL) was added under stirring and the flask was sealed using septum and left for 15 minutes under argon atmosphere in dark conditions. Finally, the reaction was left for 24 hours under magnetic agitation. Once the complex (APTES-FITC/RBITC) was obtained, the synthesis of the fluorescent silica was done, following the modified Stöber method, as follows: in a flask sealed with the help of a septum and under argon atmosphere, (50-X) mL of dry ethanol was added. Then, after 10 minutes of stirring, was added 2.02mL (50,7mmol) of ammonium hydroxide 28% and was left for 5 minutes with continuously stirring. Finally, 1.7mL (7,6mmol) of tetraethylortosilicate (TEOS) and different X mL (1,3,5 mL) volumes of APTES-FITC/RBITC complex were sequentially added in the ethanol anhydride solution maintaining constant the solvent volume. The reaction was left for 24 hours stirring in dark conditions. Dialysis was done for the purification of the unreacted precursor.

SiO_2 NPs with RBITC-AF350 mixture:

A Silane-dye was done using, Rhodamine B isothiocyanate (RBITC) and Alexa Fluor 350 NHS (AF350). First, the silane-dye complex was prepared separately as follows: RBITC 0.24mM (3.82mg) and AF350 (5mg) 0.24mM were measured accurately and dissolved in 30 mL and 50mL of dry ethanol, respectively. Then, the 3-aminopropiltriethoxysilane (APTES) 0.2mM (15µL) was added to each one under stirring and the flask was sealed using septum and left for 15 minutes under argon atmosphere in dark conditions. Finally, the reaction was left for 24 hours under magnetic agitation. Once the APTES-RBITC and APTES-AF350 were obtained, the synthesis of the fluorescent silica was done, following the modified Stöber described as follows: in a flask sealed with the help of a septum and under argon atmosphere, (50-X) mL of dry ethanol was added. Then, after 10 minutes of stirring, was added 2.02mL (50,7mmol) of ammonium hydroxide 28% and was left for 5 minutes with continuously stirring. Finally, Different proportions of 10 mL (50:50, 80:20, 90:10) of APTES-AF350/RBITC precursor and 1.7mL (7,6mmol) of tetraethylortosilicate (TEOS) were sequentially added in the ethanol anhydride solution maintaining constant the solvent volume. The reaction was left for 24 hours stirring in dark conditions. Dialysis was done for

the purification of the unreacted precursor. All the above experiments were conducted at room temperature.

5.2.2.5. Synthesis of the dual emission core-shell SiO_2 NPs core loaded with RBITC and shell loaded with FITC

In order to obtain a dual-emission multilayer core-shell silica with two different dyes, separated in the core and in the shell, first, the silane-dye complex APTES-RBITC was prepared. For this purpose, in a 5 mL vial, the dye RBITC was measured (3.0mg) accurately and dissolved in 5 mL of dry ethanol. Subsequently, 4.8uL of 3-aminopropiltriethoxysilane (APTES) was added under stirring and the flask was sealed using septum and left for 15 minutes under argon atmosphere in dark conditions. Finally, the reaction was left for 24 hours under magnetic agitation. Once the APTES-RBITC complex was prepared, in a flask sealed with the help of a septum and under argon atmosphere, 25 mL of dry ethanol was added. Then, after 10 minutes of stirring, was added 1.20mL of ammonium hydroxide 28% and was left for 5 minutes with continuously stirring. Finally, 1.7mL of tetraethylortosilicate (TEOS), 2 mL of APTES-RBITC complex and 0.50mL of water were sequentially added in the solution. The reaction was left for 24 hours stirring in dark conditions. Two cycles of centrifugation (10.000g and 15minutes) was done for the purification of the unreacted dye and precursor, and the core-doped NPs were dispersed anhydride ethanol.

Second, the silane-dye complex APTES-FITC was prepared. For this purpose, in a 5 mL vial, the dye FITC was measured (3.0mg) accurately and dissolved in 5 mL of dry ethanol. Subsequently, 4.8uL of 3-aminopropiltriethoxysilane (APTES) was added under stirring and the flask was sealed using septum and left for 15 minutes under argon atmosphere in dark conditions. Finally, the reaction was left for 24 hours under magnetic agitation. Once the APTES-FITC complex was prepared, in a flask sealed with the help of a septum and under argon atmosphere, 15 mL of the prepared SiO_2 NPs from the previous step (silica core-loaded with RBITC) were used as seed to growth a silica layer with FITC. To this solution, 1mL of the APTES-FITC was added. Then after 5 minutes, 200µL of ammonium hydroxide 28% and 200 µL mL of tetraethylortosilicate (TEOS) were sequentially added in the solution. The reaction was left for 24 hours stirring in dark conditions. Two cycles of centrifugation

(10.000g and 15minutes) was done for the purification of the unreacted dye and precursor, and the core-doped NPs were dispersed anhydride ethanol.

Finally, a flask sealed with the help of a septum and under argon atmosphere, 15 mL of the prepared SiO_2 NPs from the previous step (silica core-loaded with RBITC and shell-doped with FITC) were added. Later 20 mL of dry ethanol and 200µL of ammonium hydroxide 28% were added and after 5 minutes, 300 µL of tetraethylortosilicate (TEOS) were sequentially added in the solution. The reaction was left for 24 hours stirring in dark conditions. Two cycles of centrifugation (10.000g and 15minutes) was done for the purification of the unreacted precursor and catalyst. The dual emission core-doped silica NPs were storage in anhydride ethanol.

5.2.3 The Ninhydrine essay for determination of the degree of amine groups on the silica surface

The quantification of amino groups on the surface of the aminated silica was determined by the ninhydrin assay. A ninhydrin solution (3.5 mg/mL) in dry ethanol was freshly prepared for analysis. Standards solutions of 3-(aminopropyl)triethoxysilane (APTES) in dry ethanol in the concentration range of (0.1-1.0 mM) were prepared in order to build the calibration curve, plotting absorbance vs molarity. For the standard analysis, 2 mL of the ninhydrin reagent was reacted with 0.5mL of the corresponding APTES concentration in a closed vial, and was putted in a water bath at 65 °C for 40-45 minutes, preventing the solvent evaporation. Afterwards, the standards were allowed to cool down for 15 min and the absorbance was read at 577 nm in a Shimadzu UV-2400 spectrophotometer. Measurements were done by triplicate. For the aminated silica nanoparticles, once the samples were purifying, the samples were dried at 120 °C for 6-8 h. Then, (5.0mg) of nanoparticles were accurately measured and placed in a capped vial along with 0.5 mL of absolute ethanol. The samples were sonicated for 30 minutes. Subsequently, 2 mL of the ninhydrin solution was added to the vial containing the sample and it was sonicated for 10 additional minutes.

Later, the ninhydrin-sample solution was putted in a water bath at 65 °C for 40-45 min and allowed to cool down for 15 minutes. After completing the time, the dispersion had a blue to purple colour. Finally, the dispersion was centrifuged at 6000g for 25 min and 1 mL of the supernatant was taken and the absorbance was read at 577 nm using a spectrophotometer. Thereafter, the quantity of amino NH_2 molecules in the solution (QAM) of the treated silica nanoparticles was determined by interpolating the measured absorbance using the calibration curve and converting from mM of APTES to number of amino molecules by stoichiometry. Then, using the mass concentration of the silica nanoparticles used for the analysis (2.0mg/mL), the radius of the analysed nanoparticle calculated for electron microscopy TEM (approx. 50nm) and the density of colloidal silica (1.96 g/cm3), it is possible to calculate the total surface area per NP (SA) of the colloidal sample. Finally, the numbers of amine molecules per surface area (NH_2 molecules/nm^2) were calculated dividing the quantity of amino NH_2 molecules (QAM) by total surface area per NP (SA).

5.2.4 Confocal analysis in HEK293 cell lines of the dual-emission SiO_2 NPs doped with RBITC and FITC

Albuminization of SiO_2 NPs: A stock solution of Bovine Serum Albumin (BSA) was prepared at 10mg/ml in PB 10mM buffer. NPs were added onto the BSA solution to a final relative volume concentration 90-10%, and incubated overnight at 4ºC.

Confocal Imaging of NPs on fixed cultured cells: HEK 293 cells (DSMZ) were seeded at 100.000 cell/cm2 on an 8-well glass bottom microslide (Sarsted) pre-coated with BSA (1mg/ml) and Poly-L-Lysine (40µg/cm2), and incubated overnight. Albuminized SiO_2 NPs were added dropwise onto cell cultures and gently homogenized. At 24h cells were fixed with 4% PFA. For immunohistochemistry, samples were first permeabilized with Triton-X 0.2% - BSA 1% for 10min. Samples were incubated with Phalloidin Alexa Fluor 647 (Abcam, ab176759, 1X) for 45min for actin staining. Nuclei were stained with Hoechst 3342 (FisherScientific, H1399, dilution 1:10000) for 15min. Fading was controlled using the Prolong antifade mounting medium (11559306). Samples were observed on the High-Confocal Laser Scanning Microscope

5.3. Experimental for Chapter 4: Development of an Inorganic-Polymer Hybrid Nanostructure with Multimodal Imaging Capabilities for the In vivo and In vitro Identification of Microplastics

5.3.1. Chemicals

Styrene ReagentPlus® ≥99% with 4-tert-butylcatechol as stabilizer, sodium dodecyl sulfate ≥99.0%, potassium persulfate ≥99%, Tetrachloroauric(III) acid trihydrate (99.9% purity), sodium citrate tribasic dihydrate (≥99%), tetraethyl orthosilicate (TEOS) ≥98%, float-A-Lyzer® G2 dialysis device MWCO: 100 KDa, HAuCl4·3H2O (99%), trisodium citrate (99%), 11-mercaptoundecanoic acid 95%, 3-(trimethoxysilyl)propyl methacrylate 98% (MPS), sodium dihydrogen phosphate anhydrous p.a ≥ 99.0%, sodium taurocholate hydrate ≥ 97.0% (TLC), sodium hydroxide p.a ≥ 98.0%, sodium chloride BioXtra ≥ 99.5%, potassium carbonate A.C.S 99%, sodium phosphate dibasic anhydrous p.a ≥ 98.8%, bovine serum albumin (BSA), Dulbecco`s modified eagle medium (DMEM) without phenol red, pepsin from porcine gastric mucosa 535 U/mg, mucin from porcine stomach Type II, L-α-phosphatidylcholine from egg yolk, ~ 60% TLC, fetal bovine serum (FBS) origin: south america, sodium bicarbonate ≥ 99.7%, maleic acid ≥ 98.0% HPLC, were purchased from Sigma-Aldrich. Ammonia solution (ACS Reagent, p.a. 28-30%) and dried ethanol (seccoSolv® max 0.01% H2O) were purchased from Merck. Divinylbenzene (DVB) 80% mixture of isomers, stab. with 1000ppm 4-tert-butylcatechol were purchased from Alfa Aesar TM. All reagents were used as received without further purification and all glass material was sterilized and dehydrogenated in an oven prior to use

5.3.2. Synthetic Procedures

5.3.2.1. Synthesis of the PS NPs by the radical emulsion polymerization

The synthesis of polystyrene (PS) nanoparticles (NPs) were done modifying the emulsion polymerization method reported [3]. In detail, in a 100 mL three-necked flask equipped with a magnetic stirring bar and sealed with the help of a septum under nitrogen atmosphere, was added 30 mL of pure water. After deoxygenate by bubbling with nitrogen for 0.5h and under stirring, the flask was heated until 80°C. Then, 0.5mL of styrene (100mM), 2mL of a SDS solution (final concentration 3.85mM) were sequentially added.

Afterwards, with a help of a syringe pump, 2mL of initiator solution potassium persulfate (KPS) (5.75mM) were added and the reaction was left stirring overnight. Finally, the particles were cooled down at room temperature, were adjusted to a neutral pH 7.00 using a 10mM NaOH solution and purified by centrifugation at 3000g for 30min twice and dialyzed against pure water overnight. To stury the experimental variables and the mean size and SD of the NPs, different solvent (40mL Ethanol/water) mixtures, different styrene concentration, KPs addition rate, and SDS concentration were varied.

5.3.2.2. Synthesis of the Au@SiO_2 and SiO_2-FITC NPs as seeds for the seeded radical emulsion polymerization

Gold (Au NPs of approximately 10nm and 50nm size) synthesis: The gold particles (Au NPs) were synthesized to a desired size, following a well reported kinetically controlled seeded growth method via the reduction of HAuCl4 by sodium citrate [4]. In detail, a solution of 2.2 mM sodium citrate in Milli-Q water (150 mL) was heated with a heating mantle in a 250 mL three-necked round-bottomed flask for 15 min under vigorous stirring. A condenser was utilized to prevent the evaporation of the solvent. After boiling had commenced, 1 mL of HAuCl4 (25 mM) was injected. The color of the solution changed from yellow to bluish gray and then to soft pink in 10 min. The resulting particles (∼10 nm), are coated with negatively charged citrate ions and hence are well suspended in H_2O.224

Growing the Au NPs to a 50nm size: Immediately after the synthesis of the Au seeds and in the same reaction vessel, the reaction was cooled until the temperature of the solution reached 90 °C. Then, 1 mL of a $HAuCl_4$ solution (25 mM) was injected. After 30 min, the reaction was finished. This process was repeated twice. After that, the sample was diluted by extracting 55 mL of sample and adding 53 mL of MQ water and 2 mL of 60 mM sodium citrate. This process was repeated until achieve the desired size.

Grow a silica layer an obtain the Au@SiO_2 NPs: Once the NPs are cooled down to r.t, were directly conjugated stirring at 600 r.p.m with a solution of 11-mercaptoundecanoic acid (MUA) having a final concentration of 2mM for about 24 hours. Later, the NPs were washed and by centrifugation 5.000g for 20 minutes and were concentrated five times to achieve a concentration of NPs/mL (between ~10^{11} and ~10^{12} Nps/mL). Once the NPs were

functionalized, the Au NPs were coated with a silica layer shell by the Stöber method. In detail, in a sealed flask with the help of a septum and under argon atmosphere, 40mL of dry ethanol was added. Then, after 5 minutes of stirring at 850 rpm, 1.21mL of ammonium hydroxide 28% (0.55M of NH_3), 2mL of the concentrated Au NPs and 200 µL of tetraethylortosilicate (TEOS) solution of 120mM were sequentially added and the reaction was left stirring overnight. After this, the NPs were purified by centrifugation at 5.000g for 20 minutes and were dispersed in anhydride ethanol.

Synthesis of the core-shell SiO_2-FTIC NPs: First, the silane-dye complex was prepared. For this purpose, in a 10 mL flask, the dye FITC was measured (7.8mg) accurately and dissolved in 10 mL of dry ethanol. Subsequently, 4.8uL of 3-aminopropiltriethoxysilane (APTES) was added under stirring and the flask was sealed using septum and left for 15 minutes under argon atmosphere in dark conditions. The concentration of the APTES-FITC complex was (2mM:2mM). Finally, the reaction was left for 24 hours under magnetic agitation. Once the APTES-FITC complex was prepared, in a flask sealed with the help of a septum and under argon atmosphere, (50-X) mL of dry ethanol was added. Then, after 10 minutes of stirring, was added 2.02mL (50,7mmol) of ammonium hydroxide 28% and was left for 5 minutes with continuously stirring. Finally, 1.7mL (7,6mmol) of tetraethylortosilicate (TEOS) and X mL of APTES-FITC 2mM complex were sequentially added in the ethanol anhydride solution. The reaction was left for 24 hours stirring in dark conditions. Dialysis against pure water and centrifugation (10.000g and 15minutes) was done for the purification of the unreacted dye and precursor, and the core-doped NPs were dispersed in water or ethanol depending of its use. All the above experiments were conducted at room temperature.

5.3.2.3. Seeded radical emulsion polymerization of the Au@SiO_2 and SiO_2-FITC NPs as seeds

First, the core-shell NPs Au@SiO_2 and SiO_2-FITC NPs g were surface-modified with a coupling reagent, the methacryloxypropyltrimethoxysilane (TMSPMA), to introduce vinyl groups onto the particle surface and make the particle chemically compatible. In detail, the 2 mL of the NPs were diluted in 10mL of anhydride ethanol and thereafter 100 µL of TMSPMA were sequentially added. The reaction was left stirring overnight. After this, the NPs were purified by centrifugation at 3.000g for 15 minutes and dispersed in 2 mL of

anhydride ethanol. Once the particles were functionalized with vinyl groups, the synthesis was done adapting the emulsion polymerization method. In detail, in a 100 mL three-necked flask equipped with a magnetic stirring bar and sealed with the help of a septum under nitrogen atmosphere, was added 40mL of solvent (water or water: ethanol 40:60). After deoxygenate by bubbling with nitrogen for 0.5h and under stirring, the flask was heated until 80°C. Then, 200µL Styrene (100mM) and 5 µL DVB (5.0%), SDS (3.85mM), 2mL of the functionalized particles with TMSPMA, SiO_2–FITC NPs at a concentration ($4.25x10^{13}$ NPs/mL) or for the gold, Au@SiO_2 NPs ($6.63x10^{12}$ NPs/mL) and 2mL of KPS (5.75mM at 0.20mL/min) were added in the bottom flask and heated to 80°C in reflux conditions while stirring at 800 rpm for 24h. Finally, the particles were cooled down at room temperature, were adjusted to a neutral pH 7.00 using a 10mM NaOH solution and purified by centrifugation at 3000g for 30min twice and dialyzed against pure water overnight. For growing a bigger PS shell, the styrene concentration was increased from 25mM to 150mM), results of this process is in Figure 4.7, chapter 4 of this dissertation.

5.3.2.4. Seeded radical emulsion polymerization for developing the Multimodal Contrast Agent for Microplastics Evaluation.

Synthesis of the gold silica core-shell nanoparticles (Au@SiO_2 NPs): First, the gold particles (Au NPs) were synthesized to desirable diameter, following a well reported kinetically controlled seeded growth method via the reduction of $HAuCl_4$ by sodium citrate. Once the NPs were cooled down to r.t, were directly conjugated stirring at 600 r.p.m with a solution of 11-mercaptoundecanoic acid (MUA) having a final concentration of 2mM for about 24 hours. Later, the NPs were washed and by centrifugation 5.000g for 20 minutes and were concentrated five times to achieve a concentration of NPs/mL (between ~10^{11} and ~10^{12} Nps/mL). Once the NPs were functionalized, the Au NPs were coated with a first layer silica shell (aprox. 30nm SiO_2 shell) by the Stöber method. In detail, in a sealed flask with the help of a septum and under argon atmosphere, 40mL of dry ethanol was added. Then, after 5 minutes of stirring at 850 rpm, 1.21mL of ammonium hydroxide 28% (0.55M of NH_3), 2mL of the concentrated Au NPs and 200 µL of tetraethylortosilicate (TEOS) solution of 120mM were sequentially added and the reaction

was left stirring overnight. After this, the NPs were purified by centrifugation at 5.000g for 20 minutes and were dispersed in anhydride ethanol to a final volume of 2 mL.

Synthesis of the multilayer gold silica core-shell nanoparticles with plasmon-enhance properties (Au@SiO_2@SiO_2-FITC@SiO_2 NPs): Once the Au particles were coated with the first 30nm layer of silica, a second silica shell having the fluorescent dye fluorescein-5-isothiocyanate (FITC) within the silica matrix and a subsequent third silica shell for protecting the loaded dye from the environmental interactions, were done by doing twice the Stöber method. First, the silane-dye precursor (APTES-FITC) was prepared. For this purpose, in a 10 mL flask, 2mg of the FITC was measured accurately and dissolved in 5 mL of dry ethanol. Then, 15µL of the 3-aminopropiltriethoxysilane APTES was added under stirring and the flask was sealed using septum under argon atmosphere in dark conditions and was for left for 24 hours under magnetic agitation. Once the adduct was prepared, in a sealed flask with the help of a septum and under argon atmosphere, 7.0mL of dry ethanol was added. Then, after 5 minutes of stirring at 850 rpm, 0.5mL of the APTES-FITC adduct, 300 µL of ammonium hydroxide 28%, 2mL of the concentrated Au@SiO_2 NPs, 500 µL of pure water and 200 µL of tetraethylortosilicate (TEOS) solution of 120mM were sequentially added and the reaction was left stirring overnight. After this, the NPs were purified for removing the unbound APTES-FITC molecules by centrifugation at 3.000g for 15 minutes twice and were dispersed again in anhydride ethanol to a final volume of 2 mL. Thereafter, the third silica layer was done as follows: in a sealed flask with under argon atmosphere, 14.0mL of dry ethanol was added. Then, after 5 minutes of stirring at 850 rpm, 600 µL of ammonium hydroxide 28%, 2mL of the concentrated Au@SiO2 NPs, 500 µL of pure water and 200 µL of tetraethylortosilicate (TEOS) solution of 120mM were sequentially added and the reaction was left stirring overnight. After this, the NPs were purified by centrifugation at 3.000g for 15 minutes and dispersed in 2 mL of anhydride ethanol.

Synthesis of monodisperse multimodal imaging core-shell polystyrene nanoparticles as contras agent (Au@SiO_2@SiO_2-FITC@SiO_2@PS NPs): First, the multilayer gold silica core-shell nanoparticles with plasmon-enhance properties were surface-modified with a coupling reagent, the methacryloxypropyltrimethoxysilane (MPS), to introduce vinyl groups onto the particle surface and make the particle chemically compatible. In detail, the 2 mL of the NPs were diluted in 10mL of anhydride ethanol and thereafter 100 µL of MPS were sequentially added. The

reaction was left stirring overnight. After this, the NPs were purified by centrifugation at 3.000g for 15 minutes and dispersed in 2 mL of anhydride ethanol. Once the particle were funcionalized with vinyl groups, the synthesis was done adapting the emulsion polymerization method. In detail, in a 100 mL three-necked flask equipped with a magnetic stirring bar and sealed with the help of a septum under nitrogen atmosphere, was added 30 mL of pure water. After deoxygenate by bubbling with nitrogen for 0.5h and under stirring, the flask was heated until 80°C. Then, 2mL of the Au@SiO_2@SiO_2-FITC@SiO_2@ core-shell NPs functionalized with MPS, a mixture of 190µL of styrene (50mM) and 10 µL of divinylbenzene (DVB), 1mL of sodium dodecyl sulfate (SDS) solution (25 mg/mL) were sequentially added. Afterwards, with a help of a syringe pump, 2mL of initiator solution potassium persulfate (KPS) (35mg/mL) were added at a constant rate of 0.200mL/min, and the reaction was left stirring overnight. Finally, the particles were cooled down at room temperature, were adjusted to a neutral pH 7.00 using a 10mM NaOH solution and purified by centrifugation at 3000g for 30min twice and dialyzed against pure water overnight. The thickness of the PS shell could be tuned through varying the amount of the styrene monomer concentration.

5.3.3. Materials and Methods for the in vivo and in vitro analysis of the NPs

5.3.3.1 Simulated body fluid (SBF) intravenous and oral physiological conditions.

Intravenous conditions (I.V):

1- 10% of the NPs were conjugated with a solution (PB 10mM + BSA 2mg/mL) of final concentration, for 24h at 4 degrees. (Albuminization).
2- Then 10% of the albuminized NPs from the previous step are incubated directly on a 90% solution (DMEM 90% + FBS 10%), for 24h at 37 degrees. (Exposure to physiological media).

Oral administration (O.A):

1- 200uL of NPs as synthesized were exposed directly to the gastric and intestinal media, for 24h at 37 degrees. (10%NPs + 90% physiological medium) = 200uL NPs /2mL medium.

Reagents for preparing Gastric fluids

Reagent	Concentration
Lecithin	20 µM
Pepsin	0.1 mg/ml
Mucin gastric	1.4 g/l
Sodium taurocholate	80 µM
NaCl	34.2mM
$NaHCO_3$	8mM
HCl	<= 160mM
pH	1.6

Reagents for preparing Intestinal fluids

Reagent	Concentration
Sodium taurocholate	3mM
Lecithin	0.2mM
Maleic acid	19.12mM
NaOH	34.8mM
NaCl	68.62mM
pH	6.5

5.3.3.2 Animals used: Mice model

Adult female BALB/cAnNRj mice (Janvier), of 19-22 g and 6 – 7-week-old at the time of NP administration, were housed three to four per cage with ad libitum access to food and water during a 12 h light/dark cycle. All the experimental procedures were conducted in strict accordance with the European (Directive 2010/63/UE) and Spanish laws and regulations (Real Decreto 53/2013; Generalitat de Catalunya Decret 2114/97) on the protection of animals used for experimental and other scientific purposes, and approved by the Vall d'Hebron Research Institute (VHIR) Ethical Experimentation Committee (CEEA: 67/20).

5.3.3.3 Experimental procedure – CT imaging

CT imaging was performed under general anaesthesia using isofluorane (5% for the induction phase and 2% for the maintenance phase). After the mouse was anesthetized and before injection of the prepared NPs solution, CT scan of the animal was performed as control. Thereafter, Nanoparticles were administered either via tail-vein injection with 0.2 ml of 100 µg/ml Ag-Si-PolNPs () in suspension (n = 6) or via oral gavage with 0.2 ml of 300 µg/ml albuminized Ag-Si-PolNPs in suspension (n = 6). The injected dosage was approximately 1 mg NPs/kg body weigth and 3 mg NPs/kg body weight respectively. Another CT scan of the mouse was done 5 min and 24h after injection to visualize the in vivo distribution of NPs by means of contrast enhancement. The mouse was then euthanized via cervical dislocation and organ samples were collected (including liver, spleen, kidney, stomach, and intestine), weighted, and stored at -20°C. CT scan data were analyzed with GraphPad and outliers were excluded by means of the Grubbs' test. Data

were subjected to type I ANOVA and pairwise comparison with pre-treatment scan data. Bonferroni test was used for multiple comparisons among the different time points scan data and the pre-treatment scan data in the oral and the intravenous treatments (*$p < 0.05$; **$p < 0.01$; ***$p < 0.001$).

5.3.3.4 ICP-MS analysis of explanted tissues for quantifications of Au content.

All the mice were euthanized 24 hours post-treatment. Liver, spleen, kidneys and stomach from the different mice were collected together with the feces content of small and large intestine and the feces produced in the cages by the different group of mice during the 24 hours post-treatment. Organs were immediately frozen at -20ºC. All the organs were subjected to microwave-assisted digestion (Ethos Easy Microwave Digestion Platform, Milestone Srl, Italy). Organs were introduced in a mixture of concentrated HNO3:HCl acids at a proportion of 1:3 (aqua regia) following manufacturers indications. A minimum of 6 mL of mixture in case of samples up to 1 g or glass tubes containing a volume of 1-3 mL in water bath for samples up to 0.1 g were sealed in a 100 mL microwave teflon tube. Then, samples were heated at 200ºC for 20 minutes and then left to cool to room temperature for further quantify the AU content by ICP-MS.

5.3.3.5 Experimental procedure – Optical Microscopy of Tissue sections

1.5ug Au/ml of albuminized Au@SiO2-FITC@PS NPs were intravenously injected via tail-injection to each mouse (n=2). At 24h, mice were sacrificed euthanized via cervical dislocation and liver and organ samples were collected (including liver, spleen, and kidney). The organs were briefly washed with normal saline, slightly dried with blotting paper and immersed for 4h in 4% formalin for tissue fixation. Next, tissues were embedded in paraffin following a standard protocol. For immunohistochemistry, paraffin-embedded samples were sectioned at 4µm using a microtome and transferred to a poly-lysine coated glass slide. The paraffin was then removed with xylene and the samples rehydrated.

5.3.3.6 Immunostaining

Samples were permeabilized with Triton-X 0.2% for 10min. Sections were incubated with anti-β-Actin mouse monoclonal antibody (MAB8929, R&D Systems, at a dilution 1:100)

overnight at 4ºC, followed by an incubation with a secondary antibody goat anti-mouse Alexa Fluor568 (FisherScientific, A11019, dilution 1:500). Nuclei were stained with Hoesch 3342 (FisherScientific, H1399, dilution 1:10000). Fading was controlled using the Prolong antifade mounting medium (11559306).

5.3.3.7 Hematoxilin&Eosin

Rehydrated tissue sections were processed for haematoxylin & eosin (H&E) staining in order to evaluate morphological damage of the tissues. Samples were then mounted with a coverslip and DPX mounting medium. Samples were observed on a Uprigth Microscope (Olympus BX61).

5.4. Characterization Techniques

5.4.1. UV-Vis Spectroscopy

The optical absorption behaviour was analysed using a UV-Vis spectrophotometer. UV-Visible spectra were acquired with an Agilent Cary 60 UV-Vis Spectrophotometer. 1ml of the NPs was placed in a quartz cuvette, and spectral analysis was performed in the 200 nm to 800 nm range at room temperature. In the case of time evolution measures, aliquots of the solution were taken out and were immediately analysed, in the proper dilution to fit the range. For the concentration of the Monomer, the absorbance was measured at 400nm wavelength and calculated from the calibrated curve.

5.4.2. Dynamic Light Scattering (DLS)

The hydrodynamic size by number (nm), particle concentration (NPs/mL), Zeta Potential (mV) and conductivity (mS/cm) of the SiO_2 NPs were determined by using a Zetasizer Ultra (Malvern instruments, UK), instrument equipped with a light source wavelength of 532 nm and incorporating Non-Invasive Back Scatter (NIBS) and a uniquely Multi-Angle Dynamic Light Scattering (MADLS) technology for the measurement of particle and molecular size. A proper dilution of the colloidal SiO_2 NP solutions was placed into specific plastic cuvettes and the software was arranged with the parameters of refractive index, adsorption coefficient and solvent viscosity at 25 °C. Each value was the average of at least 3 independent measurements. All measurements used the Smoluchowski model.

In the case of time evolution measurements, aliquots of the solution were taken out after a given time and were immediately analysed with the proper dilution.

5.4.3. Electron Microscopy

Silica particles were visualized using a FEI Tecnai G2 F20 HR(S)TEM operating at an accelerating voltage of 200 keV in bright/dark field modes and also using a FEI Magellan 400L XHR SEM operated at 20 kV in transmission mode STEM. EDX of the sample was performed on an EDAX super ultrathin window (SUTW) X-ray detector coupled to a Tecnai G2 F20 microscope. The samples were prepared by drop-casting 10 µL of the sample onto a piece of ultrathin carbon-coated 200-mesh copper grid (Ted Pella, Inc.) and left to dry in air. SEM and TEM images of the prepared colloidal SiO_2 NPs were used for the size distribution measurements using Image J software. For each sample, the size of at least 300 particles was measured and the average size and the standard distribution obtained measurements.

5.4.4. Powder X-ray diffraction (XRD)

The solid-state phase structure of the SiO_2 NPs was recorder by a Malvern PANalytical X'pert Pro MPD diffractometer using a CuKα (λ = 1.540598 Å) radiation source measuring the broad diffraction peak at room temperature. In a typical experiment, the 2θ diffraction (Bragg) angles were measured by scanning the goniometer from 10° to 90°. The samples were prepared by centrifugation of the colloidal solution containing the NPs at 10.000 g to precipitate the NPs. The supernatant was discarded and samples were dried at room temperature to avoid further NP transformations. Peak positions and their full width at half maximum (FWHM) were determined using the X'Pert HighScore program after baseline correction.

5.4.5. Photoluminescence Spectroscopy

Fluorescence measurements of the NPs samples were carried at room temperature at 25 °C using a LS-45 Luminescence Spectrometer (Perkin Elmer, Inc.; Waltham, MA, USA) and the software FL WinLab (Perkin Elmer, Inc.). The spectra were recorded using a photomultiplier tube (PMT) voltage of 650 V and the spectral ranges used for the measurements covered the UV-visible region of the FITC, RBITC and AF350spectra (e.g. λex

= 400 to 700 nm) and were collected at a reasonably high resolution with an emission scan speed of 1500 nm min−1 using: an excitation wavelength of λex =495nm for FITC, λex =550nm for FITC and TRITC and finally λex =350 nm for AF350, (with an 0.5 nm bandwidth increments). For the samples measurement, 2ml of the NPs was placed in a quartz cuvette with a long axis of 10 mm (excitation axis) and a short axis of 4 mm (emission axis) and the fluorescence measurements were recorder.

5.4.6. Confocal Microscopy

Samples were observed on the High-Confocal Laser Scanning Microscope (Zeiss LSM 980 Airyscan) equipped with Quasar spectral detector (32 channels GaAsP PMT, 1 rPMT-MA, 1 conventional PMT) + transmitted light detector a Airyscan 2 detector for super-resolution/high-speed and with Additional workstation for image analysis.Hoescht 33342 (em350⁄ex461), Alexa Fluor-568 (ex578/em603), RBITC (em558/ex575) and FITC (em490/ex525) were observed using the standard fluorescence mode and pre-defined settings. Colors from the images acquired are chosen arbitrarily in each case to better discriminate all the signals collected.

5.4.7. Fourier transform infrared spectroscopy (FTIR)

The FTIR, the IR spectra of each aminated silica nanoparticles were recorded using a Tensor 27 (Bruker) spectrophotometer equipped with a single reflexion diamond window ATR accessory (MKII Golden Gate, Specac). For the experiment, The NPs were washed with milli-q water and dried at 100°C for three hours. Then, the powder of the NPs was directly analysed.

5.4.8. High-performance liquid chromatography (HPLC)

The HPLC analysis were done in collaboration with the Chemical Analysis Service (SAQ) of the Scientific and technical services of the University Autonomous of Barcelona (UAB). Th equipment is the Agilent 1100 Series HPLC system with DAD detector, Detection type, 1024-element photodiode array, Light Source of Deuterium and tungsten lamps Wavelength Range (190 - 950 nm), COLCOM, Auto Sampler, Degasser and QuarPump Métrico from Agilent Technologies. The Column used Xterra MS C18 3.5µm, 2.1x50mm

(Waters P/N: 186000400), with a mobile phase FM A: 15mM NH_4CH_3COO pH 7.5, FM B: Methanol.

5.4.9. Microwaver digestions for elemental analysis

All the organs were subjected to microwave-assisted digestion (Ethos Easy Microwave Digestion Platform, Milestone Srl, Italy), equipped with pressure sensor (50 bar) and coupled with an infrared temperature sensors combined with an in-situ temperature sensor using TFM bottles. The maximum temperature of analysis were 200 °C and pressure of 100 bar. Equipped with two 950 Watt magnetrons the systems can operate at up to 1900 Watts. The organs and Au NPs were introduced in a mixture of concentrated HNO3:HCl acids at a proportion of 1:3 (aqua regia) following manufacturers indications. A minimum of 6 mL of mixture in case of samples up to 1 g or glass tubes containing a volume of 1-3 mL in water bath for samples up to 0.1 g were sealed in a 100 mL microwave teflon tube. Then, samples were heated at 200ºC for 20 minutes and then left to cool to room temperature for further use

5.4.10. Induced coupled plasma-mass spectroscopy (ICP-MS)

Measurements for quantitative analysis of the Au metals in the NPs were carried out at the “Servei d'Analisi Quimica” (SAQ) in the UAB with by conventional nebulization glass nebulizer at a flow of 0.9 L/min with a 7500ce system (quadrupole ICP-MS) from Agilent Technologies. Samples were digested with aqua regia 1:2 in volume for 24 h and then diluted with milli-Q water to be further analyzed by ICP-MS. The accuracy of trace metal analysis was validated using the addition of a patron to a standard sample (spike) obtaining an Au recovery of 97%. Data were represented as mean ± SEM.

5.4.11. Thermogravimetry analysis (TGA)

The TGA of the samples were performed using a PYRIS 8000 Thermogravimetical analyzer Thermobalance TGA Q-500 thermal gravimetric analyzer from TA Instruments, with samples held in a platinum pan under a nitrogen atmosphere with a flow 20 mL/min and a heat rate of 1°C/min from 0°C to 500°C.The quantity of nanoparticle used was 0.500mg and the weight loss analyzed.

5.4.12. Computed tomography (X-ray CT)

CT scans were done in a (Quantum FX imaging system, Perkin Elmer, Massachusetts, USA) of all the animals was taken prior treatments to establish basal signal. Defined parameters for image acquisitions were: Field of view 40 mm, acquisition time 4.5 minutes, current voltage 50 mV and amperage 200 uA. For scanning procedure animals were anesthetized with isoflurane (5% induction phase, 2% maintenance). Air flow was set to 0.8 L/min. Once the scans were finished, animals were bringing back to their cages for recovery. NPs were administered in a saline solution (26 µg Au, 200 µL, equivalent to approximately 60 µg of polystyrene) by oral gavage in case of the OT group and in a saline solution with murine serum albumin (MSA) (9 µg, 200 µL, equivalent to approximately 20 µg of polystyrene; 2 mg/mL MSA final concentration was added which was equivalent to 20X the concentration needed to cover the surface of all NPs in the sample) in case of the IVT group. Control group was treated with the vehicles employed for the different treatments in a similar way to oral and intravenous treatment groups. Once the treatment was administered, CT scans was performed at different time-points: OT group (5 min and 1, 4, 8, 24h post-treatment), IVT group (5 and 30 min, 1 and 24h post-treatment). Imaging data were analysed by Preclinical Imaging Platform staff at VHIO. Image reconstruction was based on Feldkamp´s method. Data were represented as mean ± SE.

References

[1] H.-T. Lu, “Synthesis and characterization of amino-functionalized silica nanoparticles,” *Colloid J.*, vol. 75, no. 3, pp. 311–318, 2013, doi: 10.1134/s1061933x13030125.

[2] I. A. Rahman *et al.*, “An optimized sol–gel synthesis of stable primary equivalent silica particles,” *Colloids Surfaces A Physicochem. Eng. Asp.*, vol. 294, no. 1, pp. 102–110, 2007, doi: https://doi.org/10.1016/j.colsurfa.2006.08.001.

[3] M. N. Gorsd, M. N. Blanco, and L. R. Pizzio, “Synthesis of Polystyrene Microspheres to be Used as Template in the Preparation of Hollow Spherical Materials: Study of the Operative Variables,” *Procedia Mater. Sci.*, vol. 1, pp. 432–438, 2012, doi: https://doi.org/10.1016/j.mspro.2012.06.058.

[4] N. G. Bastús, J. Comenge, and V. Puntes, “Kinetically Controlled Seeded Growth Synthesis of Citrate-Stabilized Gold Nanoparticles of up to 200 nm: Size Focusing versus Ostwald Ripening,” *Langmuir*, vol. 27, no. 17, pp. 11098–11105, 2011, doi: 10.1021/la201938u.

VI. Conclusions

“Be the change that you wish to see in the world”

Mahatma Gandhi

Chapter 6

Conclusions and Contributions

6.1 General Conclusions and perspectives

In this dissertation we have been working with several aspects around the production of silica nanoparticles and the use of its hybrids nanostructures for biological imaging applications. The whole set of silica NPs and their hybrids nanostructures presented in this thesis were completely characterized in order to determine their: morphology, mean size and size distribution and composition by different physicochemical techniques including: UV-Vis spectroscopy, PL spectroscopy, SEM and TEM microscopy, dynamic light scattering (DLS), EDX analysis and ICP-MS spectroscopy for elemental mapping and composition analysis, FT-IR for identification of the relevant functional groups and Laser confocal microscopy (LCM) with X-ray (CT) spectroscopy for the in vitro and in vivo analysis.

We conclude herein, the main results and possible extensions of some of the main drawback addressed in the previous chapters. Although compilations of specific conclusions have been made throughout the thesis, we present here a collecting of those we consider more relevant

Synthesis of Silica Nanoparticles

We have explored the synthesis of water soluble SiO_2 NPs by a solvent-base homogenous hydrolysis and condensation of silicon precursor (TEOS) by an ammonia catalysed process. In this method, ammonia (NH_3) played three main relevant roles: (i) as a hydroxyl ion (OH^-) generator. Ammonia undergoes ionization triggering the water dissociation. This chemical reaction produces hydroxyl ions (OH^-) in solution, in which by a nucleophilic substitution SN_2 reaction, produce the silanol monomers from the TEOS. (ii) As a stabilizing agent for precipitated particles. Ammonia raises the pH of the solution by the

increased supply of hydroxyl ions, thus increase the colloidal stabilization of the nanoparticles by electrostatic repulsion, by increasing the negative charge of the silanols groups on the particle surface (Si-O-) avoiding particle aggregation. (iii) as a reaction catalyst. The ammonia decreases the ionization energy of the system required to start the nucleation. The equilibrium of the reaction was displaced favouring both, nucleation and growth process, enhancing the hydrolysis and subsequent condensation, thus, increasing the siloxane bonds in the system. However, ammonia induced the production of larger SiO_2 particles by strongly accelerating the condensation rate of the species, by generation larger branched siloxane structures that favours the growth process to bigger sizes. In addition, the increased addition of ammonia supplied the system with an increased NH_4^+ ions that compromise the electro stability of the growing particles. Therefore, despite ammonia can modify the size of the silica, the concentration of water in the continuous phase allows a better systematically fine-size tuning of the final particle size.

The relative variations of water concentrations (from 1.80 to 13.0M) allows the one-pot synthesis of SiO_2 NPs from 20 nm to 320nm with high yields, around 95%. The role of water as a key reagent in the synthesis and the mechanism of formation of the silica, were elucidated by the time evolution kinetic study of the reaction, under three different water concentrations while the others reagent remained fixed. Both of our results (experimental and the theoretical modelling) results revealed that the growth mechanism followed by the SiO_2 NPs at the beginning of the reaction is by an aggregative-growth of protoparticles and during the later stages (around 100-150 minutes) occurs by monomer addition, allowing the incorporation of atoms at the silica surface for homogenous growth of the controlled-diffusion of monomer.

The presence of water allows a better control of the kinetics of the reaction by controlling: (i) the induction time for the monomers to overcome the activation barrier of self-nucleation. Water act as a fuel for the generation of hydroxyl ions (OH-), but in a controlled manner. Therefore, these negative ions allowed the proper control of both reactions (hydrolysis and condensation) towards short or longer induction times, as a consequence to a short or faster initiation of the nucleation. This had a major effect because in the initial number of mineralized silica particles (nucleation) and in their initial

morphology (size distribution). In addition, because the controlled addition of water causes a small decrease in the double layer thickness of the growing particles, this controls the mineralization of particles, where longer nucleation times (low water concentration), produces a higher number of particles, but smaller in size and shorter nucleation time (high water concentration), produce lower number of particles, but bigger in size, due to the aggregative growth for stabilization, principle explained by LaMer model.

From these results we can conclude that the growth mechanism followed by the SiO_2 NPs presented six main steps. (1) The generation of the silanol monomers by the hydrolysis of TEOS due to the hydroxyl ions nucleophilic attack, (2) subsequent condensation of the silanol monomers for formation of siloxane branched structures, (3) nucleation by the generation of protoparticles by the collapsing of the unstable siloxane branched assembly, (4) aggregative-growth of protoparticles into subcritical clusters, (5) formation of the stable seed primary particles by the coalescence of clusters beyond a critical size and (6) growth of the NPs by diffusion of Si atoms at particles surface by a monomer-addition model.

Surface and Core Functionalization of Silica Nanoparticles

We have systematically modified the surface charge of the silica NPs by a post-grafting strategy. Our methodology Involves the functionalization of the silica negative surface using a silane coupling agent that contains an amine group by creating a strong siloxane bond, between the silanol groups (Si-OH) of the surface of the particle and the silane APTES by a substitution reaction. With our method the Zeta Potential were tuned from -40mV to 22mV at physiological pH. Furthermore, the isoelectric point of the particles was also tuned from 3 (pristine silica) to 8.8 using 11mM of APTES. The number of amino groups per surface area were determined. The ninhydrin test revealed that the number of amino groups were controlled from 1 to 4 NH_2/nm^2, important feature for bioconjugations studies or applications.

On the other hand, the core of the silica nanoparticles was loaded with different fluorescent molecules by a copolymerization sol-gel methodology, without affecting the

size control of the nanoparticles. This method involves the preparation of a complex molecule by coupling the APTES silane agent with the organic dye, via thiourea or amide linkage. This process allows the covalent incorporation of the fluorophores, demonstrated by the leaching experiments, in which 18% of the signal was decreased, after four cycles of washing. Furthermore, our one-pot strategy proven to be highly versatile, because allows the incorporation of not only a single dye (FITC, RBITC, TRITC or AF350) for achieve core-shell fluorescent probe made of silica, covering a wide range emission in the UV-Visible region, but also in the UV region with the AF350, with emits at 350nm. But, a mixture of them, by two different experimental strategies for the development of dual-emission core-shell fluorescent probes. The number of dye molecules can be systematically tuned bye controlling the concentration of the APTES-Dye complex, prior the copolymerization.

Finally, from all this results, we have developed a multilayer dual-emission probe having a core-shell architecture, loaded with a reference dye (RBITC) in the core and the sensitive dye (FITC) in a second silica outer layer, as a responsive probe suitable for biological applications. As a proof of concept, the dual-emission NPs were incubated in HEK cells, revealing the colocalization of both dyes in the intracellular space, indicating that both dyes were loaded in the nanostructure without having a quenching effect due to the proximity of the reporter molecules. Furthermore, the NPs were incubated in physiological conditions for seven days, revealing that both dyes can be released with different profiles, due to the dissolution by voids in the core of the NPs by siloxane bond breaking. This dissolution profile revealing that the functionalized NPs can display different fluorescent colours form yellow to orange-red (RBITC+FITC), upon dissolution.

Silica-Based Hybrid Nanostructures as Multimodal Contrast Agent

In this chapter we have developed a multimodal contrast agent of polystyrene nanoparticles as a model particle for the evaluation and tracking of microplastics in biological system by the combination of different imaging modalities. The particle was synthetized by a seeded radical emulsion polymerization, using an inorganic salt (KPS) as a radical initiator, presenting a mean size around 500nm, highly monodisperse. The polymer model particles were designed with a multilayer core-shell architecture,

composed of a gold Au NPs in the core and a further silica layer with a covalent entrapped fluorescent dye (FITC) within the silica matrix. Both materials were chosen due to their optical properties, the gold due their LSPR and high X-ray scattering for (CT) and the silica, due the well known as optical probes, for confocal microscopy. Furthermore, by adjusting the experimental reactions conditions, such as initiator rate at a speed 200µL/min and the addition of a 5% of a co-monomer (DVB), the growth of the PS shell were controlled from eccentrically to concentrically.

Furthermore, this multilayer strategy allows the production of a PEF-core, by the proper control of the distance between the fluorescent dye and the plasmonic Au metal. The silica was used a spacer for controlling the distance. Between both materials as labels. The SiO_2 shell thickness were growth by a modified sol-gel heterogenous process, using the Au as seeds, revealing that the optimal distance for the PEF was at approximately 30nm for achieve an enhancement of fluorescent of 3-fold.

Finally, the in vitro and in vivo correlation of the multi contrast agent PS NPs with the different medical and biological imaging techniques were explored. Our In vitro results revealed that the NPs can be colocalized by the confocal microscopy, once incubated with HEK cells for 24h. The dual-label PS NPs were identified due to the scattering of the Au and the fluorescent emission of the FITC molecules, entrapped in the silica. On the other hand, the in vivo observations reveal that were promising result. The NPs were also localized on a tissue section of an organ, using a confocal microscopy. The dual-label PS particles were observed in the liver and spleen section, once injected I.V in animal model (using a mice). In addition, the model particles were followed by ICP-MS elemental analysis of the Au, reveal that the biodistribution of the NPs were located in the same organs, in agreement with the microscopy results. On the other hand, the oral administration results, were followed by the X-ray CT. The results showed that the nanoparticles were located in the initial stage in the stomach and ta the later stages were accumulated in the large intestines. The same trend was confirmed by ICP-MS. The evaluation of the integrity of PS shell of the NPs in SBF, confirmed that the stability of the NPs without sing of dissolution. These biological results, confirms that our model particle is suitable as a multimodal contrasts agent for evaluation of MPs.

Perspectives

CHAPTER 2: Synthesis of Silica Nanoparticles

Future work should be focused on the detailed aggregative-growth mechanism in the initial stages of the SiO_2 NPs. A controlled time evolution experiments using a high-resolution analysis by a HR-TEM with EDX will be suitable for achieve the detailed morphology of the protoparticles, their size and SD and characterization. In the same trend, study in a systematically manner the formation of the branched siloxane networks. Finally, improving of the synthesis of SiO_2 NPs by the sol-gel method, using a greener and safety catalyst as an alternative for ammonia, for instance with another base such as NaOH.

CHAPTER 3: Surface and Core Functionalization of Silica Nanoparticles

Future analysis on the QY% of the fluorescent core-shell SiO_2 NPs and the dual-emission probes with a mixture of dyes are recommended for a better characterization. In addition, the loading with other reported molecules inside the SiO_2 core, for instance in the NIR-window or far infrared wavelength using NIR dyes, for increase the range of detection of the label silica particles. Finally, performs a more realistic biological applications of the dual-emission NPs, loading the core of the particles with pharmaceutical molecules, to build a superior dual-emission theragnostic silica-based probe.

CHAPTER 4: Silica-Based Hybrid Nanostructures as Multimodal Contrast Agent

Future work should be done in increasing the polymer shell of the PEF-labelled PS NPs, with other polymer materials, such as polymethyl methacrylate (PMMA) or polyethylene (PE) in order to increase the risk assessment of MPs. In addition, the PEF-core particle can be extended with other dyes having different emission wavelength than FITC. Finally, the morphology of the PEF-labelled Ps NPs can be altered to other morphology, such as rods or triangles, to increase the distribution of the nanoparticles, allowing a more realistic analysis of MPs, because they are present in nature heterogeneously in size.

6.2 Publications and Contributions

6.2.1 Publications

- Marcos Arribas Perez, **Oscar H. Moriones**, Neus G. Bastús, Victor Puntes, Andrew Nelson, Paul A. Beales. “Isolated occurrences of membrane perturbation by mechanosensing from weakly aggregating silver nanoparticles”. bioRxiv 623678; doi: https://doi.org/10.1101/623678.

- Marcos Arribas Perez, **Oscar H. Moriones**, Neus G. Bastús, Victor Puntes, Andrew Nelson, and Paul A. Beales. “Mechanomodulation of lipid membranes by weakly aggregating silver nanoparticles”. Biochemistry 2019 58 (47), 4761-4773. DOI: 10.1021/acs.biochem.9b00390.

- Francesco Barbero, **Oscar H. Moriones**, Neus G. Bastús, and Victor Puntes. “Dynamic Equilibrium in the Cetyltrimethylammonium Bromide–Au Nanoparticle Bilayer, and the Consequent Impact on the Formation of the Nanoparticle Protein Corona”. Bioconjugate Chemistry 2019 30 (11), 2917-2930. DOI: 10.1021/acs.bioconjchem.9b00624.

- Tran TA, Hesler M, **Moriones OH**, Jimeno-Romero A, Fischer B, Bastús NG, Puntes V, Wagner S, Kohl YL, Gentile L. “Assessment of iron oxide nanoparticle ecotoxicity on regeneration and homeostasis in the replacement model system Schmidtea mediterranea”. ALTEX. 2019;36(4):583-596. doi: 10.14573/altex.1902061. Epub 2019 Apr 26. PMID: 31026038.

- Elje E, Mariussen E, **Moriones OH**, Bastús NG, Puntes V, Kohl Y, Dusinska M, Rundén-Pran E. “Hepato(Geno)Toxicity Assessment of Nanoparticles in a HepG2 Liver Spheroid Model”. Nanomaterials (Basel). 2020 Mar 18;10(3):545. doi: 10.3390/nano10030545. PMID: 32197356; PMCID: PMC7153628.

- Patrick Schuller, Mario Rothbauer, Sebastian R.A. Kratz, Gregor Höll, Phillipp Taus, Markus Schinnerl, Jakob Genser, Neus Bastus, **Oscar H. Moriones**, Victor Puntes, Berthold Huppertz, Monika Siwetz, Heinz Wanzenböck, Peter Ertl. “A lab-on-a-chip system with an embedded porous membrane-based impedance biosensor array for nanoparticle risk assessment on placental trophoblast cells”. Sensors and Actuators B: Chemical,Volume 312,2020,127946,ISSN 0925-4005, https://doi.org/10.1016/j.snb.2020.127946.

- Kohl, Y., Biehl, M., Spring, S., Hesler, M., Ogourtsov, V., Todorovic, M., Owen, J., Elje, E., Kopecka, K., **Moriones, O. H**., Bastús, N. G., Simon, P., Dubaj, T., Rundén-Pran, E., Puntes, V., William, N., von, H., Wagner, S., Kapur, N., Mariussen, E., Nelson, A., Gabelova, A., Dusinska, M., Velten, T., Knoll, T. “Microfluidic In Vitro Platform for (Nano)Safety and (Nano)Drug Efficiency Screening”. Small 2021, 17, 2006012. https://doi.org/10.1002/smll.202006012.

- Dubaj T, Kozics K, Sramkova M, Manova A, Bastús NG, **Moriones OH**, Kohl Y, Dusinska M, Runden-Pran E, Puntes V, Nelson A, Gabelova A, Simon P. "Pharmacokinetics of PEGylated Gold Nanoparticles: In Vitro-In Vivo Correlation". Nanomaterials (Basel). 2022 Feb 1;12(3):511. doi: 10.3390/nano12030511. PMID: 35159859; PMCID: PMC8838925.

- Han, X., Boix, G., Balcerzak, M., **Moriones, O. H**., Cano-Sarabia, M., Cortés, P., Bastús, N., Puntes, V., Llagostera, M., Imaz, I., Maspoch, D. "Antibacterial Films Based on MOF Composites that Release Iodine Passively or Upon Triggering by Near-Infrared Light". Adv. Funct. Mater. 2022, 32, 2112902. https://doi.org/10.1002/adfm.202112902.

- Vakurov A, Drummond-Brydson R, William N, Sanver D, Bastús N, **Moriones, O.H**, Puntes V, Nelson AL. "Heterogeneous Rate Constant for Amorphous Silica Nanoparticle Adsorption on Phospholipid Monolayers". Langmuir. 2022 May 10;38(18):5372-5380. doi: 10.1021/acs.langmuir.1c03155. Epub 2022 Apr 26. PMID: 35471829; PMCID: PMC9097521.

- Francesco Barbero, Sara Michelini, **Oscar H. Moriones**, Javier Patarroyo, Jordi Rosell, Muriel F. Gusta, Michele Vitali, Luna Martín, Francesc Canals, Albert Duschl, Jutta Horejs-Hoeck, Laura Mondragón, Neus G. Bastús, and Víctor Puntes. "Role of Common Cell Culture Media Supplements on Citrate-Stabilized Gold Nanoparticle Protein Corona Formation, Aggregation State, and the Consequent Impact on Cellular Uptake". Bioconjugate Chemistry Article ASAP. DOI: 10.1021/acs.bioconjchem.2c00232.

- Aliro Villacorta, Laura Rubio, Mohamed Alaraby, Montserrat López-Mesas, Victor Fuentes-Cebrian, **Oscar H. Moriones**, Ricard Marcos, Alba Hernández. "A new source of representative secondary PET nanoplastics". Obtention, characterization, and hazard evaluation, Journal of Hazardous Materials, Volume 439,2022, 129593,ISSN 0304-3894,https://doi.org/10.1016/j.jhazmat.2022.129593.

6.2.2 Conferences

- Marie Skoldowska-Curie COFUND DOCtoral in Functional Advanced Materials (DOC-FAM) Emerging 2021 School: ICMAB Barcelona. **Poster presentation**. 02/07/2021

- The SO workshop on Environmental Monitoring and Remediation, **Speaker**. Barcelona Barcelona, Spain 17/12/2021.

- The 6th scientific meeting of PhD students of BNC-b, JPhD 2021 the Scientific Meeting of Phd Students at UAB campus. **Poster presentation**. November 25-26, 2021.

- NanoSpain2019 Conference, (Barcelona-Spain, May 28-31, 2019). **Speaker**

- 6th NANO TODAY CONFERENCE - **poster presentation**. Lisbon-Portugal. 16 to 20 of June 2019.

- NaNaX 9 Nanoscience with Nanocrystals Conference - **Poster presentation**. Universität Hamburg. 16 to 20 of September 2019.

6.2.3 Other Scientific Contributions

- Winner and awarded in the program of Generació d'Idees 12a edició | Microplàstics del Parc de Recerca - UAB Barcelona Barcelona. Spain 20/09/2021-18/12/2021. **Project developed winner, MPFood Watching**.

- **Speaker** in the Program: Bojos per la ciència de la Fundació Catalunya La Pedrera. sesiones 2018-2019-2020.

- **Nanomaterials Advisor**: Design and producer of Dual label PS NPs for Microplastics identification. Developed with APPLIED NANOPARTICLES. S.L. A nanotech engineering company, Barcelona, Spain.

- **Active Participation** in an EU H2020 Project ´´HISENTS`` High level Integrated SEnsor for NanoToxicity Screening. Workpackage: Nanomaterials expert provider and advanced characterization Techniques.

VII. Appendix

"Where ignorance is our master, there is no

possibility of real peace”

Mahatma Gandhi Dalai Lama

Chapter 7

Appendix A: Extended Characterization for Chapter 2: Kinetically Controlled Seeded Growth One-Pot Synthesis of Monodisperse Silica: The Convivence of Two Growth Mechanism

A.1 Image analysis by STEM mode by SEM of SiO_2 NPs shown in figure 2.1: (A) Effect of the TEOS, (B) Effect of ammonia and (C) Effect of water concentration.

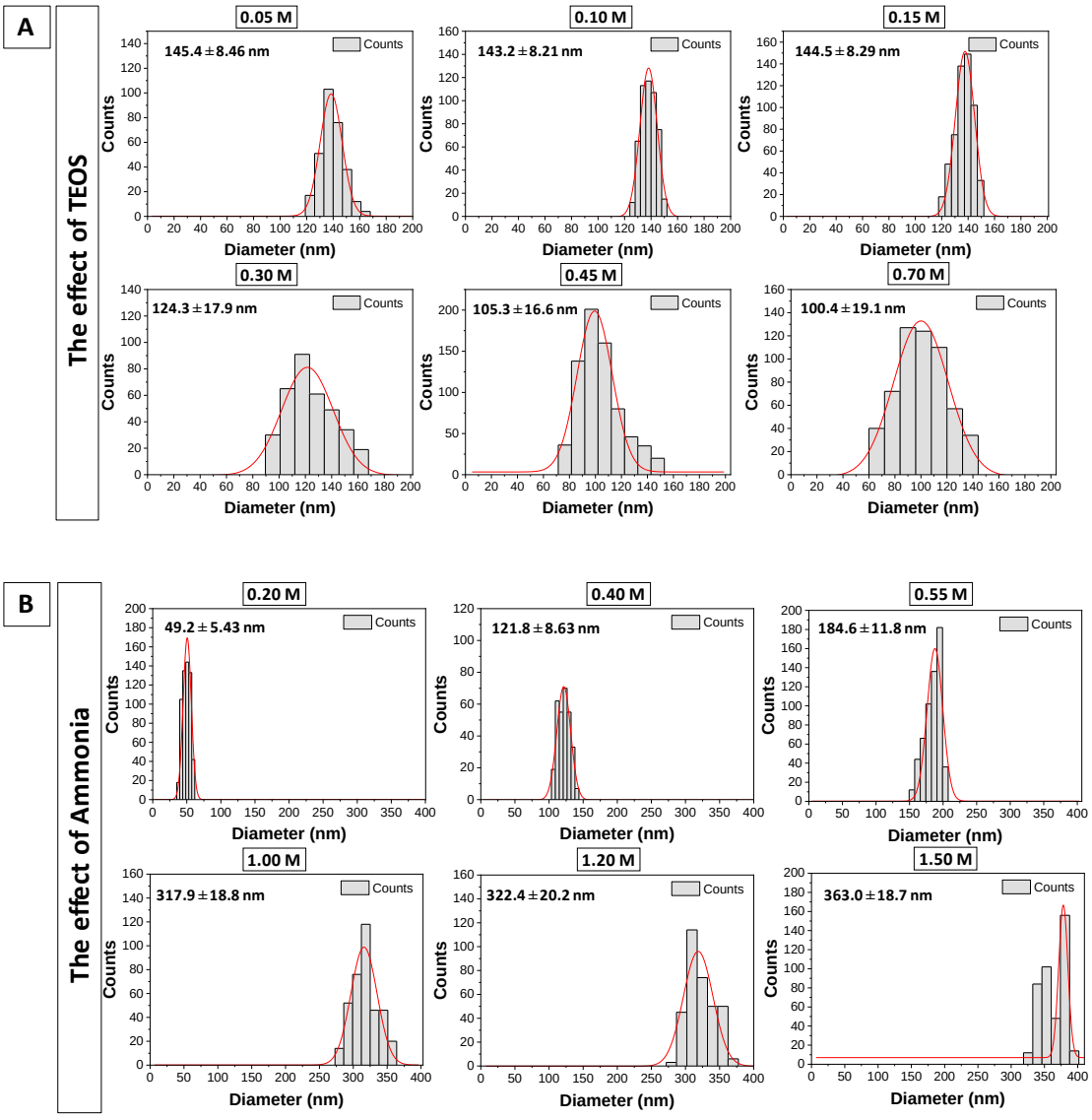

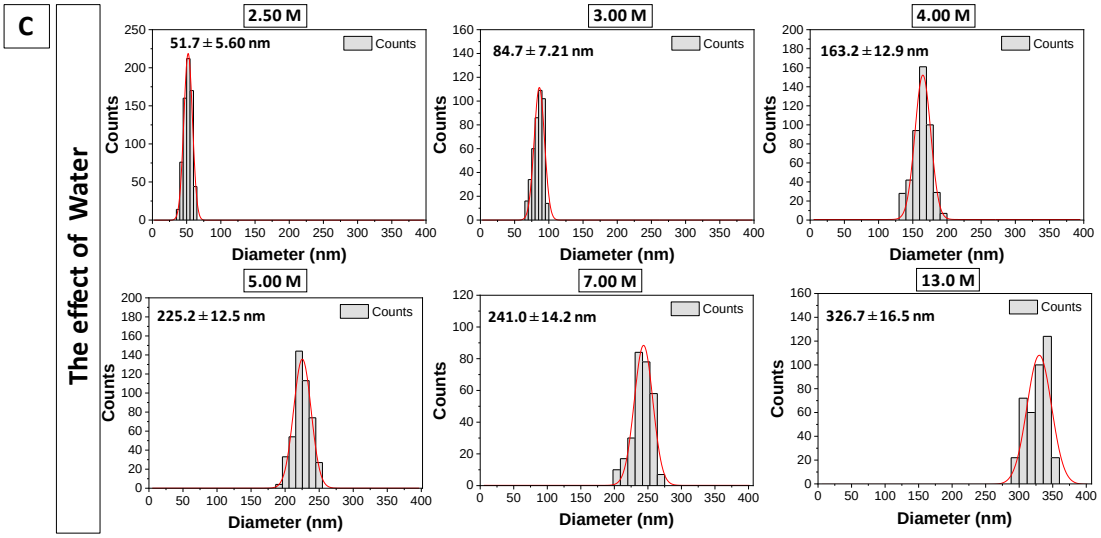

A.2 Image analysis by STEM mode by SEM of SiO_2 NPs shown in figure 2.2: (A) H_2O 2.00M, (B) H_2O 3.50M and (C) H_2O 5.00M concentration.

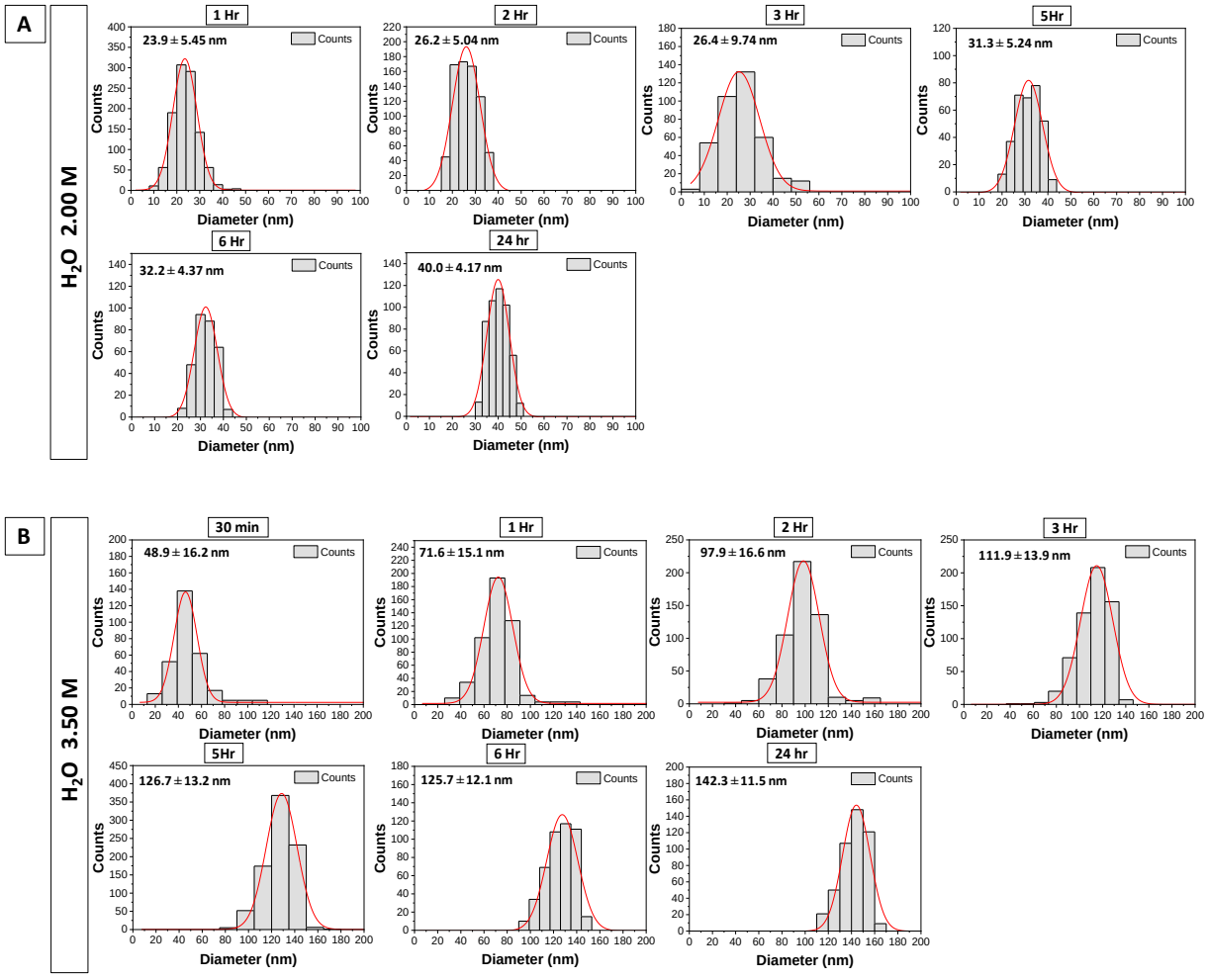

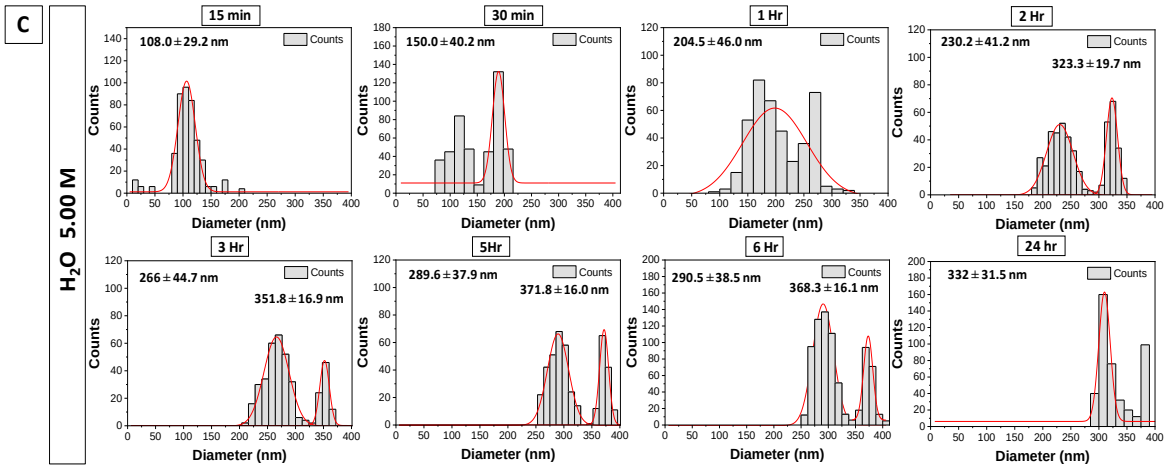

A.3 Calibration curve and UV-Vis spectrums of the measured monomer concentration in solution as a function of time by means of the silicomolybdic acid (SMA) spectrophotometric method at 400nm of SiO_2 NPs shown in figure 2.2: (A) UV-Vis spectrums of the calibration curve, (B) Calibration curve of the TEOS standards, (C) Image of the standard after exposed to the SMA method, (D) H_2O 2.00M, (E) H_2O 3.50M and (F) H_2O 5.00M concentration.

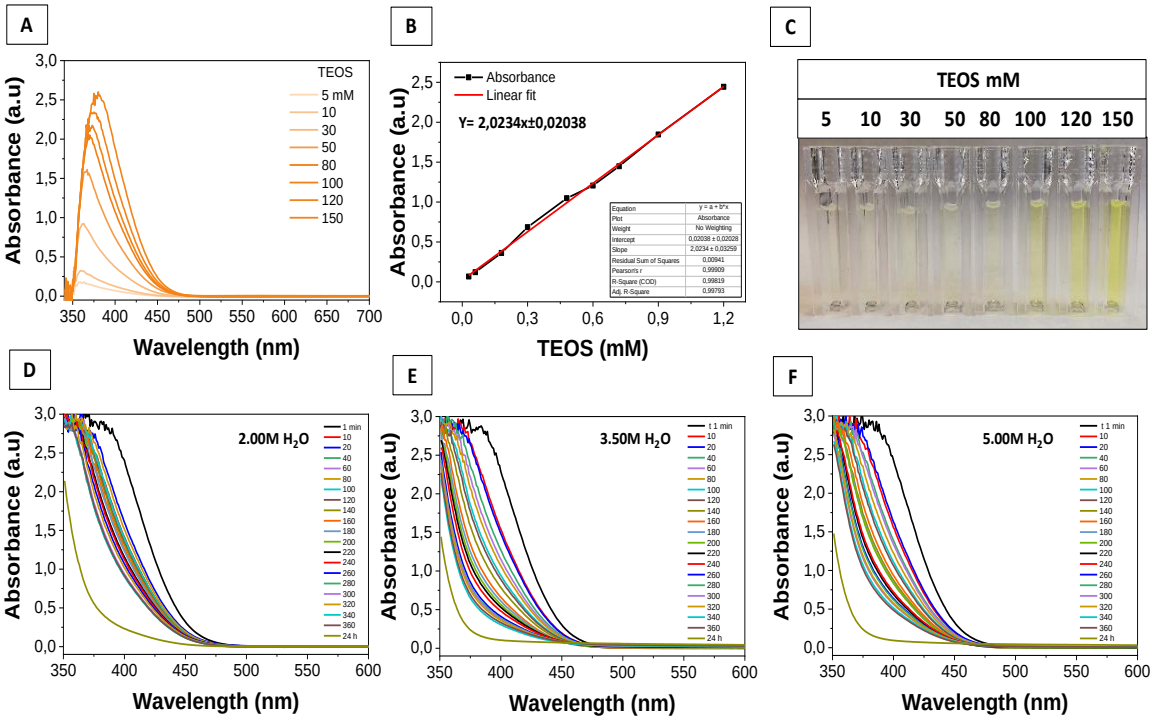

A.4 Summary of detailed experimental measurements of the temporal evolution profile of the colloidal SiO_2 particle formation by dynamic light scattering (DLS), measuring the zeta potential (mV), conductivity (mS/cm), Hydrodynamic size by number (nm) and number of particles (NPs/mL) as a function of time in the different water conditions (H_2O 2.00M, 3.50M, 5.00M) by adapting the Stöber method.

Table B.4.1 Summary of detailed experimental measurements for 2.00M H_2O

H_2O [M]	Time [min]	DLS Size * Number (nm)	±SD (nm)	ζ-potential * (nm)	±SD (mV)	Conductivity * (mS/cm)	±SD (mS/cm)	Particle Concentration* (NPs/mL)	±SD (NPs/mL)
2.00M	1	83,25	29,15	-8,45	4,463	0,02019	0,001	$6,978E^{10}$	$3,642E^{10}$
	10			-16,5	4,227	0,03188	0,002		
	25	110,4	43,13	-26,86	1,388	0,03558	0,001	$8,160E^{12}$	$1,11E^{12}$
	30			-30,12	2,698	0,03649	0,001	$1,624E^{13}$	$9,82E^{12}$
	40	27,69	0,645	-32,41	3,62	0,0378	0,003	$1,99E^{13}$	$2,62E^{12}$
	60	34,25	1,036	-35,41	4,87	0,03811	0,003	$2,371E^{13}$	$1,954E^{12}$
	80	37,8	1,036	-34,5	2,302	0,03811	0,001	$3,157E^{13}$	$2,943E^{11}$
	100	40,37	0,578	-34,1	0,9228	0,03818	0,001	$3,236E^{13}$	$5,694E^{10}$
	120	43,78	0,3462	-35,92	0,7829	0,03813	0,001	$3,195E^{13}$	$9,418E^{11}$
	140	45,13	0,7198	-39,33	1,069	0,03913	0,002	$2,613E^{13}$	$1,076E^{12}$
	160	46,07	0,4395	-39,84	1,4141	0,03957	0,002	$8,16E^{12}$	$1,11E^{12}$
	180	47,78	0,8434	-39,09	3,148	0,04005	0,001	$2,579E^{13}$	$1,794E^{12}$
	200	50,74	0,3792	-39,98	2,497	0,0397	0,002	$2,626E^{13}$	$7,15E^{11}$
	220	50,57	0,8578	-40,31	3,071	0,04143	0,003	$2,482E^{13}$	$2,172E^{12}$
	240	50,78	0,7318	-38,47	2,208	0,04169	0,001	$2,573E^{13}$	$1,288E^{12}$
	260	50,8	0,6117	-38,75	1,689	0,04196	0,003	$2,783E^{13}$	$2E1^{2}$
	280	51,44	0,6297	-38,7	1,999	0,04207	0,002	$2,805E^{13}$	$2,166E^{12}$
	300	53,82	1,122	-38,67	2,776	0,0436	0,001	$2,707E^{13}$	$1,932E^{12}$
	320			-38,6	1,58	0,04318	0,002	$3,219E^{13}$	$4,548E^{12}$
	1440	57,5	1,185	-36,53	2,186	0,04281	0,002	$2,579E^{13}$	$1,794E^{12}$

*Standard deviation mean from three independent measurements.

Table B.4.2 Summary of detailed experimental measurements for 3.50M H_2O

H_2O [M]	Time [min]	DLS Size * Number (nm)	±SD (nm)	ζ-potential * (nm)	±SD (mV)	Conductivity * (mS/cm)	±SD (mS/cm)	Particle Concentration* (NPs/mL)	±SD (NPs/mL)
3.50M	1	92,41	4,15	-17,24	3,212	0,02108	0,002	$5,418E^{9}$	$2,057E^{9}$
	5			-18,2	3,173	0,02567	0,001		
	10	110,5	18,29	-23,04	3,89	0,02963	0,003		
	20	47,68	32,9	-28,29	1,556	0,03499	0,002	$4,004E^{11}$	$3,38E^{11}$
	30	51,48	29,12	-31,62	2,29	0,0371	0,001	$4,52E^{11}$	$3,711E^{11}$
	40	86,02	3,584	-32,89	0,5228	0,03727	0,003	$6,02E1^{1}$	$1,798E^{11}$
	60	96,97	0,857	-33,72	1,405	0,0372	0,002	$7,933E^{11}$	$1,88E^{10}$
	80	97,31	0,05349	-34,13	3,851	0,03634	0,001	$1,166E^{12}$	$5,34E^{10}$
	100	105,9	0,7971					$2,65E1^{2}$	2,42E11
	120	104	1,103	-38,2	1,052	0,03798	0,003	$2,413E^{12}$	$1,88E^{11}$
	140	102,3	1,774	-35,68	1,728	0,0364	0,002	$2,66E^{12}$	$7,71E^{10}$

	160	107,5	1,863	-36,69	1,439	0,03782	0,001	$2,47E^{12}$	1,605E11
	180			-36,11	1,894	0,03811	0,003		
	200	108,9	2,633	-36,96	5,194	0,0385	0,002	$2,78E^{12}$	$2,611E^{10}$
	220	109,4	3,104	-34,18	1,557	0,04046	0,001	$2,839E^{12}$	$5,288E^{11}$
	240	114,2	4,896	-34,05	3,381	0,04194	0,003	$2,959E^{12}$	$7,622E^{11}$
	260	116,6	2,507	-37,9	2,409	0,04345	0,001	$2,427E^{12}$	$3,305E^{11}$
	280			-36,4	1,824	0,04133	0,003		
	300	118,1	2,018	-36,41	3,529	0,0431	0,001	$2,46E^{12}$	$2,476E^{11}$
	320			-38,2	2,69	0,04059	0,002		
	340			-36,89	1,146	0,04224	0,001		
	360			-37,36	2,079	0,04255	0,003		
	1440	127,2	0,7233	-36,8	1,564	0,03952	0,002	$2,176E^{12}$	$4,042E^{10}$

*Standard deviation mean from three independent measurements.

Table B.4.3 Summary of detailed experimental measurements for 5.00M H_2O

H_2O [M]	**Time [min]**	**DLS Size * Number (nm)**	**±SD (nm)**	**ζ-potential * (nm)**	**±SD (mV)**	**Conductivity * (mS/cm)**	**±SD (mS/cm)**	**Particle Concentration* (NPs/mL)**	**±SD (NPs/mL)**
5.00M	1	184,6	65,1	-24,56	3,059	0,01902	0,001	$3,01E^{8}$	$3,103E^{8}$
	5			-24,42	1,594	0,03005	0,003		
	10	206,2	2,46	-31,11	2,636	0,03461	0,001	$2,349E^{10}$	$1,035E^{10}$
	20	217,8	7,948	-32,77	1,424	0,03706	0,002	$5,744E^{10}$	$1,225E^{10}$
	30	228,6	7,95	-32,87	4,3	0,03755	0,002	$1,127E^{11}$	$1,779E^{10}$
	40	232,2	1,04	-34,55	0,7801	0,03813	0,001	$1,662E^{11}$	$2,059E^{10}$
	60	258,4	14,83	-34,37	0,6485	0,03825	0,003	$1,908E^{11}$	$1,992E^{10}$
	80	312,4	6,365	-32,23	2,996	0,03811	0,001	$2,632E^{11}$	$2,04E^{11}$
	100	362	3,547	-33,6	3,815	0,03599	0,002	$3,161E^{11}$	$2,347E^{10}$
	120	379,5	7,944	-32,22	2,059	0,03554	0,002	$2,85E^{11}$	$1,156E^{11}$
	140	382,2	5,437	-31,7	5,252	0,03591	0,001	$2,388E^{11}$	$9,044E^{10}$
	160	395,6	8,591	-31,56	3,441	0,03609	0,003	$2,19E^{11}$	$1,369E^{11}$
	180	390	11,54	-31,39	3,07	0,03603	0,001	$1,422E^{11}$	$1,0154E^{11}$
	200	403,1	2,05	-32,02	1,358	0,03598	0,002	$1,683E^{11}$	$9,287E^{10}$
	220	401	1,1044	-35,43	0,7	0,03612	0,002	$1,489E^{11}$	$1,045E^{11}$
	240	402,9	2,014	-36,89	1,931	0,03466	0,001	$9,414E^{11}$	$9,414E^{10}$
	260	404,6	8,383	-42,25	2,046	0,03557	0,003	$9,447E^{10}$	$9,947E^{10}$
	280	408,2	1,046	-40,82	2,697	0,03655	0,001	$1,60E^{11}$	$1,6E^{11}$
	300	405,8	4,184	-41,41	0,87	0,03614	0,002	$1,506E^{11}$	$1,509E^{11}$
	320			-43,05	2,122	0,03609	0,003		
	340			-42,13	2,014	0,03695	0,002		
	1440	418,5	8,703	-42,21	2,15	0,03802	0,002	$2,28E^{11}$	$2,285E^{11}$

*Standard deviation mean from three independent measurements.

A.5 Image analysis by STEM mode by SEM of SiO_2 NPs shown in figure 2.5., adding a fixed amount of water at certain intervals.

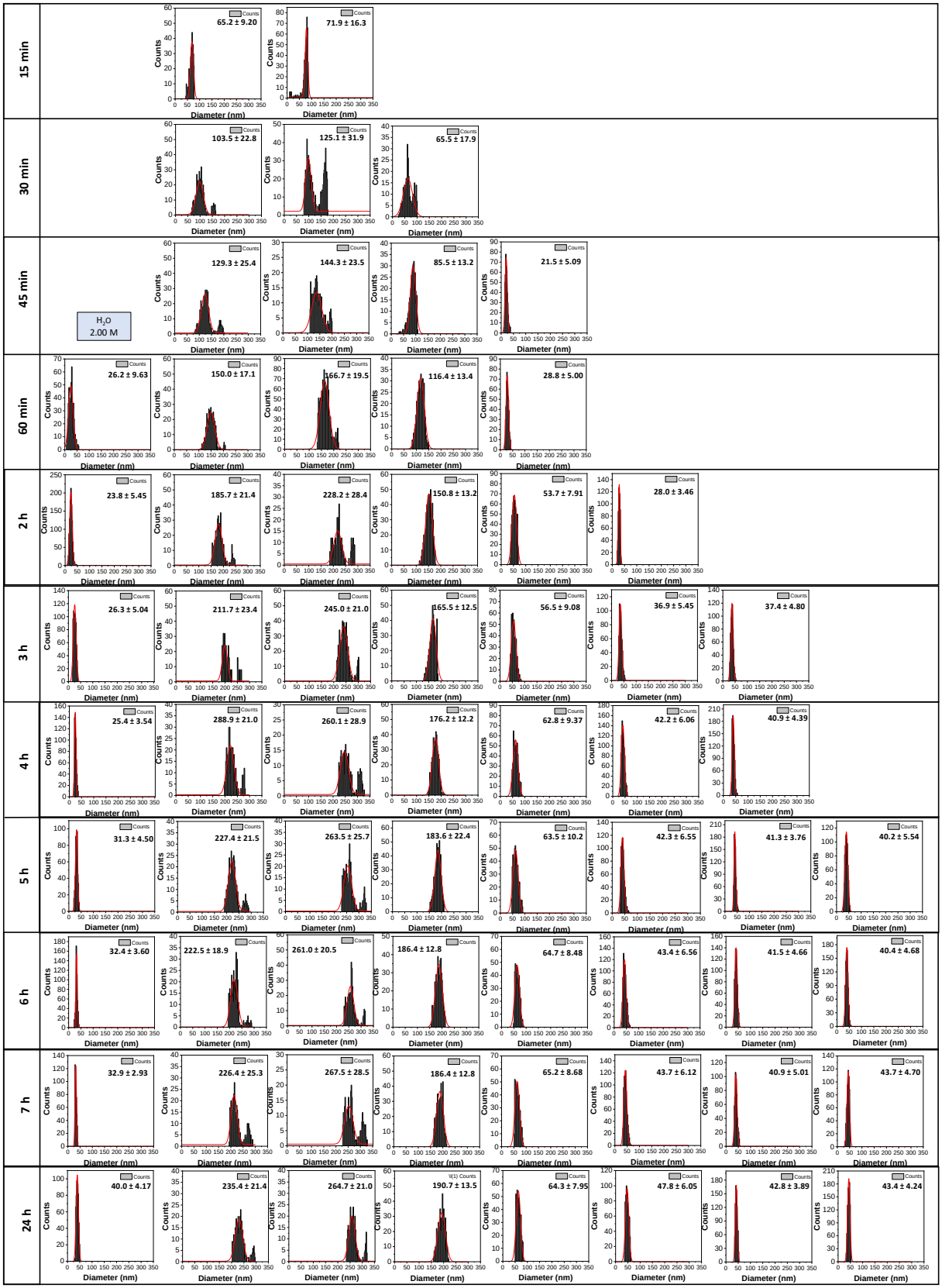

A.6 Image analysis by STEM mode of SiO_2 NPs shown in figure 2.7. increasing NaCl concentration

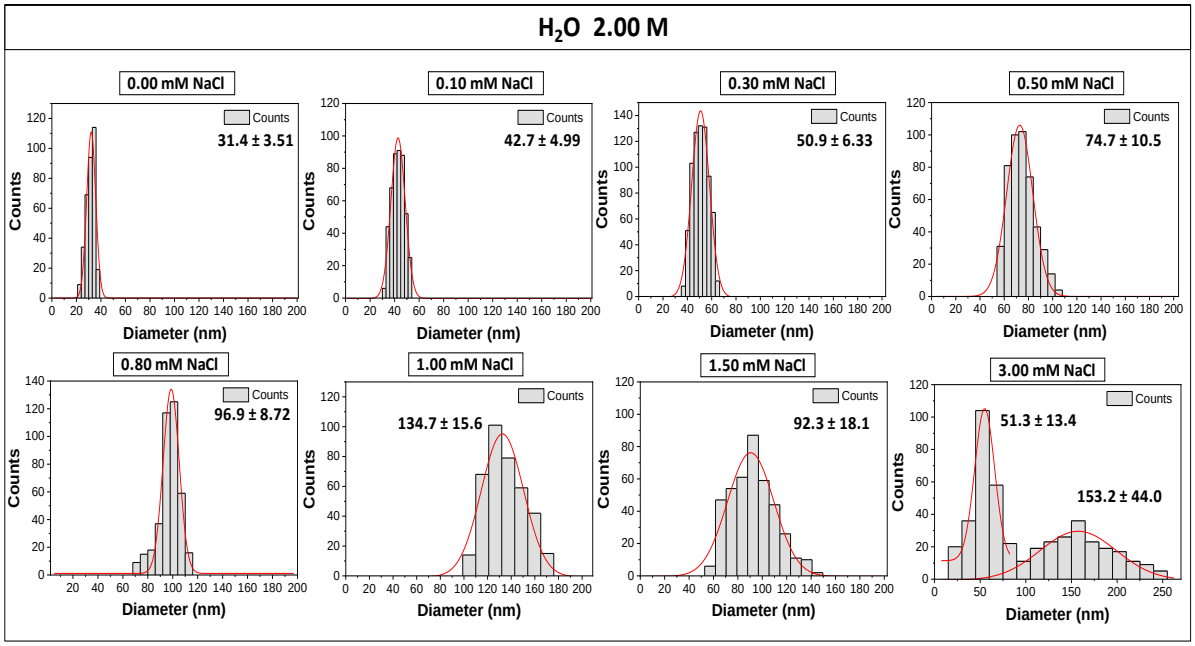

A.7 Calculations for the theoretical size evolution of the SiO_2 NPs by plotting an atom by atom growth model in which the concentration of [NPs] was maintained constant.

First, using the DLS hydrodynamic size values (nm) by number (raw data un appendix B4), the measured mineralized monomer (mg Si/mL) done in the (appendix B3) and the SiO_2 colloidal particles reported density (2.1 to 2.3 g/cm^3), we calculated the theoretical concentration of particles (NPs/mL) as a function of time, using the following formulas as follows:

$$\rho = \frac{M_{NP}}{V_{NP}} = \frac{\frac{M_{Mineralized}}{[NPs]}}{V_{NP}} \qquad V_{NP} = \frac{4}{3}\pi r^3$$

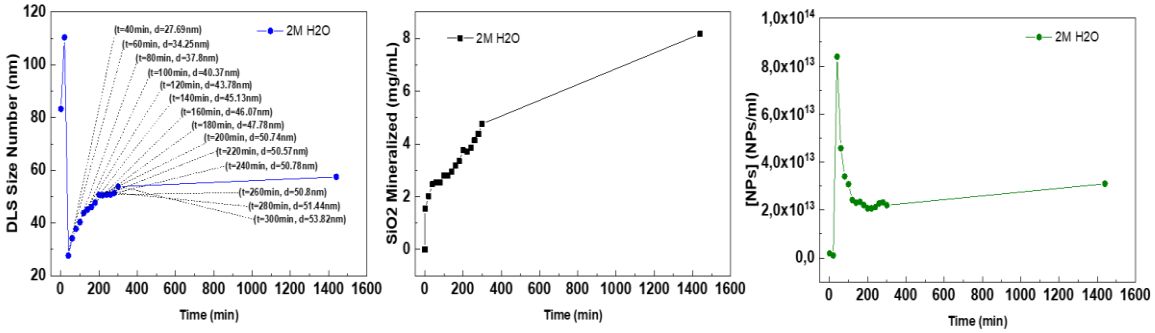

Once we found the calculated theoretical concentration of NPs/mL for every time point, using the same approach, we calculated the theoretical size of the NPs by assuming and homogeneous growth (atom by atom) for very time point while maintaining the number of NPs constant, using the concentration of the remaining monomer in solution, as follows:

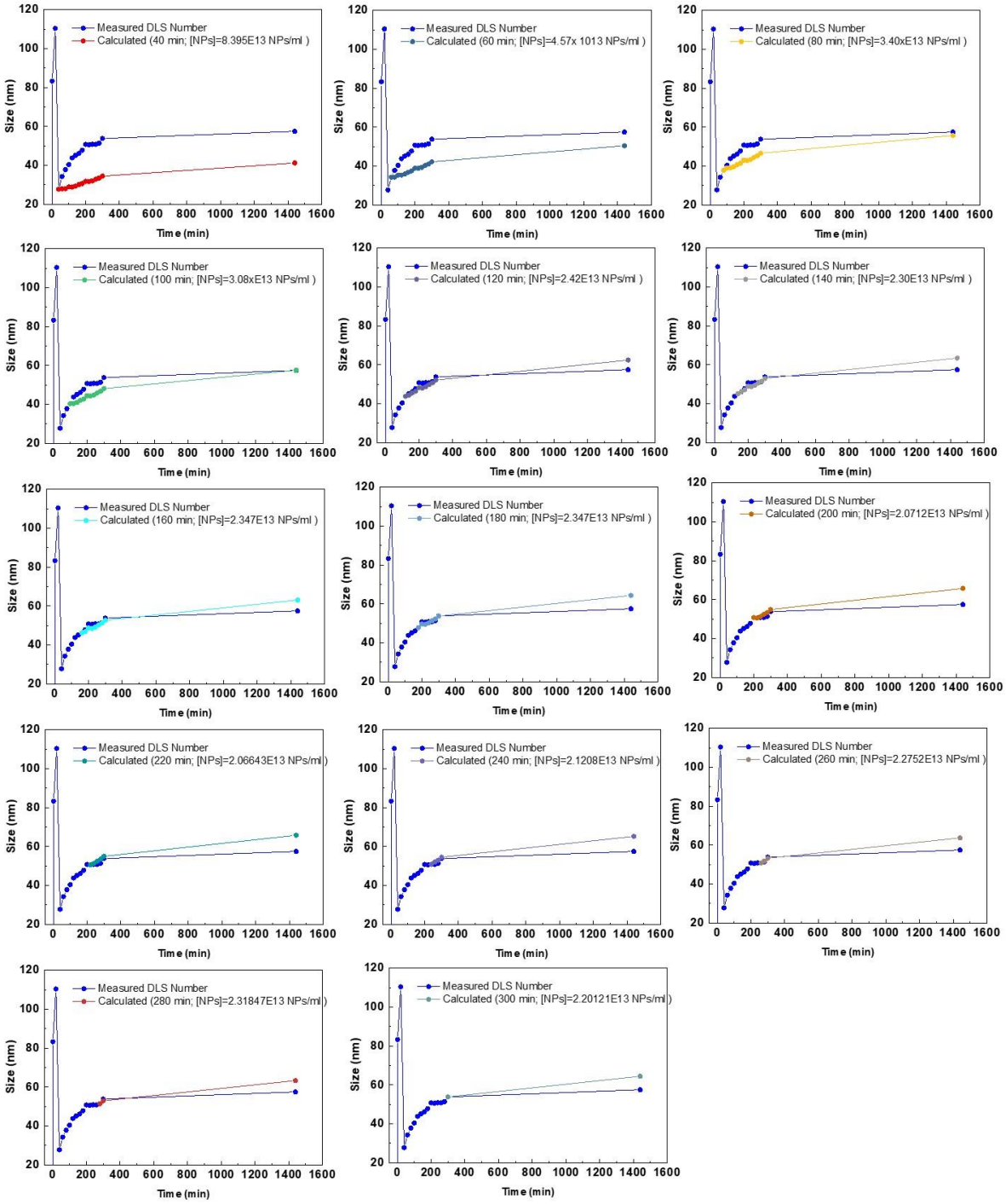

As can be observed, the size evolution of the silica NPs following a monomer-addition model for the 2.00M of water can be calculated. It can be seen, that from 100 to 140 minutes, the growth of the NPs followed the same trend, suggesting that from this point, the silica NPs growth atom by atom. The same calculations were applied for the 3.50M and 5.00M of water concentration.

A.8 Image analysis by STEM mode by SEM of SiO_2 NPs shown in figure 2.9., revealing the precise size control with the scalar addition of water

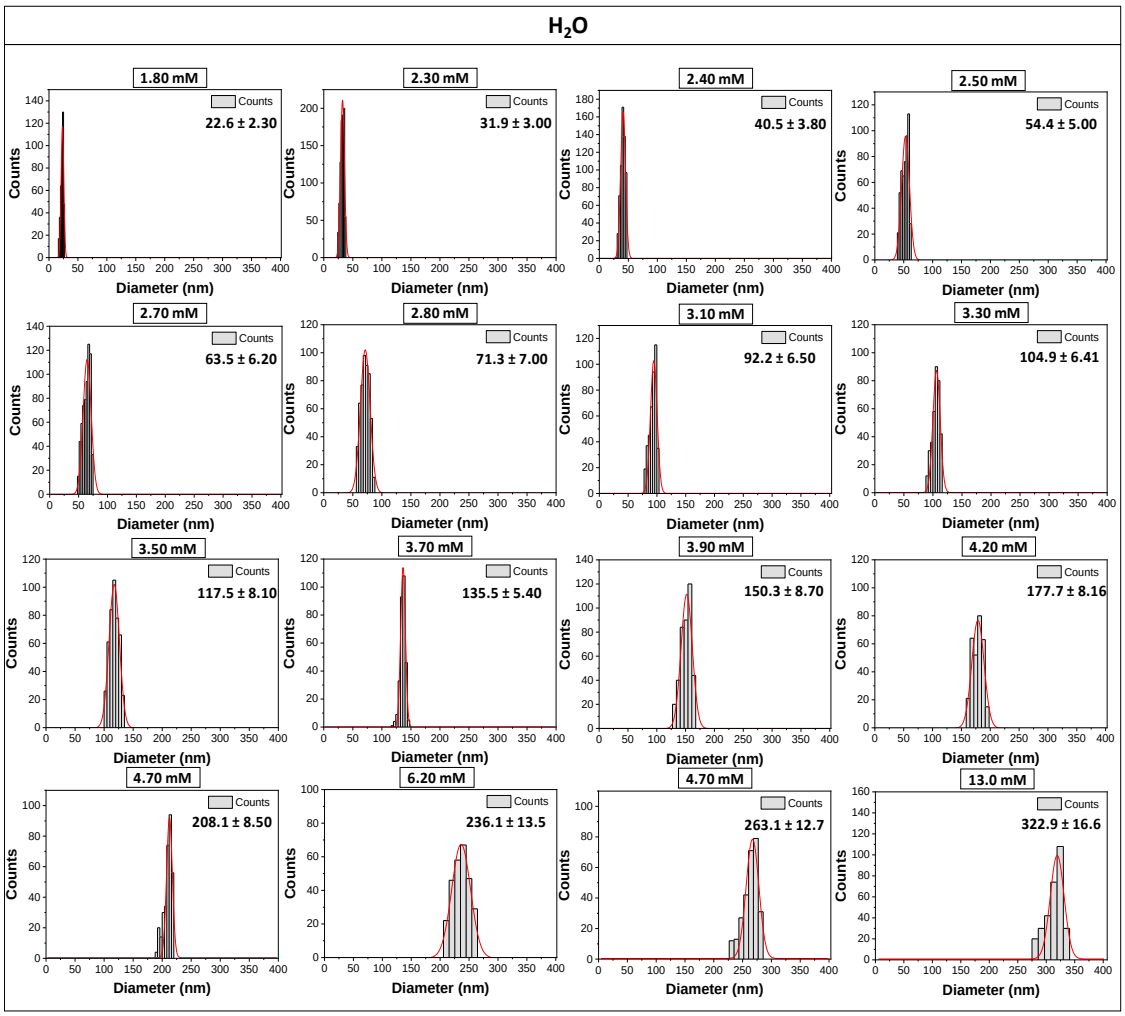

Appendix B: Extended Characterization for Chapter 3: Synthetic Strategy for Preparing Silica-Based Nanoparticles with Functional Properties for Biological Imaging

B.1 Reaction of the Ninhydrin essay with the amino groups on the nanoparticle surface

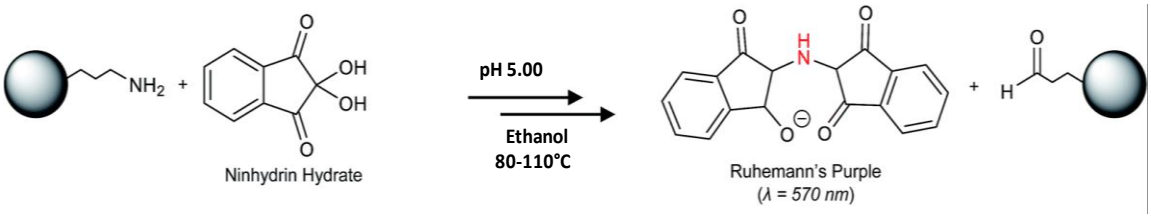

The degree of amine grafting on the surface of aminated-silica nanoparticles (SiO2-NH2) was determined by using the ninhydrin assay. The ninhydrin react with the primary or secondary amines of the nanoparticles yielding a bright purple complex known as Ruhemann´s purple that is determined at 570nm

C.2 Mechanism of reaction of the Ninhydrin essay with the amino groups

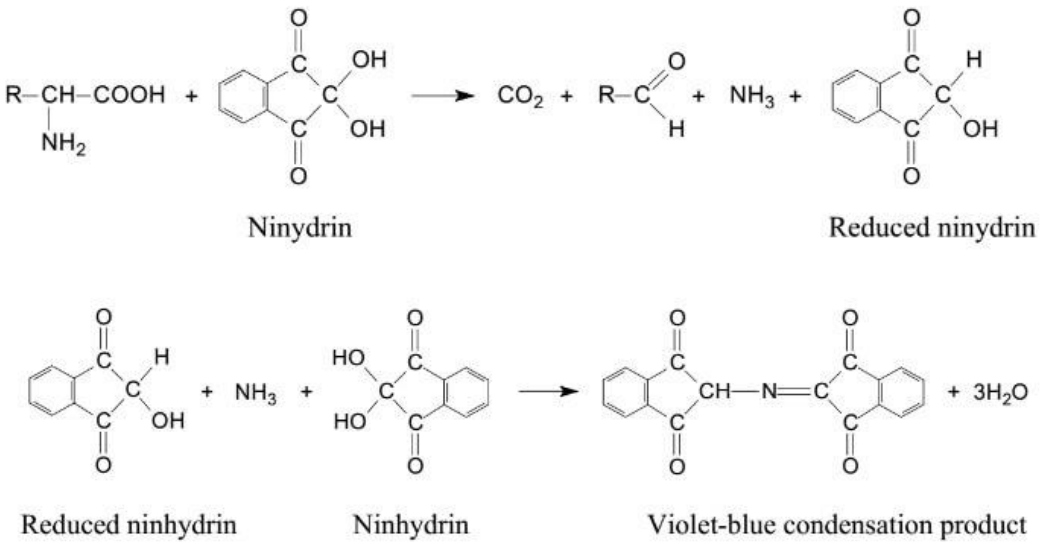

The ninhydrin reaction is basically a is a redox reaction, in which the ninhydrin acts as an oxidizing agent, getting reduced. Ninhydrin reacts with the amino group of the free amino acid in the test sample and oxidizes the compound, leading to delamination. In this reaction, two gasses get released. These are ammonia (NH_3) and carbon dioxide (CO_2). Besides the gasses, we obtain an aldehyde and hydrindantin, which is formed by the

reduction of ninhydrin. Now, the released ammonia further reacts with the ninhydrin giving rise to di-ketohydrin, which forms a coloured complex. This coloured complex is what we call Ruhemann's purple, and this gives our solution the deep blue colouration. This process is the ninhydrin test mechanism [1].

B.3 Calculations of the number of amino groups of the amino surface functionalized 50nm SiO_2 NPs.

The molar quantity of amine (mM) grafting on the surface of amino-silica NPs based on the weight of particles were calculated:

Table C3. Summary of the amino quantification

APTES (mM)	ZETA POTENTIAL (mV at pH 7.00)	ABSORBANCE At 577nm	mM APTES from c. curve	QAM[a] (molecules NH_2)	AMSA (NH_2/nm^2)[c]
0.35	-29.6 ± 1.5	0.423	0.305	$4.59x10^{17}$	1.50
0.76	-19.0 ± 2.6	0.459	0.324	$4.88x10^{17}$	1.60
1.08	-9.41 ± 0.8	0.556	0.375	$5.65x10^{17}$	1.85
1.45	2.81 ± 0.4	0.659	0.429	$6.68x10^{17}$	2.19
4.35	11.4 ± 1.6	0.808	0.507	$7.63x10^{17}$	2.50
7.25	19.6 ± 2.0	1.153	0.689	$1.04x10^{18}$	3.41
11.5	19.2 ± 0.9	1.489	0.865	$1.30x10^{18}$	4.26
14.5	21.7 ± 1.6	1.497	0.868	$1.31x10^{18}$	4.29

Where:

-Calibration curve from **figure 3.5**, Chapter 3, from main text is Y=1.90708X-0.15795

- [a] QAM = Quantity of amino NH_2 molecules in the solution were determined by interpolating from the calibration curve the measured absorbance of each aminated-silica NPs and converting from mM of APTES to mM of amino molecules (NH_2) by stoichiometry. (2.5mL of solution were used for analysis and Avogrados´s constant $6.023x10^{23}$ molecules).
- SA = The total surface area were calculated using the mass concentration of the aminated-silica nanoparticles used for the analysis (~5mg of SiO_2–NH_2 in 2.5mL of solvent= 2mg SiO_2/mL), the radius of the analyzed nanoparticle calculated for electron microscopy TEM

(diameter size of ~50 nm) and the density of colloidal silica (1.96 g/cm^3) [2]. SA=1.22x10^{17} nm^2 /mL or 3.05x10^{17} nm^2.

- [C] AMSA = The number of amine molecules per surface area (NH_2 molecule/nm^2) of the aminated-silica nanoparticles were calculated dividing the quantity of amino NH_2 molecules in solution (QAM) by total surface area (SA)

Calculations for silica nanoparticles (SiO_2 NPs) concentration

In order to calculate the number of nanoparticles per milliliter in each colloidal silica solution synthetized, first, the size diameter was calculated experimentally from the size distribution measured by STEM, assuming that 90% of the silicate precursor (TEOS) injected is consumed during the reaction (confirmed several times in Chapter 2 by yield reaction calculation) and the particles are spherical in shape (confirmed by STEM characterization). The procedure is then reduced to Equation 1:

$$\text{SiO2}[NP/\text{mL}] = [\text{SiO2}] / \vec{V}_{\text{NP}} \cdot \rho \cdot 1/MW \qquad \text{Equation 1}$$

Where [SiO2] is the concentration of silica added to the solution in moles per mL (1.02mL of TEOS used for synthesis stoichiometrically are 0.00434 moles of SiO2, 90% yield and 32.2 mL of total volume synthesis), MW and ρ are the molecular weight (60.09 g/mol) and density (1.96x10^{-21}g/nm^3) for colloidal silica, and $\vec{V}_{\text{NP}}$ is the volume occupied for NP in nm^3, calculated using the sphere volume formula ($4/3\pi r^3$), in which diameter were calculated by TEM mean size.

B.4 Extended characterization of the FITC core-doped SiO_2 NPs

Table B4.1. Summary of the Characterization

APTES-FITC (mL)	pH	Z-potential (mV)	DLS by number (nm)	PdI	SEM Size (nm)	SD (%)
1	8.01	-35.0 ± 0.5	43.4 ± 0.3	0,154	38.9 ±3.7	12.7
5	8.16	-32.9 ± 0.3	59.3 ± 2.3	0,126	36.6 ±4.5	13.7
10	7.95	-33.6 ± 1.4	61.0 ± 7.9	0,104	38.2 ±4.2	11.4
15	8.05	-31.2 ± 2.0	66.4 ± 4.9	0,159	40.1 ±4.4	12.8
20	8.22	-34.4 ± 0.2	64.9 ± 8.5	0,169	40.5 ± 5.7	14.1
30	8.79	-36.8 ± 1.4	67.5 ± 8.5	0,189	41.4 ± 5.8	11.0

Image analysis by STEM mode by SEM of SiO_2 NPs

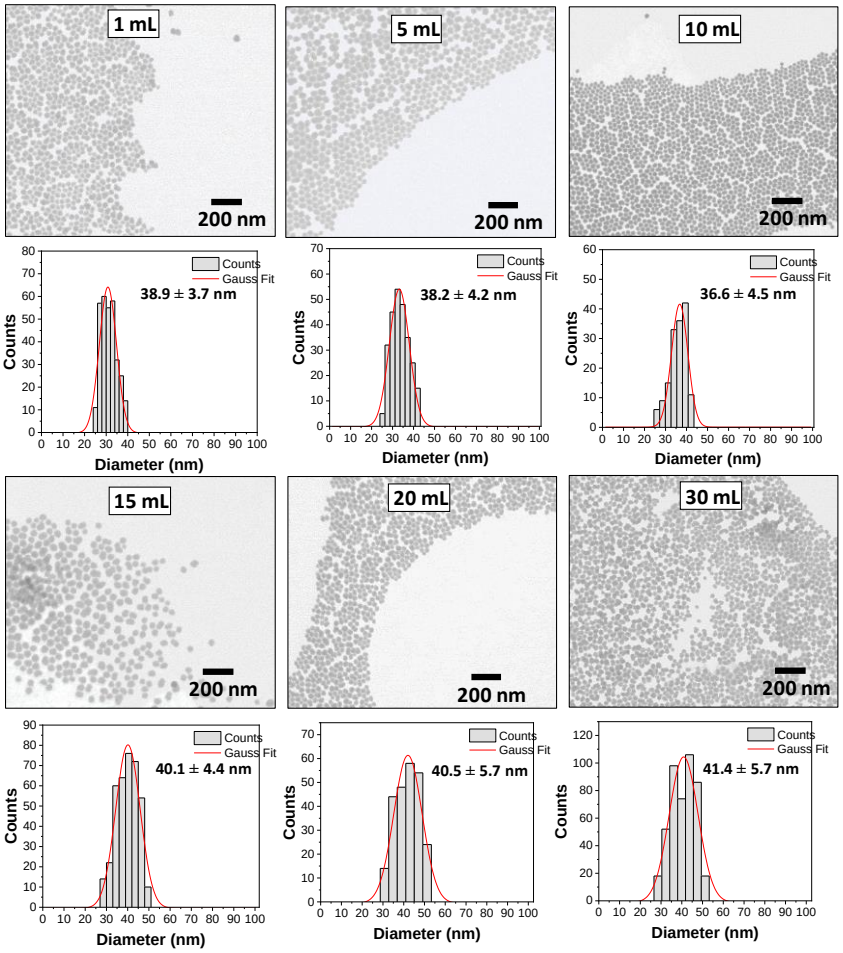

B.5 Extended characterization of the core-doped SiO_2 NPs with RBITC, TRITC and AF350

RBITC core-doped SiO2 NPs

Table B5.1 Summary of the Characterization SiO_2 NPs with RBITC

APTES-RBITC (mL)	pH	Z-potential (mV)	DLS by number (nm)	PdI	SEM Size (nm)	SD (%)
1	8.12	-43.4 ± 1.4	46.8 ± 2.6	0.065	48.0 ± 4.7	9.75
3	8.20	-41.7 ± 2.7	48.6 ± 0.8	0.077	46.8 ± 6.4	13.5
5	8.06	-43.3 ± 2.7	46.8 ± 2.6	0.104	47.6 ± 6.2	12.9
8	8.32	-41.0 ± 3.2	51.9 ± 2.0	0.119	51.5 ± 7.9	15.3
10	8.19	-49.6 ± 2.4	55.3 ± 7.8	0.111	52.4 ± 8.7	16.7
15	8.41	-50.5 ± 1.1	51.7 ± 3.3	0.205	53.2 ± 7.0	13.1

Image analysis by STEM mode by SEM of SiO_2 NPs

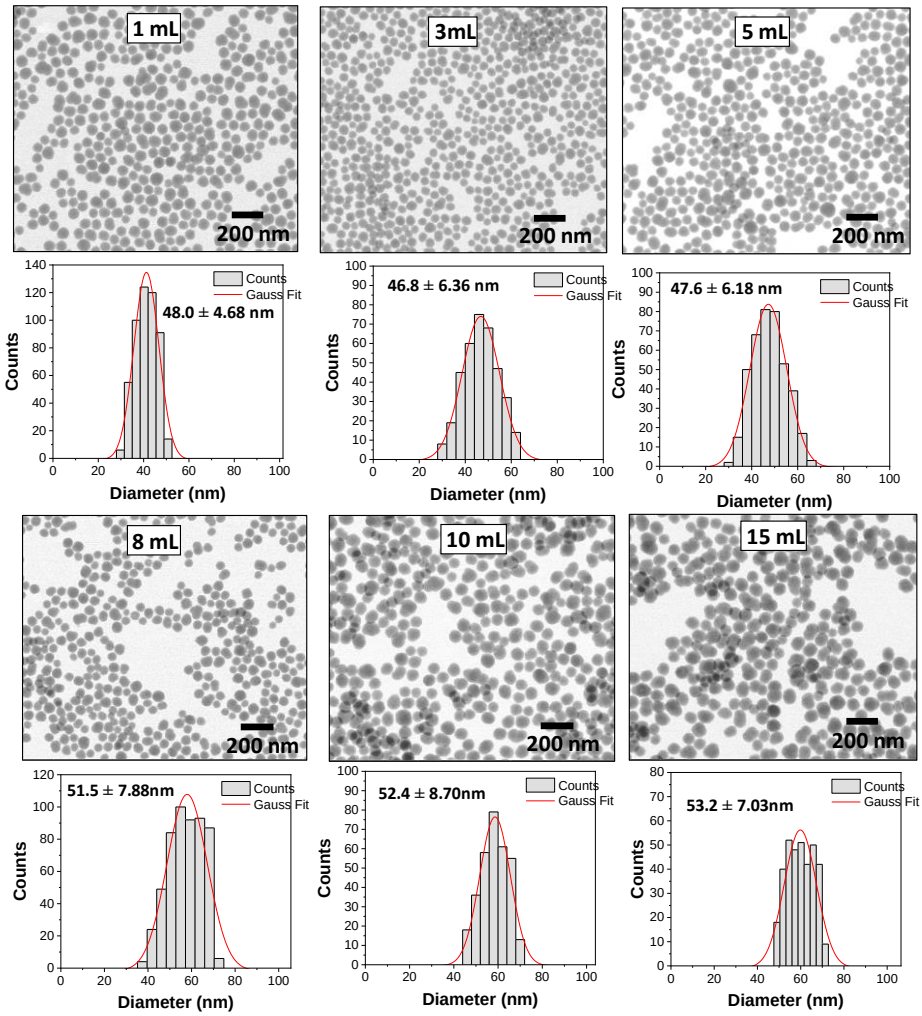

TRITC core-doped SiO_2 NPs

Table B5.2 Summary of the Characterization SiO_2 NPs with TRITC

APTES-TRITC (mL)	pH	Z-potential (mV)	DLS by number (nm)	PdI	SEM Size (nm)	SD (%)
1	8.35	-41.3 ± 1.6	46.7 ± 1.68	0.074	40.9 ± 5.3	12.9
3	8.04	-36.3 ± 4.2	47.9 ± 3.08	0.093	42.6 ± 5.2	12.2
5	8.20	-46.0 ± 3.2	44.9 ± 0.88	0.080	41.7 ± 5.0	12.0
8	8.17	-38.7 ± 0.9	44.2 ± 3.51	0.085	43.6 ± 4.6	10.6
10	8.36	-41.5 ± 2.1	42.4 ± 4.31	0.136	43.7 ± 4.9	11.3

Image analysis by STEM mode by SEM of SiO_2 NPs

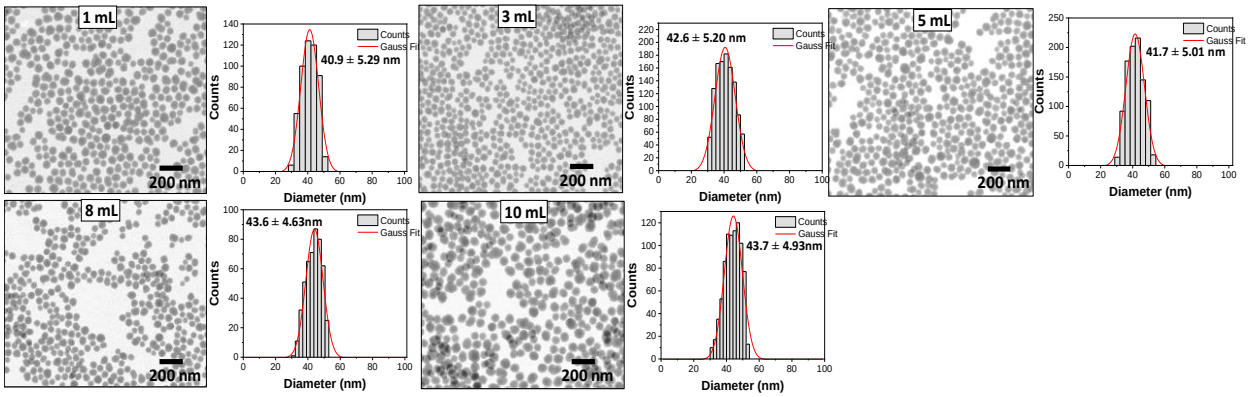

AF350 core-doped SiO_2 NPs

Table B5.3 Summary of the Characterization SiO_2 NPs with AF350

APTES-AF350 (mL)	pH	Z-potential (mV)	DLS by number (nm)	PdI	SEM Size (nm)[b]	SD (%)
1	8.25	-41.2 ± 3.46	37.5 ± 0.62	0.126	36.6 ± 4.10	11.2
3	8.36	-48.2 ± 0.83	34.8 ± 0.64	0.111	37.9 ± 4.76	12.5
5	7.88	-41.0 ± 0.31	37.2 ± 1.04	0.090	35.8 ± 4.64	12.9
8	8.12	-42.9 ± 4.55	32.7 ± 1.97	0.100	36.8 ± 4.54	12.3
10	8.75	-41.6 ± 8.25	35.4 ± 1.36	0.105	38.5 ± 4.08	10.6

Image analysis by STEM mode by SEM of SiO_2 NPs

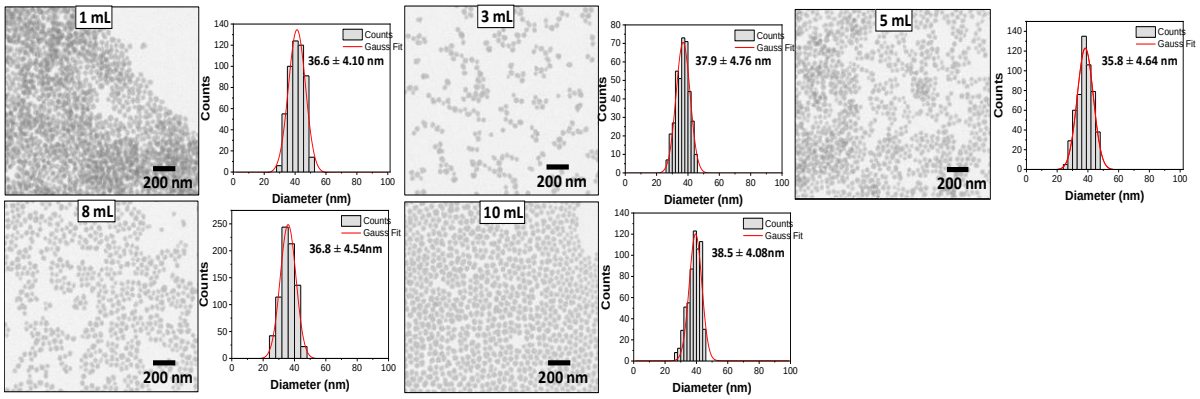

B.6 Extended characterization of the samples S1-S6 for the dual-emission SiO_2 NPs using different concentrations of APTES-RBITC/FITC and APTES-RBITC and APTES-AF350

Table B6.1 Summary of the Characterization SiO_2 NPs with APTES-RBITC(0.2mM)/FITC(1.8mM)

APTES-Dye	APTES-Dye (mL)	pH	Z-potential (mV)	DLS by number (nm)	PdI	SEM Size (nm)	SD (%)
S1	1	8.12	-45.7 ± 1.1	36.3 ± 0.4	0.065	39.8 ± 4.4	11.0
S2	3	8.48	-47.7 ± 2.1	43.5 ± 3.4	0.083	40.7 ± 5.3	13.0
S3	5	8.63	-37.5 ± 0.5	45.4 ± 2.3	0.062	40.0 ± 5.1	12.8

Table B6.2 Summary of the Characterization SiO_2 NPs with APTES-RBITC (0.24mM)/APTES-FTIC AF350(0.24mM)

APTES-Dye	APTES-AF350 (mL)	APTES-AF35 (mL)	pH	Z-potential (mV)	DLS by number (nm)	PdI	SEM Size (nm)	SD (%)
S4	5	5	8.58	-47.1 ± 0.8	36.6 ± 1.3	0.129	37.4 ± 4.9	12.9
S5	8	2	8.63	-52.9 ± 2.2	35.9 ± 1.9	0.135	32.7 ± 4.6	14.1
S6	9	1	8.15	-42.3 ± 1.4	34.6 ± 1.4	0.125	34.7 ± 4.8	13.7

Image analysis by STEM mode by SEM of SiO_2 NPs

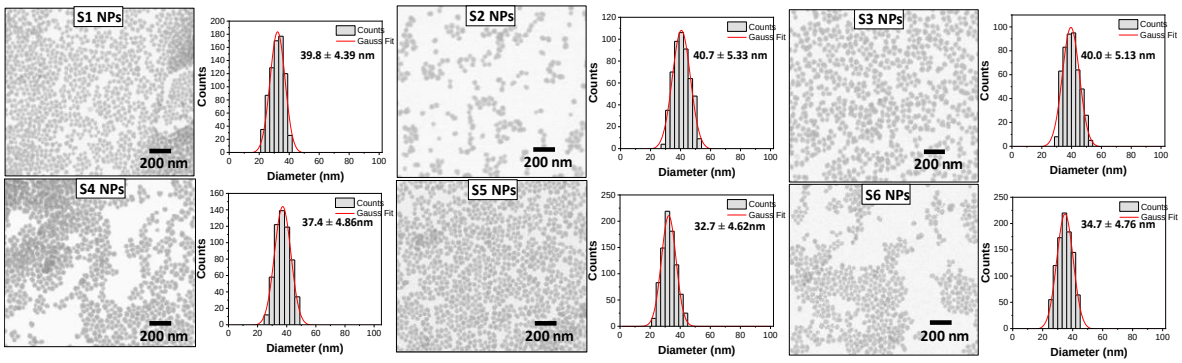

B.7 Extended characterization of the dual-emission core-shell SiO_2-RBITC@FITC@SiO_2 NP using a multi-step modified Stöber method.

Quantification of the RBITC and FITC concentration loaded in the dual-emission SiO_2 NPs, showed in on **figure 3.14** of the main text. (A)-(B) Fluorescence spectrum at different concentration using standard FITC and RBITC in water at neutral pH, recording the photoluminescence signal at excitation wavelength (Ex=490nm FTIC, Ex=550nm RBITC) of their respective emission maximum intensity (Em=525nm FTIC, Em=580nm RBITC). Calibration curve was built using the maximum fluorescence intensity of FITC and RBITC.

The concentration of the loaded dyes Were calculated measuring the difference in fluorescence between the dye added for the synthesis and the remaining dye in the supernatant. Thus, the concentration of RBITC added of the synthesis were 0.070mM and the calculated inside the NPs was 0.011 mM (15.7% of loaded yield) and for FITC, the concentration added during the synthesis were 0.050mM and the calculated was 0.0064mM (12.8% of yield).

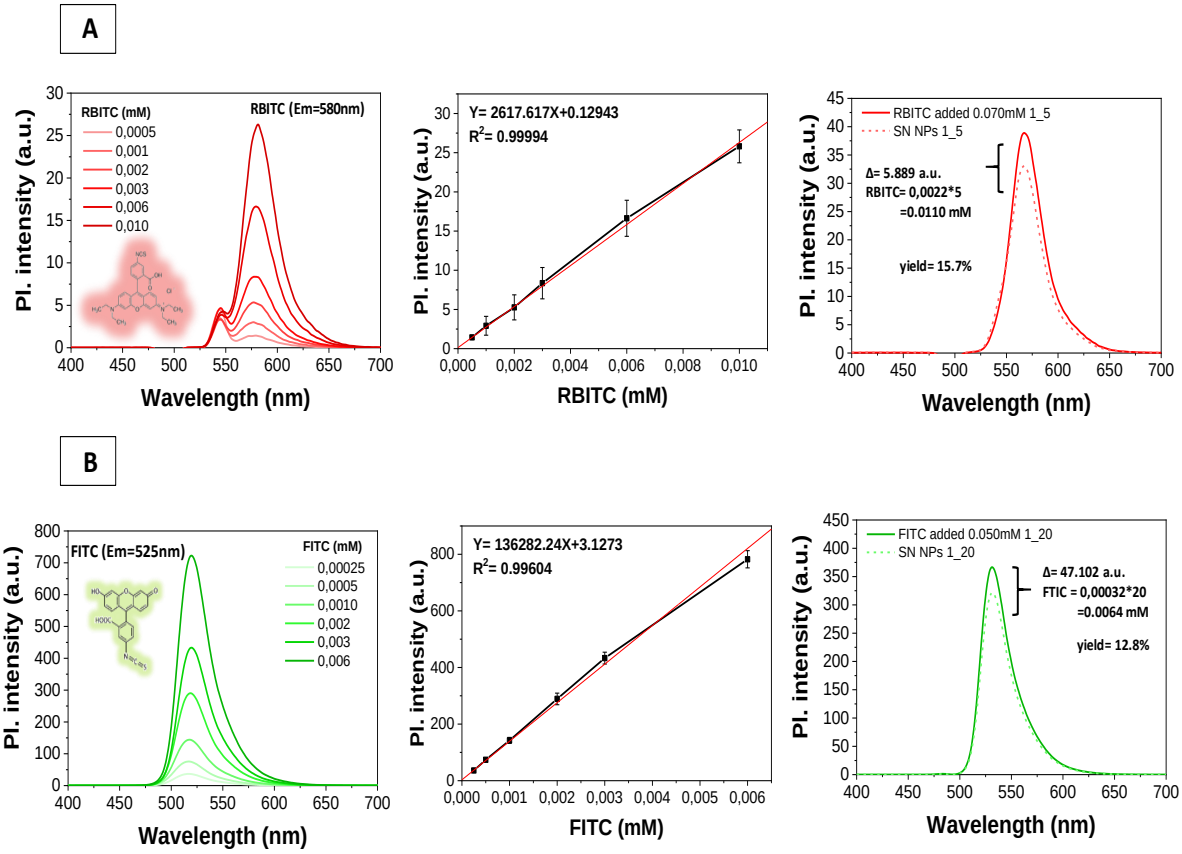

B.8 Extended characterization of the dissolution behaviour of the dual-emission core-shell SiO_2-RBITC@FITC@SiO_2 NPs using a multi-step modified Stöber method.

Quantification of the released dyes RBITC and FITC concentration inside the dual-doped NPs on Figure 3.15-3.16 of the main text. (A)-(B) Fluorescence spectrum of the SiO_2-RBITC@FITC@SiO_2 NPs and their supernatants at different times after dissolution, recording the photoluminescence signal at excitation wavelength (Ex=490nm FTIC, Ex=550nm RBITC) of their respective emission maximum intensity (Em=525nm FTIC, Em=580nm RBITC). (C)The Calibration curve used for dye calculations were showed in C7, for determine the concentration of the dyes in the supernatant.

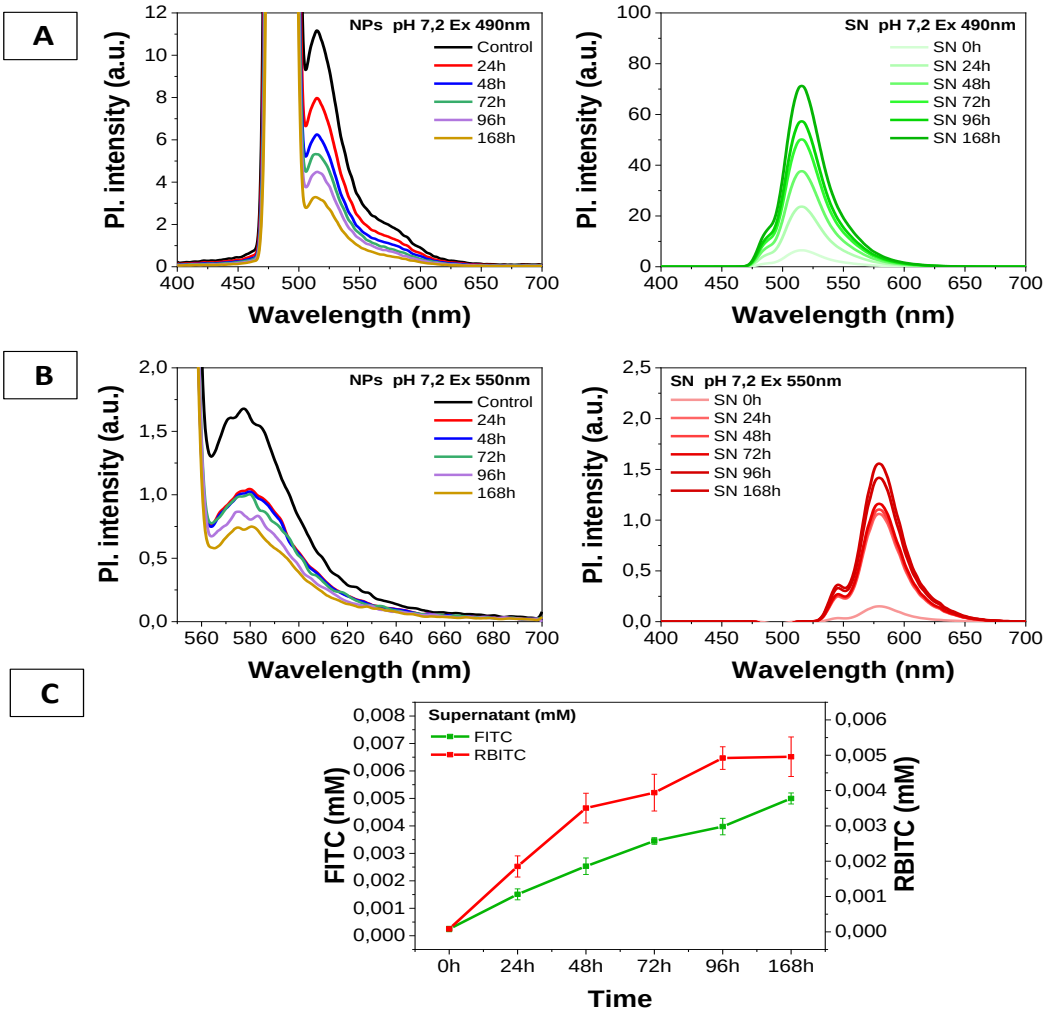

References

[1] C. B. Bottom, S. S. Hanna, and D. J. Siehr, "Mechanism of the ninhydrin reaction," *Biochem. Educ.*, vol. 6, no. 1, pp. 4–5, Jan. 1978, doi: https://doi.org/10.1016/0307-4412(78)90153-X.

[2] B. Fong and P. S. Russo, "Organophilic Colloidal Particles with a Synthetic Polypeptide Coating," *Langmuir*, vol. 15, no. 13, pp. 4421–4426, 1999, doi: 10.1021/la9815648.

Appendix C: Development of an Inorganic-Polymer Hybrid Nanostructure with Multimodal Imaging Capabilities As a Model for In vitro and In vivo Identification of Microplastics

C.1 Image analysis using STEM mode by electron microscopy of the different synthetic parameters for the synthesis of PS NPs by radical emulsion polymerization.

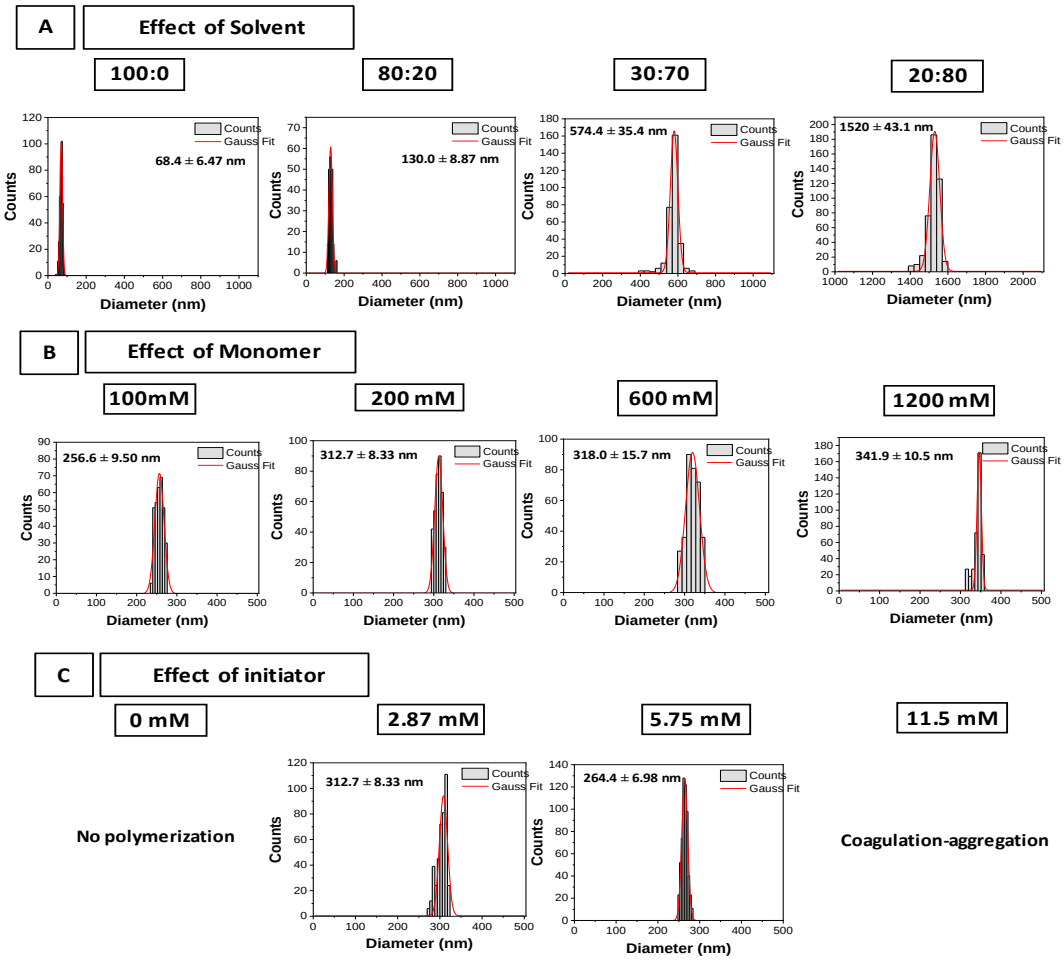

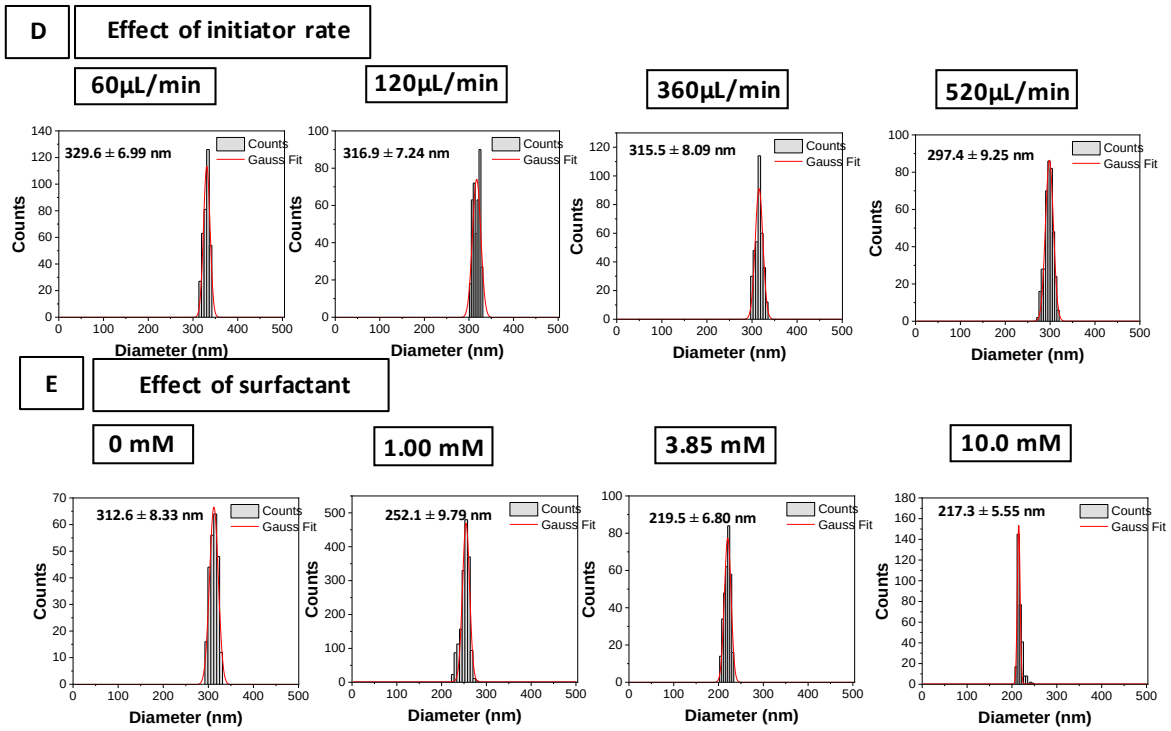

C.2 Emulsion seeded polymerization of the SiO_2-FITC NPs with and without TMSPMA.

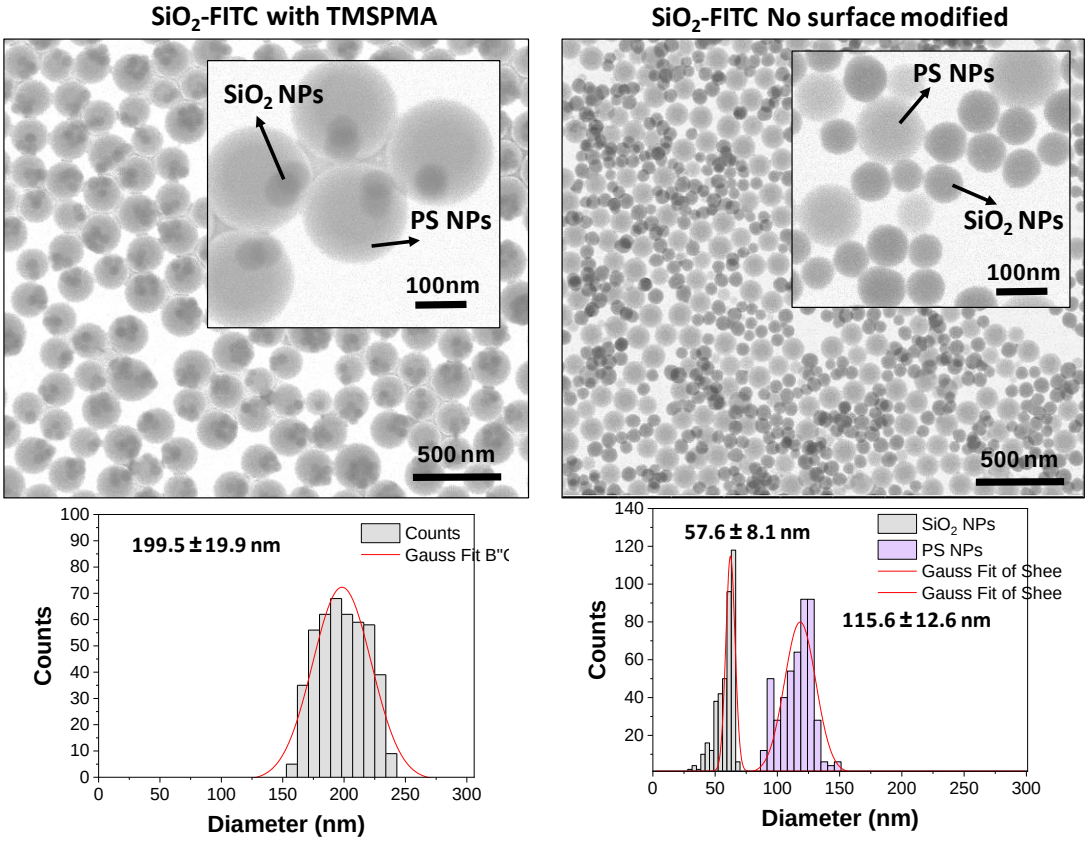

C.3 Extended physicochemical characterization of the Au@SiO_2 (60nm Au NPs) and SiO_2–FITC (200mn). (A) STEM images (B) calculates SD and UV-Vis spectrums.

Table D.1 Summary of detailed characterization by dynamic light scattering (DLS), measuring the zeta potential (mV), conductivity (mS/cm), Hydrodynamic size by number (nm), mean size and SD by STEM microscopy and UV-Vis spectroscopy.

NPs	Absorbance /$LSPR_{peak}$ (nm)	TEM size (nm)	SD (%)	DLS_{number} (nm)	PdI	ζ-potential (mV)	Media / pH	Cond. (mS/cm)
Au-SC	533.7	60.6 ± 4.1	6.7	70.6 ± 2.3	0.162	-26.7 ± 2.1	Water/ 6.0	0.2000
Au@SiO_2	545.8	99.1 ± 8.3	8.4	130.8 ± 4.2	0.068	-29.0 ± 2.1	Ethanol/ 8.1	0.00674
SiO_2-FITC	495	222.4 ± 21.1	9.5	280.2 ± 9.6	0.085	-40.4 ± 3.2	Ethanol/ 8.2	0.00865

	Concentration (mg/mL)	Particles number (NPs/mL)[a]	Concentration (FITC/NP)[b]
Au-SC	0.076	$3.24x10^{10}$	
Au@SiO_2	0.212	$9.72x10^{10}$	
SiO_2-FITC	6.06	$6.37x10^{12}$	19.500

a=theoretically calculated; b= calculated using calibration curve for FITC.

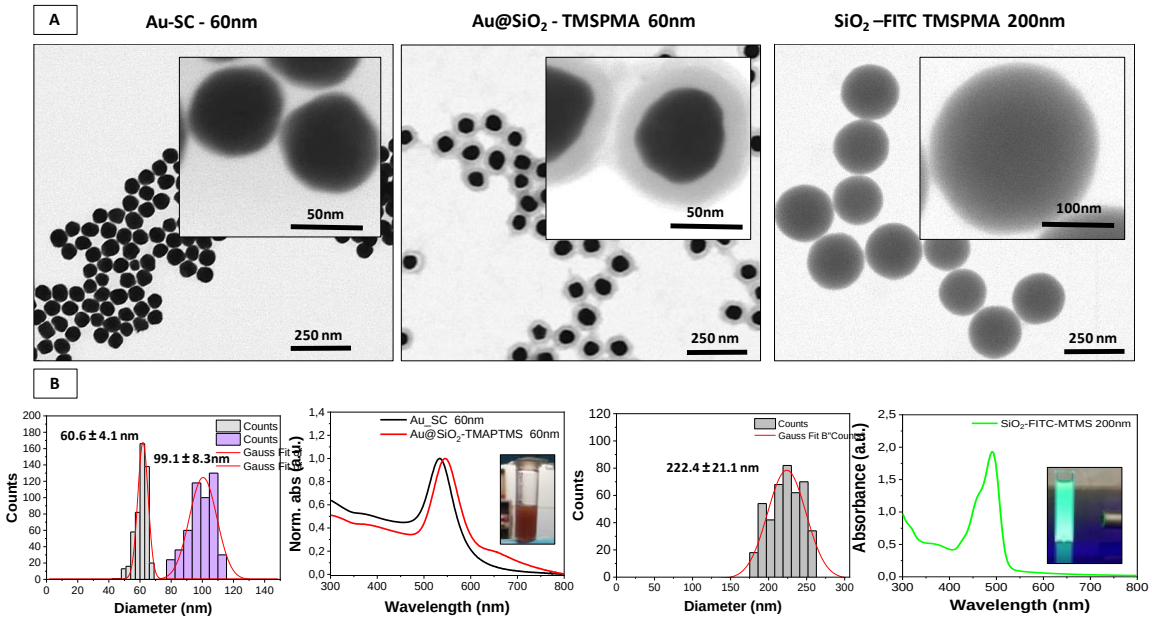

C.4 Image analysis using STEM mode by electron microscopy for growing a PS shell on top of the TMSPMA grafted SiO_2–FITC and Au@SiO_2 NPs increasing styrene (mM) (with 5% DVB) after emulsion polymerization.

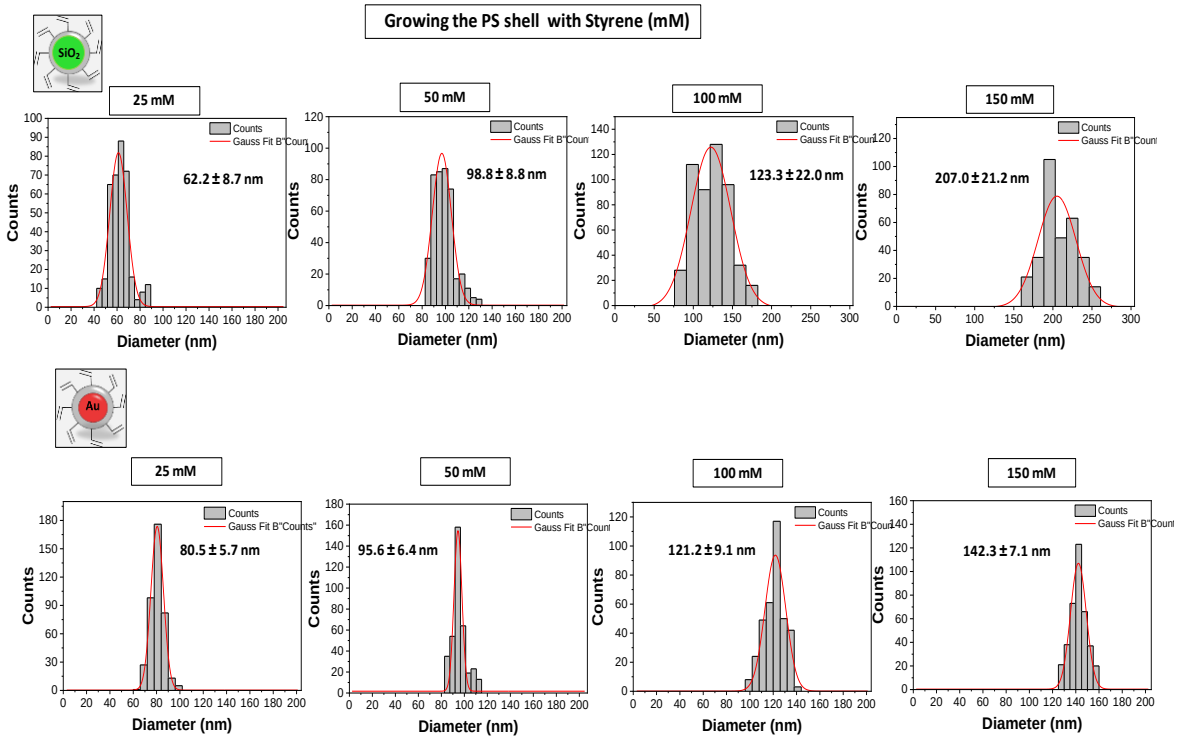

C.5 Development of The PEF core and their physicochemical characterization

The core-shell nanostructures composed of a noble metal and an oxide shell (metal@oxide) are one of the most composites architectures preferred, because allows the synergetic combination of the optical properties of the noble metal and a fluorescent molecule, separated by the oxide layer [1]. Among the noble metals, gold (Au NPs) were chosen as a suitable candidate due to their optical properties (LSPR) and silica (SiO_2) as an oxide layer due the easy surface modification and the possibility of entrap organic dyes for building optical probes. It is reported that the optical properties of a fluorescent molecule located near a metal nanoparticle are affected by the near-field electrodynamical environment [2]. This can cause an enhancement or quenching of the fluorescence depending on the distance between the dye and the metal surface. This phenomena of increased optical signal is called Plasmon Enhance fluorescence (PEF) [3], as explained in chapter 1. The PEF effect highly depends on two features: (i) the optimal distance between Au NPs and fluorophores to induce efficient excitation enhancement and (ii) the spectral overlap between SPR spectra of Au NPs and the emission spectra of fluorophores to lead to emission enhancement [4]. In this regard, to study the (PEF), core-shell Au@SiO_2 NPs were synthetized composed of a spherical gold nanoparticle Au NP as core and different

size of silica layers, used as spacers, for further covalently attached the fluorescent dye FITC, using APTES as crosslinker molecules. The purpose of this silica layer is to separate the dye molecule from the surface form the gold for avoid quenching effects, thereby increasing the fluorescence intensity. The chosen fluorescent molecule for achieve the PEF effect was the fluorescein isothiocyanate (FITC), having an exitation energy of λex = 495 nm and emission energy of λem= 525 nm. Therefore, the LSPR of the Au NPs have to be close to the emission wavelenght of FITC.

Synthesis of the core-shell gold silica nanoparticles with different SiO_2 shells (Au@SiO_2 NPs):

First, the Au NPs were synthesized to desirable diameter, following the seeded growth method via the reduction of $HAuCl_4$ by sodium citrate [5]. Once the NPs are cooled down to r.t, were directly conjugated with a solution of 11-mercaptoundecanoic acid (MUA) having a final concentration of 2mM, stirring at 600 r.p.m for about 24hours. Later, the Au NPs were coated with four different layers of (10, 20, 30, 40 nm of SiO_2 shell) by the modified Stöber method [6], using the Au cores as seeds. Characterization and summary is presented in **Table C2** and **figure C.5.1**.

Table D.2 Summary of detailed characterization by dynamic light scattering (DLS), measuring the zeta potential (mV), conductivity (mS/cm), Hydrodynamic size by number (nm), mean size and SD by STEM microscopy and UV-Vis spectroscopy.

NPs	$LSPR_{peak}$ (nm)	$LSPR_{Shift}$ (nm)	TEM diameter (nm)	SD (%)	DLS_{number} (nm)	PdI	SiO_2 shell (nm)
Au NPs	541.8	0	46.2 ± 4.4	9.5	50.6 ± 11.2	0.238	0.0
Au@SiO_2 10nm	546.9	5.1	61.5 ± 9.1	14.7	92.8 ± 3.4	0.135	7.80
Au@SiO_2 20nm	548.9	2.0	83.0 ± 6.8	8.1	125.6 ± 2.8	0.189	18.4
Au@SiO_2 30nm	551.2	2.3	105.4 ± 4.4	4.2	146.1 ± 4.3	0.165	29.6
Au@SiO_2 40nm	552.6	1.4	118.9 ± 9.2	7.7	169.6 ±6.7	0.133	36.3

As shown by the **figure C.5.1**, the morphology of the core-shell NPs remained monodisperse with different SiO_2 shells. The mean size and size distribution of the Au NPs increased along with the SiO_2 shell, as shown by the STEM images. Concomitant with this result, the hydrodynamic size by DLS also were higher and the LSPR of the Au NPs red-shifted towards higher wavelengths, as expected, due to a change in the dielectric environment on the nanoparticles surface.

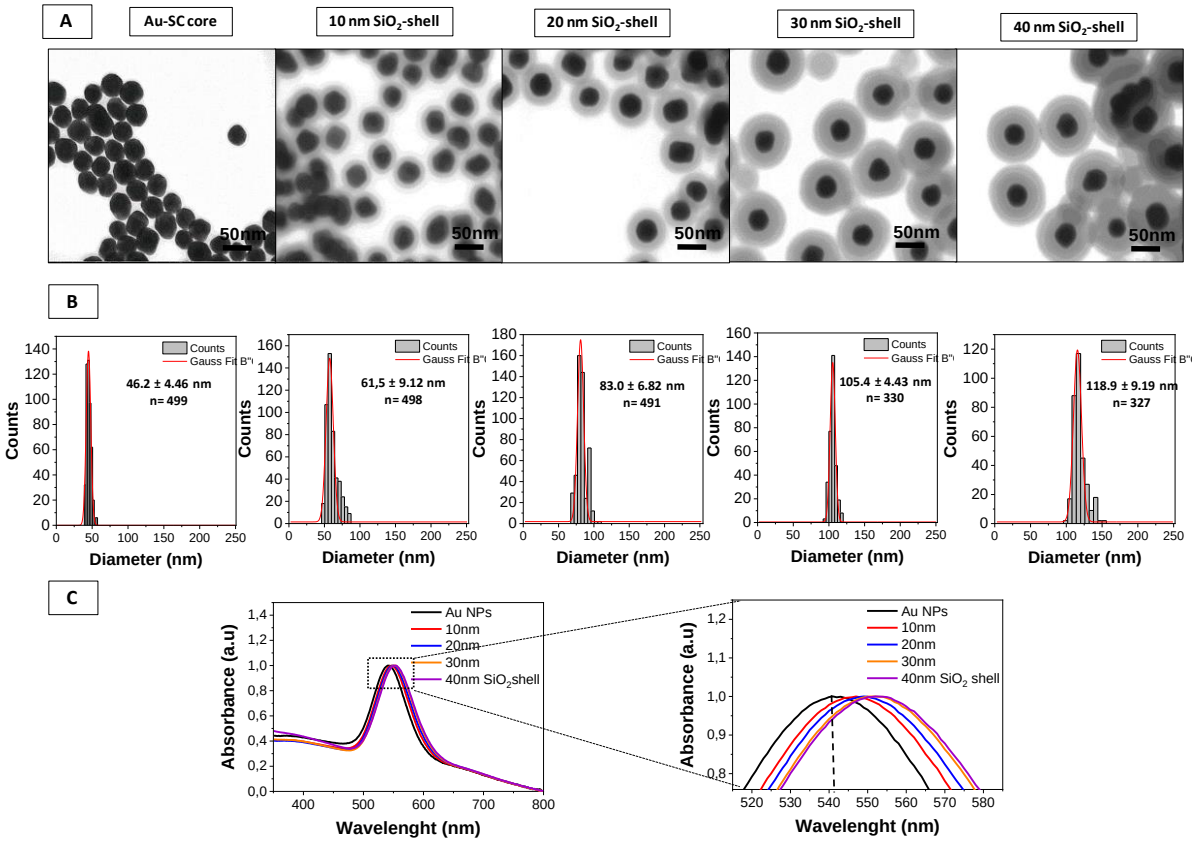

Figure C.5.1 Characterization of the SiO_2 shell formation for synthetize Au@SiO_2 NPs. From left to right Au cores and Au@SiO_2 NPs with increased shell size. (A) Representative (STEM) images. (B) Calculated size distribution profile of NPs. Mean size and Standard distribution was calculated at least counting 300 particles using software image J. (C) Absorbance spectra of the different NPs normalized. The characteristic LSPR peak of Au NPs is red shifted to longer wavelength after SiO_2 coating processes.

Once the different silica shells with different distances of the core shell Au@SiO_2 NPs were developed, a second silica shell having the fluorescent dye fluorescein-5-isothiocyanate (FITC) within the silica matrix were done by the Van blaaderen method [7], for producing Au@SiO_2@SiO_2-FITC NPs. After this, the NPs were purified for removing the unbound APTES-FITC molecules by centrifugation at 3.000g for 15 minutes twice and were dispersed again in anhydride ethanol to a final volume of 2 mL for the fluorescent measurements. Characterization presented in **figure C.5.2**.

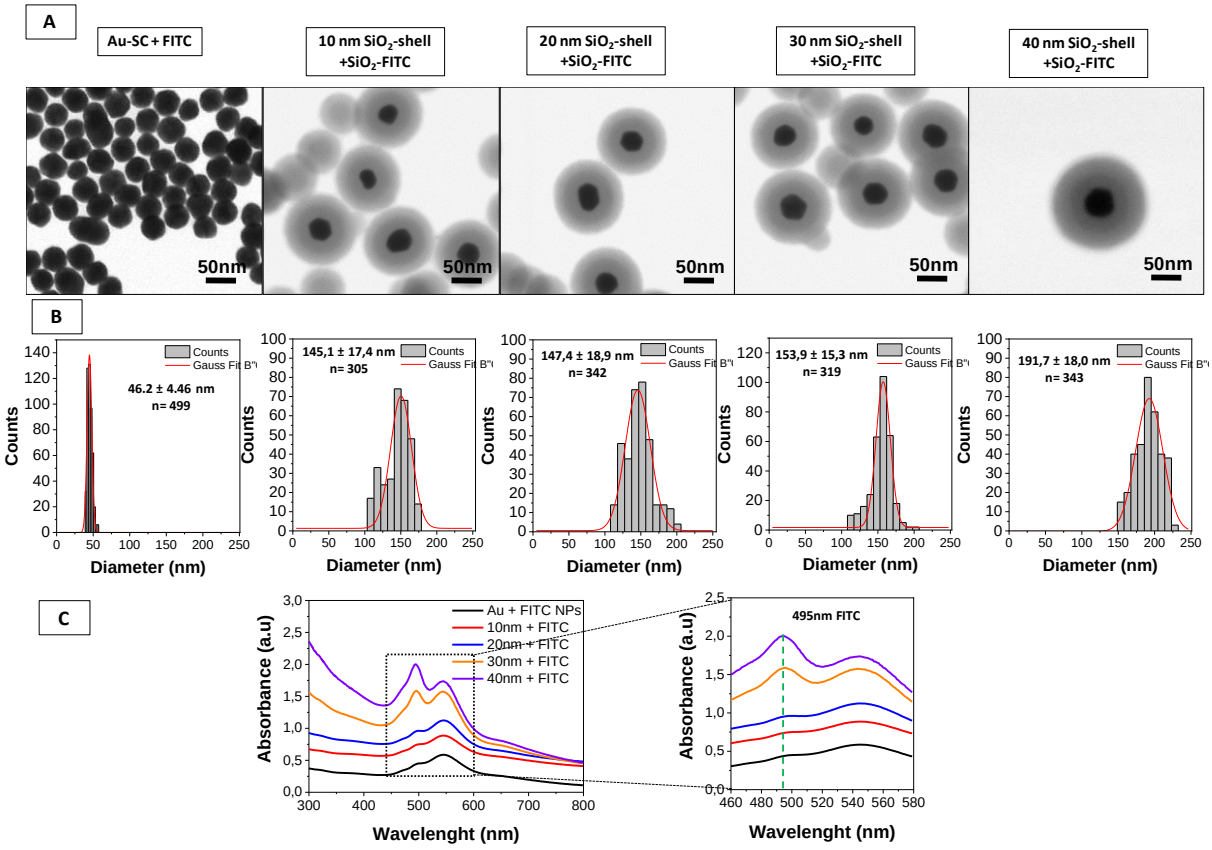

Figure C.5.2 Characterization of the Au@SiO_2@SiO_2-FTIC NPs after the incorporation of FTIC into the silica matrix. From left to right Au cores and Au@SiO_2 NPs with increased silica shells. (A) Representative (STEM) images. (B) Calculated size distribution profile of NPs. Mean size and Standard distribution was calculated at least counting 300 particles using software image J. (C) Absorbance spectra of the different NPs 1/10 dilution. The characteristic FITC absorbance peak at 495nm can be showed and the LSPR peak of Au NPs is buried as SiO_2 shell increases.

As shown in **figure D.5.2**, all the fluorescent core-shell Au@SiO_2@SiO_2-FITC NPs (from 10 to 40nm shell) were comparable in mean size and SD after the second silica coating with the FITC dye. The incorporation of the FITC molecules were assessed by the UV-Vis spectroscopy, in which it can observed the increased FTIC absorbance signal band at 495nm. The LSPR signal of the gold also can be observed, but was buried as the silica shell increases. The increase signal at shorter wavelength is signature of the silica shell due to the scattering.

Finally, the fluorescent enhancement was investigated recording the photoluminescence of the nanocomposites. The enhancement was characterized using the fluorescence enhancement factor (F):

$$F = I_{nanocomposite}/I_{released\ Dye\ (FITC)}$$

$I_{nanocomposite}$ is the fluorescence intensity of dye-doped nanocomposites measured in the fluorimeter; and $I_{released\ DYE}$ is the fluorescence intensity of released DYE without the metal core. The fluorescent enhancement was characterized by the calculation of the fluorescence enhancement factor (F), that is the diference between the fluorescent intensity of the doped core-shell gold silica nanoparticles and the released dye from the silica matrix once the the silica shell were disolved. The removal of silica layer from the AuNPs was accomplished by eroding the silica shell with NaOH 0.4M solution and separating the AuNPs by centrifugation. Results as follows:

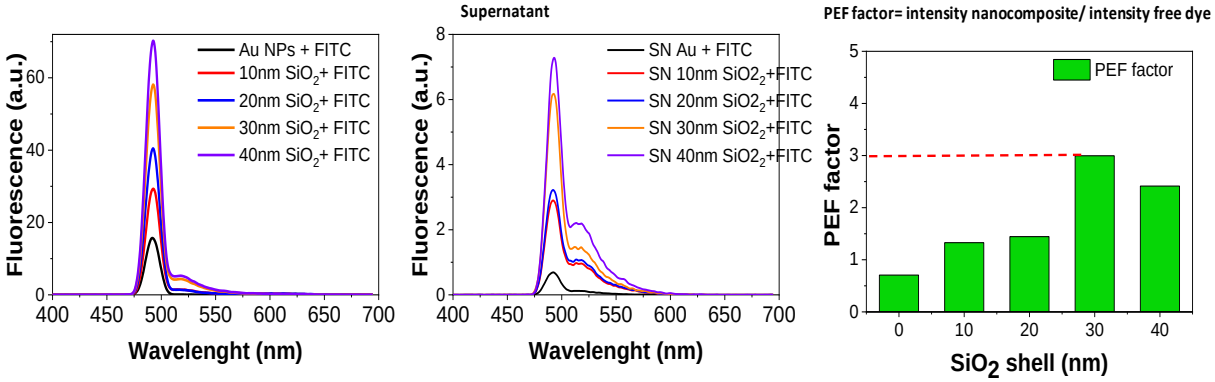

Figure D.5.3 Fluorescence enhancement characterization of the different core-shell Au@SiO_2@SiO_2-FITC nanoparticles with different SiO_2 layers as spacer. From left to right, PL emission spectra of the NPs loaded with FITC. PL emission fluorescence spectra of the supernatant after NaOH 0.4M treatment and calculated fluorescence enhancement factor of. The maximum enhance factor achieved was 3.00 using 30nm of SiO_2 shell as spacer. All the samples were measured with 1_10 dilution.

The above results showed that the distance between FITC and the AuNP could significantly affect the extent of the fluorescence enhancement at the nanoscale. A spacer thickness around 30nm, achieve the largest fluorescence enhancement factor of ~three fold (3). The fluorescence quenching effect was obvious when no spacer was used, indicating the importance of the distance between the dye molecules and the metal cores.

C.6 Fluorescence spectra of the FITC and FITC-APTES complex

Normalized absorption spectra of the fluorescein isothiocyanate (FITC) 3,0M and the formation of the adduct FITC-APTES at the same concentration, used for covalent entrapment of the dyes within the silica matrix. The excitation wavelength used is 480nm. The emission of the dye slightly shifted from 528nm to 532nm, but the fluorescent intensity was maintained. The Colloidal solution image of the FITC and the FITC-APTES adduct under white light and UV-light is presented. The reaction process did not alter the nature of the FITC dye after conjugation for 24h.

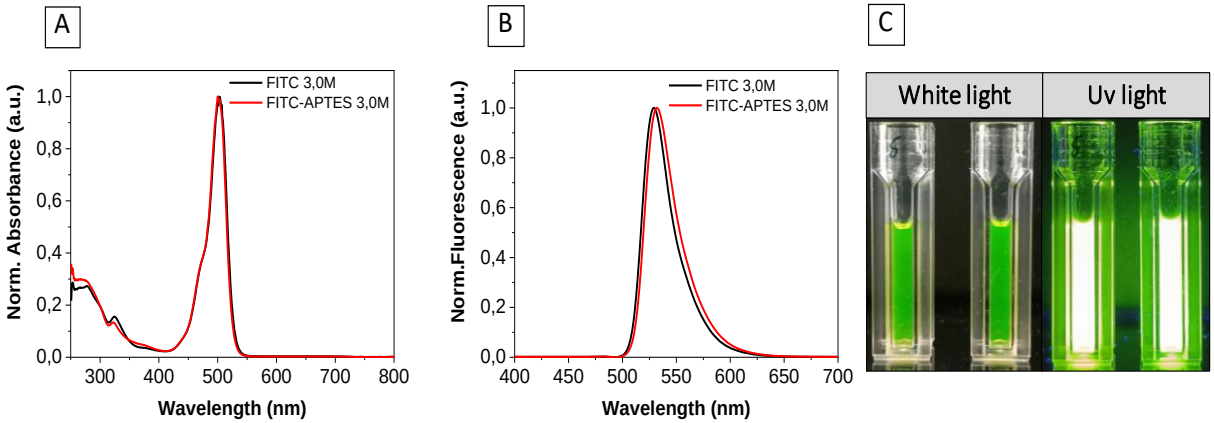

C.7 Determination of the PS content in the PEF-labelled PS NPs

The PS content of the NPs was determined by theoretical calculation of the relationship in concentration between Au gold to Polystyrene. In addition, a thermogravimetric analysis (TGA) were done for measuring the percentage of weight loss into the sample.

From the TGA curve, we can observe that the weight loss begins at around 200°C with a value of 98.63%, temperature which is in agreement to the melting point of PS ~ which is reported in the literature around 240°C. Thereafter, the curve exhibited a weight loss value of 47.2 % at around 600°C, that is related to the degradation and evaporation of PS shell. The boiling point of the PS is around 430°C, therefore we can say that the % de PS in the core-shell NPs is 51.5 %, or 2.58 mg, because 5.00mg of sample were used.

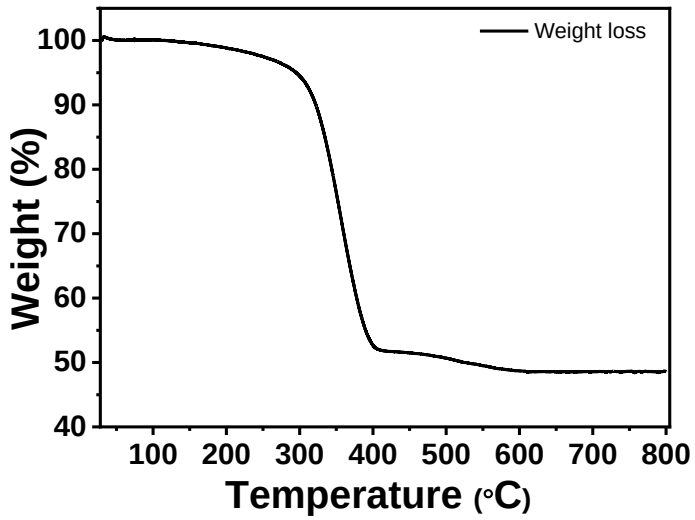

Theoretical calculation of the relationship in concentration between Au gold to Polystyrene using the ICP-MS for gold and TGA for PS

Concentration of PS by TGA= 51.5%

The total mass of the sample: $M_T = mAu(mg) + mSiO_2(mg) + mPS\,(mg)$

$$100 = mAu(mg) + mSiO_2(mg) + 51.5mPS\,(mg)$$

Calculate the mass of SiO_2 (Corona circular) = for 1NP

$$mAu(mg) + mSiO_2(mg) = 48.5\%M_T$$

We know that the mass is $mSiO_2 = \rho SiO_2 \times VSiO_2$

To calculate the mass of the SiO_2 corona we need to calculate the volume of the corona. For this, we made an assumption of 1 NP and we calculate the radius of the silica shell: SiO_2 shell was radius was 67.3nm, and the radius for the gold is 33.3nm

therefore:

The mass of 1NP is $mSiO_2 = \rho SiO_2 \times VSiO_2$

$$= 1{,}96x10^{-18}\ mg/nm^3 \times 4/3\pi\ (100.3nm)^3 - 4/3\pi\ (33.3nm)^3$$

$$= 7.98x10^{-12}mg$$

We also know that the mass of 1NP of Au 66.7nm = $2.9978x10^{-12}$ mg Au

Therefore, for calculate the total mass M_T =

$$mAu(mg) + mSiO_2(mg) = 48.5\%M_T$$

$2.997x10^{-12}$ mg Au+ $7.980x10^{-12}$mg SiO_2= 48.5/100 M_T

(($2.997x10^{-12}$ mg Au+ $7.980x10^{-12}$mg SiO_2) x 100)/48.5 = M_T

$$M_T = 2.263x10^{-11} \text{ mg}$$

Calculate the mass of PS for 1NP =

$$M_T = mAu(mg) + mSiO_2(mg) + mPS\,(mg)$$

$$mPS\,(mg) = M_T - mAu(mg) - mSiO_2(mg)$$

$$mPS\,(mg) = 2.263x10^{-11} \text{ mg} - 2.9978x10^{-12} \text{ mg Au} - 7.980x10^{-12}\text{mg } SiO_2$$

$$mPS\,(mg) = 1.165x10^{-11}\text{mg PS}$$

Finally, to see the relation in concentration between Au and the PS

$$mAu(mg)\ /mPS\,(mg) = 2.9978x10^{-12} \text{ mg Au} / 1.165x10^{-11} \text{ mg PS} = 0.257$$

$$\text{relationship} \quad mPS\,(mg) = 3.89 \times mAu(mg)_{ICP\text{-}MS}$$

Where in the sample of NPs PS (µg/mL) = 3.89x Au(µg/mL)ICP-MS = 482.4 µgPS/mL

= 3.89 x 124 µg/mL

= 482.4 PS µg/mL

C.8 Haematoxylin & eosin image analysis of the rehydrated tissue sections was done, revealing any morphological damage of the tissues

The haematoxylin & eosin image analysis of the rehydrated tissue sections was done, revealing any morphological damage of the tissues

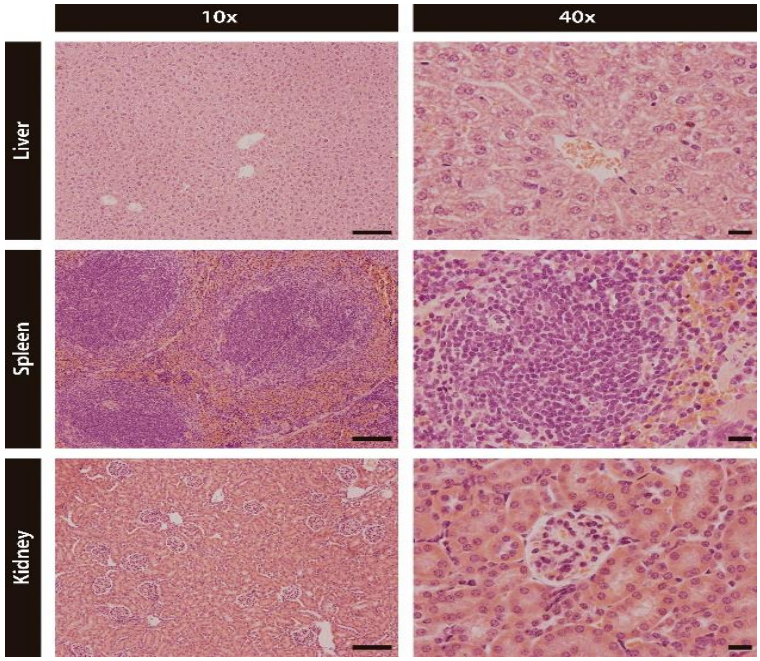

Scale bar 10x = 100um, 40x = 10um

References

[1] Y. Jeong, Y.-M. Kook, K. Lee, and W.-G. Koh, "Metal enhanced fluorescence (MEF) for biosensors: General approaches and a review of recent developments," *Biosens. Bioelectron.*, vol. 111, pp. 102–116, 2018, doi: https://doi.org/10.1016/j.bios.2018.04.007.

[2] O. G. Tovmachenko, C. Graf, D. J. van den Heuvel, A. van Blaaderen, and H. C. Gerritsen, "Fluorescence Enhancement by Metal-Core/Silica-Shell Nanoparticles," *Adv. Mater.*, vol. 18, no. 1, pp. 91–95, Jan. 2006, doi: https://doi.org/10.1002/adma.200500451.

[3] J.-F. Li, C.-Y. Li, and R. F. Aroca, "Plasmon-enhanced fluorescence spectroscopy," *Chem. Soc. Rev.*, vol. 46, no. 13, pp. 3962–3979, 2017, doi: 10.1039/C7CS00169J.

[4] S. Zhang, X. Xu, G. Zhang, B. Liu, and J. Yang, "One-pot one-step synthesis of Au@SiO2 core–shell nanoparticles and their shell-thickness-dependent fluorescent properties," *RSC Adv.*, vol. 9, no. 31, pp. 17674–17678, 2019, doi: 10.1039/C9RA02543J.

[5] N. G. Bastús, J. Comenge, and V. Puntes, "Kinetically Controlled Seeded Growth Synthesis of Citrate-Stabilized Gold Nanoparticles of up to 200 nm: Size Focusing versus Ostwald Ripening," *Langmuir*, vol. 27, no. 17, pp. 11098–11105, 2011, doi: 10.1021/la201938u.

[6] W. Stöber, A. Fink, and E. Bohn, "Controlled growth of monodisperse silica spheres in the micron size range," *J. Colloid Interface Sci.*, vol. 26, no. 1, pp. 62–69, 1968, doi: https://doi.org/10.1016/0021-9797(68)90272-5.

[7] A. Van Blaaderen and A. Vrij, "Synthesis and characterization of colloidal dispersions of fluorescent, monodisperse silica spheres," *Langmuir*, vol. 8, no. 12, pp. 2921–2931, 1992, doi: 10.1021/la00048a013.